

A study of the prevalence of patient body motion and its subsequent correction by  
projection consistency conditions

by

Chad Roger Ronald Nicholas Hunter

A thesis submitted to the Faculty of Graduate and Postdoctoral Affairs in partial  
fulfillment of the requirements for the degree of

Doctor of Philosophy

in

Medical Physics – Imaging

Carleton University

Ottawa, Ontario

© 2017, Chad R. R. N. Hunter

## **Abstract**

Patient motion is a common problem during dynamic PET scans for quantification of myocardial blood flow (MBF). The purpose of this study was to quantify the prevalence of body motion in a clinical setting, and evaluate with realistic phantoms the effects of motion on blood flow quantification, including CT attenuation correction artifacts that result from PET-CT misalignment. In addition we evaluated a consistency-based motion correction technique using noise added simulations.

A cohort of 236 sequential patients was analyzed for patient motion under resting and peak stress conditions by two independent observers. The presence of motion, affected time frames, and direction of motion was recorded. Based on these results, patient body motion effects on MBF quantification were characterized using the digital NURBS-based Cardiac-Torso (NCAT) phantom, with characteristic time activity curves (TAC) assigned to the heart wall (myocardium) and blood regions. Noise was added to sinograms using the analytical simulator ASIM.

In the patient cohort mild motion  $0.5 \pm 0.1$  cm occurred in 24%, and severe motion  $1.0 \pm 0.3$  cm occurred in 38% of patients. Motion in the superior/inferior direction accounted for 45% of all detected motion. Anterior/posterior direction motion accounted for 29%, and left/right motion occurred in 24% of cases. Computer simulation studies indicated that errors in MBF can approach 500% for scans with severe patient motion (up to 2 cm). The largest errors occurred when the heart wall was shifted left towards the adjacent lung region. Body motion effects were more detrimental for higher

resolution PET imaging (2 vs 10 mm FWHM), for the physically smaller phantom, and for motion occurring during the mid-to-late time frames. Motion correction of the reconstructed dynamic image series resulted in significant reduction in MBF errors. MBF bias was reduced further using global partial-volume correction, and using dynamic alignment of the PET projection data to the CT scan for accurate attenuation correction during image reconstruction.

To reduce MBF errors, new motion correction algorithms must be effective in identifying motion in the left/right direction, and in the mid-to-late time frames, since these conditions produce the largest errors in MBF.

## **Statement of Originality**

This thesis is original and represents the authors own work. All code was developed by the author with the exception of the 2-dimensional consistency metric provided by Dr. Adam M. Alessio of Washington University and any built-in MATLAB® functions. The prevalence data was primarily collected by Dr. Ran Klein with the author participating in the analysis of the patient data. All simulation data was generated by the author using in-house code developed in MATLAB®. Myocardial blood flow analysis of the simulated PET data was performed using FlowQuant analysis software, developed by Dr. Robert deKemp, Ran Klein and Jennifer Renaud at the Ottawa Heart Institute. All the work in this thesis was conducted under the supervision of Dr. Robert A. deKemp of the University of Ottawa Heart Institute, including compiling and revising manuscripts and all data analysis. The published documents and conference proceedings for which the author is responsible for, form the basis of this thesis and can be found on the next page.

**Peer Reviewed Papers:**

Chad R. R. N. Hunter, Ran Klein, Rob S. Beanlands, and Robert A. deKemp, *Patient motion effects on the quantification of regional myocardial blood flow with dynamic PET imaging*. Med. Phys. 2016; 43:1829-40.

**Papers submitted for Publication:**

Chad R. R. N. Hunter, Adam Alessio, Ran Klein, Rob S. Beanlands, and Robert A. deKemp, *Motion Correction for Cardiac PET Dynamic Imaging using Projection Consistency Conditions*. Medical Image Analysis. 2016; pending.

**Conference Abstracts:**

Chad Hunter, Ran Klein, Robert deKemp, R. Glenn Wells, and Amir Pourmoghaddas, *Patient body motion affects myocardial blood flow quantification with rubidium-82 PET imaging*. J Nucl Med, 2013; 54:541

Chad Hunter, Ran Klein, and Robert deKemp, *Correction for patient body motion in Rb-82 PET-CT: An NCAT simulation study*. J Nucl Med, 2014; 55:2054

Chad Hunter, Adam Alessio, and Robert deKemp, *Projection based patient body motion correction in Rb-82 PET-CT using consistency condition*. J Nucl Med, 2015; 56:486

## **Acknowledgements**

I'd like to thank Amir Pourmoghaddas and Owen Clarkin of the University of Ottawa Heart Institute for their help and expertise and various issues regarding PET. I'd also like to thank Dr. Adam Alessio of the University of Washington for his invaluable input on consistency conditions for PET imaging. Lastly, I'd especially like to thank my thesis advisor Dr. Rob deKemp for supporting both me and my research, and taking an active role in both the data analysis and formulation of protocols that ensured the highest quality data.

I'd like to thank the following financial institutions that contributed to my research, without whom this project would not have been possible: The University of Ottawa Heart Institute, and Carleton University.

Lastly, I'd like to thank my parents, who were always supportive of my work, and my father who tragically passed away May 2016.

## Table of Contents

<b>Abstract.....</b>	<b>ii</b>
<b>Statement of Originality .....</b>	<b>iv</b>
<b>Acknowledgements .....</b>	<b>vi</b>
<b>Table of Contents .....</b>	<b>vii</b>
<b>List of Tables .....</b>	<b>xi</b>
<b>List of Illustrations.....</b>	<b>xiii</b>
<b>1 Chapter: Literature Review.....</b>	<b>1</b>
1.1 Overview and History of PET Imaging .....	1
1.2 Motion Correction .....	9
1.2.1 Effects of motion.....	10
1.2.2 External tracking systems for motion correction .....	12
1.2.3 Image based motion correction methods.....	16
1.2.4 Reconstruction methods for motion correction.....	21
1.2.5 Additional methods for motion correction.....	23
<b>2 Chapter: PET Imaging and Simulation.....</b>	<b>25</b>
2.1 Radioactive Decay and the Production of Positron Emitting Isotopes.....	25
2.1.1 Positron Decay and Electron Capture .....	25
2.1.2 The Production of Positron Emitting Isotopes .....	28
2.1.3 Positron Annihilation .....	34
2.2 The PET Imaging System.....	35
2.2.1 PET Scanners .....	36
2.2.2 Data Acquisition, Projections and Sinograms.....	46
2.2.3 Scatter and Correction.....	52
2.2.4 Randoms and Correction.....	56

2.2.5	Correction for Prompt-Gamma Coincidence .....	58
2.2.6	Detector Dead Time and Pulse Pile-Up .....	60
2.2.7	Attenuation and Correction .....	66
2.2.8	Projection Consistency Conditions .....	69
2.2.9	Intrinsic and Reconstructed Spatial Resolution .....	71
2.3	Image Reconstruction from Projections .....	76
2.3.1	Filtered Back-projection.....	77
2.3.2	Iterative Reconstruction .....	80
2.3.3	OSMAPOSL Reconstruction in STIR.....	83
2.4	PET-CT Co-Registration.....	84
2.4.1	CTAC Artifacts from Left and Right Shifts.....	85
2.4.2	CTAC Artifacts from Anterior/Posterior and Superior/Inferior Shifts .....	87
2.5	Dynamic PET imaging and Blood Flow Quantification.....	88
2.5.1	The Compartment Model .....	89
2.5.2	Myocardial Blood Flow Estimation using FlowQuant© .....	95
2.6	PET Simulation .....	101
2.6.1	The Digital NCAT Phantom .....	102
2.6.2	Analytical PET Simulator (ASIM).....	105

**3 Chapter: Patient Motion Effects on the Quantification of Regional Myocardial Blood Flow with Dynamic PET Imaging ..... 109**

3.1	Introduction .....	109
3.2	Methods.....	111
3.2.1	Clinical Prevalence Cohort .....	111
3.2.2	Computer Phantom Simulations.....	113
3.2.3	Statistical Analysis .....	118
3.3	Results .....	119

3.3.1	Clinical Prevalence Cohort .....	119
3.3.2	Computer Phantom Simulations.....	121
3.3.3	Parameter Interaction Effects.....	125
3.4	Discussion.....	141
3.5	Conclusion.....	145
<b>4</b>	<b>Chapter: Motion Correction for Cardiac PET Dynamic Imaging using Projection Consistency Conditions.....</b>	<b>146</b>
4.1	Introduction .....	146
4.2	Methods .....	148
4.2.1	NCAT Dynamic Phantom .....	148
4.2.2	PET Noise Model.....	149
4.2.3	Dynamic PET Body Motion.....	151
4.2.4	Motion Correction.....	153
4.2.5	ROC Analysis of Motion Correction .....	158
4.2.6	Myocardial Blood Flow Analysis .....	159
4.3	Results .....	162
4.3.1	Motion Detection Results.....	162
4.3.2	MBF Analysis Results.....	168
4.4	Discussion.....	171
4.4.1	ASIM PET Noise Model.....	171
4.4.2	Motion Estimation.....	173
4.4.3	Motion Effects on MBF .....	174
4.4.4	Motion Correction.....	175
4.5	Study Limitations .....	175
4.6	Conclusion.....	176

<b>5 Chapter: Summary and Future work.....</b>	<b>177</b>
<b>Appendices.....</b>	<b>181</b>
Appendix A .....	181
Appendix B.....	188
<b>Bibliography or References.....</b>	<b>190</b>

## List of Tables

Table 2.1.1.1: Important radiation emissions from Rb-82 decay .....	26
Table 2.1.1.2: Common isotopes used in PET imaging [97,98] .....	28
Table 2.1.2.1: Cyclotron produced PET isotopes .....	32
Table 2.2.1.1: Desirable characteristics of a PET scintillation crystal. [104].....	40
Table 2.2.2.1: Comparison of the GEA and D690 PET scanners.....	52
Table 3.2.2.1: Computer simulation parameters (N=5,760 combinations).....	117
Table 3.3.2.1: Multivariate ANOVA analysis of the simulated parameter effects on MBF. ....	123
Table 4.2.3.1: Motion Simulations. ....	152
Table 4.2.5.1: ROC Confusion Matrix.....	158
Table 4.2.5.2: Characterization of Motion Parameters. ....	159
Table 4.3.1.1: Absolute bias in estimated motion, excluding sub-threshold values.....	165
Table 4.3.1.2: Segmental MBF values (mL/min/g) for the no-motion reference standard cases (n = 5 noise realizations) compared to ‘ideal’ noise-free simulations.....	167
Table A- 1: Analysis of variance (ANOVA) for computer simulation parameters – Part 1 .....	181
Table A- 2: Analysis of variance (ANOVA) for computer simulation parameters – Part 2 .....	182
Table A- 3: Analysis of variance (ANOVA) for computer simulation parameters – Part 3 .....	183

Table A- 4: Analysis of variance (ANOVA) for computer simulation parameters – Part 4	184
Table A- 5: Analysis of variance (ANOVA) for computer simulation parameters – Part 5	185
Table A- 6: Analysis of variance (ANOVA) for computer simulation parameters – Part 6	186
Table A- 7: Analysis of variance (ANOVA) for computer simulation parameters – Part 7	187
Table B- 1: Patient Demographics – Part 1	188
Table B- 2: Patient Demographics – Part 2	189

## List of Illustrations

Figure 2.1.2.1: Schematic of a cyclotron. Particle path is shown as a dashed red line originating at the source S. An alternating source is connected to dees A and B both held in vacuum.....	29
Figure 2.1.2.2: Basic schematic of an elution system, recreated from deKemp [100]. ....	33
Figure 2.1.3.1: Positron decay leading to an annihilation event results in the production of two gamma rays with equal energy and opposite momentum.....	35
Figure 2.2.1.1: diagram of band gap structure, production of electron hole pairs during conversion, migration of electron hole pairs during transport, and recombination resulting in emission of photon.....	38
Figure 2.2.1.2: schematic of a photomultiplier tube with detector block attached. ....	41
Figure 2.2.1.3: Schematic of a detector ring made of detector blocks (yellow) with attached photomultiplier tubes (blue). The crystals form an approximate ring with the scanner diameter defined from face-to-face on each side of the ring. ....	43
Figure 2.2.1.4: Coincident timing circuitry. ....	44
Figure 2.2.1.5: measured energy pulses from the photomultiplier tubes.....	44
Figure 2.2.1.6: coincident timing window showing two cases: (A) pulses not in coincidence and are therefore rejected and (B) pulses in coincidence. ....	45
Figure 2.2.2.1: Sinogram of a point source 'S'. Lines of response A, B, C and D from the point source are plotted on the displacement graph tracing out a sinusoidal function. ....	47
Figure 2.2.2.2: Example of some lines or response with (A) the septa in place, restricting the coincidence events to specific planes, and (B) the septa retracted allowing a larger angular acceptance along the scanner axis.....	48

Figure 2.2.2.3: Lines of response at the same angle grouped together at $0^\circ$ and $-45^\circ$ shown in (A). Stacking all the grouped sinograms by angle forms a single sinogram, as shown in (B). If we take a single projection at an angle for all slices we get stacked projection view (right side of (B)).	50
Figure 2.2.2.4: Example of some lines of response for direct planes only with numbered detector rings.	51
Figure 2.2.3.1: Representation of a scatter coincidence. Emission occurs at a point within the heart and one of the 511 keV photons scatters off of the bone of a rib. Blue line is the recorded line of response.	54
Figure 2.2.3.2: Example of a sinogram profile (black solid line) and estimated scatter from the tails of data (red dotted line).	56
Figure 2.2.4.1: Representation of a random (accidental) coincidence. The blue line is the resultant line of response.	57
Figure 2.2.5.1: Representation of a prompt coincidence. The blue line is the resultant line of response, the green line is the prompt gamma ray, and the red lines are the gamma rays from the annihilation event.	59
Figure 2.2.6.1: Count-rate measurement as a function of total phantom activity. Ideal count rate would be linear increasing in proportion to total activity. True count rate is affected by dead time.	62
Figure 2.2.6.2: Paralyzable and non-paralyzable dead time responses. Length of dead time (yellow blocks) is extended for the paralyzable response when subsequent pulses arrive close together.	62

Figure 2.2.6.3: Count rate measurement of true, scatter and random events (counts per second [cps]) as well as total prompt (T + R + S) events as a function of activity in the phantom or patient. .... 65

Figure 2.2.7.1: Example of a PET scan reconstructed without (top) and with (bottom) attenuation correction..... 67

Figure 2.2.7.2: Example of an ACF sinogram. On the right projections for a single angle along the slices are shown. The ACF values are unit-less and calculated using the negative of the exponent in equation 2.2.7.3. .... 69

Figure 2.2.9.1: Point spread function of a detector crystal. The sensitivity to various possible lines of response (LOR's) is shown as a triangle function. .... 72

Figure 2.2.9.2: Asymmetric blurring due to photon penetration into an adjacent crystal. Line of response due to penetration is shifted towards the center of the field of view. ... 73

Figure 2.2.9.3: Sampling error caused by the geometry of the LOR's in the field of view. Note the center of the field of view has far fewer LOR's..... 74

Figure 2.2.9.4: Schematic of spill-in and spill-out and the resultant measured tissue profile. True tissue profiles are shown as red rectangles. Due to spatial smoothing activity spills into adjacent regions..... 76

Figure 2.3.1.1: Simple example of back projection. Forward projection in section (A) at 0°, 45° and 90° leads to 3 projections. Parts (B), (C) and (D) the 90°, 45° and 0° projections are back-projected onto a blank matrix, while parts (E) and (F) are for scaling. .... 78

Figure 2.3.1.2: Example of the effect of the number of projections on image reconstruction. The image given at 100 and 500 projections is nearly identical to the original image. ....	80
Figure 2.3.2.1: The Poisson distribution for measuring radiation (for $\lambda = 4$ ). ....	81
Figure 2.4.1.1: Reconstruction artifacts resulting from PET-CT misalignment. CT used for attenuation correction shown on top. The PET-CT reference standard is perfectly aligned to the CT and has no CTAC artifacts. Left (-x) and right (+x) shifts in the PET data from the CT are also shown. ....	86
Figure 2.4.2.1: Reconstruction artifacts resulting from PET-CTAC misalignment. Anterior (towards chest: +y) and posterior (towards back: -y) shifts in the PET data from the CT are shown. In addition superior (towards the head: +z) and inferior (towards feet: -z) are also shown. ....	87
Figure 2.5.1.1: Sodium-potassium active transport. (A) Sodium ions bind to the protein. (B) Phosphorylation: phosphate from ATP binds to the NaK-ATPase protein causing it to change shape. (C) Sodium ions are released into the blood while potassium ions bind to the protein. (D) Potassium bound to the protein causes the phosphate to be released. Protein changes shape again releasing potassium into the cytoplasm.[158] .....	91
Figure 2.5.1.2: 1-Tissue compartment model for Rb-82. ....	92
Figure 2.5.1.3: 2-Tissue compartment model. ....	93
Figure 2.5.2.1: Orientation and selection of the LV heart wall. Identification of the heart wall is shown in transaxial (A) and sagittal (mid vertical long axis (VLA)) (B) slices. Reorientation of the myocardium to LV reference frame is shown in mid horizontal long axis (HLA) (C) and basal short axis (SA) (D). ....	96

Figure 2.5.2.2: Example of short axis slices of the heart wall (left). Short axis slices 1 to 18 are used for myocardial blood flow quantification (A). Blood pool regions (A, B and C) are shown, along with the identification of the left atrium (B). The right ventricle is shown in green but not used in this work. The left atrium is shown in red. .... 97

Figure 2.5.2.3: Example of time activity curves measured by FlowQuant© for blood flow quantification. The red curve is the blood input function. The blue dots are the measured myocardium values and the blue line is the estimated compartment model function. The total blood volume ( $TBV = FLV$ ) and  $K1$  rate constant are also shown..... 99

Figure 2.5.2.4: Example of contour maps of the heart wall and the resultant polar map. 99

Figure 2.5.2.5: Example of polar maps generated from FlowQuant©. .... 100

Figure 2.5.2.6: 5-Segment model and its anatomic regions..... 101

Figure 2.6.1.1: Various NCAT CT phantoms used in this thesis. .... 103

Figure 2.6.1.2: Digital NCAT myocardium model with myocardium and blood pool regions shown. .... 104

Figure 2.6.1.3: Example of time activity curves assigned to various organs in the body. .... 105

Figure 2.6.2.1: Example of the production of a noise added sinogram without attenuation from a voxelized NCAT phantom..... 108

Figure 3.2.2.1: (A) NCAT phantom for PET-CT simulation studies showing the CT used for attenuation correction (CTAC). (B) Homogeneous tracer distribution is observed in the LV myocardium on the PET-CT images with perfect alignment used as the no-motion reference-standard. (C) A case with CT misalignment +2 cm in the X -direction shows

the resulting CTAC artifacts evident in the LV lateral wall and lung margins (red arrows).  
..... 114

Figure 3.2.2.2: Computer simulations used to produce the patient motion and correction test cases. Attenuation of the projection data is denoted by '÷' and attenuation correction by '×'. ..... 116

Figure 3.3.1.1: (A) prevalence of patient (rigid) body motion, (B) directions and (C) times of mild or moderate body motion. .... 121

Figure 3.3.2.1: FlowQuant® analysis results for the reference standard case with no PET motion (and perfect CTAC alignment). The PET slices used to sample the LV myocardium and blood time-activity curves are shown top-left, with contours of the LV and blood-pool regions shown top-middle. 3D surface contour maps of the sampled LV uptake (2-6 min average) are shown top-right for left lateral, posterior and anterior views. The resulting time-activity curves and kinetic model parameter values used for blood flow quantification are shown in the middle panel. MBF polar-maps using regional  $[1 - \text{TBV}(\text{total blood volume})]$  and global  $[1 - \text{TBV}_{\text{mean}}]$  partial-volume corrections (PVC) are shown in the bottom panel. .... 122

Figure 3.3.2.2: Reduction in MBF error associated with each independent simulation parameter compared to the worst-case combination of parameter settings (global PVC, late CTAC alignment, high resolution, X direction,  $\pm 2$  cm magnitude, 60,120 s time of motion shift, no motion correction (MC)). Error bars are  $\pm$  SD reflecting changes in the Sign and Segment parameters. .... 124

Figure 3.3.3.1: Three-parameter interaction of CTAC alignment, motion direction and sign was highly significant ( $F=248$ ;  $p<0.0001$ ) by multivariate ANOVA. Data are shown

for 2 cm magnitude (no motion correction and CTAC-alignment correction values are combined) (N=1920). Median values are shown next to the box-plots. Polar map example is for 2 cm left shift (-X) of the PET data at 60 s, with late CTAC alignment. .... 126

Figure 3.3.3.2: Three-parameter interaction of motion correction, direction and magnitude was highly significant ( $F=35$ ;  $p<0.001$ ) by multivariate ANOVA. Data are shown for 2 cm magnitude only (N=2880). Median values are shown next to the box-plots. Polar map example is for 2 cm left shift of the PET data at 60 s, with no motion correction. .... 127

Figure 3.3.3.3: Three-parameter interaction of motion direction time of motion shift and magnitude was highly significant ( $F = 40$ ;  $p<0.001$ ) by multivariate ANOVA. Data are shown for 2 cm magnitude only (N=1920). Median values are shown next to the box-plots. Polar map example is for 2 cm posterior shift (-Y) of the PET data at 60 s with no motion correction. .... 128

Figure 3.3.3.4: Three-parameter interaction of motion direction, segment and PVC was highly significant ( $F = 20$ ;  $p<0.001$ ) by multivariate ANOVA. Data are shown for late CTAC alignment (data with no motion correction and CTAC-alignment correction are combined), for shifts at 60 and 120 s in the right (+X) and superior (+Z) directions (N=160 (A); N=160 (B)). Median values are shown next to the box-plots. Both X and Z directions are shown with regional (A) and global (B) PVC. Polar map examples are for 2 cm right shift (+X) of the PET data at 120 s, with CTAC alignment and with regional (A) and global (B) PVC. .... 130

Figure 3.3.3.5: Three-parameter interaction of motion direction, segment and PVC was highly significant ( $F = 20$ ;  $p<0.001$ ) by multivariate ANOVA. Data are shown for early

CTAC alignment (data with no motion correction and CTAC-alignment correction are combined), for shifts at 60 and 120 s in the right (+X) direction and superior (+Z) directions (N=160 (A); N=160 (B)). Median values are shown next to the box-plots. Both X and Z directions are shown with regional (A) and global (B) PVC. Polar map examples are for 2 cm superior shift (+Z) of the PET data at 60 s (A) with CTAC-alignment correction, and 2 cm right shift (+X) of the PET data at 120 s (B) with no motion correction. .... 132

Figure 3.3.3.6: Three-parameter interaction of motion direction, segment and PVC was highly significant ( $F = 20$ ;  $p < 0.001$ ) by multivariate ANOVA. Data are shown for late CTAC alignment (data with no motion correction and CTAC-alignment correction are combined), for shifts at 60 and 120 s in the left (-X) and inferior (-Z) directions (N=160 (A); N=160 (B)). Median values are shown next to the box-plots. Both X and Z directions are shown with regional (A) and global (B) PVC. Polar map examples are for 2 cm inferior shift (-Z) of the PET data at 60 s (A) with CTAC-alignment correction, and 2 cm left shift (-X) of the PET data at 120 s (B) with no motion correction. .... 134

Figure 3.3.3.7: Three-parameter interaction of motion direction, segment and PVC was highly significant ( $F = 20$ ;  $p < 0.001$ ) by multivariate ANOVA. Data are shown for early CTAC alignment (data with no motion correction and CTAC-alignment correction are combined), for shifts at 60 and 120 s in the left (-X) and inferior (-Z) directions (N=160 (A); N=160 (B)). Median values are shown next to the box-plots. Both X and Z directions are shown with regional (A) and global (B) PVC. Polar map examples are for 2 cm left shift (-X) of the PET data at 60 s (A) and (B) with no motion correction. .... 136

Figure 3.3.3.8: Three-parameter interaction of motion direction, segment and PVC was highly significant ( $F = 20$ ;  $p < 0.001$ ) by multivariate ANOVA. Data are shown for late CTAC alignment (data with no motion correction and CTAC-alignment correction are combined), for shifts at 60 and 120 s in the up (+Y) (A) and down (-Y) (B) directions ( $N=160$  (A);  $N=160$  (B)). Median values are shown next to the box-plots. Both regional and global PVC are shown. Polar map examples are for 2 cm up shift (+Y) of the PET data at 60 s (A) with no motion correction, and 2 cm down shift (-Y) of the PET data at 60 s (B) with CTAC-alignment correction. .... 138

Figure 3.3.3.9: Three-parameter interaction of motion direction, segment and PVC was highly significant ( $F = 20$ ;  $p < 0.001$ ) by multivariate ANOVA. Data are shown for early CTAC alignment (data with no motion correction and CTAC-alignment correction are combined), for shifts at 60 and 120 s in the up (+Y) (A) and down (-Y) (B) directions ( $N=160$  (A);  $N=160$  (B)). Median values are shown next to the box-plots. Both regional and global PVC are shown. Polar map examples are for 2 cm up shift (+Y) of the PET data at 60 s (A) with no motion correction, and 2 cm down shift (-Y) of the PET data at 60 s (B) with CTAC-alignment correction. .... 140

Figure 4.2.2.1: PET noise model based on global count-rate characteristics [23] measured for 2 different phantom sizes: 20 cm (A), and 35 cm (B). .... 151

Figure 4.2.4.1: Motion-correction algorithm illustrated for the simulated NCAT torso phantom (35 cm phantom) with attenuation misalignment artifact (Misaligned) and without attenuation artifact (Realigned) by minimizing  $\Phi$ , to maximize consistency in the attenuation-corrected projection sinograms. Noise is added with ASIM, attenuation is added using an aligned CT and dividing by the attenuation factors. Images in the shaded

region represent non-motion-corrected processing and are shown for information only are not necessary for implementation of the method.....	157
Figure 4.2.6.1: Initial identification of the heart wall is shown in (A). Short axis slices of the heart wall are shown in (B). The blood pool regions used as the input function for blood flow are shown in (C). The resultant countours of the left ventricle are shown in (D). FlowQuant Analysis of myocardial blood flow (MBF) using regional (Flow) and global (FlowRC) partial volume corrections are shown in (E) as polar maps. The time activity curves are shown in (F).....	161
Figure 4.3.1.1: Estimated (measured) versus simulated motion values (mean $\pm$ standard deviation) for the 20 cm (red) and 35 cm (green) phantom noise models. Dashed lines are lines of best fit. The blue solid line corresponds to perfect agreement (measured = simulated).....	162
Figure 4.3.1.2: Bias in estimated motion values for all dynamic frames using the 20 cm (A) and 35 cm (B) phantom noise models.....	163
Figure 4.3.1.3: ROC curve showing the true-positive rate (TPR) and false-positive rate (FPR) for different values of estimated vs. simulated motion, using all 56,160 motion values. Thresholds are also shown, as well as the Youden's indexes (lines that connect the linear line to the ROC curve).....	164
Figure 4.3.2.1: Absolute MBF error for 20 and 35 cm phantom sizes, before motion correction. ....	168
Figure 4.3.2.2: MBF (mL/min/g) polar-maps from FlowQuant analysis for the 35 cm phantom. The top row (A) shows an uncorrected case using 2 cm motion at 120 s. After motion-correction by the projection-based method artifacts are greatly reduced as shown	

in (B), as compared to the reference standard case with no motion shown in (C). Motion correction of the reference standard case is also shown in (D)..... 169

Figure 4.3.2.3: Motion-corrected vs. uncorrected absolute errors in segmental MBF values (N = 3,600 per group). Errors up to 4000 % occur for uncorrected data for the 35 cm phantom – those extreme outliers are not shown..... 170

Figure 4.4.1.1: Simulated count rates by frame for the 20 cm phantom..... 172

Figure 4.4.1.2: Simulated count-rates by frame for the 35 cm phantom. .... 172

Figure 4.4.1.3: Measured count-rates by frame for a 90 kg patient..... 173

## List of Abbreviations

<b>AC</b>	<b>Attenuation Correction</b>
<b>ACF</b>	<b>Attenuation Correction Factor</b>
<b>ANOVA</b>	<b>Analysis of variance</b>
<b>ARMi</b>	<b>Alternative Radiopharmaceutical for Myocardial Imaging</b>
<b>ASIM</b>	<b>Analytical Simulator</b>
<b>ATP</b>	<b>Adenosine Triphosphate</b>
<b>AUC</b>	<b>Area Under the Curve</b>
<b>BGO</b>	<b>Bismuth Germanium Oxide</b>
<b>BMI</b>	<b>Body Mass Index</b>
<b>CAD</b>	<b>Coronary Artery Disease</b>
<b>CT</b>	<b>Computed Tomography</b>
<b>CTAC</b>	<b>CT Attenuation Correction</b>
<b>D690</b>	<b>Discovery 690</b>
<b>DOF</b>	<b>Degrees of Freedom</b>
<b>ECG</b>	<b>Electrocardiogram</b>
<b>FDG</b>	<b>Fluorodeoxyglucose</b>
<b>FOV</b>	<b>Field Of View</b>
<b>FWHM</b>	<b>Full Width at Half Maximum</b>
<b>GE</b>	<b>General Electric</b>
<b>GEA</b>	<b>GE Advance</b>
<b>HLA</b>	<b>Horizontal Long Axis</b>

<b>HU</b>	<b>Hounsfield units</b>
<b>IF</b>	<b>Inter-Frame</b>
<b>INTEX</b>	<b>Internal-External</b>
<b>IR</b>	<b>Infrared</b>
<b>IS</b>	<b>Inter-Scan</b>
<b>LA</b>	<b>Left Atrium</b>
<b>LED</b>	<b>Light Emitting Diodes</b>
<b>LOR</b>	<b>Line Of Response</b>
<b>LV</b>	<b>Left Ventricle</b>
<b>LYSO</b>	<b>Lutetium-Yttrium Oxyorthosilicate</b>
<b>MAF</b>	<b>Multiple Acquisition Frame</b>
<b>MAP</b>	<b>Maximum A Posteriori</b>
<b>MBF</b>	<b>Myocardial Blood Flow</b>
<b>MC</b>	<b>Motion Correction</b>
<b>MLAA</b>	<b>Maximum Likelihood Activity and Attenuation</b>
<b>MLEM</b>	<b>Maximum Likelihood Expectation Maximization</b>
<b>MPI</b>	<b>Myocardial Perfusion Images</b>
<b>MR</b>	<b>Magnetic Resonance</b>
<b>NCAT</b>	<b>NURBS-Based Cardiac-Torso</b>
<b>NEC</b>	<b>Noise Equivalent Count</b>
<b>NEMA</b>	<b>National Electrical Manufacturers Association</b>
<b>OSEM</b>	<b>Ordered Subset Expectation Maximization</b>
<b>OSL</b>	<b>One-Step-Late</b>

<b>OSMAPOSL</b>	<b>Ordered Subsets Maximum A Posteriori One-Step-Late</b>
<b>PET</b>	<b>Positron Emission Tomography</b>
<b>PGC</b>	<b>Prompt-Gamma Compensation</b>
<b>PMT</b>	<b>Photo Multiplier Tubes</b>
<b>PVC</b>	<b>Partial-Volume Corrections</b>
<b>RA</b>	<b>Right Atrium</b>
<b>RMS</b>	<b>Root Mean Square</b>
<b>ROC</b>	<b>Receiver Operator Characteristic</b>
<b>ROI</b>	<b>Region Of Interest</b>
<b>RPM</b>	<b>Real-time Positioning Management</b>
<b>RV</b>	<b>Right Ventricle</b>
<b>SA</b>	<b>Short Axis</b>
<b>SBW</b>	<b>System Band-Width</b>
<b>SD</b>	<b>Standard Deviation</b>
<b>SPECT</b>	<b>Single Photon Emission Tomography</b>
<b>SSS</b>	<b>Simulated Single Scatter</b>
<b>STIR</b>	<b>Software for Tomographic Image Reconstruction</b>
<b>TAC</b>	<b>Time Activity Curve</b>
<b>TBV</b>	<b>Total Blood Volume</b>
<b>TOF</b>	<b>Time-Of-Flight</b>
<b>UV</b>	<b>Ultraviolet</b>
<b>VLA</b>	<b>Vertical Long Axis</b>

## List of Appendices

Appendix A..... 181

Appendix B..... 188

# 1 Chapter: Literature Review

## 1.1 Overview and History of PET Imaging

Positron emission tomography (PET) is an imaging modality that takes advantage of the physics of radioactive decay and positron annihilation. The imaging process begins with trace amounts of a radiolabeled molecule injected into a patient and is therefore called a tracer. Due to its chemical properties and to blood flow to various tissues, over time the tracer will distribute to various organs according to unique tracer kinetics. Passive measurements are made by scintillation crystals that convert the emitted radiation from the positron annihilation events into electrical signals that facilitate counting of the number of events over time (see **chapter 2.2**). Counts are collected over time and can be reconstructed to show the distribution of the tracer within the volume of the patient (see **chapter 2.2**). By using various correction techniques, the true radioactive concentration of the tracer over time can be measured. This information can then be used for example in blood flow quantification to aid in the detection of coronary artery disease (CAD). Further details about blood flow quantification are outlined in **chapter 2.5**. Tracer kinetics from a PET scan reflect the biological function of various tissues and organs, and thus PET imaging is a type of functional molecular imaging.

The production of radioactive tracers will be covered in **chapter 2.1.2**. Briefly, several blood flow tracers are currently used clinically such as: Tl-201 chloride, Tc-99m tetrofosmin for single photon emission tomography (SPECT) imaging; N-13 ammonia, and O-15 water for PET imaging.[1] Tracers like N-13, O-15 and Tl-201 are all cyclotron produced, whereas Tc-99m is eluted from a Mo-99 generator, for which the parent isotope is produced by nuclear reactor. In 2009 the unscheduled shutdown of the chalk river reactor

triggered a global shortage of the Mo-99 generator.[2] This created a crisis in the medical imaging community causing some centers to investigate alternatives to Tc-99m for perfusion imaging. One such alternative is Rb-82, since it doesn't require an on-site cyclotron and has a lower radiation dose than Tc-99m; however, the parent isotope Sr-82 is cyclotron produced. In response to this shortage, the multicenter trial alternative radiopharmaceutical for myocardial imaging (ARMI) study was launched to assess the viability of Rb-82 as an alternative to Tc-99m perfusion.[3] Recent research has shown that Rb-82 is a viable alternative with some advantages over Tc-99m, namely that it doesn't rely on reactor isotope production, has a lower dose and is excellent over Tc-99m-SPECT for assessment of myocardial blood flow and coronary flow reserve.[4] However, the initial capital cost is a limiting factor for most centers with typical PET scanners costing 2 to 3 times a SPECT scanner. One drawback of Rb-82 imaging is the roughly double per patient cost to that of Tc-99m-SPECT, largely due to the high cost of the Sr-82/Rb-82 generator.[5]

The history of rubidium begins in 1883 when Dr. Sydney Ringer compared the chemical properties of potassium in the ventricle of a frog's heart to other chemical substances.[6] The experiment involved simulating blood flow by inserting a perfusion tube in the groove separating the ventricles from the atria and syphoning fluid. The results from the experiment showed that rubidium and potassium have nearly identical chemical properties so far as their methods could determine at the time. This experiment is important because it was the first to definitively demonstrate that rubidium could be used in place of potassium for investigation into heart muscle function. In the late 19<sup>th</sup> century Henri

Becquerel discovered radioactivity, and shortly afterwards investigations using radioactive rubidium and potassium were published.[7]

One of the first in-vivo studies with radioactive potassium-42 was conducted by Greenberg et al in 1938 on rats.[8] They found that potassium has high uptake in liver, kidney, heart, muscle, stomach and large intestine. Two years later in 1940 more comprehensive studies were performed using K-42 in rats, cats, frogs and rabbits, by sacrificing the animals at specified times and measuring radioactivity in their tissues using a Geiger-Muller tube.[9,10] They found a similar uptake in tissues to Greenberg et al but also looked at whole body uptake. What they found was that potassium distributes throughout the body, but higher uptake was found in the heart, liver, kidneys, and lungs. In testes, skin, erythrocytes and brain the uptake was much lower. In the same year Noonan et al investigated the uptake of potassium-42 for active muscles in rats.[11] Rats had their leg muscles electrically stimulated for 1 hour and were sacrificed, then the tissues were dissolved in nitric acid. The radioactivity was measured in a Geiger-Muller tube. Two groups of rats were used, one set of normal rats and a control group which had the nerve to the muscle cut so stimulation was not possible. They showed that uptake of potassium was directly related to blood flow to the muscle and the amount of stimulation, which is the biological basis of tissue perfusion imaging using Rb-82.

The use of rubidium to detect CAD began in 1954 when Love et al used Rb-86 to evaluate CAD in canines.[12] They discovered that the ratio of rubidium to plasma was higher than potassium to plasma for most organs, which suggested a higher absorption rate of rubidium in these tissues. However, for the myocardium they determined that the uptake was comparable to potassium, and thus could be used as a potassium analogue. These

results were further confirmed by Relman and Kilpatrick.[13,14] Specifically, Kilpatrick determined that rubidium concentrates more than potassium in liver, kidney, intestine, heart muscle and spleen, but less so in brain and bone; however it concentrates in equal amounts to potassium in muscle and red blood cells.

One of the first CAD studies in humans with rubidium (Rb-86) was performed in 1957 by Love et al.[15] The goal of the study was to determine if there was a difference in Rb-86 uptake in healthy versus unhealthy hearts with a view towards detection of CAD. Blood samples were obtained from human volunteers with the aid of fluoroscopy to select key areas for blood extraction. The potassium concentrations in the samples were determined by flame photometry, and the concentration of Rb-86 was determined using a Geiger-Muller tube. Due to study limitations, the heart wall could not be localized. Results showed a decrease in uptake by the body as a whole for CAD patients, and a 57 % increase in the concentration of rubidium in the plasma compared to healthy patients. The decrease was attributed to a decrease in plasma flow to high uptake organs such as the liver, lungs, heart and kidneys and a redistribution to organs with normally lower uptake. Therefore, the tracer was redistributed to organs of lower uptake/perfusion and not due to a change in tissue extraction. The important finding was that the change in activity concentration is a measure of blood flow and not tissue extraction efficiency.

Due to low uptake of rubidium in a healthy brain, one early use of rubidium and PET was to test the integrity of the blood brain barrier.[16,17] Another early use of PET imaging was in localization of brain tumors as suggested by Wrenn et al in 1951.[18] The PET scanner consisted of thallium-activated sodium iodide Na(Tl) scintillation crystals. Photomultiplier tubes were used for signal amplification. To calibrate the device they used

an oscilloscope to observe coincident events as oblique reflections. Eventually this led to the development of the first clinical PET scanners for use in brain imaging.[19] Two gamma cameras rotating around the field of view were used to capture coincident events around the patient.

In the 1970's x-ray computed tomography (CT) was developed for clinical anatomical imaging.[20,21] In the early 70's Chelser developed a 3D PET reconstruction technique.[22] An external positron source was used to correct for attenuation in the transmission scans. Also, investigation was made on the effects on the number of projections on the reconstruction quality.[22] The first tomographic PET system (PC-I) was developed in 1972.[19] This PET system used 2-dimensional detector arrays with rotating and translating detector banks and stored data on magnetic drums. In 1973 Roberston et al proposed using a complete 32-ring detector system rather than rotating detectors.[23] Memory on this scanner was stored in an XDS Sigma II digital computer. Coincidence window was set to 40-100 ns, and any detected events not corresponding to the expected 511 keV energy could be rejected. The next generation of PET scanners was developed in 1976 (PC-II) and remained the only commercial PET system for human and animal studies for the next decade.[19] Early comparisons between the PET tracer Rb-81 and the SPECT tracer Tl-201 were made for myocardium imaging.[24] For PET images the acquisition time was 20 minutes and for SPECT it was 60 minutes. No differences were observed between these two tracers, which was the first indication that rubidium could be used in place of the more commonly used SPECT tracers.

In 1980 Budinger et al used Rb-82 to measure blood flow to the heart for the first time in canines and human CAD patients.[25] This was one of the earliest uses of the

Donner 280-Crystal PET scanner with Rb-82, and was one of the first scanners to use a complete ring of crystals. Canines were used as a control group, and rubidium uptake was measured in the dogs before and after simulated CAD by surgical ligation. This gave them a baseline to compare with the human case studies that were evaluated using time activity curves of the myocardium and blood pool regions obtained by sequential transverse section imaging. The ratio of uptake in left ventricle vs blood pool regions were used to estimate blood flow, and Rb-82 was infused at a constant rate to obtain equilibrium images. They validated their results using radiolabeled microsphere studies. The results indicated that Rb-82 could compete with tracers like Tl-201, N-13-ammonia and K-38 for early detection of CAD in humans. In addition it was noted that Rb-82 had a lower radiation dose than competing tracers and did not rely on the use of an on-site cyclotron.

Further validation studies with Rb-82 were conducted by Selwyn et al in 1982 on 6 canines and 10 humans (5 cardiac patients and 5 normal volunteers).[26] The canine study results revealed that as blood flow increases, myocardial uptake increases by a smaller amount. Humans were studied at rest and at stress. Stress was induced in normal subjects by getting them to do 24 to 32 kJ of work, cardiac patients could only do 11 to 21 kJ of work due to their physical condition. Normals showed a 16 % increase in uptake from stress relative to rest, whereas the CAD patients had obvious localized defects of activity in regions of the myocardium linked to disease. In 1983 a more detailed study on Rb-82 PET perfusion was conducted by Goldstein et al on 28 canines.[27] Blood flow measurements were made with Rb-82 dynamic PET and microspheres. The goal was to test the accuracy of Rb-82 for different blood flow rates. What they found was for low flow rates (0.1 ml/min/g) Rb-82 underestimated the true value, and that blood flow rate

measurements were linear up to 2.5 ml/min/g; for flow rates greater than 2.5 ml/min/g the uptake increased in a non-linear way and Rb-82 blood flow estimates were therefore underestimated. The important finding is that patients with mild CAD have flow values within this range; therefore, for Rb-82 to be useful these effects need to be accounted for. Tracer uptake is the product of blood flow and extraction, and one of the issues was the effects of first-pass extraction fraction, which is the fraction of tracer transported into the trapped-space divided by the total amount delivered during the initial phase of circulation after tracer introduction. By measuring the tracer extraction fraction as well as uptake, and correcting for first-pass extraction both the high and low flow rate effects could be compensated for. This established Rb-82 PET perfusion as a viable and accurate blood flow measurement tool.

One of the first major human studies for Rb-82 PET perfusion was done in 1986 by Goldstein et al, on 18 CAD patients and 14 normals.[28] The research goal was to safely track the progress of CAD in patients using serial Rb-82 PET perfusion studies. Results showed that Rb-82 could correctly diagnose CAD patients (independently verified by patient history and angiography) and normals with one exception due to abnormal lung activity which prevented diagnosis. Later human studies using Rb-82 by Stewart et al compared the accuracy of Rb-82 with Tl-201.[29] Patients with known or suspected CAD were chosen consisting of 52 men and 29 women. The sensitivity (also known as the true positive rate) the specificity (also known as the true negative rate), and the diagnostic accuracy was evaluated. Results showed that Rb-82 had 84 % sensitivity, 88 % specificity and 85 % accuracy; whereas Tl-201 had 84 % sensitivity, 53 % specificity and 79 % accuracy. In addition, pharmacological and physical stress testing showed no difference

with respect to sensitivity, specificity and accuracy. The short half-life of Rb-82 (76 s) allowed for fast rest-stress studies which is desirable for patients who often suffer from arthritis and have trouble exercising or enduring long scans.[30]

In the 90's x-ray CT was combined with PET for anatomical localization of tracer distribution and improved attenuation correction.[31,32] Attenuation correction is needed to compensate for photon scatter and absorption in order to reconstruct the true activity concentration within organs and tissues, and will be discussed further in **chapter 2.2**. In 1990 Demer et al investigated using dipyridamole-induced coronary arteriolar vasodilation (for simulation of stress) for detection of CAD using Rb-82 and N-13-ammonia.[33] The study compared invasive angiograms with the results from PET scans in CAD patients and normal subjects. Results showed an absolute decrease in the activity concentration of any image region for stress compared to rest for patients with known CAD. In addition, this decrease was related to the flow rate to the heart muscle, and the choice of tracer did not affect the results. These results were followed up by Garza et al in 1997 for Rb-82 in a study involving 45 CAD patients.[34] They showed that rest/stress count ratios with dipyridamole-stress PET imaging can predict the presence of CAD.

In 2001 Sdringola et al used dipyridamole-stress PET imaging on 90 subjects.[35] The purpose of this study was to investigate whether or not asymptomatic CAD could be detected with the tracer N-13-ammonia. This showed that risk factors and family history are good predictors of the potential for someone to develop CAD. Further studies by Bateman et al in 2006 and Mc Ardle et al in 2012 have compared Rb-82 PET imaging to technetium-99m SPECT.[36,37] Both studies showed that despite advances in SPECT imaging, PET imaging had superior diagnostic accuracy.

In the 90's PET systems with photomultiplier tubes (see **chapter 2**) shielded from the effects of high magnetic fields were developed.[38] These were initially developed to increase spatial resolution since due to the Lorentz force, the positrons will annihilate closer to their emission point. In 1997 Shao et al used this technology to combine PET with magnetic resonance (MR) for brain imaging.[39] This merger of PET with MR has continued to the present day, but the deployment has been slow due to the high cost of such systems, the challenge of integrating PET with the high magnetic fields present in MR, translating MR images into usable attenuation correction maps and the lack of research into its clinical benefits.[40–42]

## **1.2 Motion Correction**

The main goal of myocardial blood flow quantification is accomplished using dynamic PET imaging. This will be covered in greater detail in **chapter 2.6**, but is briefly mentioned here to introduce the topic of the patient motion problem. Dynamic imaging involves acquiring PET data to measure the tracer concentration in a tissue/organ in sequential time frames, which generates a time-activity curve. Kinetic modeling uses the arterial blood input function and tissue tracer concentration curves to extract physiological information such as blood flow to the heart wall (in units of ml/min/g). One of the assumptions in kinetic modelling is that the tissue components do not move. In addition, in clinical practice, only one CT is typically acquired for attenuation correction of all dynamic frames. Patient motion causes CTAC (CT attenuation correction) artifacts due to the misalignment between the CT and PET data for frames that have moved relative to the CT, and therefore the spatial invariance of the tissue components assumed for accurate kinetic modeling are

violated. This causes errors in the blood flow quantification and will be covered in greater detail in **chapter 3**. This chapter discusses several motion correction methods. Many of these methods were developed for cardiac/respiratory or head motion correction but may be applicable to patient body motion correction.

### **1.2.1 Effects of motion**

The need for proper CTAC alignment has been published as early as the late 1970's. In a paper by Ostertag et al it was noted that the largest CTAC errors occur in regions near the boundary of the organs. This is particularly true for organs that have very different densities.[43] Early techniques for measurement of the attenuation data involved using a rotating Ge-68/Ga-68 long-lived isotope as a known photon source and measuring the photon attenuation caused by the patient.

One of the earliest attempts to quantify effects of patient motion in PET cardiac imaging was in 1992 by McCord et al.[44] Misalignment was artificially introduced to patient data, including 1 and 2 cm translations and 36° rotations to the attenuation correction factor (ACF)/PET alignment. The study only looked at the changes to the myocardial wall activity and not to blood flow quantification. This was accomplished by manual selection of a short-axis slice through the middle of the heart wall and manually selecting 8 regions of the myocardium in this slice. The mean activity in each of these regions was used for analysis. They observed an increase from the true activity in the lateral wall by 28 % for a 2 cm right shift, and for a left shift a more severe increase was observed for the septal wall instead of the lateral wall. Upward shifts of 2 cm produced a 13 % increases in the apparent activity in the posterior wall and decreases of 19 % in the

anterior wall. A 2-cm downward shift caused increases of 16% in the anterior wall and decreases of 18 % for the lateral wall. For a rotation of 18° (counter clockwise) the lateral wall region decreased an average 24%. For a -18° rotational (clockwise) shift, the anterior region decreased by 15%, whereas the lateral wall increased by 11%.

A pivotal study on motion prevalence and clinical effects was conducted by Loghin et al in 2004 in a patient population using Rb-82.[45] This study used the older Ge-68 rotating source method to measure the attenuation correction scans, with acquisition times of 10-20 minutes. They found that 21 % of all motion cases (n = 1,177) had visible artifacts due to attenuation-emission misalignment. They also evaluated early vs late attenuation correction scans. For early alignment they found that 31 % had artifacts whereas for late alignment only 16 % had artifacts. They also found that smaller hearts were more prone to attenuation-emission mis-registration, and that the downward displacement of the diaphragm after dipyridamole injection was a significant source of motion.

A similar study to Loghin et al was performed by Gould et al with Rb-82 in 2007 but using PET-CT.[46] Both helical CT and cine CT (repeated image acquisitions at each bed position) were used for attenuation correction. The cine CT data was averaged and aligned to the locations of the PET slices. They found that CTAC artifacts caused 40 % of patients to have false positive defects. It was also found that short CT acquisitions do not account for the average attenuation of constantly changing structures during breathing over longer PET emission scan times and that cine averaging reduced this effect.

A comprehensive review of motion effects was performed by Burrell et al in 2006 in a patient population of Tl-201 SPECT scans.[47] The study indicated that a 3.25 mm (0.5 voxel) shift did not cause a detectable effect. A 6.50 mm (1 voxel) shift caused an

effect that was not usually clinically significant. And shifts of 13.0 mm (2 voxels) or more could be significant clinically. In addition, they found that motion occurring in the middle of a scan was worse than motion near the beginning or end of a scan and that gradual motion was less detrimental than abrupt motion. They also found that axial motion (superior/inferior) was more detrimental than lateral (left/right or anterior/posterior) motion, but also the reverse was also found. A more complicated type of motion covered by this paper was that of cardiac creep. Cardiac creep is the gradual drift of the internal heart position over time. If a patient exercises or is nervous and breathes heavily the lungs expand which causes the average heart position to shift downward. Then over time when the patient relaxes the lung displacement returns to normal, which causes the heart to shift upward to its original position. Organ creep is worse when imaging is acquired too soon after stress, and the recommendation from this paper was to begin PET scans 15-30 minutes after exercise or 45-60 minutes after pharmacological induced stress. They also noted that despite their recommendations cardiac creep may also occur under resting conditions.

### **1.2.2 External tracking systems for motion correction**

To correct for patient motion, the deviation from an original position must be determined. One method is to use an external tracking system. This works by measuring the change in body position, typically using a marker fixed to the skin of the patient. One of the issues with external tracking is that the internal motion of the organs can be complex and may not track with the motion of the external body (e.g. the skin), especially for cardiac imaging. Despite the limitations, several studies have shown that it is a useful method for

characterizing when motion has occurred, and external tracking has seen widespread use in brain imaging since the head can be treated as a ridged body.

An early external tracking system was developed by Green et al in 1994 for brain imaging.[48] Their method used the tracking of a low-frequency alternating magnetic field generated by an electromagnet attached to the patient to track patient motion. Later in 1995 Ruttimann et al published an optical tracking system also for brain imaging.[49] The optical tracking device used a laser directed at a mirror fixed to the patient with a dental mold. When the patient moved the angular deflection of the laser was measured to determine the amount of motion.

Video monitoring of patient head motion with correction was reported in 1997 by Picard et al.[50,51] Motion tracking was accomplished by monitoring the position of light emitting diodes (LED) on the patient using two CCT cameras. A similar tracking system was reported by Goldstein et al in 1997 but using miniature incandescent lights.[52] When motion above a certain threshold was detected, the system split the data up into a separate frame. All frames were then reconstructed independently and realigned before reassembling of the dynamic data. This is known as the multiple acquisition frame (MAF) method. As pointed out by Ruttimann et al, one of the limitations of the MAF method is the tradeoff that must be made between the motion threshold and acquisition length.[53] For instance, a high motion threshold ensures longer acquisition lengths and thus higher count rate statistics but neglects motion that occurs within a frame. A lower threshold accounts for motion within a frame but will result in multiple acquisition frames with poor count rate statistics, which in turn adversely affects the quality of the reconstructed images.

Passive optical tracking systems have also been reported as early as 1999 by Lopresti et al using the Polaris™ tracking system for brain imaging.[54] Unlike the previous system using LEDs, this tracking system used infrared (IR) sources to illuminate passive IR reflectors placed on the patient. The advantage is that the sensors can be made very small since they do not need a power source. Another optical tracking system was developed by Nehmeh et al in 2003 using IR markers for radiotherapy respiratory gating. [55] The goal was to reduce respiratory motion artifacts for radiation therapy in PET lung imaging. This was unusual in that the markers were not placed on the patient, but on a block of lightweight plastic attached to the thorax to track respiratory motion.

One of the very first attempts of cardiac motion correction using O-15-labelled water was in 2005 by Naum et al.[56] This technique was unique in that it used radioactive markers and employed both manual and automated motion correction. Both the manual and automated correction realigned the images to a reference frame based on the displacement of the markers from the reference image. Automated correction was achieved by the registration of point pairs (where the markers were) placed on the reference image and on the image to be registered using a least squares registration algorithm. One important finding was that the frequency of motion in frames was more common at stress (45 % pharmacologic, 80 % exercise) than at rest (18 %). Also, they found that either automated or manual correction methods worked well, and that the number of frames with motion and the severity of motion dropped significantly with motion correction enabled. In addition, it was noted that ideally motion correction should rely on cardiac markers and not external markers; however, placing markers within the patient is not feasible. Another external tracking system using radioactive markers was reported by Nehmeh et al in

2003.[55] The markers consisted of a F-18 fluorodeoxyglucose (FDG) point source affixed by a rod to the chest and a Styrofoam block. Respiratory motion can be tracked by measuring the movement of the point source at the end of the rod as the patient breaths.

A purely optical tracking system was developed by Kyme et al using stereo-optical motion tracking.[57,58] The stereo images are used to track high-contrast checkered motifs which can be printed on paper and attached to the patient. Motion tracking can be done for 6 degrees of freedom at a rate of 30 Hz, and is used for small animal motion tracking. A different optical tracking system was published in 2012 by Noonan et al using a 3D depth sensor (Microsoft Kinect) for head motion in 6 degrees of freedom.[59] The depth sensor uses IR lasers to calculate the distance to surfaces of objects in its field of view. This data is used to create a 3D model of the patient. When the patient moves, a global transform is determined that describes the change in position and can be used to reposition the patient data.

A study characterizing the effect of motion on MBF was completed by Koshino et al in 2012 using O-15-labelled water in 10 patients.[60] Inter-scan (IS) and inter-frame (IF) motion was measured using external markers with an optical tracking system; however transmission and emission alignment were not corrected. Average IS and IF frame motion ranged from 2 mm to 10 mm. MBF was reported as the mean of all segments, and correction for motion showed a 1 % to 21 % change in MBF following correction.

In 2011 Liu et al published a paper on internal-external (INTEX) motion estimation for respiratory motion correction in phantoms and patients.[61] External motion was measured using a Real-time Positioning Management (RPM™) gating system that uses optical tracking of reflective external markers on a block fixed to the patient or phantom.

The assumption made is that the tumor in the lung is correlated with the external breathing motion of the body. To track internal motion, the list mode data was binned into 1 s dynamic frames. All frames were then aligned to a common reference frame using the RPM tracking information and summed together and reconstructed. The CT was aligned to the reference frame using the consistency conditions for 2D Radon transforms.[62]

In 2014 an external tracking system using positron emitting markers from list mode data was developed by Chamberland et al.[63] The algorithm can detect multiple markers placed on the subject, activities ranged from 92.5 kBq to 150 kBq. The method begins with determining an estimate for the markers initial position. Each coincident line that crosses a point closest to the estimated marker position should form a circle. The true marker position is located along the circumference of this circle, opposite the estimate. Markers can be tracked in real time with updated positions every 500 ms. The algorithm was evaluated using Monte Carlo and physical phantom studies. They found that a marker could be tracked with 0.8 mm precision.

### **1.2.3 Image based motion correction methods**

A more direct way to measure the motion is to use image-based methods. By comparing frames with motion to a reference frame assumed to not have motion, parameters that define this motion can be estimated. Then these frames can be realigned to the reference frame and thus correct for motion. Some methods do not compensate for the CT/PET misalignment that causes CTAC errors. One way to correct for the CTAC artifacts could be to reconstruct the frames using CT images aligned to each individual frame, then realign

the frames at the end of the process to correct for CTAC and PET misalignment. However, this effectively doubles the reconstruction time.

Methods using cine CT have been developed for cardiac motion correction such as that published in 1991 by Song et al.[64] These methods use multiple CT images taken in rapid succession to capture heart motion. A 4D CT imaging technique for respiratory motion compensation was developed by Nehmeh et al.[65] One major issue with these methods is the increase in CT radiation dose, making it hard to justify its use in a clinical setting for cardiac imaging.

For cardiac PET imaging an early attempt for motion correction was conducted by Muzik et al in 1993.[66] They used manual realignment of the heart wall by using edge-enhanced images of the epicardial and endocardial edges of the heart wall. A reference ellipse was fitted to the short axis slices of the late frame where the heart wall was well defined. Frames where the ellipses did not align with the edges were realigned manually. Similar work was done by Khurshid et al by segmenting the heart wall in PET and CT. However, in this case an alignment was done automatically by calculating motion vectors derived from the average distance between the heart wall boundaries on the CT and PET data.[67]

In 1995 a post reconstruction patient body motion correction algorithm was published by Friston et al for PET and MRI in brain imaging.[68] It works by minimization of the sum-of-squares between two images. They found that non-linear approaches to minimization were not as good as a least squares approach, this is due to the fact that the least squared approach was able to find the global minimum rather than local minima.

A method of motion correction by aligning frames based on mutual information was published by Maes in 1997 for use in brain imaging.[69] For mutual information, the assumption is made that image intensity values of corresponding voxel pairs is maximal if the images are aligned. They tested this algorithm for CT-MR and PET-MR image registration and demonstrated that the algorithm had sub-voxel accuracy. The use of mutual information for CT alignment was further validated by Bond et al in 2008.[70] The technique also involved cropping the left ventricle to prioritize left ventricle alignment, it used a gradient operator for deformable alignments and Powell's method of unconstrained optimization. Results showed a 98 % success rate for registration of 26 patients, and was comparable to manual alignment.

In 1999 an entropy-based method was developed for PET-CT and PET-MR image registration by Studholme et al.[71] When two images with the same anatomy are superimposed, any anatomical features that do not overlap are duplicated; thus, increasing the complexity (or entropy) of the resulting image. A joint probability distribution could be used to estimate how often pairs of values occurred together. In a similar way, the authors proposed using joint entropy derived from the joint probability distribution. By minimizing the joint entropy function, the images could be aligned. Results were mixed however, as several significant failures in registration were encountered.

An automated motion correction technique using N-13-ammonia for cardiac imaging was published by Khurshid et al in 2008.[72] Their method used an image segmentation technique to isolate the cardiac region. The cardiac region on the CT was also segmented using the PET data to help define the heart location. The PET and CT are aligned by aligning these segmented regions. One important finding was they found that

the superior/inferior motion (z direction) made up 40 % of motion cases, for anterior/posterior (y direction) it was 22 % and for left/right (x direction) it was 38 % of motion cases. The mean shifts were 8 mm in the z direction, 4 mm in the x direction and 2 mm in the y direction; and the maximum approached 2.6 cm for z and 1 cm for the x and y directions.

A respiratory motion correction algorithm using optical flow with respiratory gating was published in 2008 by Dawood et al using both digital NURBS-based Cardiac-Torso (NCAT) phantom simulations and patient data.[73,74] First, raw gated data not corrected for attenuation was used in conjunction with an optical flow algorithm to align the respiratory phases to a common respiratory phase. Then these were added together to build the final motion corrected imaged, but without attenuation correction. A list mode reconstruction algorithm using the motion parameters determined by the optical flow algorithm was suggested to provide both motion correction and attenuation correction simultaneously – see **chapter** 1.2.4. Due to deformations (eg tissue compression) and the partial volume effect the activity concentration can change from the true value. A mass preserving method that can be used to compensate for these changes was proposed by Gigengack et al in 2012 for cardiac and respiratory motion correction.[75] This method preserves mass by incorporating the Jacobian determinant into the registration functional. The algorithm was evaluated using digital phantoms, physical phantoms and patient data. Results showed substantial reduction in cardiac and respiratory motion.

One of the very first papers on motion correction for Rb-82 was published in 2010 by Woo et al.[76] Their method works by segmentation of the heart wall, then defining a bounding box around the segmentation. Then automated cross-correlation was used to

align all frames to a common reference frame. Another image-based technique involving cardiac segmentation was developed by Martinez-Möller in 2007.[77] This technique involved comparing the position of the segmented left ventricle to the CT image. If part of the left ventricle (LV) overlapped with tissue that was very different from heart tissue (for example lung) then the corresponding voxel on the CT was set to heart tissue.

Another method of frame-by-frame image-based motion correction was published by Ye et al in 2014 for brain imaging.[78] By segmenting the patient's head outline, the CT image was aligned with a reference frame that was reconstructed with and without attenuation correction. The non-reference PET frames were initially reconstructed without attenuation correction. Then the non-reference uncorrected frames were aligned to the uncorrected reference frame. Then the spatial information was used to align the CT to all non-reference frames, and the frames were individually reconstructed with attenuation correction using their respective aligned CT. Then all attenuation corrected frames were re-aligned back to the reference frame.

A maximum correlation method was validated by Turkington et al in 1997.[79] A cross correlation function was used to align cardiac PET frames for N-13 Ammonia. One long frame (5 min) was used as a reference frame, to which all other frames were aligned. The method was evaluated on a cardiac phantom and human data. The study concluded that it performed well for the cardiac phantom and qualitatively well for human studies; however, since the true alignment in the human studies was unknown the performance could not be shown definitively for human studies.

In 2014 Slomka et al published a study comparing automated CTAC alignment with manual CTAC alignment for Rb-82 with static images.[80] It was found that

automated alignment performed better than manual alignment, likely due to the removal of operator bias. That same year Slomka et al published a paper on motion correction using dual-gated motion-frozen cardiac PET with F-18 flurpiridaz for static imaging.[81] Stress images were acquired using dual cardiac and respiratory gating. Results showed significant improvement in contrast and image resolution using the dual gated technique. Similar work with motion-frozen methods was conducted by Le Meunier et al in 2011 but applied to cardiac imaging alone for F-18 fluorodeoxyglucose.[82] This method used cardiac gating and aligned all cardiac phases to a single heart phase (end-diastole). Results showed an increase maximum LV counts to defect contrast and myocardial to blood contrast. In addition, noise levels were similar to static summed images.

#### **1.2.4 Reconstruction methods for motion correction**

Reconstruction methods have also been developed for PET motion correction. These methods are advantageous in that the PET motion and CTAC misalignment can be corrected for simultaneously. Most of these methods need the data to be in list-mode format which older scanners did not have but is now widely available.

One of the earliest attempts at patient body motion correction during reconstruction was published by Fulton et al in 1993 for brain imaging.[83] Their method assumed that the motion is accurately estimated using an unspecified method, and then uses this information in a maximum a posteriori (MAP) algorithm by expectation maximization using a one-step-late (OSL) algorithm (see **chapter 2** for image reconstruction). This was accomplished by modifying the probabilities of the detection of photons in a PET system by a transformation matrix representing the motion of a pixel. The limitation of this motion

correction algorithm is the fact that these algorithms cannot correct for motion within a frame. In addition, image artifacts may be caused by the fact that some LOR's can be shifted into positions where there are no crystal pairs (EG outside the scanner geometry). To compensate for this a modification of the MAF was proposed by Rahmim et al in 2004 using motion correction with list-mode data.[84] This method used comprehensive modeling of motion into the histogram-mode and list-mode EM reconstruction routines to account for these shifted LOR's. One can pre-correct sinograms by scaling the counts to account for these shifted LOR's as suggested by Thielemans et al and later expanded upon by Zhou et al.[85,86] The novel suggestion by Rahmim et al was to correct these effects during reconstruction by use of motion weighting by modifying the system matrix to take motion into account. This changes the sensitivity correction factors and thus may reduce noise effects. These methods were extended to 4D reconstruction by Verhaeghe et al in 2010 for head motion.[87]

A reconstruction algorithm to correct for intra-frame motion was developed by Mohy-ud-Din et al in 2012 for brain imaging.[52] This algorithm used an optical tracking system to measure motion in conjunction with the MAF approach. The research was an attempt to overcome the shortcoming of MAF acquisitions during the reconstruction, and avoid the need for list-mode acquisitions required by the line of response (LOR) method. Inter-frame motion is corrected by use of the average motion in each reconstructed frame individually. Next correction for CTAC errors was done by use of time-weighted attenuation images for each reconstructed frame. Intra-frame motion are then corrected during reconstruction using a Richardson-Lucy iterative deconvolution algorithm.

A list-mode based reconstruction algorithm for respiratory motion correction was developed by Lamare et al in 2007.[89] The algorithm was evaluated using a digital NCAT phantom and Monte Carlo simulations. This reconstruction method incorporated elastic transformations in the system matrix, which meant it could account for deformations in the organs that often occur due to motion. Results showed marked improvements in contrast for lesions in lung using motion-compensated reconstruction.

### **1.2.5 Additional methods for motion correction**

With recent developments of PET/MRI motion correction in PET using simultaneous PET/MR acquisitions are possible, and may prove to be more accurate. As pointed out by Catana et al one of the issues is that the motion of internal organs may be complex and impossible to characterize with external tracking.[90] The issue with CT images is that you cannot continuously monitor organ motion with CT due to the radiation exposure, and that PET and CT are acquired sequentially. However, there is no radiation dose from MRI imaging and thus MRI offers a way to measure the precise organ configuration during a PET acquisition. This is especially true since PET and MR can be acquired simultaneously and thus it allows for motion modeling of the organs and for accurate motion correction.

In 2012 Hamill et al published a paper on Maximum Likelihood Activity and Attenuation estimation (MLAA).[91] This is a reconstruction algorithm that takes advantage of the time of flight information that modern PET scanners such as the GE Discovery 690 have available. During reconstruction the algorithm estimates the expected attenuation and activity simultaneously. Any motion will be compensated for during reconstruction by creating an attenuation map that matches the PET data. The

disadvantages are that currently reconstructions requires several hours to converge and the PET scanner must have time of flight capability. In addition, this method only corrects for CTAC misalignment, any frame-to-frame misalignment in the PET data would need to be corrected separately.

## **2 Chapter: PET Imaging and Simulation**

### **2.1 Radioactive Decay and the Production of Positron Emitting Isotopes**

When the nucleus of an atom is unstable, the atom has a probability of losing energy by emission of radiation, to reach a more stable (lower energy) configuration. The important type of radioactive decay in PET medical imaging is positron emission. Positron emission competes with electron capture; however, electron capture is not important for PET imaging since it produces no measurable emissions. This chapter will discuss both radioactive decay, and various other physical processes important in PET imaging such as positron annihilation and photon/electron scattering, as well as the production of isotopes used in PET imaging. In addition, the purpose of PET imaging is to perform functional imaging such as myocardial blood flow (MBF) quantification; therefore, image reconstruction and MBF will also be covered.

#### **2.1.1 Positron Decay and Electron Capture**

Positrons were first predicted by Paul Dirac when he noticed that the wave equation contains negative solutions. He argued that these negative solutions predict a particle whose mass is equal to that of an electron but would carry a positive coulomb charge.[92] A short time later, the particle was discovered by Carl D. Anderson for which he won the Nobel prize.[93] Positron emission is a process whereby a proton in an unstable nucleus loses energy to become a neutron by emission of a positron. For instance, the parent atom Rb-82 has 82 nucleons and 37 protons. After the positron emission process the daughter

atom Kr-82 (which is stable) will have 82 nucleons and 36 protons. The process for positron decay with Rb-82 is illustrated in **equation 2.1.1.1**.



In order for this process to happen, the mass energy difference ( $E = mc^2$ ) between the parent and daughter atom must be at least twice the rest mass energy of an electron (at least 1.022 MeV to account for the positron and the loss of an electron). The emission energy excluding the rest mass of a positron, and a very small amount to the neutrino, will be shared between the positron and neutrino. Since the amount of energy shared may vary for any given emission, the positron is emitted with variable energy levels forming an energy emission spectrum for the positron. The average emission energy  $E(i)$  and energy yield ( $y(i)$ , number of emissions per second) for Rb-82 is given in Table 2.1.1.1.[94]

**Table 2.1.1.1:**

**Important radiation emissions from Rb-82 decay**

Radiation	$y(i)$ 1/(Bq-s)	$E(i)$ MeV
$\beta^{+}$	0.116	1.157
$\beta^{+}$	0.833	1.523
$\gamma$	1.91	0.511
$\gamma$	0.134	0.777

If the minimum energy threshold of 1.022 MeV is not met the decay mode will be electron capture. For electron capture an electron combines (is captured) by a proton to become a neutron. Once the electron is absorbed, a hole is left in the shell of the atom thus leaving the atom in an excited state. The atom will further stabilize by emission of a

characteristic x-ray when an electron in a higher energy shell fills this hole. This process is more prevalent in heavier nuclei due to the fact that electrons in the inner K or L shells experience a strong attraction to the nuclei due to the Coulomb force; additionally the characteristic x-ray will be higher in energy for larger nuclei. The process for electron capture with Rb-82 is illustrated in **equation 2.1.1.2**.



A list of various PET isotopes is given in **table 2.1.1.2** with the mean emission energy, half-life and the root mean square (RMS) positron range. One of the main advantages of PET isotopes is that most of them are identical to commonly found elements in biology. This means that by the use of radiochemistry, tracers which exactly mirror common biological chemicals can be constructed to exactly investigate those chemical functions in the body. In addition, most positron emitters have short half-lives, and thus the radiation dose to the patient tends to be lower compared to the longer-lived SPECT isotopes (for example Technetium-99m which has a half-life of 6 hours). As shown in **table 2.1.1.2**, Rb-82 is an ultra-short-lived isotope with the shortest half-life of all PET tracers. Therefore, its effective dose to a patient is very low approaching 0.8 mSv/GBq.[95] By comparison the annual background radiation dose in the Ottawa valley is 2 mSv/year.[96] Most of the PET tracers are cyclotron produced, which means any clinic wanting to perform PET scans with these tracers must have access to a cyclotron nearby. The tracer Rb-82 is generator produced, which means it is eluted from a parent isotope (Sr-82) and does not require an on-site cyclotron. This is covered in further detail in **chapter 2.1.2**.

**Table 2.1.1.2:**  
**Common isotopes used in PET imaging [97,98]**

Isotope	Isotope Source	Positron Fraction	$E_{max}$ MeV	$E_{mean}$ MeV	Half-life min	Range (RMS) mm
C-11	Cyclotron	0.99	0.96	0.386	20.4	0.28
N-13	Cyclotron	1.00	1.19	0.492	9.96	0.45
O-15	Cyclotron	1.00	1.72	0.735	2.07	1.04
F-18	Cyclotron	0.97	0.64	0.250	109.8	0.22
Cu-64	Cyclotron	0.19	0.58	-	762	0.2
Ga-68	Generator	0.89	1.90	0.83	67.7	1.35
Rb-82	Generator	0.96	3.35	1.40	1.27	2.60

The positron fraction is due to the fact that for the heavier elements, positron emission competes with electron capture. Here the positron range is the mean travel distance from the source of emission of a positron in water, expressed as root mean square (RMS) distance in mm.

### 2.1.2 The Production of Positron Emitting Isotopes

A cyclotron is a type of particle accelerator that accelerates charged particles using an alternating electric field that causes the particles to accelerate in an outward spiral path. A basic schematic of a cyclotron is shown in **figure 2.1.2.1**. The acceleration process begins at the source where a stream of hydrogen gas is ionized and becomes a plasma. This is accomplished typically by keeping the source between two high-voltage tantalum

cathodes. The electrons emitted by the cathodes ionizes the hydrogen turning it into a plasma consisting of both negative and positive ions (some neutral hydrogen atoms are also present). Deuterons and alpha particles can also be used in place of protons, and either positive or negative ions are pulled out of the chamber by a narrow charged slit where the particle enters the main chamber of the cyclotron. The main accelerating chamber consists of two trough-like half circle- (or D-) shaped copper ‘dees’ kept in vacuum. For acceleration of negative ions, the vacuum must be much higher than with positive ions, since a negatively charged proton can easily lose its electron to stray molecules. The dees are located between two poles of a powerful electromagnet (2 T) and connected to a high-voltage alternating potential at frequencies in the MHz range. Charged particles are attracted to a dee and are accelerated until they enter the dee. While in the dee they travel in an arc due to the magnetic field. When the field switches direction the charged particle is accelerated across the gap to the adjacent dee and the process continues. The frequency of the voltage shifts is set such that as particles reach the end of one dee, the polarity shifts to accelerate the particles to the other dee.

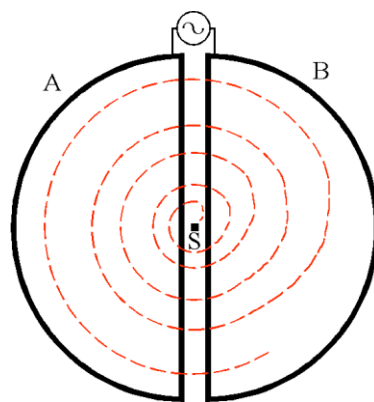


**Figure 2.1.2.1: Schematic of a cyclotron. Particle path is shown as a dashed red line originating at the source S. An alternating source is connected to dees A and B both held in vacuum.**

The kinetic energy 'K' of particles traveling in the cyclotron is given in **equation 2.1.2.1**, and is dependent on the radius and magnetic field of the cyclotron

$$\mathbf{K} = \frac{(qMr)^2}{2m} \quad \mathbf{(2.1.2.1)}$$

where: q is the particle charge, M is the main magnetic field, r is the cyclotron radius, and m is the particle mass.[99] Typical proton beams from cyclotrons have energies in the 10 to 30 MeV range. Negative ions do not interact with the target nuclei; therefore, a thin sheet of carbon foil is placed just in front of the target to strip the electrons away and create a proton beam. At first glance, negative ion acceleration may not appear to have any advantages as it requires a carbon foil and a much higher vacuum to be used. However, it does offer the possibility to produce more than one isotope with the same beam by partially converting a beam of negative ions to positive ions, then redirecting the rest of the negative ions to a separate target through another carbon foil to produce two separate proton beams.[99] In addition, positive ion acceleration relies on a long acceleration channel to direct the beam to the target with an extraction efficiency of 80 %, the rest is lost in the housing, thus necessitating increased radiation shielding. By contrast negative ion acceleration relies only on the carbon foils (which is nearly 100 % efficient) and a shorter path-length for extraction, and thus requires less shielding. For these reasons, medical cyclotrons typically use negative ion acceleration.

When a high-energy particle like a proton interacts with the nucleus of an atom the proton may be absorbed into the atom, or it may scatter departing some of its energy to the nucleus. This in turn may or may not cause the release of some nucleons from the atom which causes the atom to transmute to a different element, or the element may not change but it will change to a different isotope. Spallation reactions involve high energy

interactions where many nucleons are ejected from the nucleus; for medical imaging purposes this is used to create the Sr-82 source for Rb-82 imaging and will be discussed in more detail later. Other interactions involve the absorption of a proton and the ejection of a neutron, which is often the method used in medical imaging to produce tracer isotopes. This is further explained in **equation 2.1.2.2**, where a given atom  ${}^A_ZX$  (A nucleons, Z protons) absorbs a proton and ejects a neutron, then the atom is transmuted to a new element  ${}^A_{Z+1}Y$  (A nucleons, Z+1 protons).



This creates an element “Y” that is neutron deficient, which is typical for positron emitting isotopes. In addition, charged particles like deuterons (d) or alpha particles ( $\alpha$ ) are sometimes used in the production of PET isotopes with cyclotrons. Due to the different possible interactions for different isotopes and atoms, it is necessary for the target atom to be monoisotopic (one isotope) ideally, and pure so that the production reaction can be controlled. In addition, after such interactions take place the nucleus will be left in an excited state and will release its energy in the form of photons which could deposit some of their energy in the sample and surrounding housing, causing the target pressure and housing temperature to increase. The beam of high energy protons undergoes a large number of elastic scattering events which also deposit energy in the sample and housing which can cause temperature increases of up to 1000 °C. Therefore, to cool down the sample water/helium gas or other coolant is typically used, or the target surface area is increased.

Many PET isotopes are produced using liquid targets. Common targets used are O-18 enriched water for the production of F-18, N-14(1 %)/O-13 gas for the production of

C-11 and N-15/O-16(2.5 %) gas for the production of O-15. A list of cyclotron-produced PET isotopes is given in **table 2.1.2.1**. [99]

**Table 2.1.2.1:**

**Cyclotron produced PET isotopes**

Nuclide	Half-life [min]	Common Production Method
C-11	20.4	$^{10}_5\text{B}(d, n)^{11}_6\text{C}$ $^{14}_7\text{N}(p, \alpha)^{11}_6\text{C}$
N-13	10	$^{12}_6\text{C}(d, n)^{13}_7\text{N}$ $^{16}_8\text{O}(p, \alpha)^{13}_7\text{N}$
		$^{13}_6\text{C}(p, n)^{13}_7\text{N}$
O-15	2	$^{14}_7\text{N}(d, n)^{15}_8\text{O}$
		$^{15}_7\text{N}(p, n)^{15}_8\text{O}$
F-18	110	$^{18}_8\text{O}(p, 2n)^{18}_9\text{F}$

The PET tracer Rb-82 is so short-lived (76 s) that it would be impractical to use cyclotron production since most of the tracer would decay long before injection into the patient. Therefore, Rb-82 is strictly a generator-produced isotope. Generators work by having a long-lived parent isotope which decays into the desired daughter product. The parent isotope is often bound to a substance for which it has a high affinity (such as aluminum or tin oxide) whereas the daughter product is not tightly bound. Due to the lower binding affinity of the daughter product, it can be easily removed. In the case of Rb-82, the parent used is Sr-82 which is typically bound to a tin oxide column. To get access to

the Rb-82 daughter, a simple saline solution is flushed through the column and by diffusion the Rb-82 isotope enters the fluid and the solution becomes RbCl in saline, which can be immediately injected into the patient for imaging. A simple schematic of such an elution device is shown in **figure 2.1.2.2**, recreated from deKemp [100]. Sterile saline is flushed from the intake through the Sr-82/Rb-82 generator column where the isotope is dissolved into the fluid. A controlled valve directs the fluid to the calibration and/or patient elution system; any excess fluid is deposited into a shielded waste system.

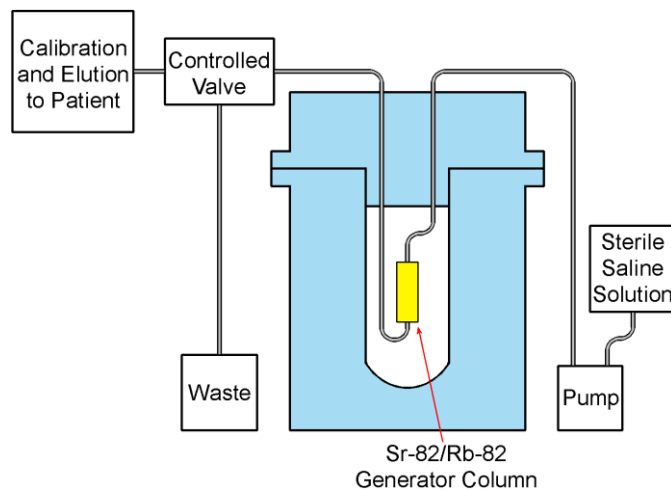


**Figure 2.1.2.2: Basic schematic of an elution system, recreated from deKemp [100].**

Natural sources of the long-lived (25.55 days) Sr-82 isotope do not exist and therefore need to be artificially produced. Two methods are used to produce Sr-82, first by bombardment of stable Rb-85 (Rb-Cl in solution or Rb metal) by high energy protons, or bombardment of Mo-99 (with 500-600 MeV protons). Due to the high energy of the incident beam and the large change in the atomic nucleus, the latter is a spallation process. The bombardment of natural rubidium for Sr-82 production produces a purer sample of strontium-82, but has a lower yield.[30] During the spallation process other isotopes are produced such as Br-77 which can be extracted for use in SPECT imaging. An ion-

exchange method is used to separate the Sr-82, after which it is purified and bound to a stannic oxide or aluminum column for use with a generator elution system.

### **2.1.3 Positron Annihilation**

When Rb-82 undergoes positron decay the parent atom transmutes to stable krypton and ejects a positron with some initial kinetic energy as was previously shown in **equation 2.1**. The newly ejected positron will then travel through the surrounding medium and lose energy by undergoing Bhabha scattering which are positron-electron scattering events. Positrons and electrons have the same mass so the momentum transfer is large, and thus even high energy positrons do not travel more than 2-3 mm on average in water. Eventually, the positron will lose too much energy to resist the coulomb force of attraction to an electron in the medium, and the two particles will combine and undergo annihilation. In most cases the positron and electron will have very little kinetic energy compared to their respective rest mass energy. When matter and antimatter meet under these conditions their total energy is transformed into electromagnetic energy. Due to conservation of momentum and energy the only possible emission is two photons with equal energies but opposite momentum. This emission was first proven by Robert Beringer and C. G. Montgomery in 1942.[101] Their apparatus consisted of two rotating detectors with a copper positron source in the center of rotation. There is an angular distribution of about  $\pm 0.5^\circ$  to the emitted photons due to the fact that the electron and positron may not be entirely at rest when they annihilate, this is illustrated in **figure 2.1.3.1**.

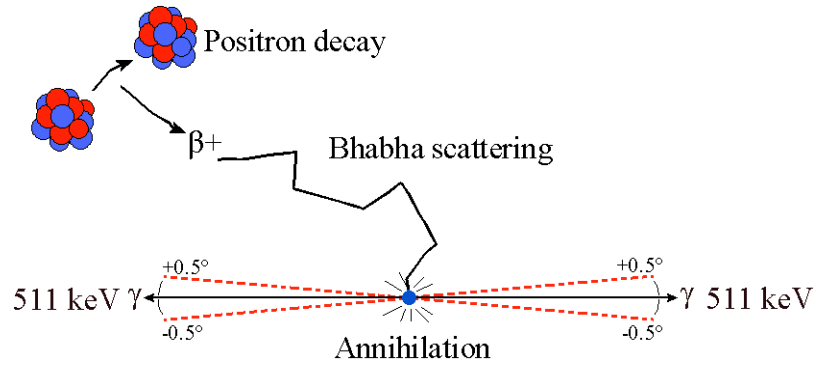


**Figure 2.1.3.1: Positron decay leading to an annihilation event results in the production of two gamma rays with equal energy and opposite momentum.**

Since annihilation photons are emitted simultaneously, detectors placed equidistant from the point of annihilation should detect both photons in coincidence, the physics of which is the basis of the PET imaging system and the subject of the next section.

## 2.2 The PET Imaging System

The PET imaging system takes advantage of the physics of positron annihilation. In order to do tomographic image reconstruction (this is discussed further in **chapter 2.3**) projection information must be collected for as many angles as possible around the object or subject being scanned. In SPECT imaging the emissions from the patient need to be collimated using a lead mesh which rejects all photons that have too high an incident angle. The issue is that the sensitivity of the scanner is greatly reduced due to the rejection of the majority of the incident photons. Since the geometry of the emission from a positron annihilation event is always the same ( $180^\circ$ ), collimation is naturally built into the imaging physics for PET. Detectors placed around the radiation source only need to look for coincident events, and it is the line of response between the two detectors that provides the angular

information needed to form the projection information. Early PET scanners used rotating pairs of detectors, but all modern PET systems use a ring (or cylinder) of detector crystals.

### **2.2.1 PET Scanners**

Since the 1950's when PET imaging began, PET scanners have increased in complexity and sophistication both in terms of the software for image reconstruction and blood flow analysis, and hardware for coincident detection and data storage. Since the GE Advance (herein called GEA) scanner will be used in subsequent chapters it is fitting to describe this system, in addition the more modern Discovery 690 (herein called D690) scanner will be covered for comparison purposes. Both the GEA and D690 scanners use complete crystal rings around the patient for detection of coincident events, as do modern Siemens PET scanners. The GEA scanner uses bismuth germanium oxide (BGO) scintillation crystals for detection of the 511 keV photons whereas the D690 uses lutetium-yttrium oxyorthosilicate (LYSO) scintillation crystals which have a higher light output and energy resolution.[102]

Scintillation is a process where a photon of higher energy is transformed into many photons of lower energies, typically in the visible spectrum. These photons can then be collected and measured using a photo-detector to give an electronic reading of the amount of total energy deposited by the initiating photon. The scintillation process occurs in three steps: conversion, transport and luminescence.[103]

Conversion is the process by which the incident high energy photon deposits its energy through multiple interactions with the scintillation crystal, promoting several electrons to the valence shell. This is done through Compton scattering and the

photoelectric effect. Compton scattering is dominant at energies near 1 MeV. Compton scattering is when a photon scatters with an electron, depositing some energy to the electron (called a Compton electron) and thus the scatter photon will have a different wavelength and a lower energy. The energies of the scattered photon and the Compton electron are given in **equations** 2.2.1.1, 2.2.1.2 and 2.2.1.3 respectively.

$$h\nu' = h\nu \left( \frac{1}{1 + \alpha(1 - \cos\theta)} \right) \quad (2.2.1.1)$$

$$E_{\beta-} = h\nu \left( \frac{\alpha(1 - \cos\theta)}{1 + \alpha(1 - \cos\theta)} \right) \quad (2.2.1.2)$$

$$\alpha = \frac{h\nu}{m_0c^2} \quad (2.2.1.3)$$

where:  $h\nu'$  is the scattered photon energy,  $h\nu$  is the energy of the incident photon,  $E_{\beta-}$  is the energy of the Compton electron,  $\theta$  is the scatter angle of the photon,  $c$  is the speed of light and  $m_0$  is the rest mass of an electron.

The photoelectric effect is important for all interactions at or below 100 keV, and occurs when the photon is completely absorbed by the electron which is ejected from the atom. Scintillation crystals are designed to maximize the photoelectric effect, so that all the incident energy of the incident photon is absorbed and measured. The energy of the ejected photon is given by **equation** 2.2.1.4:

$$E_{\beta-} = h\nu + E_b \quad (2.2.1.4)$$

where:  $E_{\beta-}$  is the energy of the ejected electron,  $h\nu$  is the energy of the incident photon and  $E_b$  is the binding energy of the electron.

During the conversion stage, multiple electron hole pairs are created in the crystal lattice, which is important for the transport stage. The crystals have a band gap structure consisting of a valence band, conduction band and a forbidden region where electrons

cannot exist. Electrons must be given at least the energy of the band gap to be excited from the valence to the conduction band. When electrons are promoted (excited) to the conduction band they leave a deficit of charge called a hole in the valence band and create a surplus of charge in the conduction band, these are called the electron hole pairs. During the transport stage the electron hole pairs migrate, and sometimes energy is lost to non-radiative re-combinations. These electron hole pairs will try to recombine but due to imperfections in the crystal lattice carriers may become trapped, usually in the band gap energy range. During the luminescence stage, recombination occurs and radiative emission produces the characteristic scintillation light, this process is illustrated in **figure 2.2.1.1** – recreated from [103].

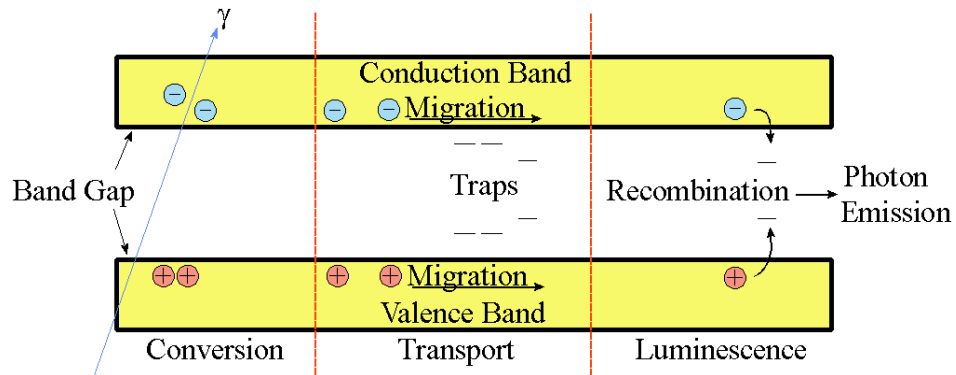


**Figure 2.2.1.1: Diagram of band gap structure, production of electron hole pairs during conversion, migration of electron hole pairs during transport, and recombination resulting in emission of photon.**

The detector efficiency for the conversion process in a scintillation crystal is given in **equation 2.2.1.5**. [104]

$$\eta = \beta SQ \quad (2.2.1.5)$$

where:  $\eta$  is the detector efficiency,  $\beta$  is the conversion efficiency from the incident  $\gamma$ -ray to electron hole pairs,  $S$  is the efficiency of the transfer of energy from the electron-hole pairs to the activator ions or luminescence centers and  $Q$  is the quantum efficiency of the luminescence centers. The conversion efficiency  $\beta$  can be calculated from the properties of the crystal, whereas  $S$  and  $Q$  can be measured. Clearly we want a detector with as high an efficiency as possible; in addition, for coincident detection a short decay-time of the scintillation light is desirable especially if time-of-flight information is desired (this is discussed in **chapter 2.2.2**). Some crystals deteriorate when exposed to moisture (hygroscopic) so non-hygroscopic crystals are more desirable since they do not need an air-tight seal. Also, crystals should be resistant to radiation damage (or hard) since the detectors need to be stable over as long a time as possible. Scintillation crystals such as BGO can be sensitive to damage by ultraviolet (UV) light and must be shielded, and can change efficiency with ambient temperature. Typical desirable characteristics for scintillation crystals are shown in **table 2.2.1.1**. Scintillation crystals with a high density are chosen to maximize the photoelectric effect and minimize the Compton effect since scatter events will likely not deposit enough necessary energy for detection.

**Table 2.2.1.1:**

**Desirable characteristics of a PET scintillation crystal. [104]**

Crystal Characteristic	Benefit
High $\eta$	High $\gamma$ -ray detection efficiency
Short decay time	Good coincidence timing
High light output	Large number of crystals per PMT
Good energy resolution	Full identification of energy events
Emission wavelength near PMT response	Good PMT response
Transparent at emission wavelength	Good transport of light output to PMT
Same index of refraction as PMT coupling	Good optical coupling to PMT
Radiation hardness	Stable response over time
Non-hygroscopic	Easier to package crystals
Rugged	Easier to produce smaller crystal elements

Once scintillation light is produced, it travels through the crystal which is transparent and acts like a light guide to carry the signal to the photo multiplier tubes (PMT). Depending on the size of the crystal up to 50 % of the scintillation light can be lost in a LYSO crystal and up to 40 % in a BGO crystal.[102] A typical PET detector block consists of a 2D array of crystals. Typically, a crystal block has grooves cut into it to form the crystal array: this makes coupling the crystals to a PMT easier (i.e. we do not require a PMT for each crystal), and the detector block easier to manufacture. The grooves act as optical guides to direct the scintillation photons towards the PMT, and typically Teflon is placed in the grooves to protect the crystals; in addition, a mylar sheet is placed in front of

the detector block to prevent visible light interference and to protect against UV radiation. When the scintillation photons interact with the photo-cathode, electrons are ejected towards the dynode through a focusing electrode to direct the electrons toward the first dynode. Dynodes are held at ever increasing voltage potentials which causes more electrons to be accelerated thus acting as an amplifier. After passing through several dynodes, the initial signal is greatly amplified and measured by an electric circuit to record the amplitude of the pulse. A schematic of the photomultiplier tube attached to part of a detector block is given in **figure 2.2.1.2**.

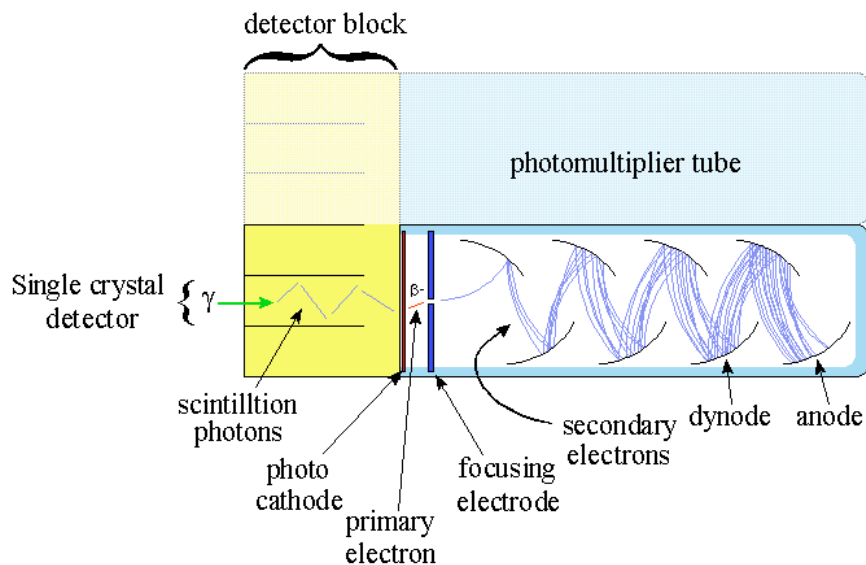


**Figure 2.2.1.2: schematic of a photomultiplier tube with detector block attached.**

Typically 4 photomultiplier tubes are used for each detector block as was suggested initially by Casey et al.[105]. Blocks are arranged in a ring around the patient, each crystal in the block also forms a ring of crystals around the patient; thus, a 24 ring scanner has 24 crystal rings made up of detector blocks rings. This is illustrated in **figure 2.2.1.3**. In this case 16 detector blocks form a single ring. In this example, each block has 4 transaxial crystals, thus this detector has 64 crystals per ring. If each block had 6 axial crystals and

the scanner had two block rings then the scanner would have 12 crystal rings, typically we would call this configuration a 12 ring scanner since scanners are not identified by the block arrangement. At the present time, most clinical scanners have 500-600 crystals per ring and 24-60 crystal rings (between 3-5 block rings). Often detector blocks are grouped into modules with shared electronic circuitry.

Photons travel at the speed of light ( $\approx 3 \times 10^8$  m/s in a vacuum), thus the travel time for photons in a 60 cm diameter scanner would be 2 ns. As previously discussed when positrons annihilate they produce two gamma rays of equal energy (511 keV) but opposite momentum (traveling in opposite directions,  $180^\circ$  of separation), and there is a good chance that both these photons will escape the body. When both these photons interact with the scintillation crystals they do so at nearly the same time due to their high speed. These signals are then amplified by the photomultiplier tubes. Signals from the photomultiplier tubes are checked for coincident timing, i.e. events that are so close to each other they could be considered simultaneous and thus most likely originated from the same positron decay.

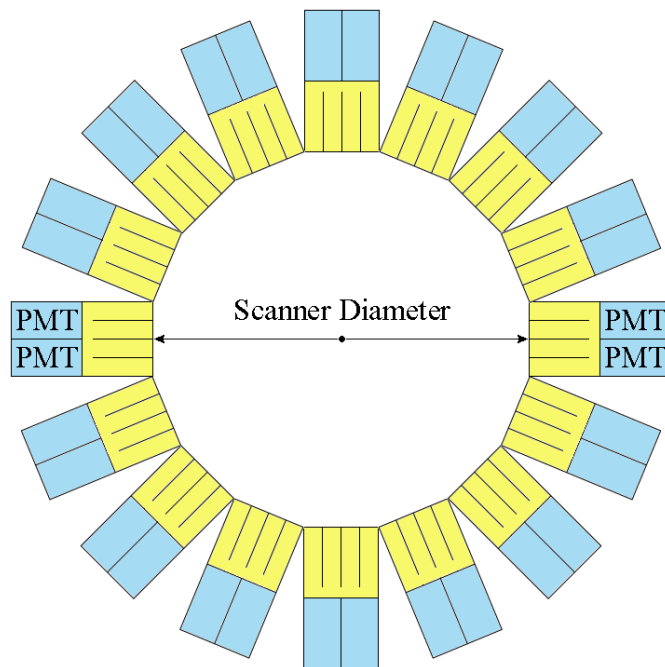


**Figure 2.2.1.3: Schematic of a detector ring made of detector blocks (yellow) with attached photomultiplier tubes (blue). The crystals form an approximate ring with the scanner diameter defined from face-to-face on each side of the ring.**

Following tracer injection, there are many decay events within the patient occurring simultaneously; many photon detections can occur per second depending on the activity within the field of view. In addition, there is no way to discriminate between the emission of two separate annihilation events, thus a coincidence timing window must be applied to decide to reject or accept a measured coincidence, as illustrated in **figures** 2.2.1.4, 2.2.1.5 and 2.2.1.6.[106] The process begins with the signal from the PMT entering the pulse generator. Here the signal is transformed into a sharp pulse with an amplitude proportional to the deposited energy as shown in **figure** 2.2.1.5. Due to imperfect energy deposition and variations in the detector efficiency, annihilation photons may not deposit the same amount of energy in the crystal. In addition, when we account for events like electron capture and other interactions within the body, photons that do not correspond to an annihilation event may still interact with the detector crystal. To eliminate these possibilities, an energy threshold is used to decide if a photon is likely due to an annihilation event. An example of the logic circuit for detection of a coincident event is shown in **figure** 2.2.1.4 – recreated from [106]. The sharp pulses from the pulse generator are then fed into a gate-pulse generator, which transforms it into a square wave with width twice the coincident window ( $2\tau$ ).

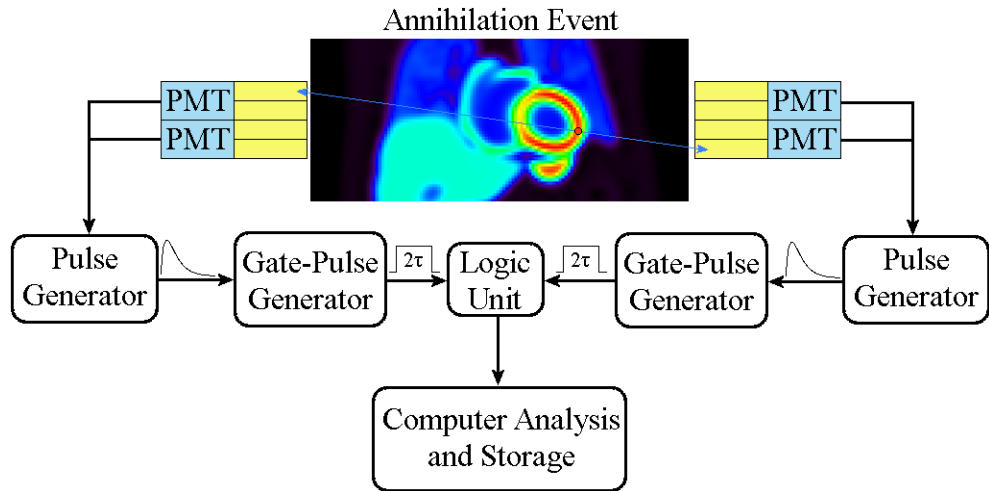


**Figure 2.2.1.4: Coincident timing circuitry.**

Signals received from the PMT are not processed by the pulse generator until the amplitude reaches a threshold level ( $V_T$ ). As is shown in **Figure 2.2.1.5** (recreated from [106]), pulses with different amplitudes can cross this threshold at different times, and have their own intrinsic time delay.

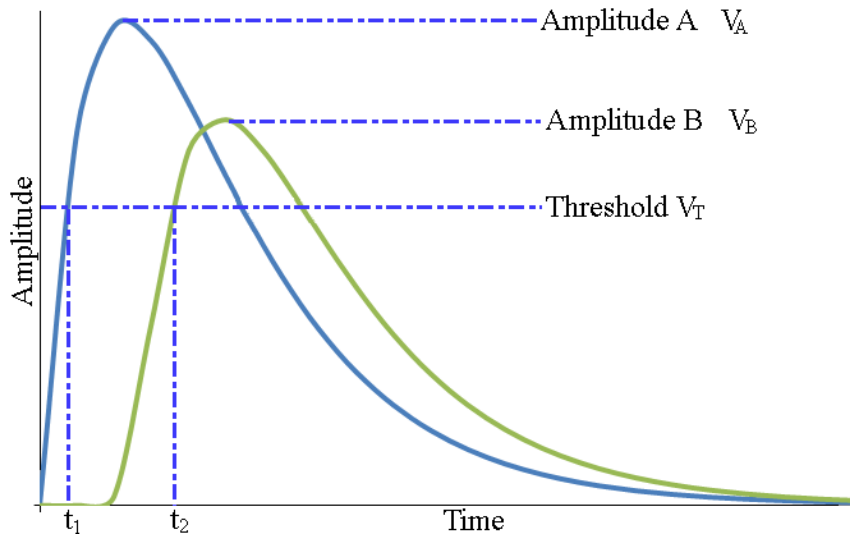


**Figure 2.2.1.5: measured energy pulses from the photomultiplier tubes.**

When these pulses are transformed by the gate-pulse generator it is then fed into a logic unit. The logic unit simply looks for a logical AND condition which occurs when the pulses overlap. Once this condition is met, the event is considered 'in coincidence' and

the annihilation event is assumed to have occurred somewhere along the line-of-response (LOR) between the two corresponding detector crystals. An example of coincident pulses and non-coincident pulses are shown in **Figure 2.2.1.6** – recreated from [106].

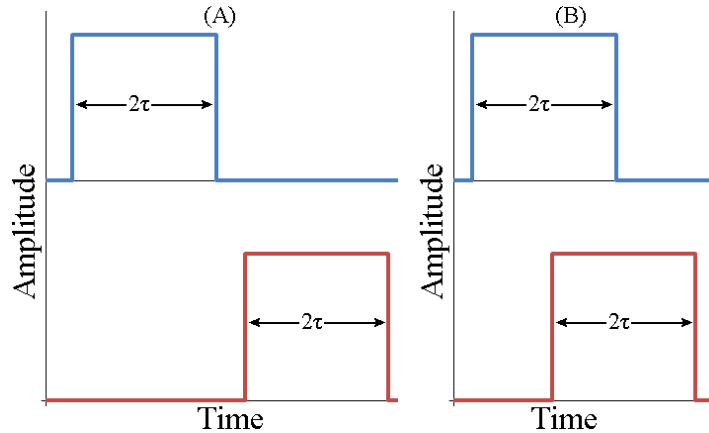


**Figure 2.2.1.6: coincident timing window showing two cases: (A) pulses not in coincidence and are therefore rejected and (B) pulses in coincidence.**

Once a coincident event has been accepted, the position on the block must be determined. Since the grooves in the crystal do not go all the way to the base of the crystal, there is some light diffusion through the base and each PMT will get a small amount of signal from an adjacent deposited event. The final position on the crystal face of the block can be easily calculated from the outputs of the 4 PMT's (numbered  $P_1$ ,  $P_2$ ,  $P_3$  and  $P_4$ ) from **equations 2.2.1.6 and 2.2.1.7.**[106] The final coordinates are then mapped to the nearest crystal in the detector block which causes some geometric distortion and must be corrected for.

$$\mathbf{X} = \frac{P_1 + P_2 - P_3 - P_4}{P_1 + P_2 + P_3 + P_4} \quad (2.2.1.6)$$

$$\mathbf{Y} = \frac{P_1 - P_2 + P_3 - P_4}{P_1 + P_2 + P_3 + P_4} \quad (2.2.1.7)$$

The measured coincidence only gives information about the possible line of response between the two crystals where the annihilation event happened, but not exactly

where along that line this event took place. With the increased timing resolution of the D690 scanner, it is possible to use the time difference between coincident photon pairs to estimate the approximate location of the annihilation event along the line of response, this is known as time-of-flight imaging, and by using this information higher quality reconstructions of the tracer distribution are possible.

For a coincident event to be accepted several conditions must be met, namely: both photons must fall within the expected energy window, the photons must deposit their energy within the time window, and the line of response between the two detector crystals in coincidence must have a valid acceptance angle. These valid events are collected and stored in a data structure called a sinogram, or as detector-pair events such as in list-mode format which is the subject of the next section.

### **2.2.2 Data Acquisition, Projections and Sinograms**

If we put a small point source in the transaxial field of view at location 'S'. Emission lines from measured coincidence events cross this point at many angles. If you plot the displacement from the center of the scanner as a function of angle from the horizontal, the points trace out a sinusoidal function as shown in **Figure 2.2.2.1** – recreated from [107].

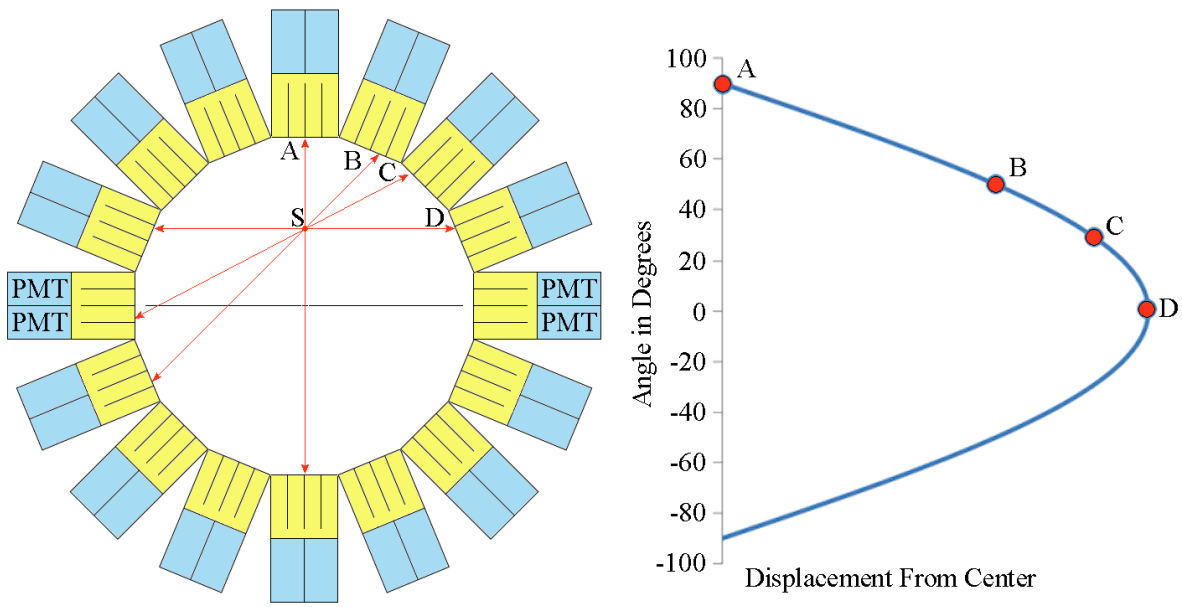


**Figure 2.2.2.1: Sinogram of a point source ‘S’. Lines of response A, B, C and D from the point source are plotted on the displacement graph tracing out a sinusoidal function.**

The diagram in **Figure 2.2.2.2** (recreated from [106]) shows an axial view of the scanner with the detector blocks arranged in a ring. Along the axial length (long axis) of the scanner the rings are stacked next to each other. For some scanners such as the GEA, in between the detector rings a thin tungsten septa can be inserted to limit the possible axial angles for detection. This serves to separate the axial planes for 2D reconstruction. For modern scanners like the D690 this feature does not exist since advancements in 3D reconstruction and 2D Fourier re-binning (if 2D reconstruction is desired) make it unnecessary. In addition, the sensitivity is lower with the septa in place since photons are highly absorbed in dense tungsten.

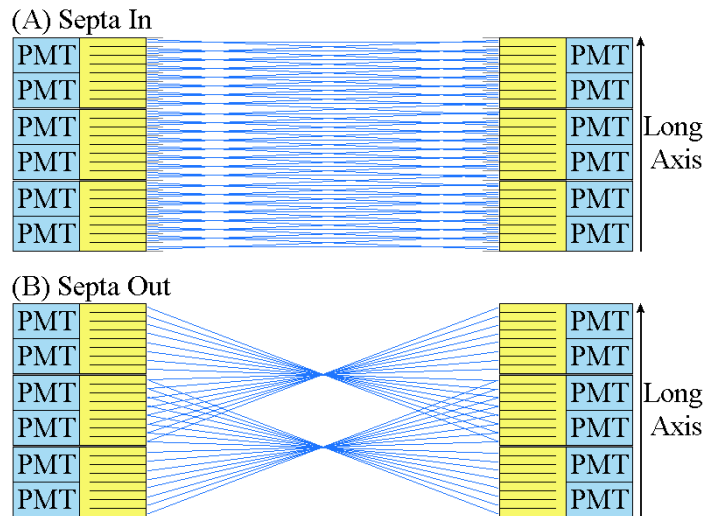


**Figure 2.2.2.2: Example of some lines of response with (A) the septa in place, restricting the coincidence events to specific planes, and (B) the septa retracted allowing a larger angular acceptance along the scanner axis.**

Each line of response has a defined axial and transaxial angle. For tomographic image reconstruction, the parallel lines of response can be grouped together to form projections. Reconstruction is covered later in **chapter 2.3**. In part (A) of **Figure 2.2.2.3** (recreated from [108,109]) lines of response at  $0^\circ$  and  $-45^\circ$  to the x axis are grouped together for multiple crystals. The grouping forms parallel lines of response. Coincidence events (counts) along each line of response are summed over time forming a 1D projection of all counts along that line of response. Projections can be stacked in increasing angular displacement along the radial axis. A data structure with stacked projections in this way is known as a sinogram because as **Figure 2.2.2.3** shows each point in the field of view traces out a sinusoidal function. A sinogram contains all projection information for a single slice (or plane) within the axial length of the scanner. The sinograms for each slice are stacked in a 3D matrix. If a single common angle is selected for all slices, and stacked accordingly,

an angular projection view of the object is formed as shown in **Figure 2.2.2.3 (B)**. The donut shaped heart wall is clearly visible in the projection image.

If we describe a tomographic image as an intensity function with  $x$  and  $y$  coordinated, a line that lies in the plane of the image can be defined as:

$$\mathbf{L}(\boldsymbol{\ell}, \boldsymbol{\theta}) = \{(\mathbf{x}, \mathbf{y}) | \mathbf{x} \cos \boldsymbol{\theta} + \mathbf{y} \sin \boldsymbol{\theta} = \boldsymbol{\ell}\} \quad (2.2.2.1)$$

**Figure 2.2.2.3 (A)** shows multiple lines ‘L’ with lateral displacement along an angular vector  $\boldsymbol{\ell}$  at two different angles. An example of the projection profile is also shown.

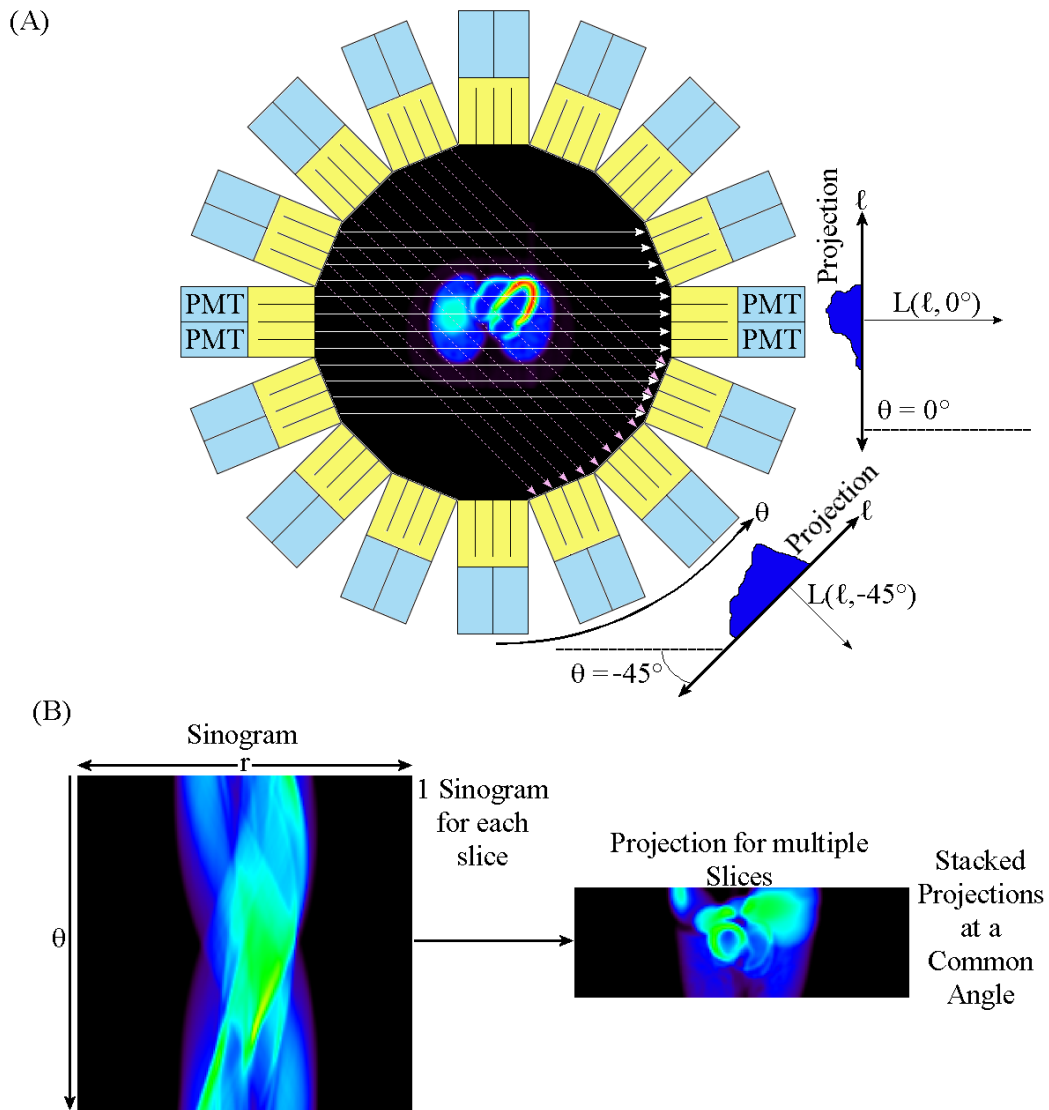


**Figure 2.2.2.3: Lines of response at the same angle grouped together at  $0^\circ$  and  $-45^\circ$  shown in (A). Stacking all the grouped sinograms by angle forms a single sinogram, as shown in (B). If we take a single projection at an angle for all slices we get stacked projection view (right side of (B)).**

The line integral of the image function would be:[109]

$$\mathbf{g}(\ell, \theta) = \int_{-\infty}^{\infty} \int_{-\infty}^{\infty} \mathbf{f}(\mathbf{x}, \mathbf{y}) \delta(\mathbf{x} \cos \theta + \mathbf{y} \sin \theta - \ell) \, dx dy \quad (2.2.2.2)$$

The impulse function forces the integral to be zeros except along the line L, therefore this function represents the projection at different angles around the patient, or the sinogram of the data. This function is also known as the continuous radon transform.

In addition to physically constraining which planes are measured by using a tungsten septa as shown in **figure 2.2.2.4**, measured planes may also be determined using axial acceptance angles if so desired. If only direct planes are allowed, then coincident events measured only in the same ring are considered. As shown in **figure 2.2.2.4**. In this case, there are 12 direct planes, and the reconstructed volume will have 12 slices.

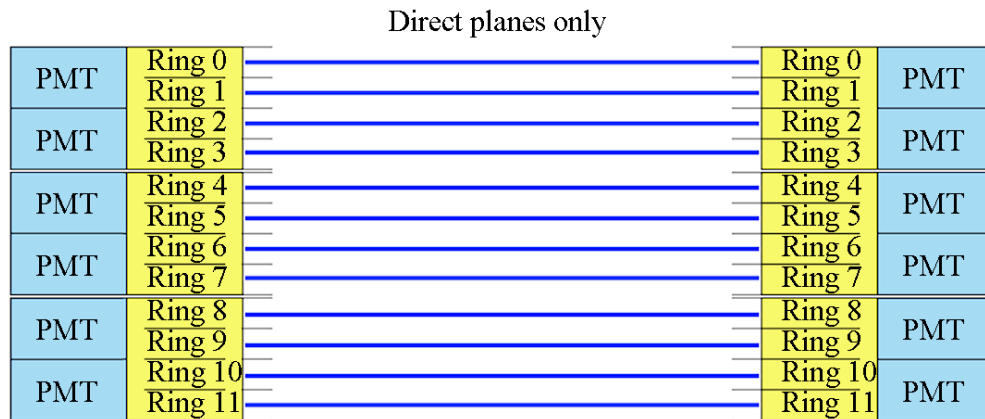


**Figure 2.2.2.4: Example of some lines or response for direct planes only with numbered detector rings.**

As previously mentioned the GE Advance scanner was used for the motion correction simulations described in this thesis. However, for comparison purposes the Discovery 690 scanner characteristics will also be shown. **Table 2.2.2.1** shows the overall characteristics of these two scanners. Typical reconstructed 3D image sizes are 128 by 128 voxels with the GEA having 35 slices and the D690 having 47 slices.

**Table 2.2.2.1:**  
**Comparison of the GEA and D690 PET scanners.**

	GE Advance	Discovery 690
Model	(GEA)[108]	(D690)[110]
Detector crystals/Block (transaxial × axial)	6 × 6	9 × 6
Detector crystal size [mm <sup>3</sup> ] (transaxial × axial × depth)	4.0 × 8.1 × 30	4.2 × 6.3 × 25
Detector rings	18	24
Detector crystals/ring	672	576
Axial FOV [cm]	15.2	15.7
ring diameter [cm]	92.7	80.99
Detector crystal type	BGO	LYSO

### 2.2.3 Scatter and Correction

A scatter event occurs when one of the annihilation photons scatters in the surrounding medium but both photons are detected and recorded as a coincident event, this is illustrated in **figure 2.2.3.1** with the photon paths shown in red. The line of response (shown in blue) does not cross the point where the annihilation event occurs. This shift of the line of response contributes to the noise of the reconstructed image and reduces contrast. Depending on the activity level and acquisition mode (2D vs 3D) scatter events can make up 20-50 % of all measured coincident events (sometimes called prompt events). In

addition, if the true activity concentration in the field of view is required (such as in the case for quantitative blood flow imaging) this effect must be corrected for.

There are many strategies to correct for scatter in images. One of the first methods was suggested by Cherry et al in 1993.[111] This method relies on the fact that as discussed in **chapter 2.2.2** in both 2D and 3D scans direct plane coincidences are acquired, and in the 3D cases sensitivity increases. If the sensitivity can be accounted for, the only difference between the 2D (septa extended) and 3D (septa retracted) acquisitions will be due to scatter events. Efficiency can be measured with a source in air so that scatter is not present. Thus the efficiency ‘ $\epsilon$ ’ can be used with the 2D ( $\text{LOR}(\mathbf{r}, \theta)_{2\text{D}}$ ) and 3D ( $\text{LOR}(\mathbf{r}, \theta)_{3\text{D}}$ ) lines of response (LOR) using **equation 2.2.3.1** to calculate the amount of scatter along that LOR.

$$\mathbf{S}(\mathbf{r}, \theta) = \text{LOR}(\mathbf{r}, \theta)_{3\text{D}} - \epsilon \text{LOR}(\mathbf{r}, \theta)_{2\text{D}} \quad (2.2.3.1)$$

For each LOR, the quantity  $\text{S}(\mathbf{r}, \theta)$  is scaled to be equal to the total scatter counts of the counts measured outside the object (ie in the tails of the data which is due to scatter alone). Therefore, the scatter contributions can be calculated for each LOR and removed.

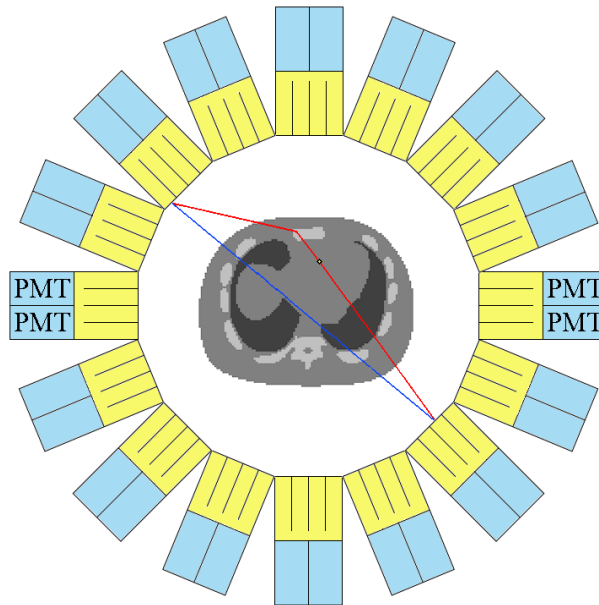


**Figure 2.2.3.1: Representation of a scatter coincidence. Emission occurs at a point within the heart and one of the 511 keV photons scatters off of the bone of a rib.**

**Blue line is the recorded line of response.**

A method for measuring the scatter fraction consists of a line source of Ge-68 placed in the center of the field of view. First the source is placed in air and counts are counted over a period of time. Then the source is placed in a water phantom with known dimensions, and counts are acquired over the same length of time. Since scatter in air is virtually nonexistent, and accounting for attenuation, the subtraction of these two images will be the scatter alone. The scatter function is modeled as a mono-exponential function derived from the scatter profile determined with the Ge-68 line source (counts outside the line source (the tails) are due to scatter at these activities).

Another method suggested by Bailey et al in 1994 was to treat the problem as a convolution between the image without scatter ( $I_{w0}$ ) and the scatter function (S); which is a function that describes how scatter events distribute through the image, **equation 2.2.3.2** describes this process.[112]

$$\mathbf{I}_s = \mathbf{I}_{wo} \otimes \mathbf{S} \quad (2.2.3.2)$$

where:  $\mathbf{I}_s$  is the image with scatter. Therefore, if we can determine  $\mathbf{I}_s$  and subtract it from the measured image ( $\mathbf{I}_m$ ) (after accounting for the scatter fraction), we would be left with an image without scatter (note:  $\mathbf{I}_{wo}$  will still contain random events). The measured image is used as an initial estimate for  $\mathbf{I}_{wo}$ , and the process can be repeated iteratively until convergence, as shown in **equation 2.2.3.3**. [112]

$$\mathbf{I}_{wo}^n = \mathbf{I}_m - f_s(\mathbf{I}_{wo}^{n-1} \otimes \mathbf{S}) \quad (2.2.3.3)$$

where:  $n$  is the iteration number and  $f_s$  is the scatter fraction. Scatter fraction is the ratio of total scatter events to total measured events. Since this method of scatter correction works with 2D planar images, the initial estimate for one plane is used as a starting estimate for other planes to correct the 3D sinogram.

In 1996 Ollinger et al developed a simulated single scatter (SSS) algorithm for scatter correction. [113] Here it is assumed the majority of scatter events result from only a single Compton interaction, and the multiple scatter distribution can be modelled by an integral transformation of the single scatter distribution. The effect of multiple scatters is small but not negligible. To account for the multiple scatter the assumption is made that multiple scatter arises from a convolution of the single-scatter distribution with a one-dimensional Gaussian kernel. Analytical models of single scatter are used incorporating the Klein Nishina formula to simulate single scatter events along a LOR. To do this an initial estimate of the scatter is needed, which is done after random and dead time corrections. Initial scatter is typically estimated using a back-projection of the emission data at low resolution (sometimes as low as 1 cm<sup>3</sup> voxel volume). Typically this initial estimate is then used within an ordered subset expectation maximization (OSEM)

algorithm by incorporating the SSS information in the forward projection and updating these estimates for each subsequent iteration.[114–117] The tails of the scatter estimate are used for normalization, which scales the data to the true activity concentration.

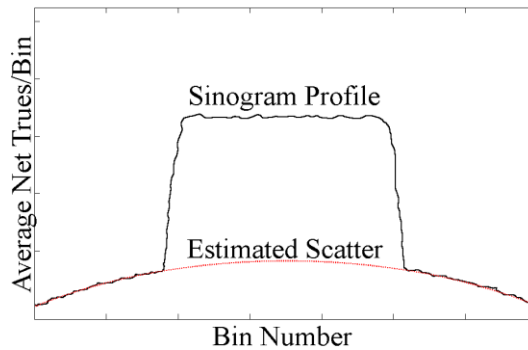


**Figure 2.2.3.2: Example of a sinogram profile (black solid line) and estimated scatter from the tails of data (red dotted line).**

Other methods of scatter correction involve performing a Monte Carlo simulation to simulate the amount of scatter, but this is much slower than the analytical methods.[118,119] Without a doubt, scatter correction is one of the most difficult PET corrections to implement, due to the difficulty of accurately modeling and determining scatter in the patient, which in theory requires a priori knowledge of both the scattering medium and the emission distribution.

#### **2.2.4 Randoms and Correction**

A random event occurs when two photons from two different annihilation events are detected by the system and recorded as a coincident event. The paths of the incident photons are shown in red in **figure 2.2.4.1**, and the resultant (erroneous) line of response is shown in blue.

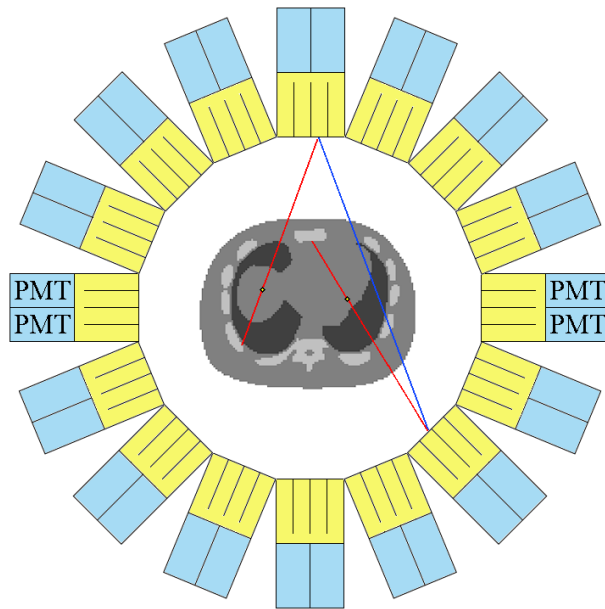


**Figure 2.2.4.1: Representation of a random (accidental) coincidence. The blue line is the resultant line of response.**

The rate ( $R_{ij}$ ) at which detector crystal pairs 'i' and 'j' detect random events is given by the singles rate of the two detector crystals as shown in **equation 2.2.4.1**. [120]

$$R_{ij} = 2\tau S_i S_j \quad (2.2.4.1)$$

Where:  $2\tau$  is the coincidence time window,  $S_i$  is the singles rate of detector crystal 'i' and  $S_j$  is the singles rate of detector crystal 'j'. To use this 'randoms from singles' correction method you must have a PET camera capable of accurately measuring the singles rates for each detector crystal. One of the issues with this method is that you would need to estimate the singles rate for each individual detector crystal. In reality you can only measure a system average which can have averaging biases due to asymmetric PET sources such as a patient. [121] Another method would be to try to estimate the randoms from the projection data outside the patient (the tails) and subtract them from the measured data. [122] This is called the profile method. The issue with this method is that the estimate

can change depending on the shape of the object and residual uncorrected scatter outside the object.

The most commonly used method is the delayed coincidence method.[123] To utilize this method the scanner must have a dual coincidence circuit to measure the delayed coincidences. The second circuit has a delay in the coincidence timing such that any true coincidence will not be detected. Thus, in the delayed window the only coincidences measured would be randoms. None of these methods remove the random events from the data set, so randoms add a background noise in the image. What we are estimating is the number of random events likely to have occurred during an acquisition. This then corrects for bias in the measured activity concentration of the image, but not the noise.

When we correct for randoms by subtracting the delayed events we also increase the uncertainty on the estimated true rate. This is expressed in **equation 2.2.4.2** as

$$\sigma_T = \sqrt{T + 2 \times R} \quad (2.2.4.2)$$

where:  $\sigma_T$  is the error on the estimate of the true rate, T are the number of true events and R is the number of random events.[124]

### **2.2.5 Correction for Prompt-Gamma Coincidence**

In addition to the emission of a positron, Rb-82 also emits a gamma ray at 776 keV for about 13 % of all decay emissions.[125] Since prompt gammas occur during the Rb-82 decay, they are emitted from the site of the decay event. The positron annihilation event may occur some distance from the decay event due to the positron range. It is possible for some of these prompt gammas to be detected within the energy window and coincidence timing window and be counted as a coincident event. An example of a prompt gamma

coincidence is shown in **figure 2.2.5.1**. Unlike random coincidences which occur due to two separate decay events, prompt coincidences will be correlated in time with the positron annihilation gamma photons since they occur at almost the same time, thus the delayed window random correction technique does not correct for prompt events. The resultant line of response (the blue line in **figure 2.2.5.1**) from such a prompt coincidence is shifted from the annihilation event, and thus needs to be corrected. The distribution of prompt events is nearly uniform since the prompt emission is isotropic and not correlated to the emission of the positron.[125] The prompt emission and annihilation locations do not necessarily occur at the same location. In figure 2.2.5.1 the purple dot is where the gamma emission occurred (decay of Rb-82) and the yellow dot is where the annihilation event occurs.

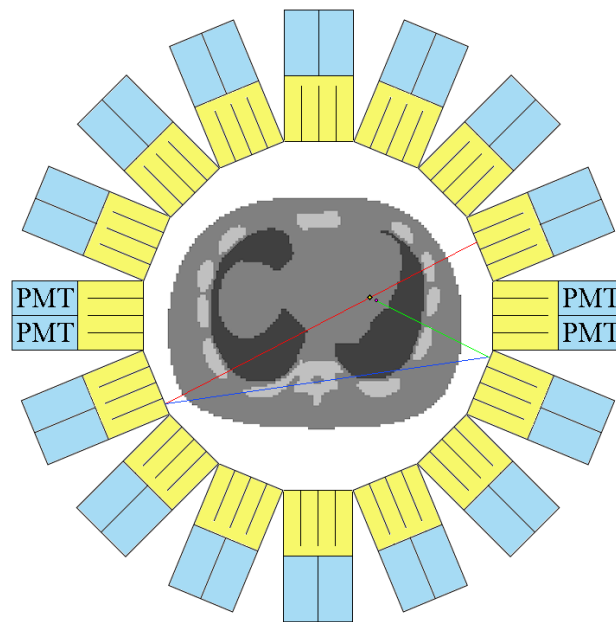


**Figure 2.2.5.1: Representation of a prompt-gamma coincidence. The blue line is the resultant line of response, the green line is the prompt gamma ray, and the red lines are the gamma rays from the annihilation event.**

Correction for this effect can be combined with scatter correction since after random and dead time corrections the only accidental coincidences left are scatter and prompt-gamma events – see **chapters** 2.2.4 and 2.2.6. First the sinogram is corrected for randoms, attenuation (see **chapter** 2.2.7) and dead time. The shape of the prompt gamma distribution is estimated from a prompt-gamma compensation (PGC) kernel. The shape of the SSS distribution is also determined. A threshold is applied to the sinogram to mask everything outside the body. The data outside the body contains only scatter and prompt-gamma events and are fit to a linear combination of the PGC and SSS distributions, and after scaling these are subtracted from the data.[125]

### **2.2.6 Detector Dead Time and Pulse Pile-Up**

After conversion of a photon there is a finite time required for the light integration process to result in a signal production, and a detection pulse to be generated. If another photon interacts with the detector (either at the crystal, block or module level) while the previous photon is being processed, the secondary photon will not be detected. This is due to the finite time it takes for the electronic system to integrate the incoming signal from the detector. The latency time under which the detector cannot detect photons is known as the dead time since the detector is effectively ‘dead’ to subsequent photons. Pile up is when two different photons deposit energy in the same crystal close enough to each other that their signals are combined into one apparent signal.

In the scintillation crystal, the process starts with conversion as outlined in **chapter** 2.2.1. Since the conversion process takes  $< 1$  ps it is not a significant source of dead time. Significant delay from transport to luminescence can occur due to the time it takes to

recapture the electron hole pairs. The total decay time from conversion to luminescence (crystal response time) for BGO scintillation crystals is 300 ns and for YLSO scintillation crystals it is 40 ns.[126–128] The speed of the whole process from conversion to luminescence is related to the merit ‘M’ which is the speed of the crystal as shown in **equation 2.2.6.1**. [129]

$$\mathbf{M} = \frac{10^6 \beta S}{2.3 \tau_r E_g} \quad \mathbf{(2.2.6.1)}$$

Where: M is the merit related to the speed of the crystal,  $\beta$  is the conversion efficiency from the incident  $\gamma$ -ray to electron hole pairs, S is the efficiency of the transfer of energy from the electron-hole pairs to the activator ions or luminescence centers,  $\tau_r$  is the radiative decay time and  $E_g$  is the bandgap energy of the crystal.

**Figure 2.2.6.1** shows the measured count rate as a function of the total phantom (or patient) activity. With low activity in the field of view, the true count rate measurement and ideal count rate measurement are almost the same behaving like a linear function. Ideally we would want a linear response rate from the detector system for all levels of activity. In practice the count rate linearity drops off at high activity levels due to events lost to detector dead time; and the precision decreases due to the increase in randoms and detector dead time effects. Since the number of random events rises exponentially with the increase in activity and dead time effects become more significant at high count rates, at high count rates the system response becomes saturated where any further increase in total activity results in little to no improvement in image quality.

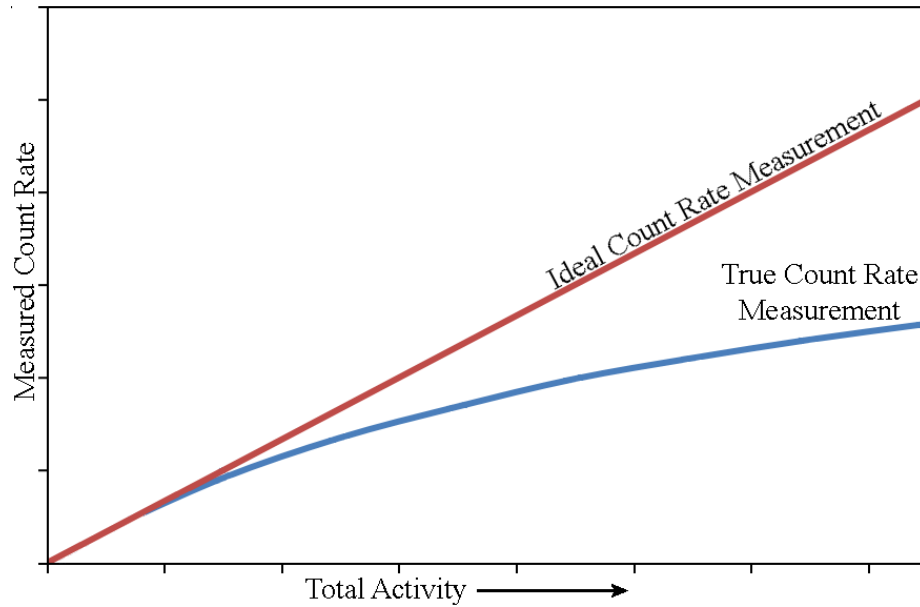


**Figure 2.2.6.1: Count-rate measurement as a function of total phantom activity. Ideal count rate would be linear increasing in proportion to total activity. True count rate is affected by dead time.**

Dead time can be paralyzable or non-paralyzable as shown in **figure 2.2.6.2**. If a detector is non-paralyzable then the dead time is fixed and pulses arriving within this window have no effect. For paralyzable detectors, pulses arriving during the dead time effectively resets the dead time clock, thereby extending the length of the dead time and all photons are integrated together. PET detectors can contain circuits that are paralyzable, non-paralyzable or a combination of the two.

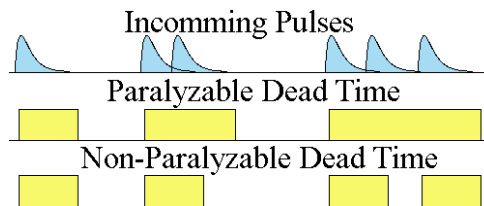


**Figure 2.2.6.2: Paralyzable and non-paralyzable dead time responses. Length of dead time (yellow blocks) is extended for the paralyzable response when subsequent pulses arrive close together.**

It is relatively easy to determine the random events (R) in an acquisition (see **chapter 2.2.4**) using the delayed window technique. The prompt window coincidences (trues (T) + randoms (R) + scatter (S)) and randoms will both suffer from the same dead time losses since they are acquired from timing windows of the same length. Therefore, the determination of T + S can be made accurately, and will be proportional to the activity in the field of view. The ratio of the measured T + S to the ideal T + S is called the live time fraction ( $F_L$ ). Mathematical models suggested by Eriksson et al of the live time fractions for paralyzable, non paralyzable and the combination dead times are given in **equations 2.2.6.2, 2.2.6.3 and 2.2.6.4** respectively.[130]

$$F_L(\textit{paralyzable}) = k e^{-n\tau} \quad (2.2.6.2)$$

$$F_L(\textit{non - paralyzable}) = k \frac{1}{1+n\tau} \quad (2.2.6.3)$$

$$F_L(\textit{combination}) = k \sqrt{\frac{e^{-n\tau}}{1+n\tau}} \quad (2.2.6.4)$$

Where: k is a constant (usually set to 1),  $\tau$  is the dead time and n is the true input count rate.

The live-time fractions can also be described at the detector block (scintillation and PMT) and data handling (data processing and storage) levels as shown in **equations 2.2.6.5 and 2.2.6.6**.[130]

$$F_L(\textit{block}) = e^{-NS_i\tau_{block}} \quad (2.2.6.5)$$

$$F_L(\textit{data}) = e^{-C_L\tau_{sys}} \quad (2.2.6.6)$$

Where: N is the total number of crystals in a detector block,  $S_i$  is the average singles rate of crystal 'i' in the detector block,  $C_L$  is the coincidence load (ideal count rate),  $\tau_{block}$  is the block dead time and  $\tau_{sys}$  is the data processing dead time. The quantity  $C_L$  can be

calculated from **equation** 2.2.6.7, and the overall system live-time fraction can be calculated from **equation** 2.2.6.8.[130]

$$\mathbf{C}_L = \mathbf{P} \times \mathbf{F}_L(\mathbf{block})^2 \quad (2.2.6.7)$$

$$\mathbf{F}_L(\mathbf{sys}) = \mathbf{F}_L(\mathbf{block})^2 \times \mathbf{F}_L(\mathbf{data}) \quad (2.2.6.8)$$

Where: P is the prompt coincident rate.

Another approach to dead-time modelling suggested by Moisan et al in 1997 was to modify the detector efficiency to account for dead time losses. Here we model block dead-time as discussed earlier, but we separate detector modules' dead-time from the system bandwidth. As was discussed in **chapter** 2.3.1 blocks are grouped together in modules to a common circuit called a bucket which has a separate dead-time due to the multiplexing and processing speed of the bucket. The detector efficiency for block and bucket dead-times are given in **equations** 2.2.6.9 and 2.2.6.10.[131]

$$\epsilon_{bl} = \epsilon_d \frac{e^{-\frac{\tau_{bl} N_i(\epsilon_d)}{n_{bl}}}}{1 + \frac{\tau_{bl} N_s(\epsilon_d)}{n_{bl}}} \quad (2.2.6.9)$$

$$\epsilon_{bu} = \epsilon_{bl} \frac{1}{1 + \frac{\tau_{bu} N_i(\epsilon_{bl}) n_{bbk}}{n_{bl}}} \quad (2.2.6.10)$$

Where:  $\epsilon_{bl}$  is the detector block efficiency,  $\epsilon_{bu}$  is the bucket detector efficiency,  $\epsilon_d$  is the regular detector efficiency,  $\tau_{bl}$  is the block dead time,  $\tau_{bu}$  is the bucket dead time,  $N_i(\epsilon_d)$  is the singles rate corrected for scatter with the regular detector efficiency,  $N_i(\epsilon_{bl})$  is the singles rate corrected for scatter with the detector efficiency of the block,  $n_{bl}$  is the number of blocks in the scanner and  $n_{bbk}$  is the number of blocks per bucket. The total system bandwidth is accounted for in **equation** 2.2.6.11, where the rates of all the blocks cannot exceed a certain level due to the processing speed of the electronics.[131]

$$N_s(\epsilon_{bu}) = N_i(\epsilon_{bu}) \frac{SBW}{\sum_i N_i(\epsilon_{bu})}, \quad \text{if } \sum_i N_i(\epsilon_{bu}) \geq SBW \quad (2.2.6.11)$$

Where:  $N_s(\epsilon_{bu})$  is the total system singles rate,  $N_i(\epsilon_{bu})$  is the singles rate corrected for scatter with the bucket detector efficiency, SBW is the system band-width which describes the maximum allowable singles rate, and  $\sum_i N_i(\epsilon_{bu})$  is the total singles event rate for all blocks and buckets. Several experiments with Monte Carlo simulations have shown that this model gives excellent agreement with measured data.[132,133]

An example of the possible effect of dead-time on the count rate measurement of a PET camera is given in **figure 2.2.6.3**. With low activity, the randoms rate is usually below both scatter and trues rate, in addition the trues rates dominate and behaves linearly. At higher activities randoms dominate, for some phantom sizes the scatter rate will sometimes equal or exceed the trues rate. At very high activities the randoms rate can actually decrease, and trues and scatter rates fall as the system band-width is reached.

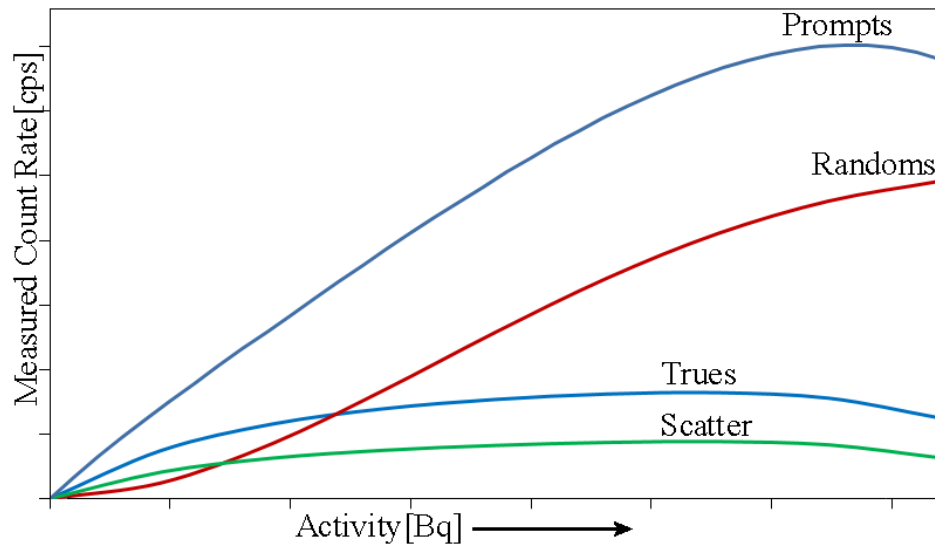


**Figure 2.2.6.3: Count rate measurement of true, scatter and random events (counts per second [cps]) as well as total prompt (T + R + S) events as a function of activity in the phantom or patient.**

The GEA PET scanner can be modeled by two paralyzable dead times, one at the individual crystal level (332 ns) and one at the block level (625 ns).[134] For the D690

there is a 200 ns paralyzable dead time at the block level where pileup occurs followed by 200 ns non-paralyzable circuit reset time. The D690 is a modern scanner which takes advantage of fast computers and has a system band-width limit of (1Gbit/s data transfer rate) 15M cps.[135] Dead-time correction can be accomplished by using these system models and adjusting the measured data accordingly, or by using the randoms measurements and extrapolating the ideal randoms without dead-time to estimate the correction factors.[124,136]

### **2.2.7 Attenuation and Correction**

Radiation sources located in a patient or phantom lose photons through attenuation, caused by the physical interactions of scatter and absorption. Since this loss would cause an underestimation of the true activity concentration inside the patient it must be corrected for. An example of uncorrected PET data after reconstruction is shown in **figure 2.2.7.1** with attenuation corrected data shown for comparison.

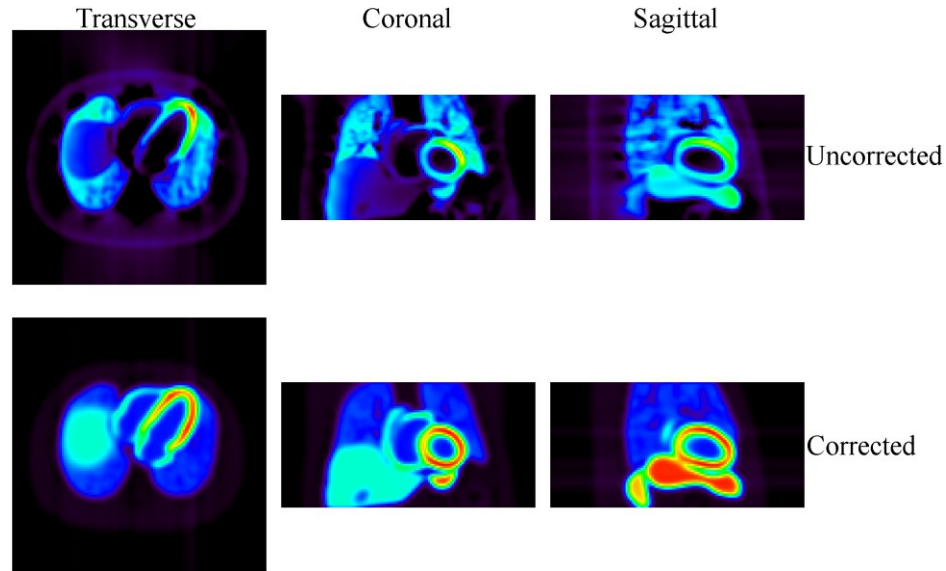


**Figure 2.2.7.1: Example of a PET scan reconstructed without (top) and with (bottom) attenuation correction.**

The fraction of photons leaving an attenuating medium ‘ $\phi$ ’ as a function of travel distance ‘ $x$ ’ and linear attenuation coefficient ‘ $\mu$ ’ is given by **equation 2.2.7.1**. [106]

$$\phi = e^{-\int \mu(x) dx} \quad (2.2.7.1)$$

If we assume the total thickness of the patient is  $D$  (that is:  $\sum x = D$ ) for a photon traveling in the opposite direction, we would get:

$$\phi = e^{-\int \mu(x)(D-x) dx} \quad (2.2.7.2)$$

The total probability for two photons from a positron annihilation event to be detected by our PET system is:

$$\phi_T = e^{-\int \mu(x) dx} \times e^{-\int \mu(x)(D-x) dx} = e^{-\int \mu(x)(x+D-x) dx} = e^{-D \int \mu(x) dx} \quad (2.2.7.3)$$

Or simply the probability of detection is independent of the location along the line of response where the annihilation event took place. If the negative of the exponent in **equation 2.2.7.3** is taken and multiplied by the appropriate line of response, then

attenuation along that line of response is corrected for. This is called the attenuation correction factor (ACF).

There are two common methods for determining the ACF. The original method used a Ge-68 point or line source rotating around the patient. Acquisitions were made with (transmission scan) and without (blank scan) the the patient in the field of view, and the ACF projection data was determined by using **equation 2.2.7.4** as:

$$\mathbf{ACF} = \frac{I_{bl}}{I_{tr}} \quad (\mathbf{2.2.7.4})$$

where:  $I_{bl}$  is the blank scan and  $I_{tr}$  is the transmission scan.[43]

Most modern PET scanners have an x-ray CT scanner attached to the device. While the CT can be used to correlate the regions of tracer uptake with anatomic location of the organs in the body, its main purpose is for attenuation correction.[31] A CT works by producing a beam of photons from a rotating x-ray source around the patient and detecting them with position sensitive detector located on the opposite side. The measurements from a CT scan are in Hounsfield units (HU) but can be converted to units of photon attenuation for 511 keV photons [137]; thus, information from a CT can be used in the direct calculation of the ACF. By stacking the CT projections appropriately an ACF sinogram can be used to correct measured coincidence sinograms for attenuation as shown in **figure 2.2.7.2**.

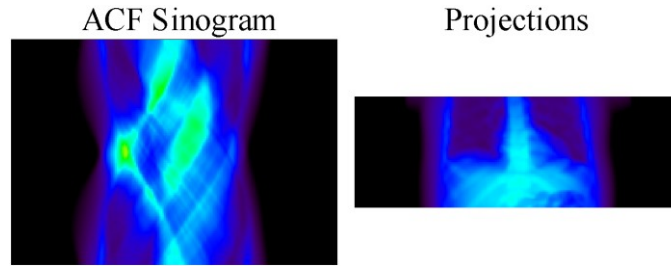


**Figure 2.2.7.2: Example of an ACF sinogram. On the right projections for a single angle along the slices are shown. The ACF values are unit-less and calculated using the negative of the exponent in equation 2.2.7.3.**

## 2.2.8 Projection Consistency Conditions

As discussed in **chapter 2.2.2** measured PET data is essentially the radon transform (or forward projection) of the emission distribution. Radon transforms have several mathematical properties such as the consistency property. If we denote  $S$  as the space for rapidly decreasing functions:  $C^\infty \in \mathbb{R}$  (where:  $C^\infty$  are functions that are infinitely differentiable and  $\mathbb{R}$  implies these are real functions). A rapidly decreasing function  $f(x)$  satisfies the following conditions:[138]

- 1)  $f(x)$  is infinitely differentiable
- 2)  $\sup_x ||x|^m P(\partial_1, \dots, \partial_n) f(x)| < \infty$ , for positive integers  $m$ , polynomials  $P$  in the operators  $\partial$  (supremum or ‘sup’ means the largest as  $x$  varies).

If a function  $g(\ell, \theta)$  is a function of the 2D radon transform of a function  $f \in S$  it must satisfy the following consistency conditions:[139]

- (a)  $g(\ell, \theta) \in S$
- (b)  $g(\ell, \theta + \pi) = g(-\ell, \theta)$  (i.e. past 180° the information is repeated (periodicity))

which is true for cylindrical geometry)

(c) the integral  $\int_{-\infty}^{\infty} g(\ell, \theta) \ell^m d\ell$  is a homogeneous trigonometric polynomial of degree m. The variable ‘m’ is also called the moment.

When  $m = 0$  (the first moment) condition ‘c’ reduces to the following condition ( $\forall \theta$ ):[139]

$$\int_{-\infty}^{\infty} \mathbf{g}(\boldsymbol{\ell}, \boldsymbol{\theta}) d\boldsymbol{\ell} = \int_{\mathbf{x} \in \mathbb{R}^2} \mathbf{f}(\mathbf{x}) d\mathbf{x} \quad (2.2.8.1)$$

where:  $f(x)$  is a function describing the object ( $x$  is a 2D vector). This is known as the mass constraint and basically states that the sum of any projection at any given angle is the same. For the second moment when  $m = 1$  we get the center-of-mass sinogram constraint shown as follows:[139]

$$\int_{-\infty}^{\infty} \mathbf{g}(\boldsymbol{\ell}, \boldsymbol{\theta}) \boldsymbol{\ell} d\boldsymbol{\ell} = \mathbf{c}_1 \cos \theta + \mathbf{c}_2 \sin \theta \quad (2.2.8.2)$$

where  $c_1$  and  $c_2$  are constants. This constraint states that the 1D center of mass of a projection is the same as the 2D projection of the object’s center of mass, thus a collection of the center of masses for different angles of these projections will form a sinusoidal function.[140]

One such formulation of these conditions for attenuation correction in PET imaging is the Helgason-Ludwig consistency conditions on 2D Radon transforms as shown in the following equation:[62,141]

$$\Phi_{\mathbf{m}, \mathbf{k}} = \int_0^{2\pi} \int_{-\infty}^{\infty} \mathbf{s}^m \mathbf{e}^{i\mathbf{k}\boldsymbol{\theta}} \mathbf{e}^{A(\mathbf{s}, \boldsymbol{\theta})} \mathbf{E}(\mathbf{s}, \boldsymbol{\theta}) d\mathbf{s} d\boldsymbol{\theta} \quad (2.2.8.3)$$

where:  $A(\mathbf{s}, \boldsymbol{\theta})$  is the radon transform (forward projection) of the attenuation image (CT, IE  $e^{A(\mathbf{s}, \boldsymbol{\theta})}$  is the CTAC correction factors - see **chapter 2.2.5**),  $\mathbf{k}$  are the Fourier components,  $\mathbf{m}$  are the transform moments,  $\mathbf{E}(\mathbf{s}, \boldsymbol{\theta}, z)$  is the measured emission sinogram

(see **chapter 2.2.2**). This is extended this to 3D with **equation 2.2.8.4** where we sum over all slices in the sinogram:[62]

$$\hat{\Phi} = \sum_z \sum_{m=0} \sum_{k=m+1} \Phi_{m,k}(z) \quad (2.2.8.4)$$

where:  $z$  is the slice number. For a sinogram properly aligned to the CT we expect this metric to yield a zero value; however, with the addition of noise it is proper to minimize this function to the lowest value since it will never be exactly zero.

## 2.2.9 Intrinsic and Reconstructed Spatial Resolution

Spatial resolution is a measure of the minimum resolvable size of an object in an image. After a positron decay the positron travels a short distance in tissue before it loses enough energy to combine with an electron and annihilate. That means that the line of response determined between two crystals may not cross the exact point of decay. The difference in spatial position of the decay and annihilation points adds a blurring effect to the reconstructed images, which in turn reduces the image resolution. It is important to remember we are measuring the distribution of annihilation events and assuming this is the tracer distribution (i.e. the decay points). Isotopes with shorter half-lives tend to have more energetic positrons and thus have a larger positron range and lower image resolution, see **table 2.1.1.2** (for Rb-82 it is ~6 mm full width at half maximum FWHM). There is also a small loss in resolution that occurs due to the angular distribution ( $\pm 0.5^\circ$ ) of the annihilation photons caused by conservation of momentum, called acollinearity, see **figure 2.1.3.2**. This blurring effect can be calculated using the relationship  $0.0044R$  where  $R$  is the radius of the detector ring.[142]

Another factor limiting image resolution is the detector crystal size. This creates an uncertainty in the position on the crystal face between two detector crystals. A detector crystal has a triangular point spread function that starts at zero at the crystal edge and reaches a maximum for coincidence detection at the middle of the detector crystal. The spatial resolution is equal to half the detector crystal width as shown in **figure 2.2.9.1**, where H is the point of high coincidence sensitivity and L is the point of low coincidence sensitivity.[142]

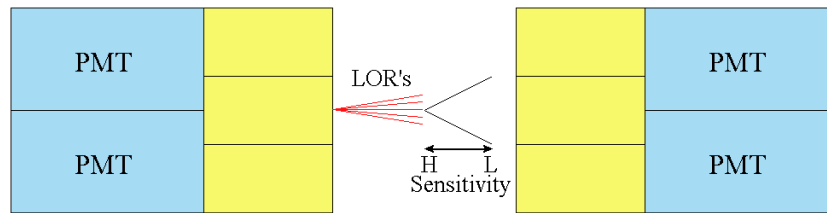


**Figure 2.2.9.1: Point spread function of a detector crystal. The sensitivity to various possible lines of response (LOR's) is shown as a triangle function, with the most sensitive region being the middle of the crystal.**

The high energy of the annihilation photons is highly penetrating, therefore if the incident angle is not 90° it may penetrate the initial crystal and deposit some or all of its energy to the adjacent crystal. This causes the LOR to be assigned to the wrong crystal which in turn causes an asymmetric blurring effect in the radial direction as shown in **figure 2.2.9.2**. [142] As emissions occur closer to the edge of the detector ring this effect becomes more pronounced. This penetration can be modeled as a Gaussian function with a FWHM defined by the following equation: [142]

$$\frac{12.5r}{\sqrt{r^2+R^2}} \quad (2.2.9.1)$$

where: r is the distance from the center of the detector ring and R is the radius of the detector ring.

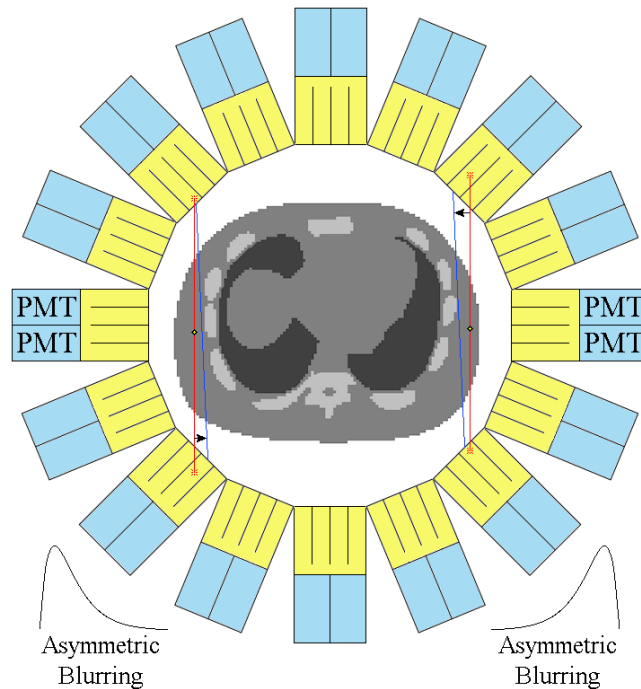


**Figure 2.2.9.2: Asymmetric blurring due to photon penetration into an adjacent crystal. Line of response due to penetration is shifted towards the center of the field of view.**

Crystal blocks are grouped together and coupled to a single PMT. Typically, there are 4 PMT's for each crystal block, e.g. consisting of a  $6 \times 6$  or  $9 \times 6$  array. The position of the detected event must be decoded using **equations** 2.2.1.6 and 2.2.1.7. Since this is an approximation there is an error associated with the determination of the position in the LOR. This can be calculated using a Gaussian function with a full width at half maximum:  $FWHM = d/3$  where  $d$  is the width of the crystal.[142]

One final limiting factor for spatial resolution is the sampling error. If all possible line of response are plotted as in **figure** 2.2.9.3 for a simple PET system, the distribution is non uniform across the field of view with some regions having more LOR's than other regions. Typically, this resolution limit multiplies all other factors by  $\sim 1.25$ .

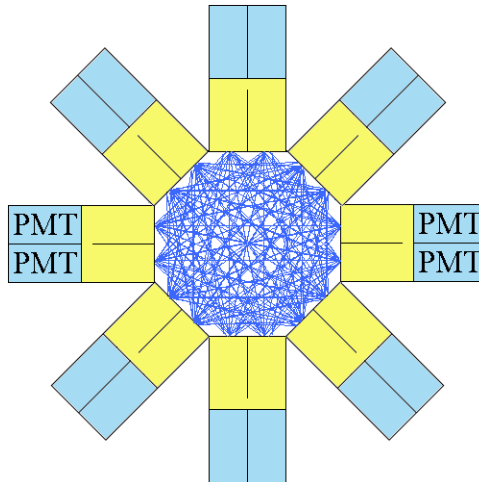


**Figure 2.2.9.3: Sampling error caused by the geometry of the LOR's in the field of view. Note the center of the field of view has fewer LOR's.**

The final system resolution is given by adding all the resolution contributions in quadrature. The final resolution for a point located a distance  $r$  from the center can be calculated using the following formula:[142]

$$\Gamma = 1.25 \sqrt{\left(\frac{d}{2}\right)^2 + (s)^2 + (0.0044R)^2 + \left(\frac{d}{3}\right)^2 + \left(\frac{12.5r}{\sqrt{r^2+R^2}}\right)^2} \quad (2.2.9.2)$$

where:  $d$  is the width of the crystal,  $s$  is the positron range (in FWHM), and  $R$  is the detector ring radius.

The intrinsic resolution ( $I$ ) of the D690 (ignoring the penetration effect) is 6 mm FWHM and typically to reduce noise an 8 mm Gaussian filter ( $F$ ) is applied to the reconstructed images, thus the final reconstructed resolution for Rb-82 PET is:

$$Res = \sqrt{I^2 + F^2 + P^2} = \sqrt{6^2 + 8^2 + 6^2} = 11.7 \approx 12 \text{ mm FWHM} \quad (2.2.9.3)$$

where:  $P$  is the FWHM positron range.

Another source of image blurring is the partial volume effect, which can be represented as a convolution of the tissue profile with the point spread function of the

scanner. The causes of partial volume effect include both periodic patient motion and the scanner resolution as well as any smoothing applied to the reconstructed images. **Figure 2.2.9.4** is a schematic of a cross section of a tissue profile (e.g. through the heart walls). True tissue profiles are shown as red rectangles. The rectangular tissue profiles are convolved with the Gaussian point spread function to give the blue measured curves, **figure 2.2.9.4 (A)**. Spill-in and spill-out are shown in blue and yellow respectively. The individual measured profiles are added to give the final combined profile shown in **figure 2.2.9.4 (B)**. For structures with a small spatial separation, two objects may be indistinguishable due to the partial volume effect.

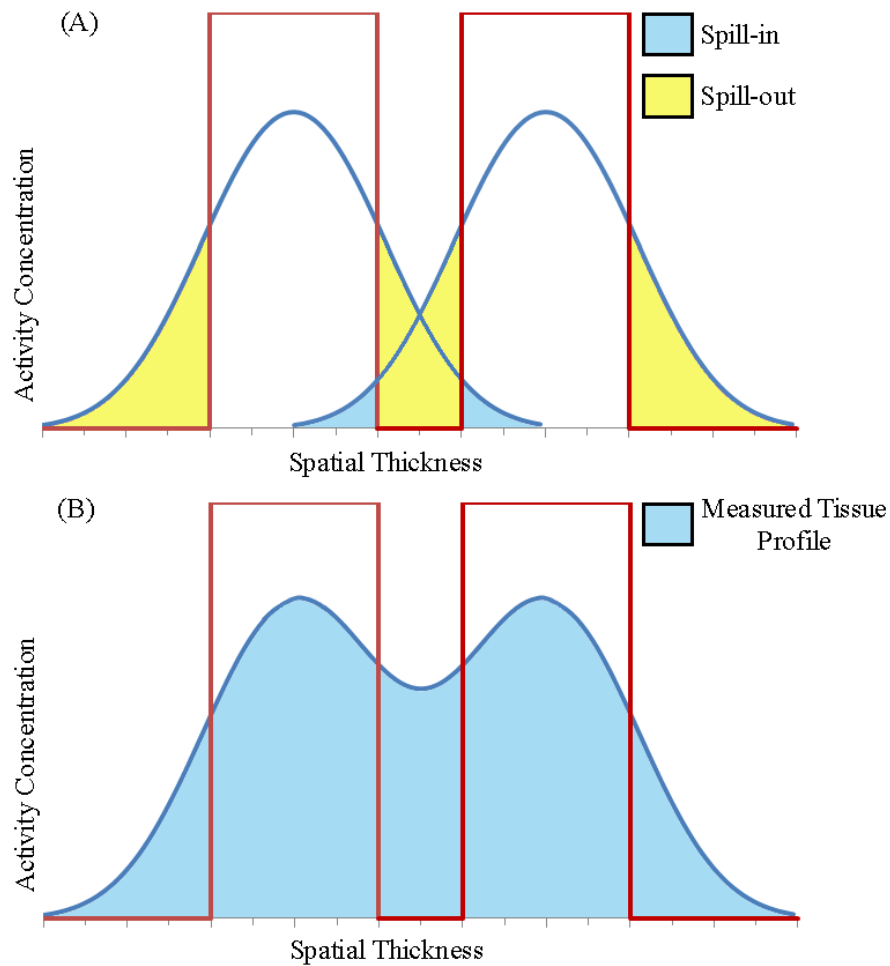


**Figure 2.2.9.4: Schematic of spill-in and spill-out and the resultant measured tissue profile. True tissue profiles are shown as red rectangles. Due to spatial smoothing activity spills into adjacent regions.**

### 2.3 Image Reconstruction from Projections

Tomographic image reconstruction is a mathematical method of combining projection information and reconstructing an estimate of the 2D (or 3D) object used to create it. The mathematics of projection was first discovered by Johan Radon in 1917, and first applied to image reconstruction in 1956.[143,144] A projection is a collection of LOR's at the

same angle but spatially distributed across the object, i.e. spanning an image plane. In PET, a LOR is the summation of all counts between two detector crystals.

### 2.3.1 Filtered Back-projection

In medical imaging, back-projection methods were originally developed for CT imaging purposes; however, the mathematical principles of image reconstruction can be applied to any set of projection data.[145] Back-projection begins with the understanding of the radon transform outlined in **equation 2.2.2.2**. If we start with the radon transform for only one specific angle  $g(\ell, \theta')$  (i.e. a single projection) it is impossible to reconstruct the image function  $f(x,y)$  that produced the projection. If we look at the projection profile and follow it along its length  $\ell$  (see **figure 2.2.2.3**), we will find some minima and maxima at location  $\ell'$  that describe regions along the length of the object  $L(\ell', \theta')$  where the signal is greater, signifying more activity in that region of the object. Therefore, to reconstruct the data we need to assign every point on  $L(\ell', \theta')$  the corresponding value from  $g(\ell', \theta')$ , which is known as a back-projection. This process can be described by **equation 2.3.1.1**: [109]

$$\mathbf{b}_{\theta}(\mathbf{x}, \mathbf{y}) = \mathbf{g}(\mathbf{x}\cos\theta + \mathbf{y}\sin\theta, \theta) \quad (2.3.1.1)$$

To reconstruct the whole image, we need to sum all contributions at all angles  $\theta$  and displacements  $\ell$  (or integrate in the continuous case, i.e. back-project for all possible cases) such as in **equation 2.3.1.2**: [109]

$$\mathbf{f}_b(\mathbf{x}, \mathbf{y}) = \int_{-\infty}^{\infty} \mathbf{b}_{\theta}(\mathbf{x}, \mathbf{y}) \mathbf{d}\theta \quad (2.3.1.2)$$

This process is illustrated in **figure 2.3.1.1**, where the initial  $g(\ell, \theta)$  for three different angles is calculated in part (A). Parts (B), (C) and (D) of this figure assign values  $g(\ell', \theta')$  to each corresponding  $L(\ell', \theta')$  on an initial blank matrix. Next in part (E) the

values in the matrix have the sum along the projection (which is the same for any angle) subtracted out, this operation can cause negative values. Lastly the matrix is scaled by 2 to produce the final reconstructed image. Notice this construction is not without loss of information as the initial and final matrices are not identical. Further improvements can be made as more projection angles are sampled.

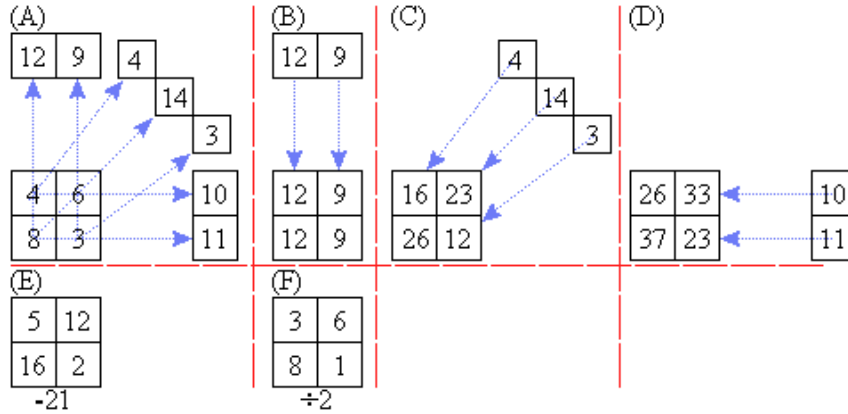


**Figure 2.3.1.1: Simple example of back projection. Forward projection in section (A) at 0°, 45° and 90° leads to 3 projections. Parts (B), (C) and (D) the 90°, 45° and 0° projections are back-projected onto a blank matrix, while parts (E) and (F) are for scaling.**

An important extension of this theory is the projection slice theorem. We begin with the 1D Fourier transform of the random transform:

$$\mathbf{G}(\mathbf{q}, \theta) = \mathcal{F}_{1D}\{\mathbf{g}(\ell, \theta)\} = \int_{-\infty}^{\infty} \mathbf{g}(\ell, \theta) e^{-j2\pi\mathbf{q}\ell} d\ell \quad (2.3.1.3)$$

where:  $\mathcal{F}_{1D}$  is the 1D Fourier transform of the random transform ( $\mathbf{g}(\ell, \theta)$ ), and  $\mathbf{q}$  is the spatial frequency. This leads to:[109]

$$\mathbf{G}(\mathbf{q}, \theta) = \int_{-\infty}^{\infty} \int_{-\infty}^{\infty} \int_{-\infty}^{\infty} \mathbf{f}(\mathbf{x}, \mathbf{y}) \delta(\mathbf{x} \cos \theta + \mathbf{y} \sin \theta - \ell) e^{-j2\pi\mathbf{q}\ell} d\mathbf{x}d\mathbf{y}d\ell \quad (2.3.1.4)$$

$$\therefore \mathbf{G}(\mathbf{q}, \theta) = \int_{-\infty}^{\infty} \int_{-\infty}^{\infty} \mathbf{f}(\mathbf{x}, \mathbf{y}) \int_{-\infty}^{\infty} \delta(\mathbf{x} \cos \theta + \mathbf{y} \sin \theta - \ell) e^{-j2\pi\mathbf{q}\ell} d\ell d\mathbf{x}d\mathbf{y} \quad (2.3.1.5)$$

where we can use the identity:[109]

$$\int \mathbf{f}(\mathbf{b})\delta(\mathbf{r} - \mathbf{b}) \, d\mathbf{b} = \mathbf{f}(\mathbf{r}) \quad (2.3.1.6)$$

$$\therefore \mathbf{G}(\mathbf{q}, \theta) = \int_{-\infty}^{\infty} \int_{-\infty}^{\infty} \mathbf{f}(\mathbf{x}, \mathbf{y}) e^{-j2\pi\mathbf{q}(x \cos \theta + y \sin \theta)} \, d\mathbf{x}d\mathbf{y} \quad (2.3.1.7)$$

We can make a change of variables:[109]

$$\mathbf{u} = \mathbf{q}\cos \theta, \quad \mathbf{v} = \mathbf{q}\sin \theta \quad (2.3.1.8)$$

$$\therefore \mathbf{G}(\mathbf{q}, \theta) = \int_{-\infty}^{\infty} \int_{-\infty}^{\infty} \mathbf{f}(\mathbf{x}, \mathbf{y}) e^{-j2\pi(\mathbf{x}\mathbf{u} + \mathbf{y}\mathbf{v})} \, d\mathbf{x}d\mathbf{y} \quad (2.3.1.9)$$

Which leads to the projection slice theorem:[109]

$$\mathbf{G}(\mathbf{q}, \theta) = \mathbf{F}(\mathbf{u}, \mathbf{v}) \quad (2.3.1.10)$$

This represents a slice of the 2D Fourier transform of the object. We can reconstruct the image function using the 2D inverse Fourier transform as shown below:[109]

$$\mathbf{f}(\mathbf{x}, \mathbf{y}) = \mathcal{F}_{2D}^{-1}\{\mathbf{G}(\mathbf{q}, \theta)\} = \int_0^{2\pi} \int_{-\infty}^{\infty} \mathbf{G}(\mathbf{q}, \theta) e^{-j2\pi\mathbf{q}(x \cos \theta + y \sin \theta)} \, \mathbf{q}d\mathbf{q} \, d\theta \quad (2.3.1.11)$$

$$\mathbf{f}(\mathbf{x}, \mathbf{y}) = \int_0^{2\pi} \int_{-\infty}^{\infty} |\mathbf{q}| \mathbf{G}(\mathbf{q}, \theta) e^{-j2\pi\mathbf{q}(x \cos \theta + y \sin \theta)} \, d\mathbf{q} \, d\theta \quad (2.3.1.12)$$

since:  $\ell = x\cos\theta + y\sin\theta$  we write

$$\mathbf{f}(\mathbf{x}, \mathbf{y}) = \int_0^{2\pi} \int_{-\infty}^{\infty} |\mathbf{q}| \mathbf{G}(\mathbf{q}, \theta) e^{-j2\pi\mathbf{q}\ell} \, d\mathbf{q} \, d\theta \quad (2.3.1.13)$$

which: is the filtered back-projection formula where  $|\mathbf{q}|$  is a ramp filter. Filtering is required for the Fourier method since the sampling frequency is inversely proportional to  $\mathbf{q}$  and this must be compensated for. **Figure 2.3.1.2** shows the effect on the number of projections for a filtered back-projection reconstruction. For a single projection angle, only 1 projection is back-projected onto a blank matrix as in the numerical example in **figure 2.3.1.1**. As the number of projection angles increases, the approximation becomes closer and closer to the true object. For 100 and 500 projection angles the reconstructed object is very close to the original image, thus any increase above 100 projection angles results in little to no improvements in image quality.

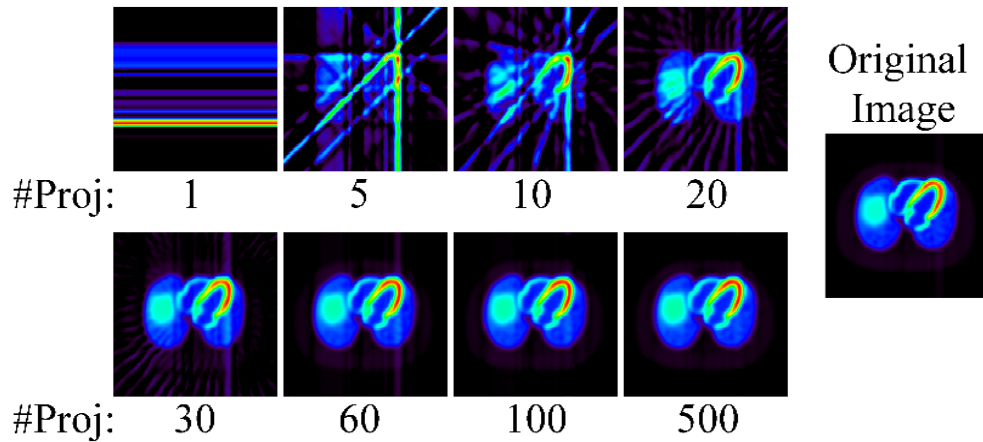


**Figure 2.3.1.2: Example of the effect of the number of projections on image reconstruction. The image given at 100 and 500 projections is nearly identical to the original image.**

### 2.3.2 Iterative Reconstruction

Iterative reconstruction begins with the understanding that the measurement of events using radiation detectors is a Poisson process. That is the probability of counting the number of events from a radiative process follows a Poisson distribution as shown in the histogram in **figure 2.3.2.1**.

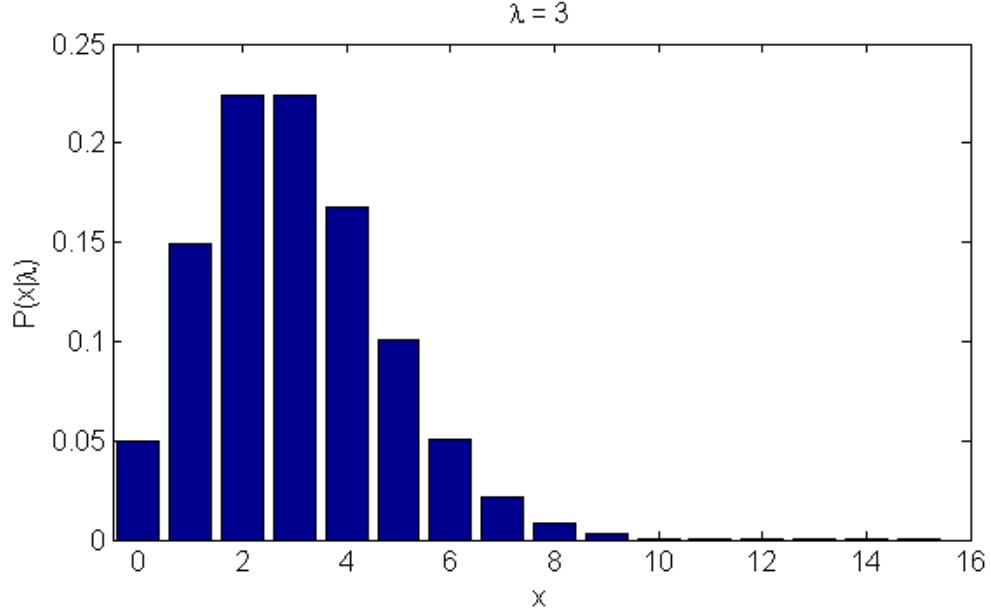


**Figure 2.3.2.1: The Poisson distribution for measuring radiation (for  $\lambda = 3$ ).**

The mean number of observed events on a given detector pair ‘i’ from the expected value of a point (voxel) that produced the pair is given by:[146]

$$\lambda_i = \sum_j f_j a_{ij}, \quad i = 1 \cdots m \quad (2.3.2.1)$$

where:  $a_{ij}$  is the expected value of pixel  $j$ ,  $f_j$  is the probability that emission in ‘j’ will be detected by detector pair ‘i’. We know that detected radiation follows a Poisson distribution therefore using these definitions we have:[146]

$$p_i(n_i) = \frac{\lambda_i^{n_i} e^{-\lambda_i}}{n_i!} \quad (2.3.2.2)$$

with:  $\lambda_i$  the mean and variance of the measured events in detector pair ‘i’ and  $n_i$  is the total number of measured events in detector pair ‘i’.[146] The total probability of all observed detections given a parameter ( $\lambda$ ) is defined as the likelihood and is shown in **equations 2.3.2.3 and 2.3.2.4.**

$$\mathcal{L}(\lambda) = \frac{\lambda_1^{n_1} e^{-\lambda_1}}{n_1!} \times \frac{\lambda_2^{n_2} e^{-\lambda_2}}{n_2!} \times \frac{\lambda_3^{n_3} e^{-\lambda_3}}{n_3!} \cdots \frac{\lambda_k^{n_k} e^{-\lambda_k}}{n_k!} \quad (2.3.2.3)$$

$$\mathcal{L}(\lambda) = \prod_i \frac{\lambda_i^{n_i} e^{-\lambda_i}}{n_i!} \quad (2.3.2.4)$$

If we can maximize the likelihood function, we find the most probable image (f) that generated the parameters ( $\lambda$ ). A computationally simpler method is given by the log likelihood function shown in **equation 2.3.2.5**.

$$\ln(\mathcal{L}(\lambda)) = \ln\left(\frac{\lambda_1^{n_1} e^{-\lambda_1}}{n_1!}\right) + \ln\left(\frac{\lambda_2^{n_2} e^{-\lambda_2}}{n_2!}\right) + \ln\left(\frac{\lambda_3^{n_3} e^{-\lambda_3}}{n_3!}\right) \dots \ln\left(\frac{\lambda_k^{n_k} e^{-\lambda_k}}{n_k!}\right) \quad (2.3.2.5)$$

Using the rules of logarithms, we can simplify **equation 2.3.2.5** to:

$$\ln(\mathcal{L}(\lambda)) = \ell(\lambda) = \sum_i \ln\left(\frac{\lambda_i^{n_i} e^{-\lambda_i}}{n_i!}\right) \quad (2.3.2.6)$$

Now we expand this result to:

$$\ell(\lambda) = \sum_i (\mathbf{n}_i \ln(\lambda_i) - \lambda_i - \ln(n_i!)) \quad (2.3.2.7)$$

Substituting **equation 2.3.2.1** into this results in:

$$\ell(\lambda) = \sum_i \left( \mathbf{n}_i \ln(\sum_j \mathbf{f}_j \mathbf{a}_{ij}) - \sum_j \mathbf{f}_j \mathbf{a}_{ij} - \ln(n_i!) \right) \quad (2.3.2.8)$$

To find the maximum, we take to derivative and set this equal to zero:

$$\frac{d(\ell(\lambda))}{d(\mathbf{f}_j)} = \frac{d(\sum_i (\mathbf{n}_i \ln(\sum_j \mathbf{f}_j \mathbf{a}_{ij}) - \sum_j \mathbf{f}_j \mathbf{a}_{ij} - \ln(n_i!)))}{d(\mathbf{f}_j)} = \mathbf{0} \quad (2.3.2.9)$$

thus:

$$\frac{d(\ell(\lambda))}{d(\mathbf{f}_j)} = \sum_i \left( \mathbf{n}_i \frac{d(\ln(\sum_j \mathbf{f}_j \mathbf{a}_{ij}))}{d(\mathbf{f}_j)} - \sum_j \frac{d(\mathbf{f}_j)}{d(\mathbf{f}_j)} \mathbf{a}_{ij} - \frac{d(\ln(n_i!))}{d(\mathbf{f}_j)} \right) = \mathbf{0} \quad (2.3.2.10)$$

Finally we get the result:

$$\max \left( \frac{d(\ell(\lambda))}{d(\mathbf{f}_j)} \right) = \sum_i \left( \mathbf{n}_i \frac{\sum_j \mathbf{a}_{ij}}{\sum_j \mathbf{f}_j \mathbf{a}_{ij}} - \sum_j \mathbf{a}_{ij} \right) = \mathbf{0} \quad (2.3.2.11)$$

Here we add an accent to the ‘j’ subscript to distinguish the sum on the denominator with the one on the numerator. This is useful since the term  $\sum_j \mathbf{f}_j \mathbf{a}_{ij}$  (a sum across the

pixels ‘j’ of an image for each detector pair ‘i’) is a forward projection which can be done separately. Next, we fix all other ‘j’ values to a fixed arbitrary ‘j’.

$$\mathbf{f}_j \sum_i \mathbf{n}_i \frac{a_{ij}}{\sum_j f_j a_{ij}} - \mathbf{f}_j \sum_i a_{ij} = \mathbf{0} \quad (2.3.2.12)$$

Rearranging we find the usual form for the maximum likelihood expectation maximization (MLEM) algorithm:

$$\mathbf{f}_j^{k+1} = \frac{f_j^k}{\sum_i a_{ij}} \sum_i \frac{n_i a_{ij}}{\sum_j f_j^k a_{ij}} \quad (2.3.2.13)$$

A way of optimizing the convergence speed of this algorithm is to split up the angular projections into even subsets and then iterate over each subset. Since the whole matrix is updated for each subset (which are computationally faster), far fewer iterations are required to reach convergence and the whole algorithm converges faster.

$$\mathbf{f}_j^{k+1,S} = \frac{f_j^{k,S}}{\sum_{i \in S} a_{ij}} \sum_{i \in S} \frac{n_i a_{ij}}{\sum_j f_j^{k,S} a_{ij}} \quad (2.3.2.14)$$

The OSEM (ordered subsets expectation maximization) algorithm converges to MLEM provided the following conditions are met:

- (1) An image  $f_j^*$  satisfying the consistency condition:  $n_i = \sum_{i \in S} f_i^* a_{ij}$  exists.  
Effectively this means we must have a valid sinogram to perform unbiased image reconstruction (see **chapter 2.4.1**).
- (2) The balancing condition for all  $k = 1 \dots m - 1$ ,  $a_j = m \sum_{i \in S} a_{ij}$  is met.

### 2.3.3 OSMAPOSL Reconstruction in STIR

The Software for tomographic image reconstruction (STIR) is an open source software package with tools for image reconstruction. The software package contains both iterative

and filtered back-projection algorithms that are well documented.[147–153] One of the issues with the OSEM algorithm is that the log likelihood function in **equation 2.3.2.5** could be a noisy function (i.e. with frequent changes in the sign of the gradient), as pointed out by Good et al.[154] A possible solution for the MLEM (or OSEM) algorithm suggested by Greene was to subtract a roughness penalty function ( $U(f)$ ) from **equation 2.3.2.6** before maximizing. One such algorithm that takes this into account is the ordered subsets maximum a posteriori one-step-late (OS-MAP-OSL) iterative algorithm shown in **equation 2.3.3.1**. [155,156]

$$f_j^{k+1,S} = \frac{f_j^{k,S}}{\sum_{i \in S} a_{ij} + \beta \frac{d}{df_j} U(f_j) \Big|_{f=f^k}} \sum_{i \in S} \frac{n_i a_{ij}}{\sum_j f_j^{k,S} a_{ij}} \quad (2.3.3.1)$$

where:  $\beta$  is a scaling factor and  $U(f_i)$  is the roughness (or energy) function. The function

$\frac{d}{df_j} U(f_j) \Big|_{f=f^k}$  is the gradient of the energy function as shown here for OSMAPOS L:

$$\beta \frac{d}{df_j} U(f_j) \Big|_{f=f^k} = \beta \frac{f_i^k - M_i(f^k)}{M_i(f^k)} \quad (2.3.3.2)$$

where:  $M_i(f^k)$  is the median filtered image.[153] Since the gradient of the roughness function is determined from the current estimate ( $f^k$ ) rather than the new estimate it is called one step late (OSL).[155]

## 2.4 PET-CT Co-Registration

As mentioned in **chapter 2.2.7** photons are attenuated as they travel through a medium such as a patient, and this is corrected for by using a CT scan of the patient. Since the CT and PET scans are not performed simultaneously, alignment of the CT to the PET data may be suboptimal. Typically, cardiac patients are older and suffer from arthritis; therefore, remaining still for the scan duration which may be 10 minutes or more is unlikely. In

addition, there may be a gradual deformity in the morphology of the organs which can cause an effect called ‘organ creep’ where organs slowly drift over the course of the scan. Periodic effects such as cardiac and respiratory motion are also important for their degrading effects on spatial resolution. Any misalignment from the CT and PET data will cause reconstruction artifacts as shown in **Figure 2.4.1.1** and **Figure 2.4.2.1**. These artifacts are a direct result of inconsistency between the measured emission vs attenuation correction sinograms (or projection) data, as described in **section 2.2.7**. Artifacts cause increases (overcorrections) and decreases (undercorrections) from the true activity concentration.

#### **2.4.1 CTAC Artifacts from Left and Right Shifts**

**Figure 2.4.1.1** shows the reconstruction artifacts that result from left (-x) and right (+x) shifts.

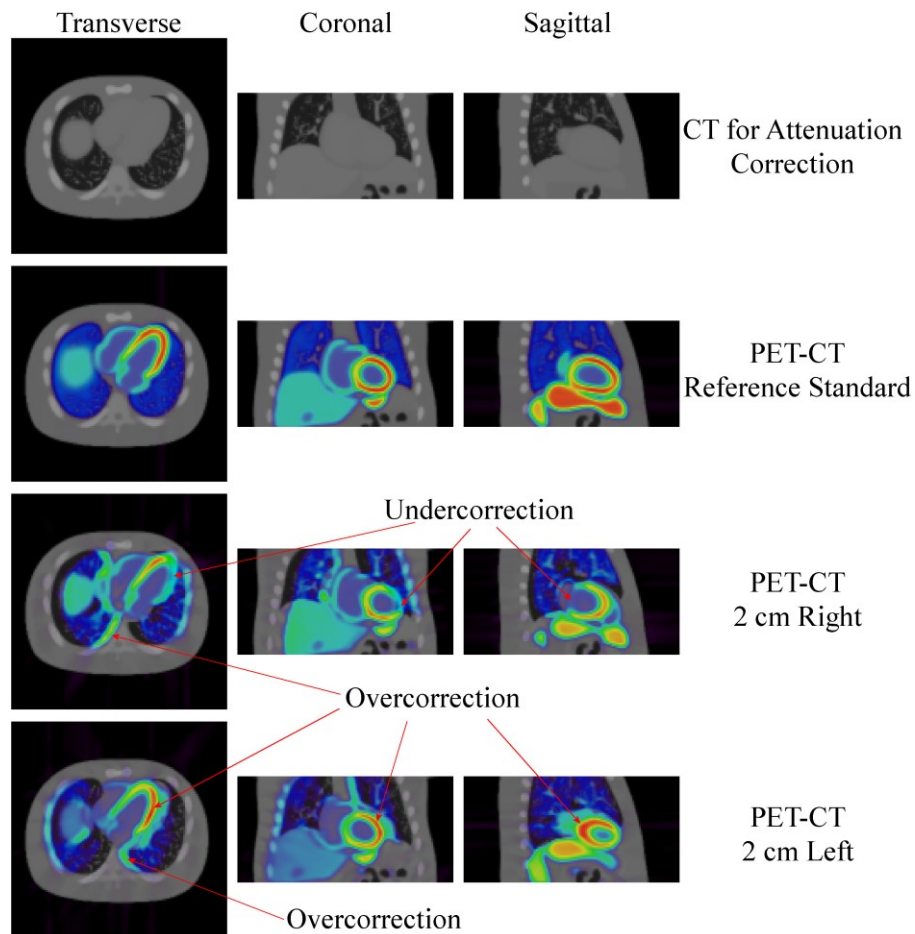


**Figure 2.4.1.1: Reconstruction artifacts resulting from PET-CT misalignment. CT used for attenuation correction shown on top. The PET-CT reference standard is perfectly aligned to the CT and has no CTAC artifacts. Left (-x) and right (+x) shifts in the PET data from the CT are also shown.**

A right shift (+x) of the PET image (left shift of the body) results in the most severe CTAC artifacts. Right shifts can cause a 300 % over-correction near the lung-tissue boundary, with under-corrections in the lateral heart wall of 50 %, and 10 % in the septal wall. A 2 cm left shift (-x) in PET data results in a 20 % over-correction in the lateral heart wall and a 15 % under-correction in the septal wall. Left shifts can also cause a 50 %

overcorrection near the lung-liver boundary, and a 500 % over-correction near the lung-tissue boundary.

### 2.4.2 CTAC Artifacts from Anterior/Posterior and Superior/Inferior Shifts

**Figure 2.4.2.1** shows the reconstruction artifacts that result from anterior (+y), posterior (-y) shifts, superior (+z) and inferior (-z) shifts.

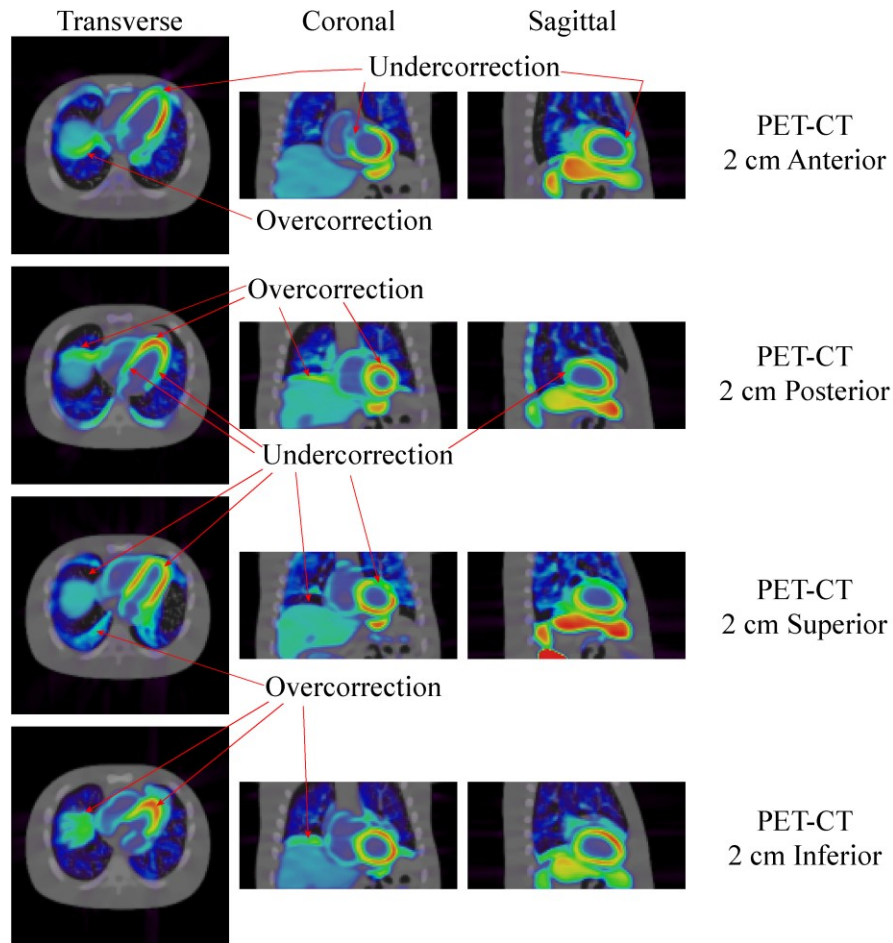


**Figure 2.4.2.1: Reconstruction artifacts resulting from PET-CTAC misalignment. Anterior (towards chest: +y) and posterior (towards back: -y) shifts in the PET data from the CT are shown. In addition superior (towards the head: +z) and inferior (towards feet: -z) are also shown.**

An anterior shift (+y) in PET data results in a 40 % undercorrection in the apex of the heart wall and a 20 % undercorrection in the septal heart wall. Shifts also cause a 70 % overcorrection near the lung-liver boundary. A posterior shift (-y) in PET data results in a 10 % overcorrection in the apex of the heart wall, and a 10 % undercorrection in the septal heart wall and a 40 % undercorrection in the lateral heart wall. A superior shift (+z) in PET data results in a 30 % undercorrection in the whole the heart wall except for the top of the heart wall where the undercorrection is 50 %. Shifts also cause a doughnut artifact near the top of the liver with the inside of the doughnut 88 % undercorrection and the lung liver boundary (outside the doughnut) a 50 % overcorrection. An inferior shift (-z) in PET data results in a 10 % overcorrection in the whole the heart wall except for the septal wall. In addition, the top part of the liver is overcorrected by 80 %.

## **2.5 Dynamic PET imaging and Blood Flow Quantification**

As mentioned in **chapter** 1.1 PET imaging is functional as opposed to anatomical imaging. The purpose of functional imaging is to measure the concentration of radioactive tracer within the body with the goal of quantifying the interaction of the tracer with a physiological process. Both static (time-independent) and dynamic (time-dependent) functional imaging provide useful information for clinicians. Static imaging involves determining where the tracer is located at a particular point in time (i.e. where the physiological processes defined by the tracer chemistry are most prevalent), whereas dynamic imaging can determine both the tracer spatial distribution and temporal kinetics (rate of tracer absorption vs rate of extraction by tissues).

A PET image consists of the superposition of many signals dependent on the unique physiological processes present. The spatial separation for some processes is great enough that they can be isolated and analyzed separately. Quantification of a physiological process is achieved by the use of mathematical models which relate the image data to the tracer dynamics for possible states that the tracer can take. Each state described using these models can be considered as a compartment, which is the distribution of a tracer at a specific location and time. In the next section we will discuss the 1 and 2 compartment models used for blood flow imaging.

### **2.5.1 The Compartment Model**

To perform compartment modeling the rate of exchange of tracer over time between the compartment and other systems must be defined. Differential equations with coefficients describing the exchange rates can be solved for the physiological quantity of interest. The coefficients making up the differential equations reflect the steady state (or average state) of the kinetic properties of the tracer in the system. The tracer concentration in arterial blood over time is used as the input function, and the concentration in the tissue compartments as the model output. The most difficult task is the determination of the blood/plasma input function; often a direct measurement of the input function using arterial blood samples is not possible. By comparing the input function to the measured data, the coefficients for the differential equations describing the exchange between compartments can be estimated. For tracer studies the following assumptions are made:[157]

- (1) The tracer is injected in very small (trace) amounts so no physiological changes are made on the system by the tracer.

- (2) The compartments are spatially invariant, but not time invariant.
- (3) The tracer has the chemical properties needed to characterize the physiological process under investigation (usually by mimicking a known biological chemical that is important to that process).
- (4) There are no isotope effects.
- (5) The coefficients (parameters) in the differential equations are time invariant.
- (6) Often the assumption is made that all organs (or parts of the organs) see the same input function, particularly in PET imaging.

The first task in blood flow quantification is to define the path the tracer takes from the input function (blood) to the important components (tissues/systems) taking into account extraction from those components. This knowledge is then used to formulate a compartment model for that system. For heart blood flow imaging, we are concerned with tracer uptake in the myocardium (heart wall), and the input function is the arterial blood supply to the heart. To further understand the mechanism of Rb-82 uptake in the heart muscle it is useful to look at the active transport across the muscle cell membranes since that is how Rb-82 is taken up into the muscle tissue. As discussed in **chapter 1.0** Rb-82 is a potassium analogue, an illustration of active sodium-potassium transport can be found in **figure 2.5.1.1**.

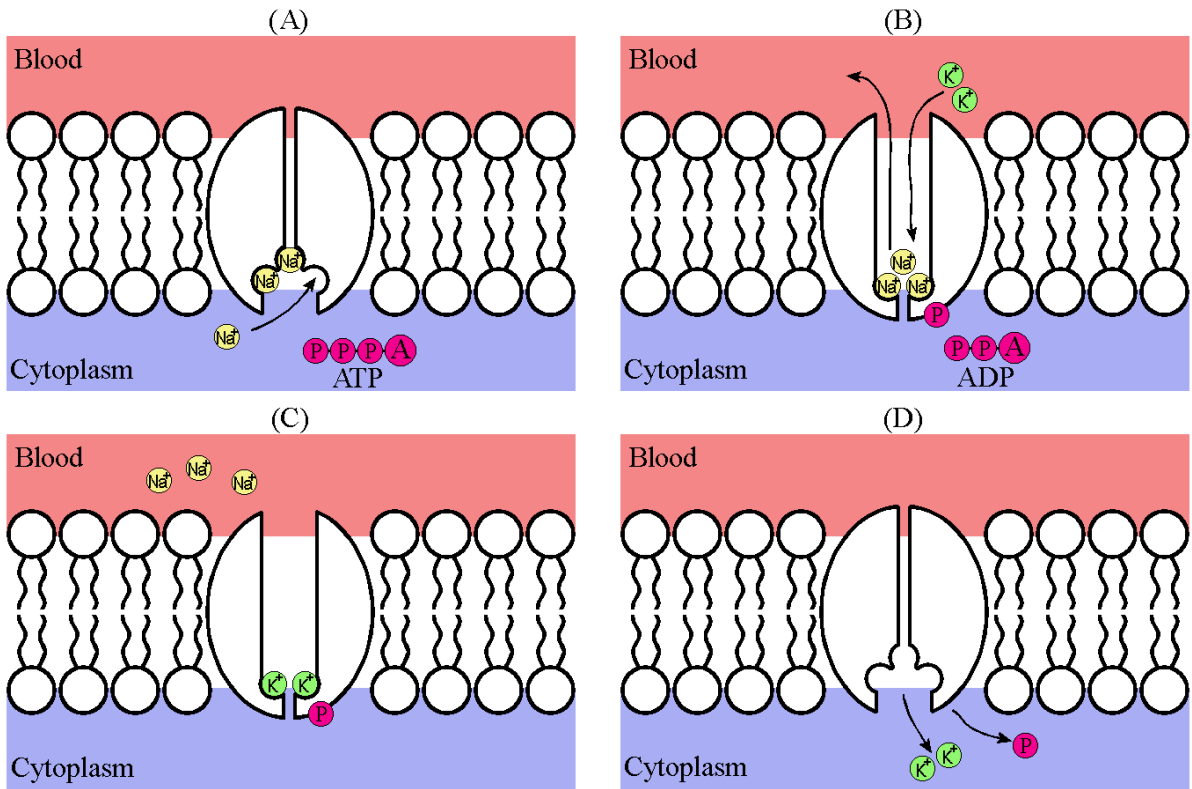


**Figure 2.5.1.1: Sodium-potassium active transport. (A) Sodium ions bind to the protein. (B) Phosphorylation: phosphate from ATP binds to the NaK-ATPase protein causing it to change shape. (C) Sodium ions are released into the blood while potassium ions bind to the protein. (D) Potassium bound to the protein causes the phosphate to be released. Protein changes shape again releasing potassium into the cytoplasm.[158]**

As **figure 2.5.1.1** shows the active transport in cell muscles exchanges 3 sodium ions for every 2 potassium (or Rb-82) ions. One could model this using a single compartment called the 1-compartment model where the input function is the blood plasma, and the compartment is the myocardium tissue cells. This is illustrated in **figure 2.5.1.2** where the activity concentration over time in the myocardium is given by  $C_{myo}(t)$ ,

in the blood plasma it is given by  $C_b(t)$ , coefficient  $K_1$  is the uptake (influx) rate constant and coefficient  $k_2$  is the clearance (efflux) rate constant.

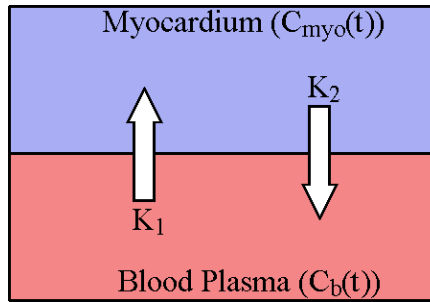


**Figure 2.5.1.2: 1-Tissue compartment model for Rb-82.**

The differential equation that describes **figure 2.5.1.2** will define each unknown quantity (in this case just 1,  $C_{myo}(t)$ , since the blood plasma input function is assumed to be known and is therefore not a variable). An equation that describes this system is shown in **equation 2.5.1.1.**[159]

$$C_{myo}(t) = K_1 e^{-k_2 t} * C_b(t) \quad (2.5.1.1)$$

where: \* is the convolution integral. To accurately assess the correct activity concentration in the heart wall, partial volume effects must be accounted for (see **figure 2.2.6.4**). To account for these effects  $C_{myo}(t)$  is usually modified by the following relationship:

$$\hat{C}_{myo}(t) = F_{LV} C_b(t) + (1 - F_{LV}) C_{myo}(t) \quad (2.5.1.2)$$

where:  $\hat{C}_{myo}(t)$  is the estimated tracer concentration in the myocardium including partial volume effects,  $F_{LV}$  is the spillover of the blood activity into the myocardium region of interest. This formulation assumes that the region of interest (ROI) volume includes only myocardial tissue and blood pool. Therefore, the quantity  $(1 - F_{LV})$  is the fraction of volume of myocardial tissue. This quantity can be calculated on a regional (breaking up the myocardium into small regions and calculating each individually) or global (considering the myocardium as one single unit with a single correction factor) basis.

Another model is to define two compartments:

- (1) The vascular (blood) and interstitial spaces, which is the fluid surrounding the cell membranes but still outside the cell and the main blood supply.
- (2) The intracellular space, i.e. inside the cell.

This model is illustrated in **figure 2.5.1.3**.

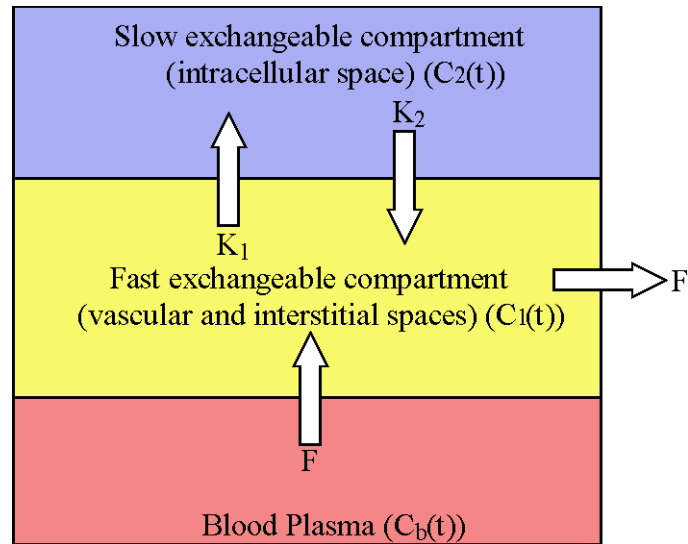


**Figure 2.5.1.3: 2-Tissue compartment model.**

In this case the myocardium is represented as two compartments (2-compartment model), with  $F$  being the flow rate [ml/min] into the region. The coefficient  $k_1$  is the uptake rate constant and coefficient  $k_2$  is the clearance rate back into the vascular and interstitial spaces. The differential equations that describe this system is defined as follows:

$$\frac{dq_1(t)}{dt} = F \left( C_a(t) - \frac{q_1(t)}{V_1} \right) - k_1 q_1(t) + k_2 q_2(t) \quad (2.5.1.3)$$

$$\frac{dq_2(t)}{dt} = k_1 q_1(t) - k_2 q_2(t) \quad (2.5.1.4)$$

where:  $q_1(t)$  and  $q_2(t)$  is the amount of tracer in compartment 1 and 2 respectively,  $F$  is the flow rate,  $C_a$  is the arterial tracer concentration,  $V_1$  is the volume of compartment 1, and  $k_1$

and  $k_2$  are the fractional rate constants of compartment 1 and 2 respectively. The solution to these differential equations is:

$$\mathbf{q}_1(\mathbf{t}) = \left[ \frac{\mathbf{F}}{\beta - \alpha} \right] [(\beta - \mathbf{k}_2)e^{-\beta \mathbf{t}} + (\mathbf{k}_2 - \alpha)e^{-\alpha \mathbf{t}}] \mathbf{C}_a(\mathbf{t}) \quad (2.5.1.5)$$

$$\mathbf{q}_2(\mathbf{t}) = \left[ \frac{\mathbf{F}k_1}{\beta - \alpha} \right] [e^{-\alpha \mathbf{t}} - e^{-\beta \mathbf{t}}] \mathbf{C}_a(\mathbf{t}) \quad (2.5.1.6)$$

with the following definitions:

$$\alpha, \beta = \frac{1}{2} \left[ \mathbf{a} \pm \sqrt{\mathbf{a}^2 - 4\mathbf{b}} \right] \quad (2.5.1.7)$$

and ‘a’ and ‘b’ are defined as follows:

$$\mathbf{a} = \left( \frac{\mathbf{F}}{v_1} \right) + \mathbf{k}_1 + \mathbf{k}_2 \quad (2.5.1.8)$$

$$\mathbf{b} = \left( \frac{\mathbf{F}}{v_1} \right) + \mathbf{k}_2 \quad (2.5.1.9)$$

Partial volume correction is achieved using the **equation** 2.5.1.2 to correct for partial volume losses. Coefficients for these compartment models can be solved using a weighted least squares method.

The equation that describes this 2-tissue component model is shown in **equation** 2.5.1.3.

$$\mathbf{C}_T(\mathbf{t}) = (\mathbf{A}e^{-\alpha \mathbf{t}} + \mathbf{B}e^{-\beta \mathbf{t}}) * \mathbf{C}_b(\mathbf{t}) \quad (2.5.1.10)$$

where:  $\mathbf{C}_T(\mathbf{t})$  is the activity concentration in the tissue and  $\mathbf{C}_b(\mathbf{t})$  is the activity concentration in in the arterial system, and the variables A and B are defined as follows:

$$\mathbf{A} = \frac{\mathbf{F}}{\beta - \alpha} (\mathbf{K}_1 + \mathbf{K}_2 - \alpha) \quad (2.5.1.11)$$

$$\mathbf{B} = \frac{\mathbf{F}}{\beta - \alpha} (\beta - \mathbf{K}_1 - \mathbf{K}_2) \quad (2.5.1.12)$$

The observed activity concentration is given by the following equation:

$$\mathbf{C}_{T_{PET}}(\mathbf{t}) = \mathbf{F}_{MM} \mathbf{C}_T(\mathbf{t}) + \mathbf{F}_{BM} \mathbf{C}_a(\mathbf{t}) \quad (2.5.1.13)$$

where:  $C_{T_{PET}}(t)$  is the observed activity concentration,  $F_{MM}$  is the tissue recovery coefficient,  $F_{BM}$  is fraction of activity in the blood pool region,  $C_T(t)$  is the activity concentration in the tissue and  $C_b(t)$  is the activity concentration in in the arterial system.

### **2.5.2 Myocardial Blood Flow Estimation using FlowQuant©**

In **chapters** 3 and 4 quantification of regional myocardial blood flow (MBF) will be accomplished using an in-house validated software program called FlowQuant© (Ottawa, ON). While the implementation details of the program are beyond the scope of this thesis, a structural overview of the program is covered here.

PET imaging begins with a controlled injection of Rb-82 into the left arm which carries the tracer to the heart via the superior vena cava to the right atrium. From the right atrium, it travels to the lungs through the pumping action of the right ventricle. From the lungs, the blood circulates back to the left atrium and ventricle where afterward it is pumped to the rest of the body. Therefore, early time frames have significant activity in the atria/ventricle cavities and little in the myocardium. As time progresses the Rb-82 is taken up by various organs (liver/spleen/stomach/kidneys/thyroid and myocardium) and the activity in the blood diminishes. Due to the action of the NaK active transport in the myocardium, in the late time frames the myocardium has typically retained more activity than surrounding tissues.

The FlowQuant© program begins first by identifying the myocardium in order to define the uptake images. As such the contrast between the left ventricle (LV) and the surround tissue must be high enough for clear delineation of the LV. To achieve this, uptake images are generated by averaging the last 6 minutes of the dynamic image data (2-

8 min) typically the last 4-5 frames. Using a smoothing filter image noise is reduced, then the myocardium is identified and reoriented from the body reference frame to a LV axis reference frame. An example of this can be seen in **figure 2.5.2.1**.

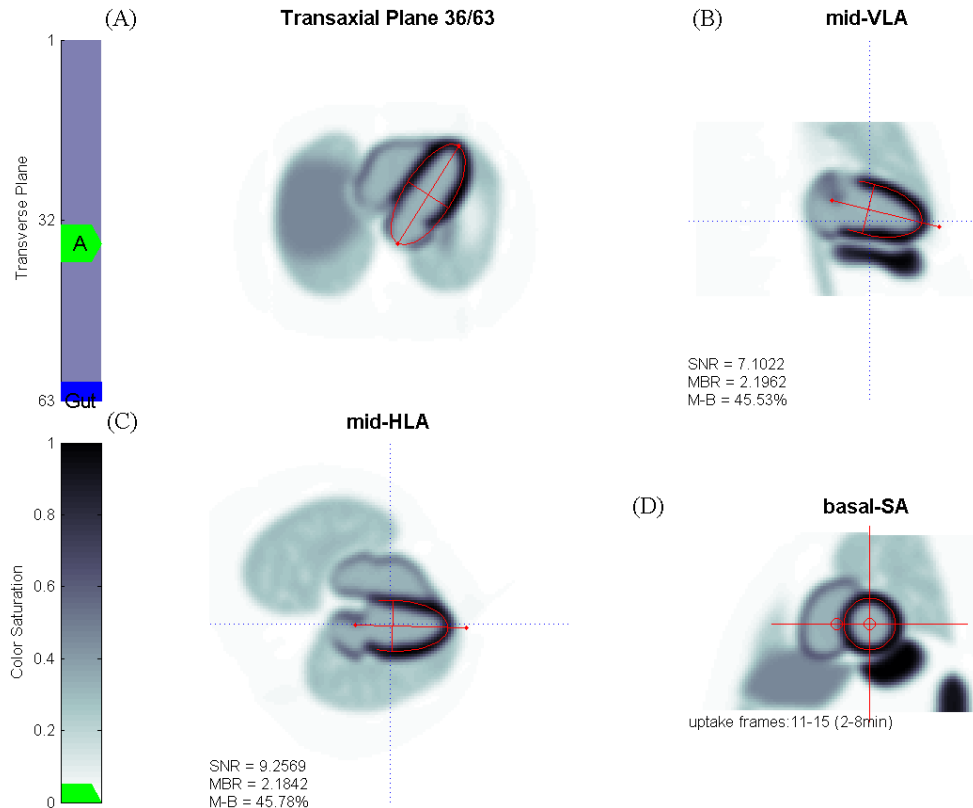


**Figure 2.5.2.1: Orientation and selection of the LV heart wall. Identification of the heart wall is shown in transaxial (A) and sagittal (mid vertical long axis (VLA)) (B) slices. Reorientation of the myocardium to LV reference frame is shown in mid horizontal long axis (HLA) (C) and basal short axis (SA) (D).**

The user can manually select the slice on the transaxial plane used to identify the heart wall, and the contours can be modified if so desired. The initial contours found in (A) and (B) help inform the algorithm where to look for the whole heart wall, and to

reorient the image matrix to the LV reference frame as shown in (C) and (D) as shown in **figure 2.5.2.2**.

In the next step, the heart wall is reoriented so that the long axis of the heart is orthogonal to the image plane. Then contours of the entire LV heart wall are defined (using a cubic b-spline smooth function outside the scope of this thesis) and the blood pool regions for the arterial input function are identified. Regions of interest with fixed epicardial (outside surface of the heart) and endocardial (inside surface of the heart) extent are generated, and used to sample the dynamic image sequence to derive myocardial time-vs-activity curves (TACs). **Figure 2.5.2.2** gives an example of the results from this process. Blood pool regions in the LV cavity ‘C’, base ‘B’ and left atrium ‘A’ are identified. The median of TAC values from these three regions is used as the arterial blood input function for kinetic modeling.

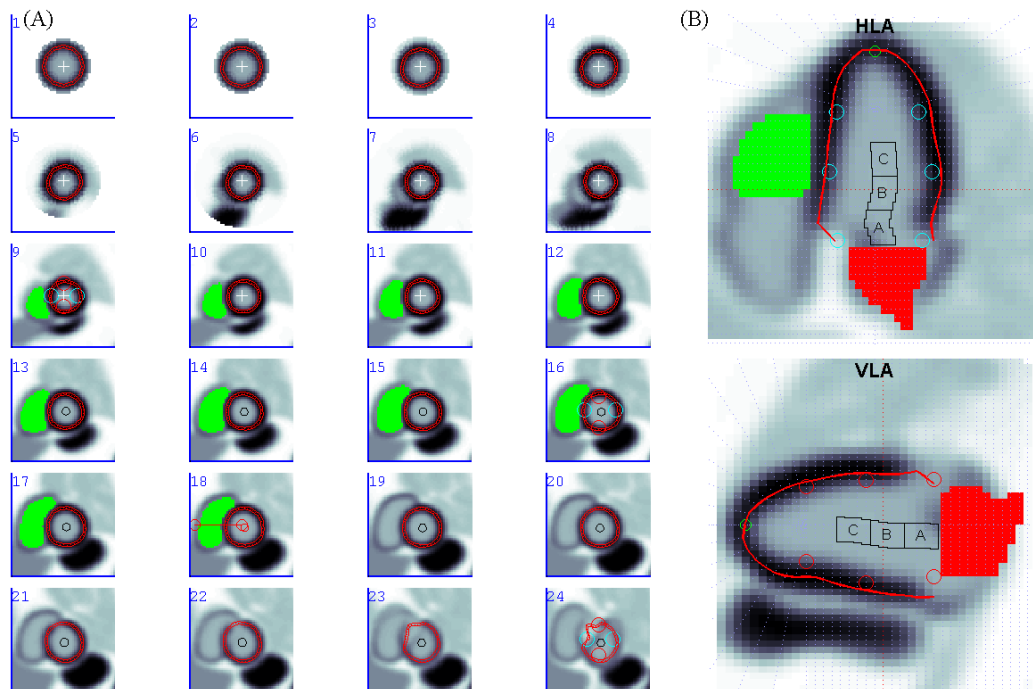


**Figure 2.5.2.2: Example of short axis slices of the heart wall (left). Short axis slices 1 to 18 are used for myocardial blood flow quantification (A). Blood pool regions (A,**

**B and C) are shown, along with the identification of the left atrium (B). The right ventricle is shown in green but not used in this work. The left atrium is shown in red.**

The next step is the kinetic modeling of the time activity curves used for myocardial blood flow quantification. As mentioned in the previous section, by comparing the measured blood input to the output (myocardium) TAC functions, the parameters of the compartment model are determined. In all cases for this thesis the 1-tissue-compartment model is used for blood flow quantification. An example of a time activity curve measured by the FlowQuant© program is given in **figure 2.5.2.3**.

Various orientations of the resultant contour maps from identification of the myocardium is shown in **figure 2.5.2.4**. The resultant shape resembles a paraboloid. To make the analysis of this data easier the contours are projected onto a 2-dimensional plane called a polar map.

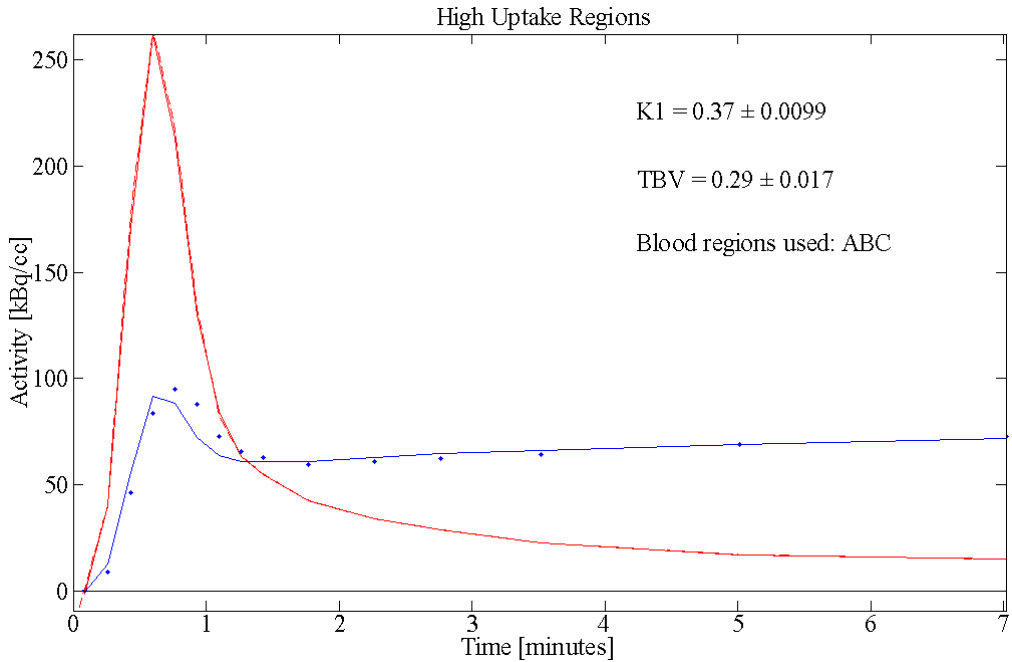


**Figure 2.5.2.3: Example of time activity curves measured by FlowQuant© for blood flow quantification. The red curve is the blood input function. The blue dots are the measured myocardium values and the blue line is the estimated compartment model function. The total blood volume (TBV =  $F_{LV}$ ) and K1 rate constant are also shown.**

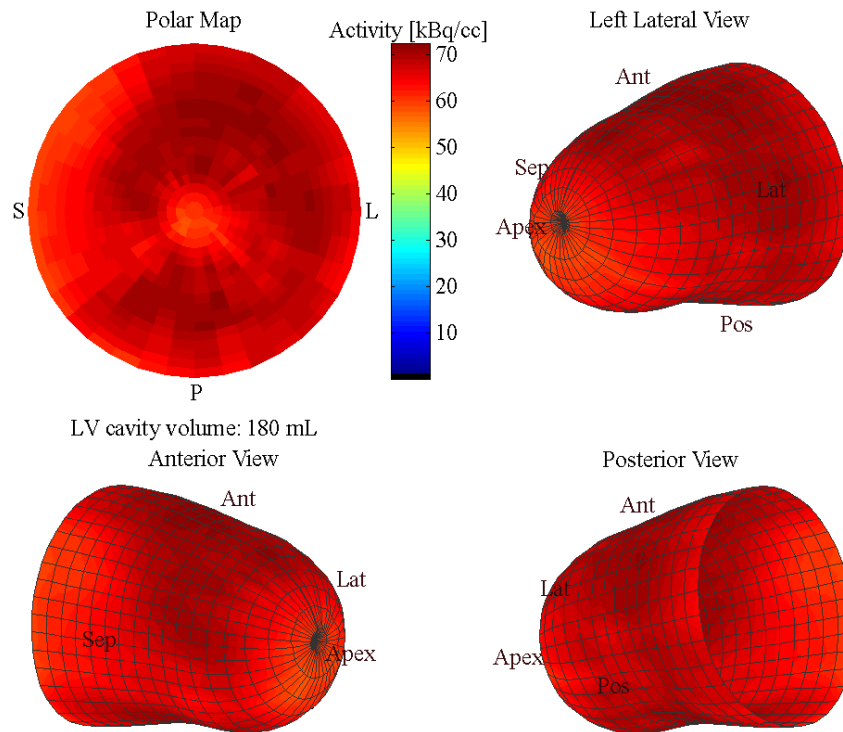


**Figure 2.5.2.4: Example of contour maps of the heart wall and the resultant polar map.**

FlowQuant produces values of MBF in units of mL/min/g using regional and global partial-volume corrections (PVC). This is done by splitting the myocardium into ~500 sectors and defining an ROI on a sector by sector basis and calculating  $(1-TBV)$  for each sector. Global PVC is accomplished by using an average of these values and applying it globally. Regional PVC is accomplished by using each  $(1-TBV)$  on the corresponding sector. Polar maps generated from FlowQuant© are shown in **figure 2.5.2.5**. The TBV and K1 polar maps are the estimated parameters from the kinetic model. This data used in

conjunction with the assumed tracer extraction function produces the regional and global PVC polar maps in units of tissue blood flow [mL/min/g]. Flow can be calculated using the following equations:[160]

$$\mathbf{MBF} = \frac{K_1}{E(\mathbf{MBF})} \quad (2.5.2.1)$$

where:  $E(\mathbf{MBF})$  is the extraction function which is tracer specific and describes the nonlinear tracer extraction and is a function of MBF. This quantity can be calculated using **equation 2.5.2.2**: [160]

$$\mathbf{E}(\mathbf{MBF}) = \mathbf{1} - \mathbf{e}^{-(\alpha\mathbf{MBF}+\beta)/\mathbf{MBF}} \quad (2.5.2.2)$$

where:  $\alpha$  and  $\beta$  are constants that are tracer specific. The purpose of the extraction function is to effectively calibrate the blood flow measurements to a known standard (for example microsphere studies).

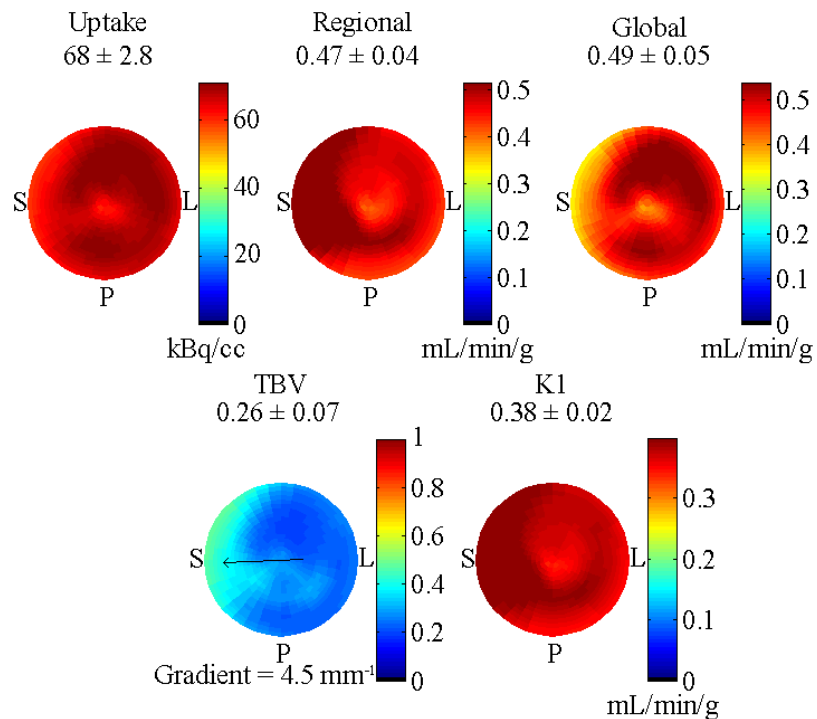


**Figure 2.5.2.5: Example of polar maps generated from FlowQuant©.**

Typically, the polar maps are divided into larger regions called segments. In subsequent chapters the polar maps are divided into 5 segments (called the 5-segment model) consisting of the following anatomic regions: anterior, posterior, septal, lateral, and apex – see **figure 2.5.2.6**. The average MBF value in each segment is reported as the data value for that segment.

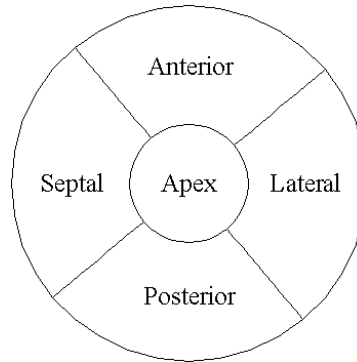


**Figure 2.5.2.6: 5-Segment model and its anatomic regions.**

## **2.6 PET Simulation**

When evaluating the performance of an algorithm used to analyze PET data, one of the biggest issues is how to separate the algorithm's inherent limitations from the multiple competing physiological processes. Sometimes we need to know that the limitations in the algorithm's performance is due to one physiological process as opposed to a different one. One method would involve using physiological phantoms which can be expensive and time consuming to use. In addition, often one cannot change the internal anatomy to include things like abnormal lesions or other defects, and one cannot introduce controlled and known time activity curves on all organ systems. In this thesis, digital simulations have been used extensively. The advantage of digital simulations is that they can simulate whole bodies, blood flow defects (lesions) can be introduced; time activity curves can be defined

on all major organs, and they are inexpensive. The disadvantages include limitations in the internal morphology (i.e. inability to simulate complex congenital abnormalities), and you can only simulate known tracer dynamics.

### **2.6.1 The Digital NCAT Phantom**

The non-uniform rational B-spline cardiac torso (NCAT) phantom is a digital phantom that is derived from real patient CT and MRI scans.[161–163] The NCAT phantom has the capacity to simulate both cardiac and respiratory motion. Real patient data from an electrocardiogram (ECG) can be used to determine the respiratory and cardiac periods and amplitudes, or a set period and amplitude of motion can be defined for each. This feature is not used in this thesis and therefore will not be discussed further. NCAT phantoms are generated using an executable program with an appropriate parameter file to describe the time activity curves and various physiological options that are exhaustive and beyond the scope of this thesis. A detailed description can be found in [161–163].

An example of the NCAT phantom generated for the examination of body motion in this thesis is shown in **figure 2.6.1.1**. Both the matrix and voxel size can be defined, in this thesis the transaxial field of view is always 40 cm. Shown in **figure 2.6.1.1** is a phantom with a  $256 \times 256 \times 256$  matrix. The voxel size is 1.5625 mm/pix which is less than clinical scans with a transaxial voxel size usually around 3.1 mm/pix, therefore herein this phantom is called the ‘high resolution’ phantom. The ‘low resolution’ phantom is anatomically identical to the high resolution phantom but with a clinically similar voxel size of 3.125 mm/pix. The final phantom shown in **figure 2.6.1.1** is the 20 cm phantom. The phantom is anatomically identical to the other two phantoms but is proportionally

smaller so that the transaxial dimension of the chest is 20 cm (the field of view is still 40 cm), with the same voxel size of 3.125 mm/pix.

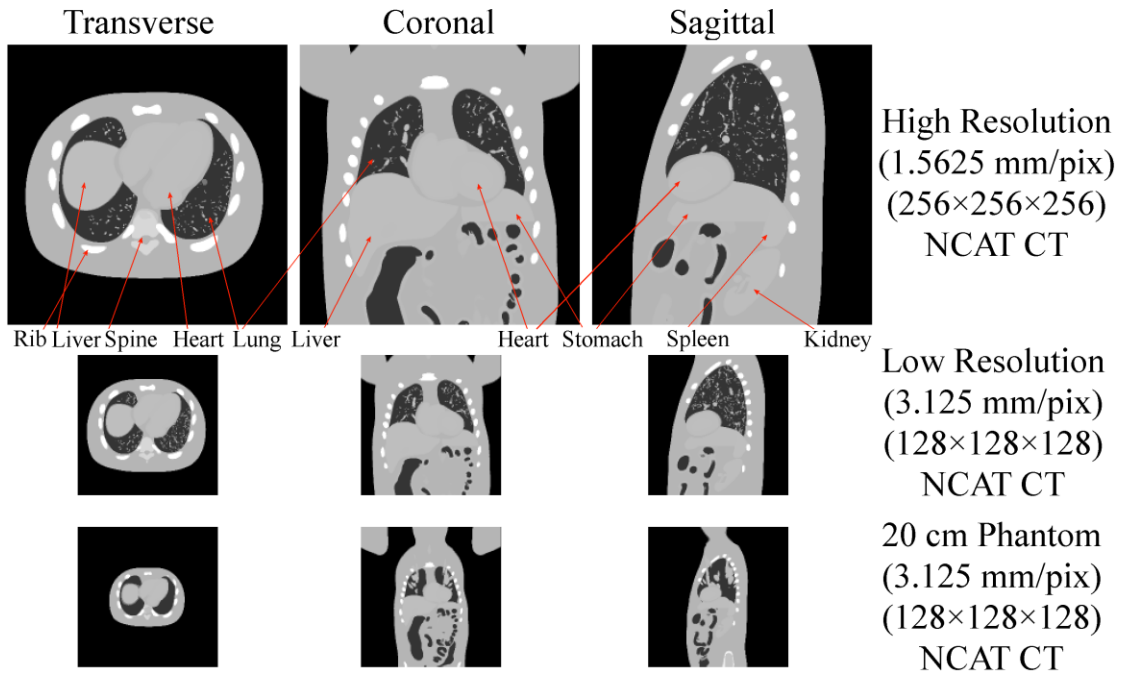


**Figure 2.6.1.1: Various NCAT CT phantoms used in this thesis.**

The CT generated in the NCAT phantom takes into account the photon energy desired. The voxels are unit-less, expressed as  $\mu \times x$  where  $x$  is the voxel size and  $\mu$  is the linear attenuation coefficient. Therefore, to generate an ACF, the CT can be forward projected and each element of the forward projected CT can be exponentiated to give an appropriate ACF sinogram.

The following organs can be assigned time activity curves in the NCAT phantom: remainder body (what is not on this list for example fat), liver, gall bladder, lungs, stomach wall, stomach contents, kidney, spleen, ribs, spine head, spine process, pelvis, bone cartilage, arteries, veins, bladder (content and wall), prostate, ascending large intestine, transcending large intestine, descending large intestine, small intestine, rectum, seminal vesicles, vas deferens, and testes. In addition, a constant activity can be assigned to the

following regions: ascending large intestine air, transverse large intestine air, descending large intestine air, small intestine air, rectum air, ureter, urethra, lymph normal, lymph abnormal, and airway tree. The heart can also be assigned separate time activity curves to its 4 myocardium regions (left ventricle (LV), right ventricle (RV), left atrium (LA) and right atrium (RA)) and their corresponding 4 blood pool regions as shown in **figure 2.6.1.2**.

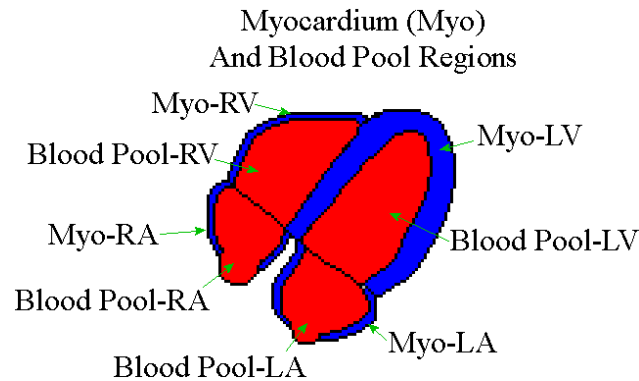


**Figure 2.6.1.2: Digital NCAT myocardium model with myocardium and blood pool regions shown.**

An example of a decay corrected dynamic sequence of the low resolution NCAT phantom is given in **figure 2.6.1.3**. The first 9 frames are 10 seconds in duration and frames 2, 4, 7 and 9 are shown. Frame 2 shows the initial high activity in the blood pool regions, frame 4 shows the activity at the peak of the blood pool curve and frame 7 shows the activity when the concentration in the myocardium and blood pool regions are almost the same. Frames 9 and 15 show the progression near the end of the scan as the myocardium becomes the dominant source of Rb-82 activity.

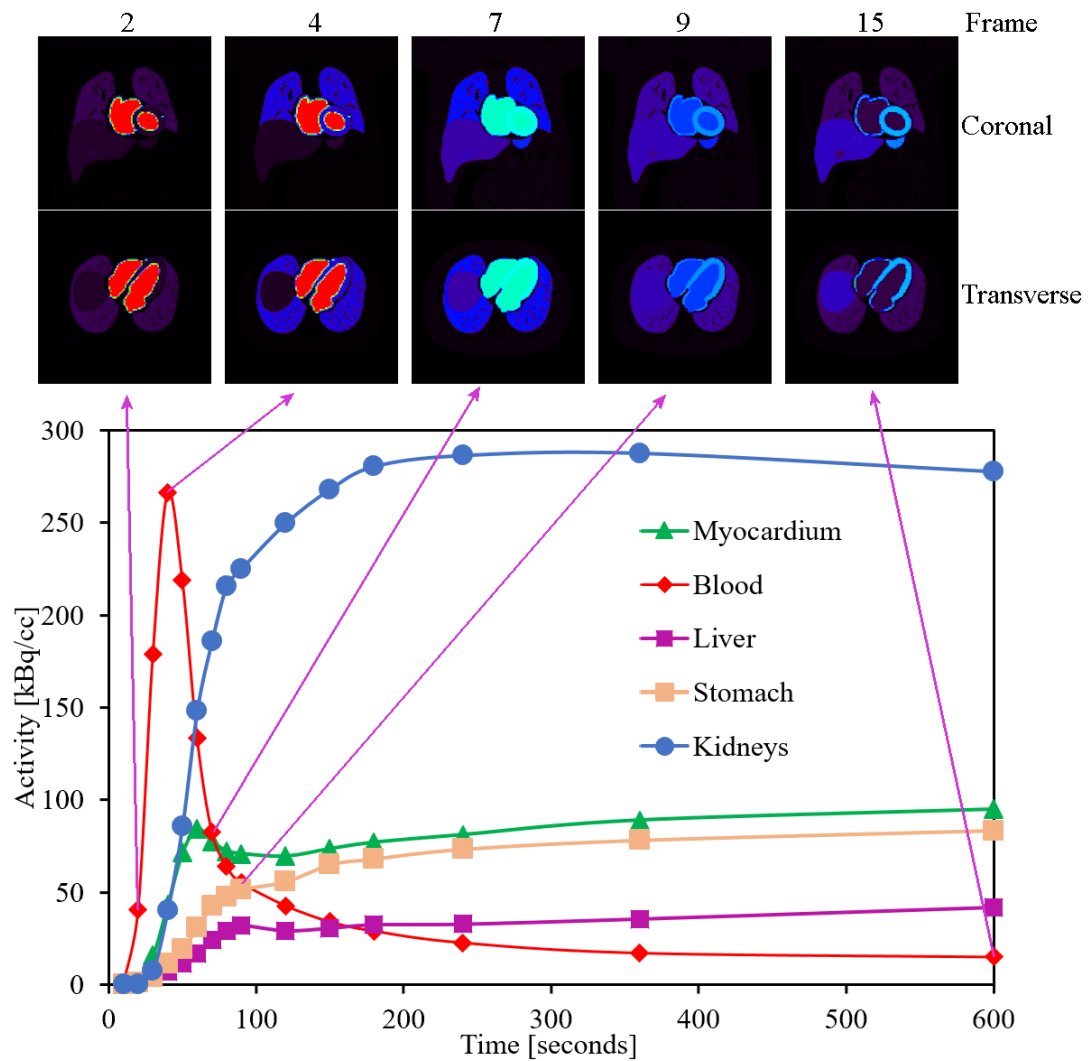


**Figure 2.6.1.3: Example of time activity curves assigned to various organs in the body.**

## 2.6.2 Analytical PET Simulator (ASIM)

The NCAT phantom program does not include physical effects from processes such as: noise, positron range, photon attenuation and scanner resolution. Therefore, all these effects if they are desired must be simulated. One method would be Monte Carlo simulations, which can accurately simulate the physical interaction of particles with matter. A major disadvantage of Monte Carlo simulations is the amount of computational time

required to simulate the data and the degree of complexity required to create an accurate simulation. If a large number of simulations are required, the simulation time may render the Monte Carlo method prohibitively slow. Monte Carlo simulations are beyond the scope of this thesis and will not be discussed further.

In this work the analytical simulator ASIM (Analytical SIMulator) is used, which is an ultra-fast way to add noise to a noiseless PET sinogram [164]. One disadvantage of analytical simulators is that the noise model must be provided, and effects such as scanner resolution and positron range must be added by post hoc blurring of the simulated data rather than a simulation of these physical effects. In addition, more accurate photon tracking algorithms like Monte Carlo methods can simulate all physical effects such as true, random and scatter events whereas in analytical simulations these are calculated using approximate methods.

The amount of noise introduced by scatter can be estimated relative to other noise sources, but the residual bias from scatter can only be approximated.[113,165,166] This leaves a residual bias that must be estimated to give accurate scatter correction. ASIM overcomes this limitation by using the mean estimated scatter to calculate the added noise from scatter and then use this for scatter correction.[164] This process leaves no residual bias and therefore the computed scatter correction is very accurate. The total activity in the phantom is assumed to be concentrated along the axis of the specified scanner and not the voxelized input phantom, thus activity outside the field of view is not considered. A uniform cylindrical phantom scan is used to measure the typical scatter fraction. A Monte Carlo integration technique incorporating the Klein-Nishina Compton scatter cross-section formula is used to estimate the axial scatter profile. This is done with the following three

integrations taking into account the lower energy threshold and the energy resolution of the scanner:[164]

- (1) over the position of the positron annihilation along the scanner axis
- (2) over the Compton scatter location in the attenuating medium
- (3) over the Compton scatter angle

Random coincidences are calculated taking into account that the annihilation events must take place within the phantom. Final prompts are calculated using these profiles and a Poisson pseudo-random realization for the mean value of each sinogram element.

The work flow to generate a noise-added sinogram for the NCAT phantom is shown in **figure** 2.6.2.1. We begin with physical estimates of the count rate statistics of the phantom we wish to model. This is typically done using a National Electrical Manufacturers Association (NEMA) phantom scan starting at high count rates. Two example phantoms are shown with diameters of 20 cm and 35 cm. From the count rate statistics, we get plots of the global count rates for measured true, random and scatter events as a function of the total phantom activity. These are then used in conjunction with an activity phantom to get estimates of the measured true, random and scatter events taking into account the total activity concentration and scan length time. The activity phantom and number of true, random and scatter events are defined as input to the ASIM program which distributes the events according to the true, random and scatter profiles defined in the process described earlier. The output sinograms have no attenuation and are fully corrected for random and scatter effects, but have all the noise characteristics one would expect from a measured clinical PET scan.

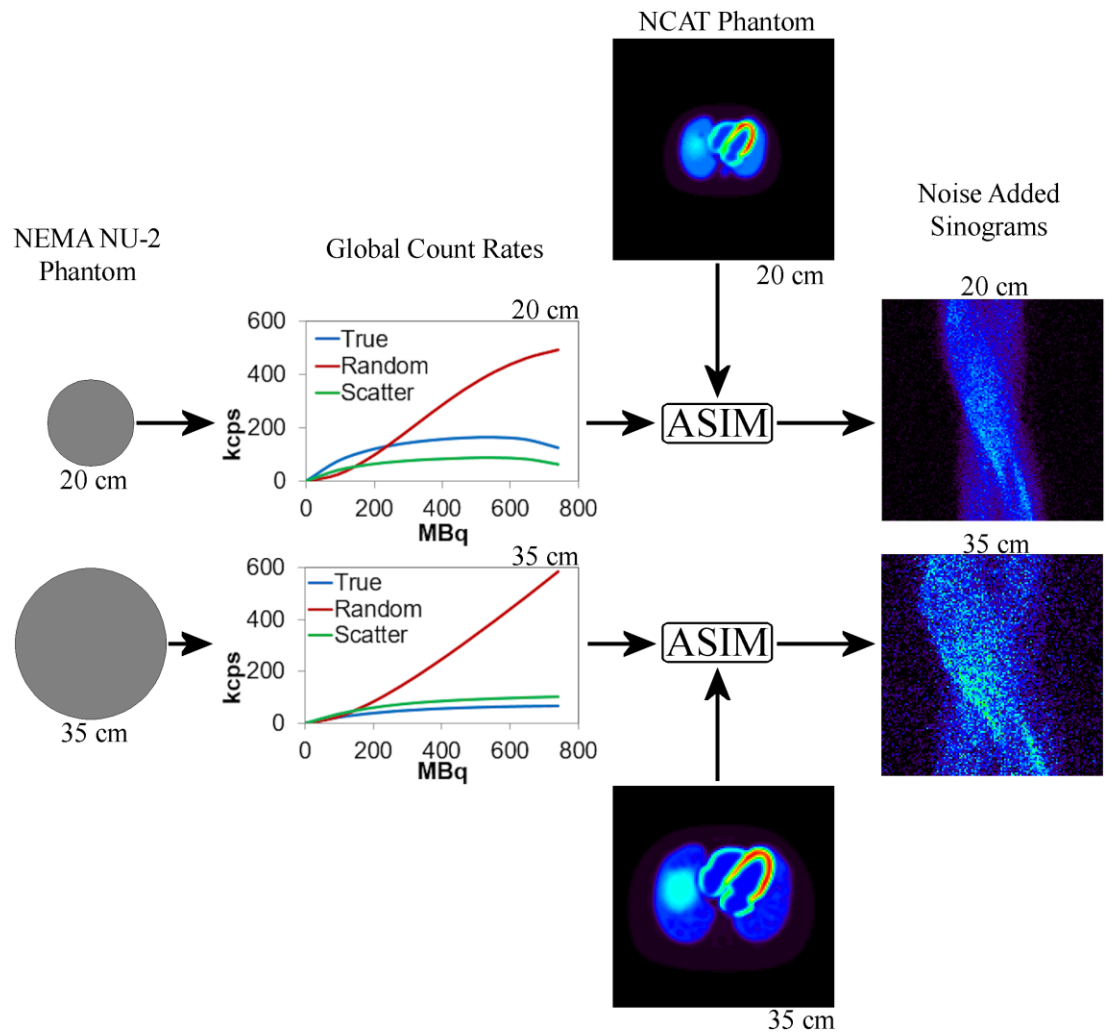


**Figure 2.6.2.1: Example of the production of a noise added sinogram without attenuation from a voxelized NCAT phantom.**

### **3 Chapter: Patient Motion Effects on the Quantification of Regional Myocardial Blood Flow with Dynamic PET Imaging**

#### **3.1 Introduction**

This chapter discusses “Patient Motion Effects on the Quantification of Regional Myocardial Blood Flow with Dynamic PET Imaging”. The content was previously published in *Medical Physics* and selected for Editors Pick. The content of this paper has been modified in the current document to improve readability.[167]

Studies have shown that quantification with positron emission tomography (PET) imaging and Myocardial blood flow quantification has superior diagnostic and prognostic value compared to conventional relative perfusion imaging.[168–172] Dynamic imaging begins with intravenous injection of a tracer and passive acquisitions over time are binned into frames reconstructed as images. Later frames reflect the completion of biodistribution of the tracer to the perfused tissues which can take several minutes. As covered in **chapter 2.5**, these images are analyzed using regions of interest (ROI) to sample the tissue time-activity curves (TAC) of the heart muscle (myocardium) and LV cavity (arterial blood) regions to be processed using kinetic modelling for regional myocardial blood flow quantification (MBF).

As shown in **chapter 2.5**, MBF quantification requires dynamic imaging and assumes that the tissue components in the kinetic model are spatially invariant. Recent studies have indicated that the occurrence of patient body motion is highly prevalent.[173,174] Patients are typically elderly and may suffer from arthritis, and chest discomfort can occur due to the pharmacologic stress agents used. Therefore, it can be

uncomfortable for the patient to stay still for the long periods of time needed to acquire the dynamic data and patients often move. Motion also occurs due to coughing and organ creep. This then leads to misalignment between the attenuation correction (AC) map and PET data which causes CT attenuation correction (CTAC) errors after reconstruction, and violates the spatial invariant assumptions for kinetic modelling; therefore, affecting blood flow quantification.[44,175] Inter-frame motion leads to distorted TAC's since the frame-to-frame spatial sampling is inconsistent, whereas intra-frame motion leads to spatial blurring within the frame. The effects of CT misalignment on the heart wall activity have been studied to some degree for PET and SPECT.[43,44,173] The accuracy of MBF quantification is reduced due to these motion effects.[60]

A review of motion correction techniques was presented in **chapter** 1.2. Primarily, motion correction can be performed by applying a tracking protocol using external radioactive, optical markers, cross correlation algorithms in the late time frames or manual realignment.[56,66,76] It has been previously pointed out that motion correction should be based on cardiac (internal) markers due to the fact that external markers do not necessarily reflect the complex internal motion of organs when a patient moves.[56] However, placing markers in the cardiac region would be highly invasive and is not practical. The issue with image-based correction is that often CTAC errors are left uncorrected, and late frame motion correction would leave any early frame motion uncorrected. In addition, manual correction is hindered by operator bias.

The purpose of this study was to evaluate the prevalence of patient body motion in a typical clinical population for Rb-82 rest and stress perfusion imaging, and to quantify the possible MBF errors associated with motion using noiseless computer simulations. The

clinical prevalence study results are used to define the simulation parameters (direction, sign, magnitude and time of motion shift). In addition, the effects from spatial resolution, PET-CTAC misalignment, LV polar-map regions, partial-volume and motion corrections were evaluated. Computer-generated phantom studies were chosen due to the fact that ground-truth physiology is known, and any deviations from the standard case can be evaluated precisely. In this study, sources of MBF error were evaluated without cardiac and respiratory motion in order to quantify the effect from patient body motion on MBF error by itself. While attempts at such a study have been done in part for various tracers, to our knowledge a comprehensive 3-dimensional modeling study using an NCAT phantom for Rb-82 cardiac imaging has not been conducted.

## **3.2 Methods**

### **3.2.1 Clinical Prevalence Cohort**

The clinical prevalence cohort consisted of 236 patients recruited from August to November 2010 for Rb-82 PET rest-stress myocardial perfusion imaging (MPI) at the University of Ottawa Heart Institute. All patients gave written informed consent as part of the Rubidium-ARMI ([NCT01128023](https://clinicaltrials.gov/ct2/show/study/NCT01128023)) research protocol approved by the University of Ottawa Human Research Ethics Board. Perfusion imaging began with a low-dose (0.2 mSv) normal-end-expiration CT attenuation scan acquired before the start of the PET acquisition (120 kVp, axial and angular mA modulation in the range 20–200 mA, with 40% noise index and a 1.5 s helical scan time). Infusion of Rb-82 (RubyFill™, Jubilant DraxImage, Kirkland, QC) chloride at 10 MBq/kg was performed by a 30 second constant-

activity-rate ‘square-wave’. PET data was acquired for 8 minutes in list-mode using a Discovery 690 PET-VCT scanner (GE Healthcare, Waukesha, WI), and data was reconstructed by filtered back-projection with an 8 mm Hann window of the Ramp filter. A dipyridamole (0.14 mg/kg/min) 5-minute infusion was used to induce cardiac stress, and a second  $^{82}\text{Rb}$  PET scan was initiated 3 minutes later. Final 3D images had a matrix size of  $128 \times 128 \times 47$  voxels of size  $3.125 \times 3.125 \times 3.270$  mm, and final isotropic spatial resolution was  $\sim 10$  mm (using 6 mm FWHM positron range, 6 mm FWHM intrinsic resolution and 6 mm FWHM post reconstruction smoothing). All corrections for detector efficiency, dead-time, isotope decay, photon attenuation, and scatter, random and prompt-gamma coincidences were used to reconstruct quantitative images of activity concentration (Bq/cc). The PET acquisition was split up into the following time frames:  $9 \times 10\text{s}$ ,  $3 \times 30\text{s}$ ,  $1 \times 60\text{s}$ , and  $2 \times 120\text{s}$ , and Rb-82 PET image registration was verified manually (the vendor ACQC program was used for manual adjustment if required) using a static PET image of tracer uptake (2-8 min).

The reconstructed dynamic images were analyzed using the FlowQuant[176] software (uOHI, Ottawa, ON) in cine-mode, which allowed the user to sweep back and forth through the time frames. The view was centered on the heart in the transaxial, sagittal and coronal axes. Visual assessment by two independent observers was used to determine the severity, time and direction of motion. Disagreements between the two observers was resolved by both observers reviewing the scan until consensus was reached. The affected time frames, presence or absence of heart motion, and direction was recorded by each observer. The magnitude of motion was determined by estimating how far the edge of the heart wall shifted in pixels. Magnitude was classified as *mild* (1-2 pixels or 3-7 mm) or

*moderate* (>2 pixels or >7 mm). Some (3 %) low image quality scans could not be assessed (NA) since the absence or presence of motion could not be determined. Motion was only assessed in the frames after the first-pass transit of tracer through the heart which was typically > 90 s, since motion in only those frames could be determined with confidence. Rest and stress scans were both evaluated, therefore the total number of scans reviewed was 472.

### **3.2.2 Computer Phantom Simulations**

The NURBS-based Cardiac-Torso (NCAT) digital phantom program as described in **chapter 2.6.1** was used to produce the noiseless anatomical images, as illustrated in **Figure 3.2.2.1**. [177,178] The final matrix size of the phantoms was  $128 \times 128 \times 63$  voxels with cubic voxels of size of 3.125 mm; therefore, final image sizes were  $40 \times 40 \times 19.7$  cm.

Time activity curves (TAC) were derived from a previous Rb-82 dosimetry study in human patients.[95] The following organs had time activity curves assigned: Myocardium, blood pool regions, liver, lungs, spleen, kidney, gall bladder and heart wall. The same time activity curve was assigned to all blood pool regions and myocardial regions. Respiratory and cardiac motion was not simulated to eliminate the characteristic blurring from these effects, thus patient body motion was characterized by itself.

The PET NCAT images were smoothed using a 3D Gaussian function to simulate positron range and the intrinsic resolution of the D690 PET/VCT scanner. The NCAT phantom CT volume image was used to calculate the tissue attenuation factors scaled to the known values at 511 keV by forward projection as described in **chapter 2.6.1**. Attenuation was simulated by forward projection the PET NCAT images using the

MATLAB® 2D radon transform (128 angles) to create PET sinograms and then dividing by the tissue attenuation factors derived from the NCAT CT. The PET sinograms were then corrected for attenuation and reconstructed with filtered back-projection, then smoothed to a final resolution of 10 mm FWHM to recreate the post-reconstruction filtering used in clinical practice, herein this data set is called the low-resolution data set. Another data set was generated with a final resolution of 2 mm FWHM, herein called the high-resolution data set. This data set had a final matrix size of  $256 \times 256 \times 126$  voxels with cubic voxels of size of 1.5625 mm; therefore, final image sizes were  $40 \times 40 \times 19.7$  cm. Final reconstruction was achieved using MATLAB® 2D filtered back-projection. Noise was not simulated to avoid potential effects of noise-bias in the estimation of myocardial blood flow.

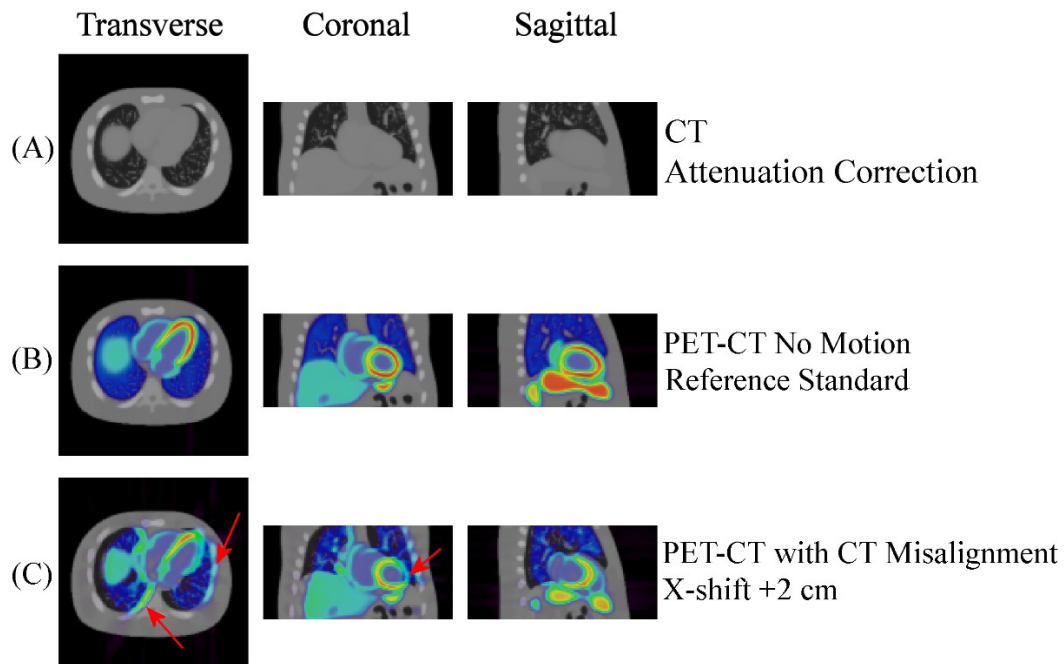


**Figure 3.2.2.1: (A) NCAT phantom for PET-CT simulation studies showing the CT used for attenuation correction (CTAC). (B) Homogeneous tracer distribution is observed in the LV myocardium on the PET-CT images with perfect alignment used**

**as the no-motion reference-standard. (C) A case with CT misalignment +2 cm in the X -direction shows the resulting CTAC artifacts evident in the LV lateral wall and lung margins (red arrows).**

**Figure 3.2.2.2** shows the work-flow used to generate all the motion and correction combinations. A reference standard was simulated without any PET motion or CTAC artifacts (**Figure 3.2.2.2: No motion, Figure 3.2.2.1 (B)**), and all PET motion-shifted images were compared to this standard. Frames possessing both CTAC misalignment and PET dynamic frame misalignment artifacts were generated to replicate uncorrected motion cases seen in a clinical setting (**Figure 3.2.2.2: PET motion and CTAC misalignment, Table 3.2.2.1: None**). Frames with PET dynamic motion artifacts, but no CTAC misalignments were also generated (**Figure 3.2.2.2: CTAC misalignment, Table 3.2.2.1: CTAC-alignment**) to study the effect of patient motion in the PET data alone. To replicate the effect of post-reconstruction motion correction datasets were generated with no residual motion in the PET data, but with CTAC misalignment artifacts remaining (**Figure 3.2.2.2: PET motion, Table 3.2.2.1: PET-dynamic**).

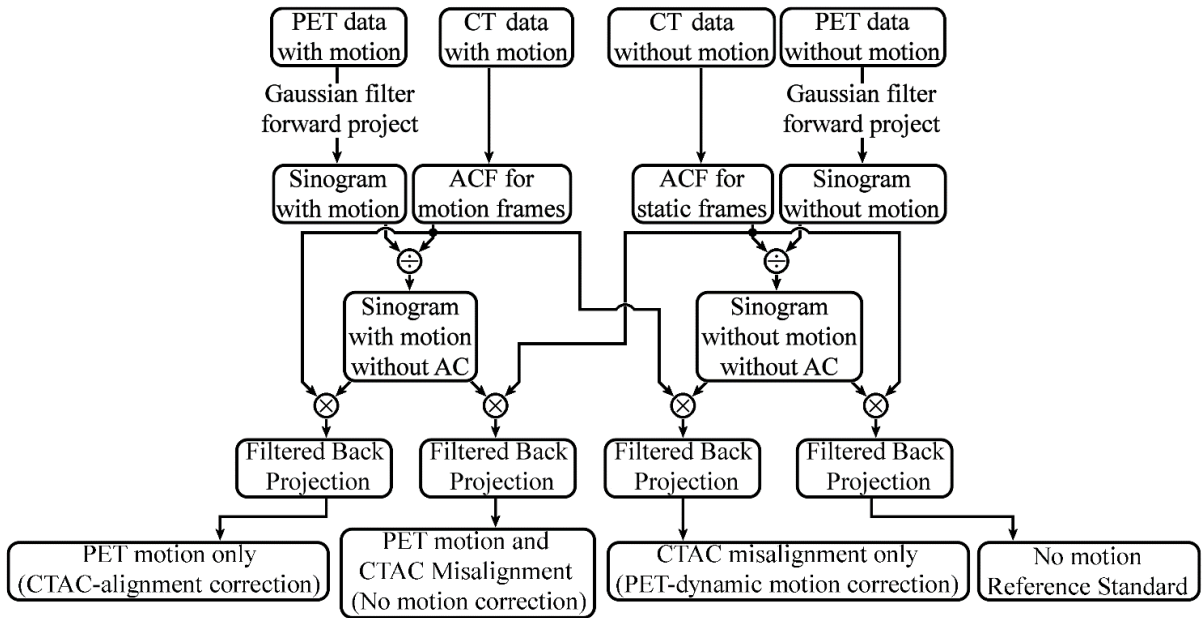


**Figure 3.2.2.2: Computer simulations used to produce the patient motion and correction test cases. Attenuation of the projection data is denoted by '⊖' and attenuation correction by '⊗'.**

Table 3.2.2.1 gives a list of all simulated motion and correction parameters. Rigid inter-frame motion of  $\pm 0.9375$  (herein called  $\pm 1$  cm) and 1.8750 cm (herein called  $\pm 2$  cm) was simulated by a discrete shift of the PET data at in one of 6 directions ( $\pm X$  right/left,  $\pm Y$  posterior/anterior, and  $\pm Z$  superior/inferior) at 30, 60, 120, and 240 s. Nonlinear effects and rotations present in some clinical motion cases were not simulated. As in clinical practice, a single CT aligned to the late PET frames was used to correct for attenuation of all frames. Therefore, any motion in the early frames will have CTAC errors due to the PET-CT misalignment of those frames. To interrogate the effects of early frame alignment we also simulated alignment in the blood pool time frames, this motion misalignment occurs in the late time frames for those data sets. Motion correction was achieved by

excluding PET motion and/or CTAC misalignment from motion corrected frames, thus these are perfectly corrected for motion.

**Table 3.2.2.1:**

**Computer simulation parameters (N=5,760 combinations).**

<b>Stage</b>	<b>Parameter</b>	<b>Description</b>
<b>Acquisition</b>	Motion Direction	X (left/right), Y (anterior/posterior), Z (superior/inferior)
	Motion Sign	Positive (left/anterior/sup), Negative(right/posterior/inferior)
	Motion Magnitude	1, 2 cm
	Motion Time (of shift)	30, 60, 120, 240 s
<b>Reconstruction</b>	Spatial Resolution	High, Low (2, 10 mm FWHM)
	CTAC Alignment	Early, Late PET reference frames
	Polar-Map Segment	Anterior, Posterior, Lateral, Septal, Apex
<b>Analysis</b>	Partial-Volume Correction	Regional, Global
	Motion Correction	None, PET-dynamic, CTAC-alignment

Our in-house validated software program (FlowQuant©, Ottawa, ON) was used to quantify regional myocardial blood flow (MBF).[172,176,179,180] In this specific study the average of the last 6 minutes of the dynamic image data (2-8 min) was used to generate the uptake images due to the high myocardium-to-blood-pool contrast at those times. A

more detailed description of FlowQuant© is given in **chapter 2.5.2**. [176] Data was analyzed using a 1-tissue-compartment kinetic model and the globally-derived average distribution volume was estimated from the blood (input) and myocardium (output) TAC functions. [181] Both regional and global MBF in units of mL/min/g were calculated as described previously in **chapter 2.5.1**. The polar maps were organized according to a standard 5-segment model consisting of the average MBF value with the following anatomic regions (segments): anterior, posterior, septal, lateral, and apex. The absolute relative difference (in %) of each segment in the 5-segment model from the reference standard case was used to calculate the % MBF error as shown in equation 3.2.2.1.

$$\text{MBF error} = \frac{|\text{Measured MBF} - \text{Standard MBF}|}{\text{Standard MBF}} \times 100\% \quad (3.2.2.1)$$

A total of 5,760 total data points over 9 simulated parameters were generated from this study – see **Table 3.2.2.1**.

### 3.2.3 Statistical Analysis

In the clinical cohort, the recorded magnitudes of motion are reported as the mean  $\pm$  standard deviation, and the proportions of magnitudes (severe/moderate) and directions are reported as a percentage.

Multivariate analysis of MBF errors was carried out using analysis of variance (ANOVA) on the computer simulation studies for the individual simulation parameters. In addition, analysis on the 2- and 3-parameter interactions was performed – see **Appendix A** for more detail. The most highly significant 2- and 3-parameter interactions were chosen for analysis. The median interaction effects were analyzed in box plots. Potential outliers were defined as  $> 1.5$  times the inter-quartile range above the median values. The

Wilcoxon rank-sum test at the 95 % confidence level was used for post-hoc pair-wise comparison of median values.

MATLAB® (Mathworks, Natick, MA) was used for all statistical analyses and calculated probabilities (P-values) < 0.05 were considered statistically significant.

### 3.3 Results

#### 3.3.1 Clinical Prevalence Cohort

The average age for our patients was  $64 \pm 11$  years (range 33 to 89), and 51 % of the patients were male. For more detail please see **Appendix A**.

**Figure 3.3.1.1(A)** shows the prevalence of motion magnitude in percentage. Moderate motion (>7 mm) made up 38 % of all motion cases, mild motion made up 35 % of all motion cases, 24 % of cases had no motion and for 3 % of cases the direction and/or magnitude could not be assessed (NA). Cross-correlation of sequential time-frame images in FlowQuant© was used to automatically measure the mean magnitude of motion. Results showed that mild motion had a mean value of  $0.5 \pm 0.1$  [0.3 to 0.7] cm whereas moderate motion had a mean value of  $1.0 \pm 0.3$  [0.7 to 1.8] cm, which agreed with the visual classification of motion magnitude. There were no significant differences between rest and stress in the direction or magnitude of motion.

The prevalence of motion direction is shown in **Figure 3.3.1.1(B)** with mild and moderate data combined. Axial motion was the most common making up 45 % of all motion cases with 30 % in the superior (+Z) direction and 15% in the inferior (-Z) direction. Motion in the Y direction (anterior/posterior) was almost entirely posterior (29%), whereas

motion in the X direction had a similar proportion in the left (+X) and right (-X) directions and accounted for 24% of cases. Computer simulations were based upon the moderate-motion (worst-case) results. Shifts were simulated in all three axes (X, Y and Z) with bidirectional magnitudes of  $\pm 0.9375$  cm and  $\pm 1.8750$  cm reflective of the average moderate (1.0 cm), and maximum of the moderate cases (herein called severe or 1.8 cm) results.

The prevalence of motion time (following a detected shift) is shown in **Figure 3.3.1.1(C)**, demonstrating a relatively constant probability (dashed line median) of motion shift over the entire time-course of the scans. A substantially lower frequency of motion was recorded during the first minute, due to the confounding effects of the rapidly changing biodistribution during the tracer first-pass through the heart and lungs immediately following injection. Visual assessment of motion in the first minute may be underestimated. Based on these results, the times for simulated body motion were selected to cover most of the scan length, with added focus on the early times when the tracer activity was changing rapidly at 30, 60, 120 and 240 s, as shown in the example time-activity curves (**Figure 3.3.2.1**).

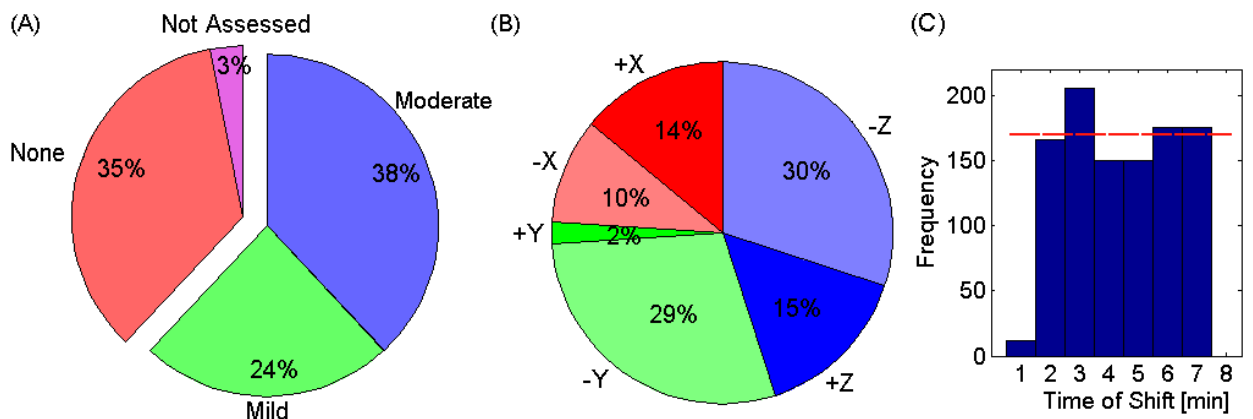


**Figure 3.3.1.1: (A) prevalence of patient (rigid) body motion, (B) directions and (C) times of mild or moderate body motion.**

### 3.3.2 Computer Phantom Simulations

Example MBF polar-maps computed for the reference case (without any PET motion) are shown in **Figure 3.3.2.1**. Without motion, the polar-map using regional PVC looks quite similar to that with global PVC, indicating relatively uniform partial-volume effects over different regions of the simulated LV myocardium. No defects on the myocardium were simulated; therefore, only homogeneous polar maps are expected.

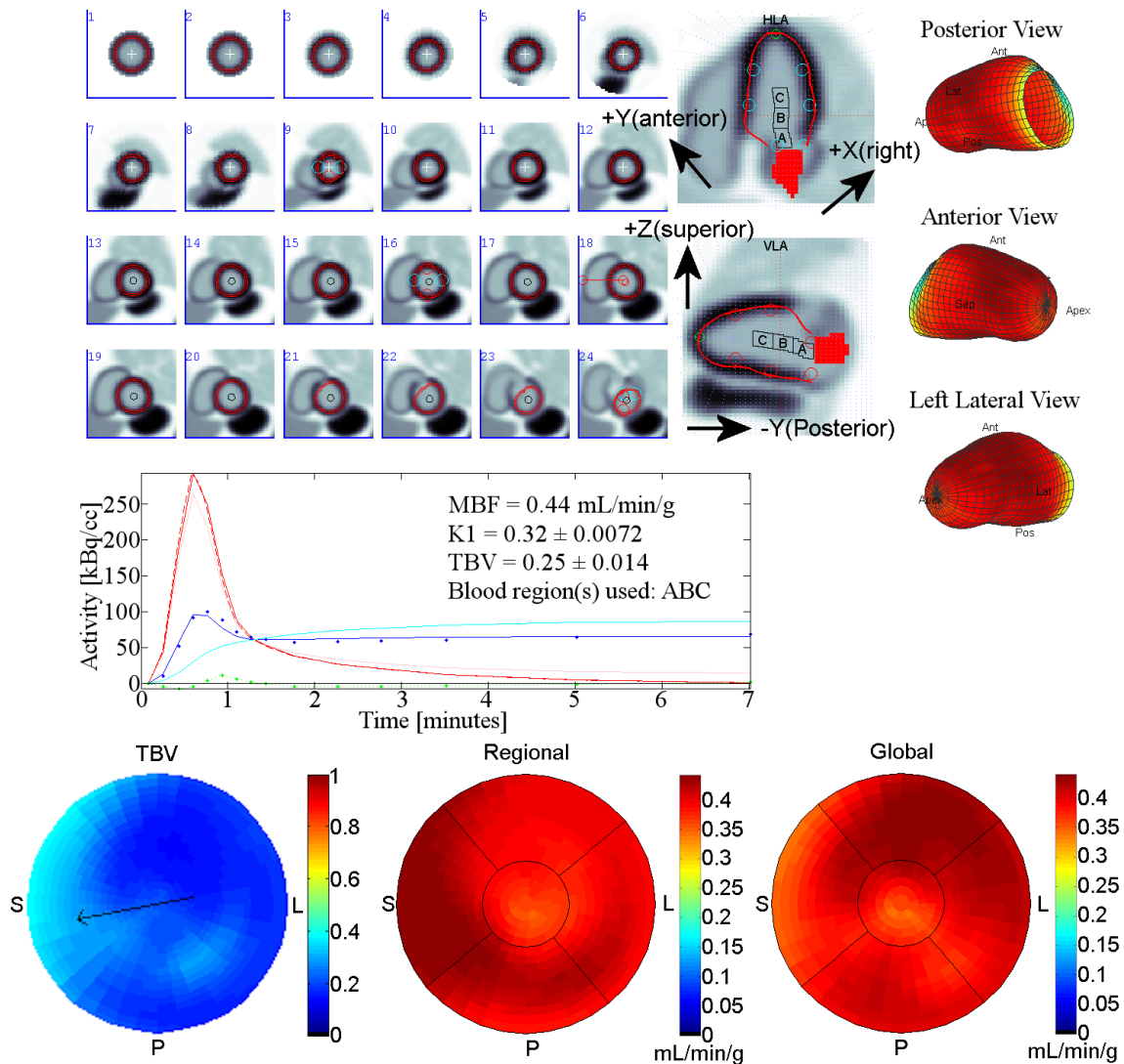


**Figure 3.3.2.1: FlowQuant® analysis results for the reference standard case with no PET motion (and perfect CTAC alignment). The PET slices used to sample the LV myocardium and blood time-activity curves are shown top-left, with contours of the LV and blood-pool regions shown top-middle. 3D surface contour maps of the sampled LV uptake (2-6 min average) are shown top-right for left lateral, posterior and anterior views. The resulting time-activity curves and kinetic model parameter values used for blood flow quantification are shown in the middle panel. MBF**

**polar-maps using regional [1 – TBV(total blood volume)] and global [1 – TBV<sub>mean</sub>]  
partial-volume corrections (PVC) are shown in the bottom panel.**

All of the simulated parameters had a statistically significant effect on the MBF error, as shown in **Table 3.3.2.1**; this includes the F-statistics which compare the variability within the groups to the variability to other groups.

**Table 3.3.2.1:**

**Multivariate ANOVA analysis of the simulated parameter effects on MBF.**

Parameter	Degrees of freedom	Main-effect statistics*	
	(n-1)	<b>F-statistic</b>	<b>p-value</b>
<b>Correction (None/CTAC/PET)</b>	2	192	<0.001
<b>CTAC (Early/Late)</b>	1	19	<0.001
<b>PVC (Global/Regional)</b>	1	71	<0.001
<b>Resolution (High/Low)</b>	1	57	<0.001
<b>Direction (X/Y/Z)</b>	2	192	<0.001
<b>Magnitude (1/2 cm)</b>	1	588	<0.001
<b>Sign (+/-)</b>	1	7.9	0.005
<b>Time of motion shift (30/60/120/240)</b>	3	178	<0.001
<b>Segment (ant/pos/sep/lat/apex)</b>	4	6.4	<0.001

\*main-effects should be interpreted with caution

The reductions in MBF error associated with each simulated parameter are illustrated in **Figure 3.3.2.2**. The worst-case combination of parameter values results in a mean MBF error of 240%. The effects of changing a single parameter value at a time from

this worst-case combination are shown in rank order from smallest to largest improvement in MBF error. Data is averaged over all segments and positive-negative directions (10 points total). As expected, PET-dynamic motion correction results in the single largest improvement from 240% using the worst-case combination down to 10%, with residual errors due mainly to the effects of CTAC misalignment. Regional partial-volume correction has the least effect, still resulting in ~220% residual error. CTAC alignment with the early (blood-pool) PET images reduces the MBF error by a factor of 2 to ~120%. These results show that patient body motion in the dynamic PET image sequence is a much larger source of error than CTAC misalignment effects, and therefore should be the first priority for accurate correction.

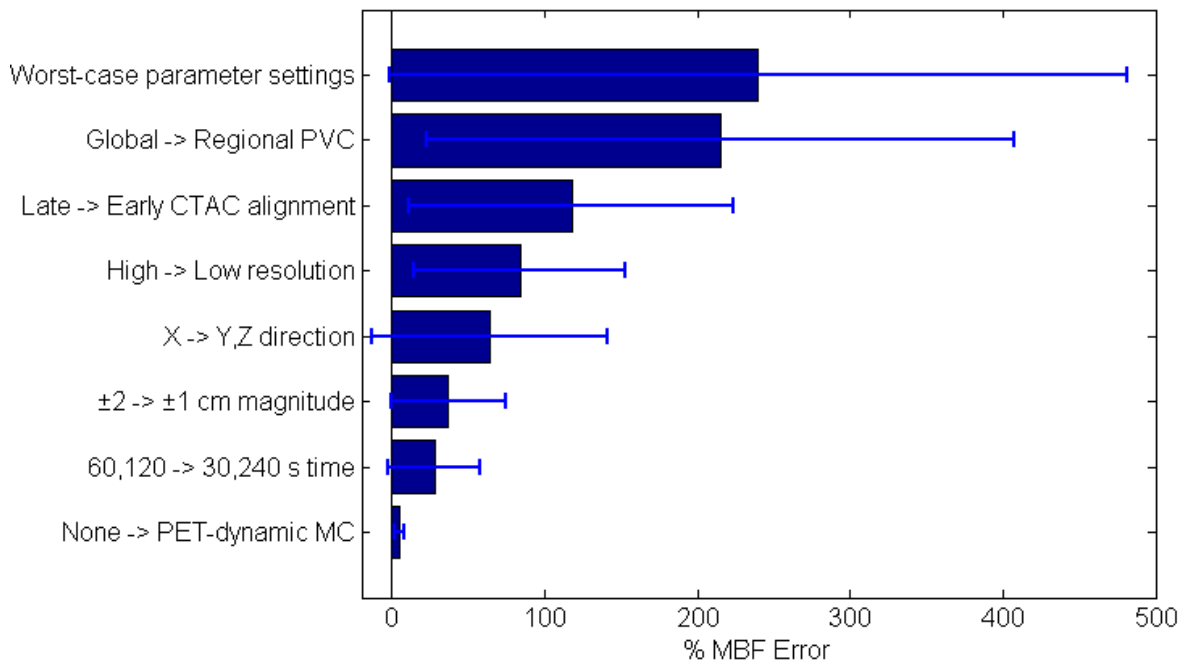


**Figure 3.3.2.2: Reduction in MBF error associated with each independent simulation parameter compared to the worst-case combination of parameter settings (global PVC, late CTAC alignment, high resolution, X direction, ±2 cm**

**magnitude, 60,120 s time of motion shift, no motion correction (MC)). Error bars are  $\pm$  SD reflecting changes in the Sign and Segment parameters.**

### **3.3.3 Parameter Interaction Effects**

**Figure 3.3.3.1** shows the most highly significant interaction (CTAC alignment, motion direction and sign) affecting MBF error. The largest MBF errors occurred for right (+X) motion when the CTAC was aligned with the late PET frames, and for left (-X) motion when the CTAC was aligned with the early PET frames. This corresponds with the well-established CTAC alignment artifacts observed clinically in the lateral wall, at the interface of low attenuating lung and high attenuating heart tissue. Similar magnitude MBF errors were measured in the septal segments (**Figure 3.3.3.1** polar-map insert), associated with misalignment of the RV blood pool sampling in early frames. There were significant differences in the effect of X-direction motion vs. other directions.

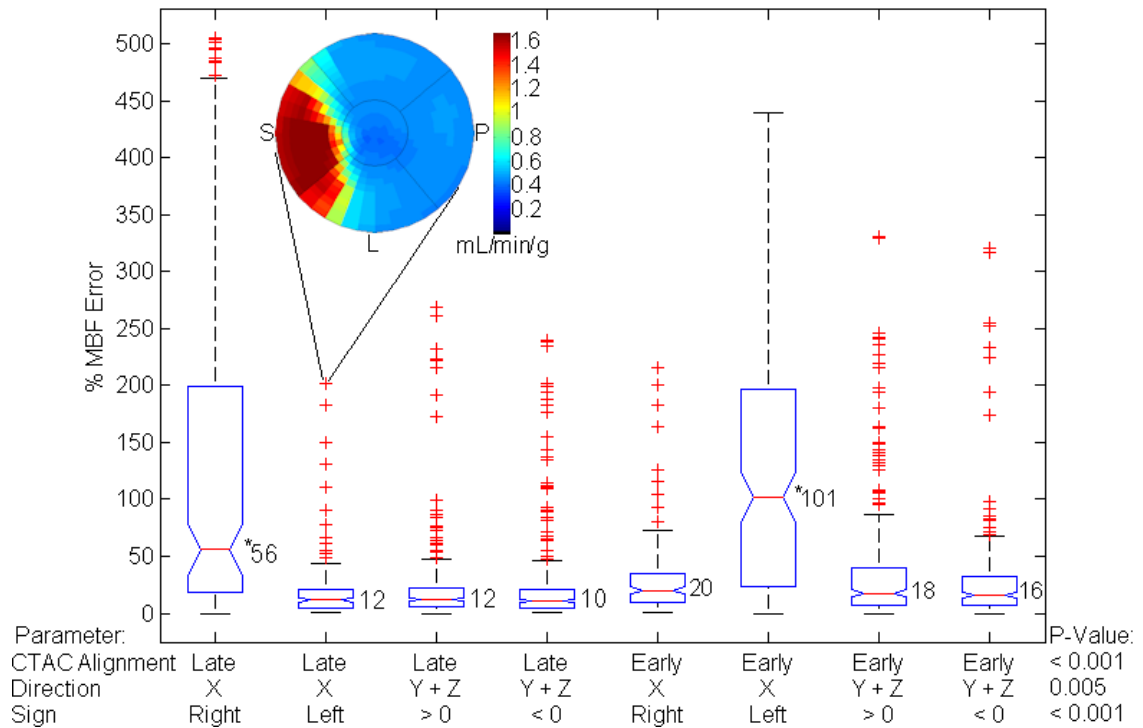


**Figure 3.3.3.1: Three-parameter interaction of CTAC alignment, motion direction and sign was highly significant ( $F=248$ ;  $p<0.0001$ ) by multivariate ANOVA. Data are shown for 2 cm magnitude (no motion correction and CTAC-alignment correction values are combined) ( $N=1920$ ). Median values are shown next to the box-plots. Polar map example is for 2 cm left shift ( $-X$ ) of the PET data at 60 s, with late CTAC alignment.**

\* $p < 0.05$  X vs Y, Z and left vs right.

**Figure 3.3.3.2** shows the significant interaction of motion direction and motion correction (at 2 cm magnitude) on MBF error. Errors were highest in the cases with no motion correction (None) or with CTAC-alignment correction only, regardless of direction. When PET-dynamic motion correction was performed, errors were significantly decreased ( $p<0.05$ ), and residual errors were due solely to CTAC misalignment. MBF errors were

significantly higher for motion in the X vs Y, Z directions, with or without CTAC-alignment correction ( $p < 0.05$ ).

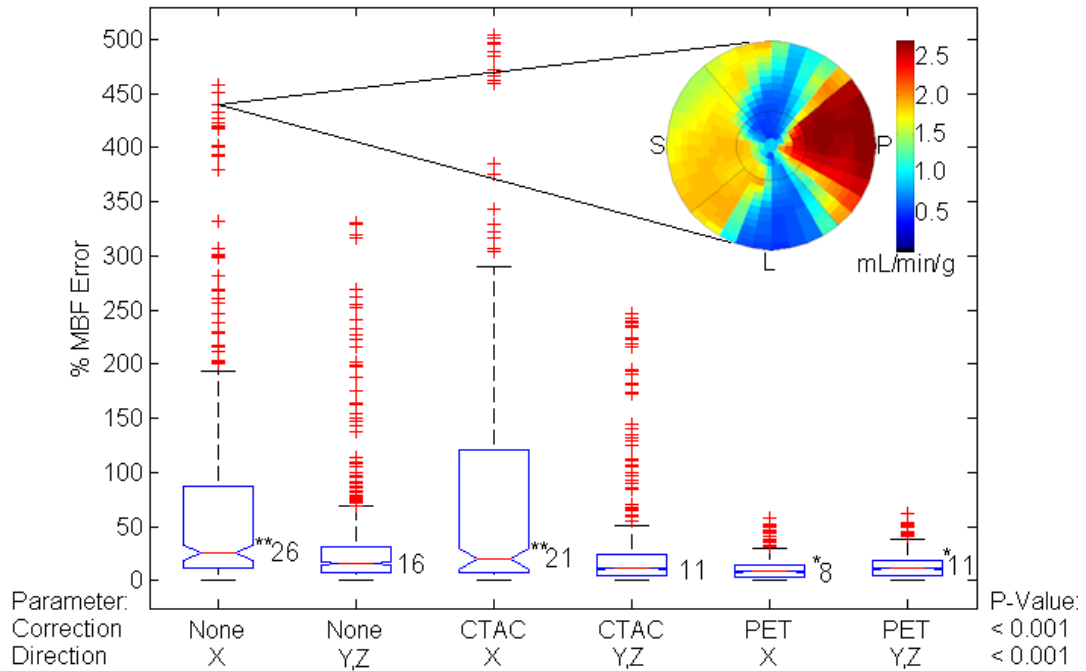


**Figure 3.3.3.2: Three-parameter interaction of motion correction, direction and magnitude was highly significant ( $F=35$ ;  $p<0.001$ ) by multivariate ANOVA. Data are shown for 2 cm magnitude only ( $N=2880$ ). Median values are shown next to the box-plots. Polar map example is for 2 cm left shift of the PET data at 60 s, with no motion correction.**

\* $p < 0.05$  PET-dynamic vs No motion correction (None) and CTAC-alignment only.

\*\* $p < 0.05$  X vs Y, Z directions.

**Figure 3.3.3.3** shows the significant interaction of motion direction and time of motion shift (at 2 cm magnitude) on MBF error. The errors for motion at 60 and 120 s were similar,

and significantly higher than motion at 30 and 240 s. These results confirm that the MBF error is again higher for X motion vs. Y, Z motion, and that mid-scan motion (e.g. 1 to 2 min) is much worse than motion near the start or end of the scan only. The highest over-estimation in MBF occurred with motion in the X-direction, at 60 or 120 seconds after scan start-time.

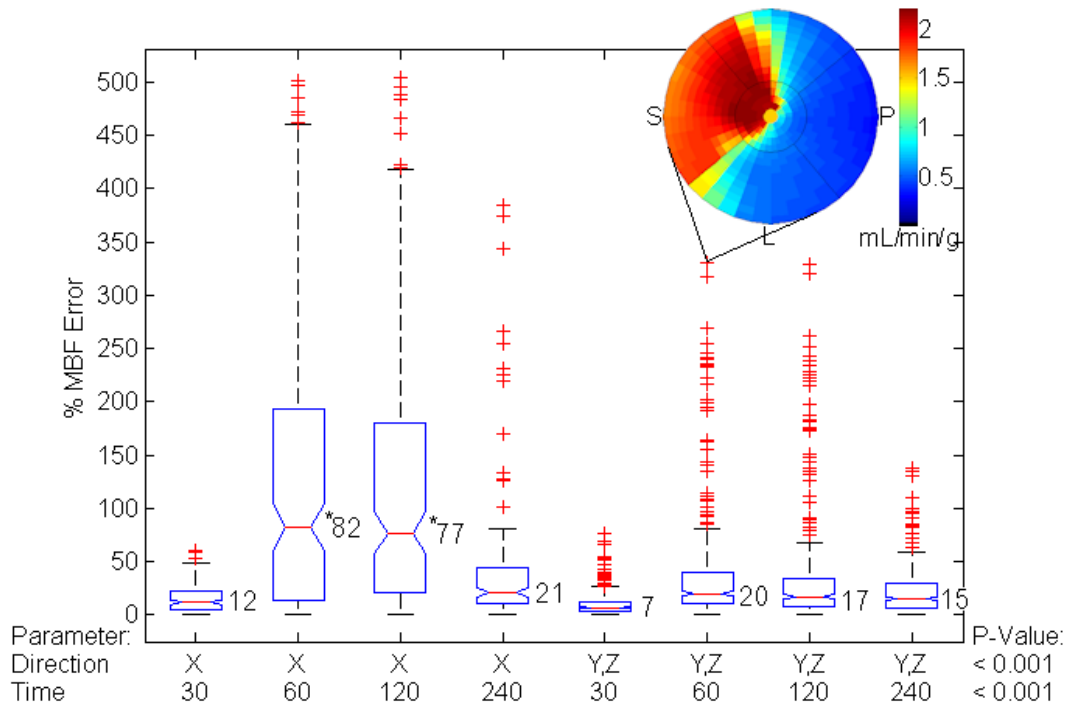


**Figure 3.3.3.3: Three-parameter interaction of motion direction time of motion shift and magnitude was highly significant ( $F = 40$ ;  $p < 0.001$ ) by multivariate ANOVA. Data are shown for 2 cm magnitude only ( $N=1920$ ). Median values are shown next to the box-plots. Polar map example is for 2 cm posterior shift (-Y) of the PET data at 60 s with no motion correction.**

\* $p < 0.05$  X direction motion at 60 and 120 s vs all other groups.

**Figure 3.3.3.4** shows the significant effect of PVC, segment and direction (for late CTAC alignment as per clinical practice). Regional (A) and global (B) partial-volume correction (PVC) in each segment are shown for motion in the right (+X) direction and +Z-direction (superior) directions. The greatest errors occurred using late CTAC alignment with motion at 60 or 120 s. For negative early-frame CTAC alignment the median values were higher segment by segment - **Figure 3.3.3.7**. In the presence of motion, regional PVC generally produced greater regional MBF errors compared to global PVC, indicating that the global PVC method may be more robust against body motion effects than regional PVC. There were significant differences in the median values between the posterior/anterior and lateral/septal walls and in the anterior and septal segments using regional partial volume correction. Median MBF error drops significantly for the left (-X) direction for both regional and global partial volume correction methods. Similar regional effects to the +Z-direction (superior) were observed for the -Z (inferior) direction, with the posterior wall increasing to 158% and the septal wall decreasing to 9% using regional PVC. There is much improved regional uniformity across segments using global vs. regional PVC.

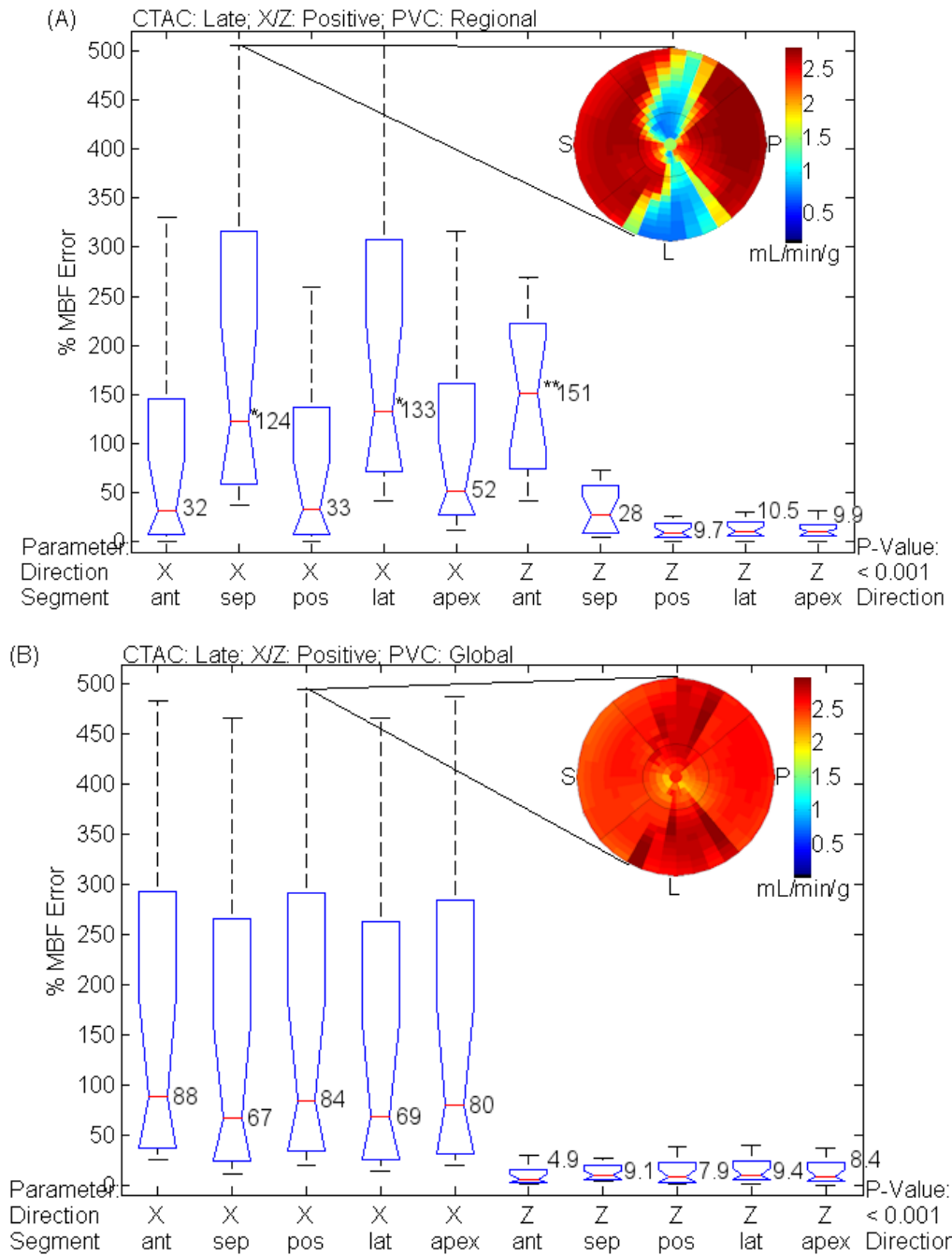


**Figure 3.3.3.4: Three-parameter interaction of motion direction, segment and PVC was highly significant ( $F = 20$ ;  $p < 0.001$ ) by multivariate ANOVA. Data are shown for late CTAC alignment (data with no motion correction and CTAC-alignment correction are combined), for shifts at 60 and 120 s in the right (+X) and superior (+Z) directions (N=160 (A); N=160 (B)). Median values are shown next to the box-**

**plots. Both X and Z directions are shown with regional (A) and global (B) PVC.**

**Polar map examples are for 2 cm right shift (+X) of the PET data at 120 s, with**

**CTAC alignment and with regional (A) and global (B) PVC.**

\*p < 0.05 septal or lateral vs anterior or posterior segments using regional PVC for the X direction.

\*\*p < 0.05 anterior vs all other segments using regional PVC for the Z direction.

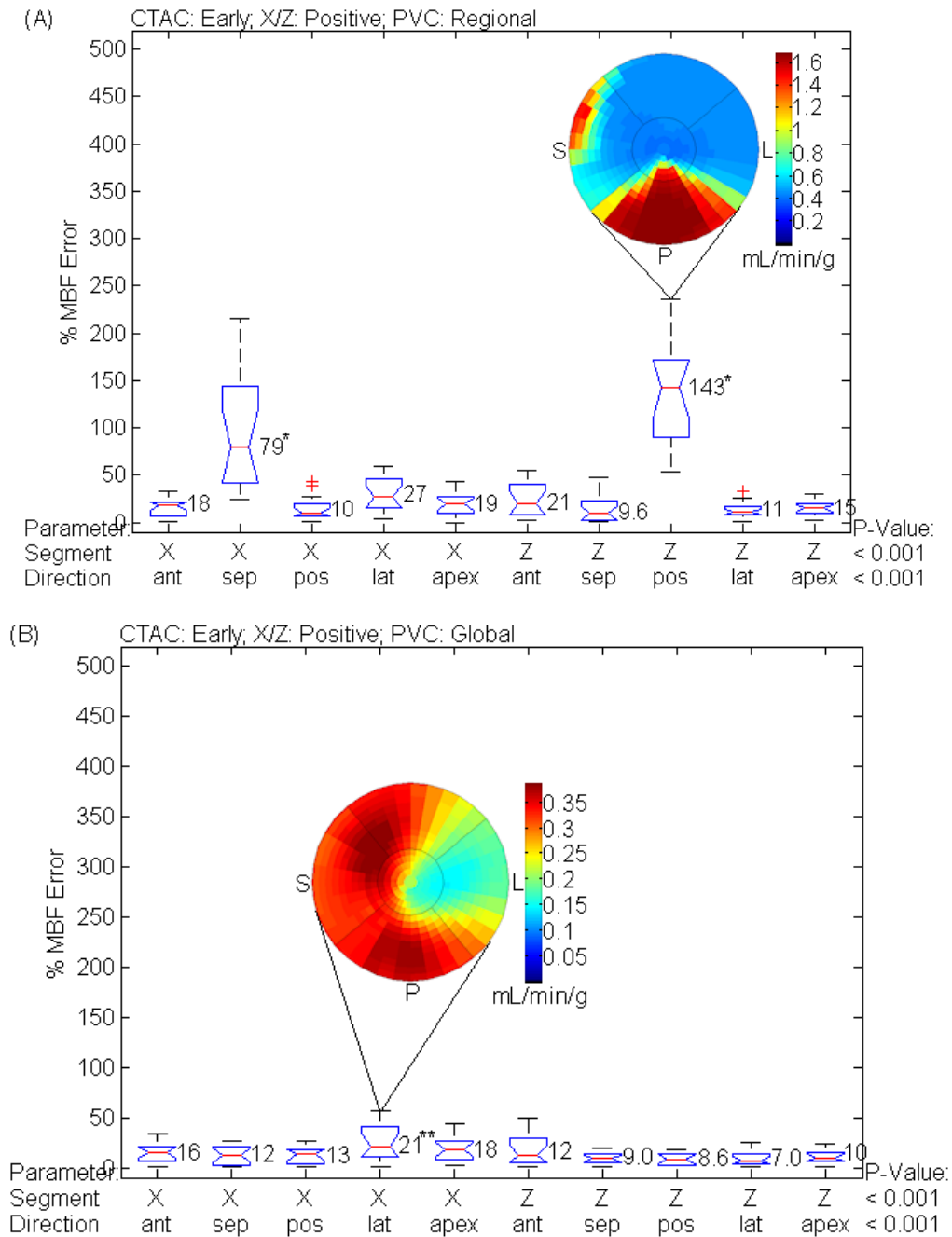


**Figure 3.3.3.5: Three-parameter interaction of motion direction, segment and PVC was highly significant ( $F = 20$ ;  $p < 0.001$ ) by multivariate ANOVA. Data are shown for early CTAC alignment (data with no motion correction and CTAC-alignment correction are combined), for shifts at 60 and 120 s in the right (+X) direction and superior (+Z) directions (N=160 (A); N=160 (B)). Median values are shown next to**

**the box-plots. Both X and Z directions are shown with regional (A) and global (B) PVC. Polar map examples are for 2 cm superior shift (+Z) of the PET data at 60 s (A) with CTAC-alignment correction, and 2 cm right shift (+X) of the PET data at 120 s (B) with no motion correction.**

\*p < 0.05 septal wall vs all others for X and posterior wall vs all others for Z (A).

\*\*p < 0.05 lateral vs anterior and apex for X (B).

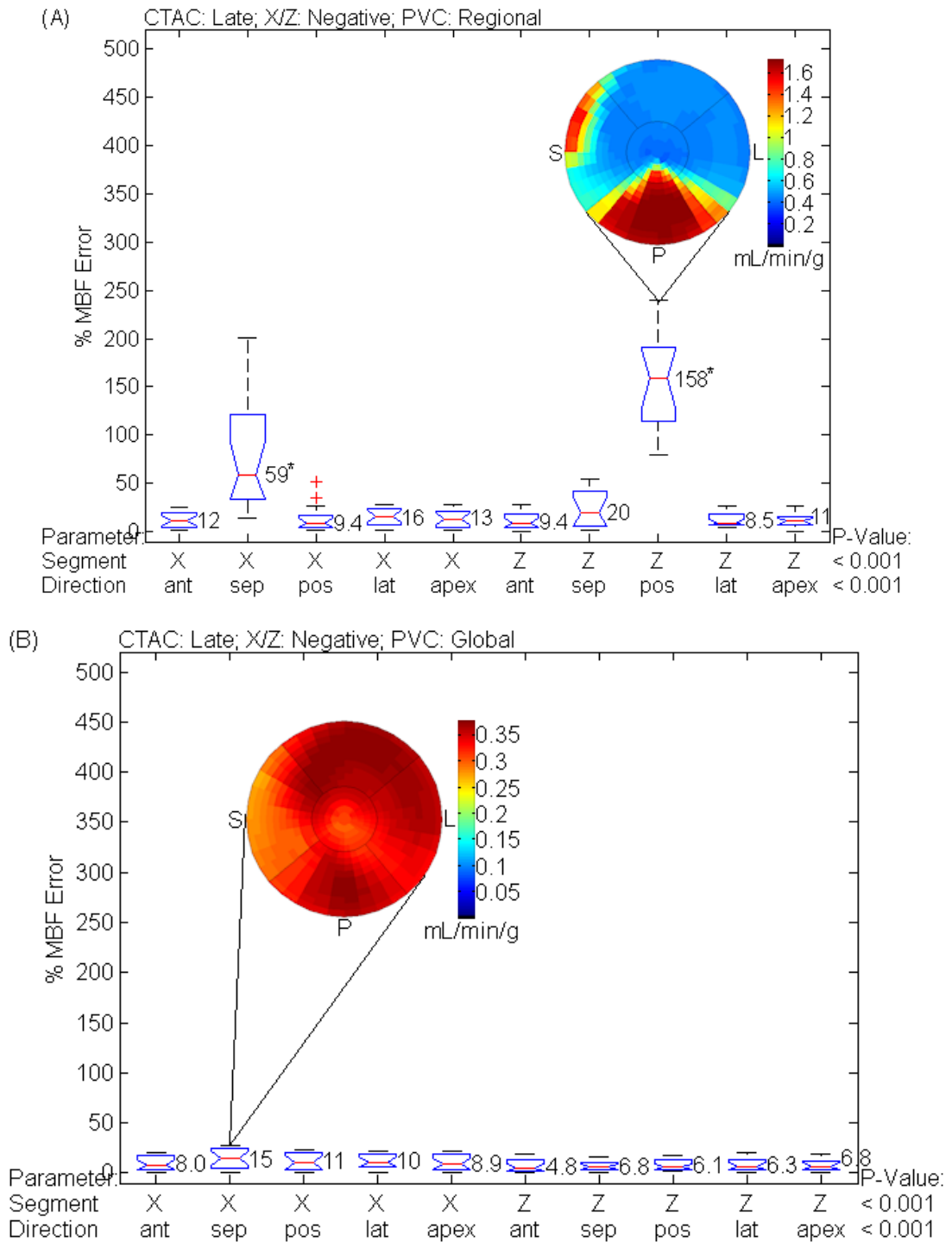


**Figure 3.3.3.6: Three-parameter interaction of motion direction, segment and PVC was highly significant ( $F = 20$ ;  $p < 0.001$ ) by multivariate ANOVA. Data are shown for late CTAC alignment (data with no motion correction and CTAC-alignment correction are combined), for shifts at 60 and 120 s in the left (-X) and inferior (-Z)**

**directions (N=160 (A); N=160 (B)). Median values are shown next to the box-plots.**

**Both X and Z directions are shown with regional (A) and global (B) PVC. Polar**

**map examples are for 2 cm inferior shift (-Z) of the PET data at 60 s (A) with**

**CTAC-alignment correction, and 2 cm left shift (-X) of the PET data at 120 s (B)**

**with no motion correction.**

\*p < 0.05 septal wall vs all others for X and posterior wall vs all others for Z (A).

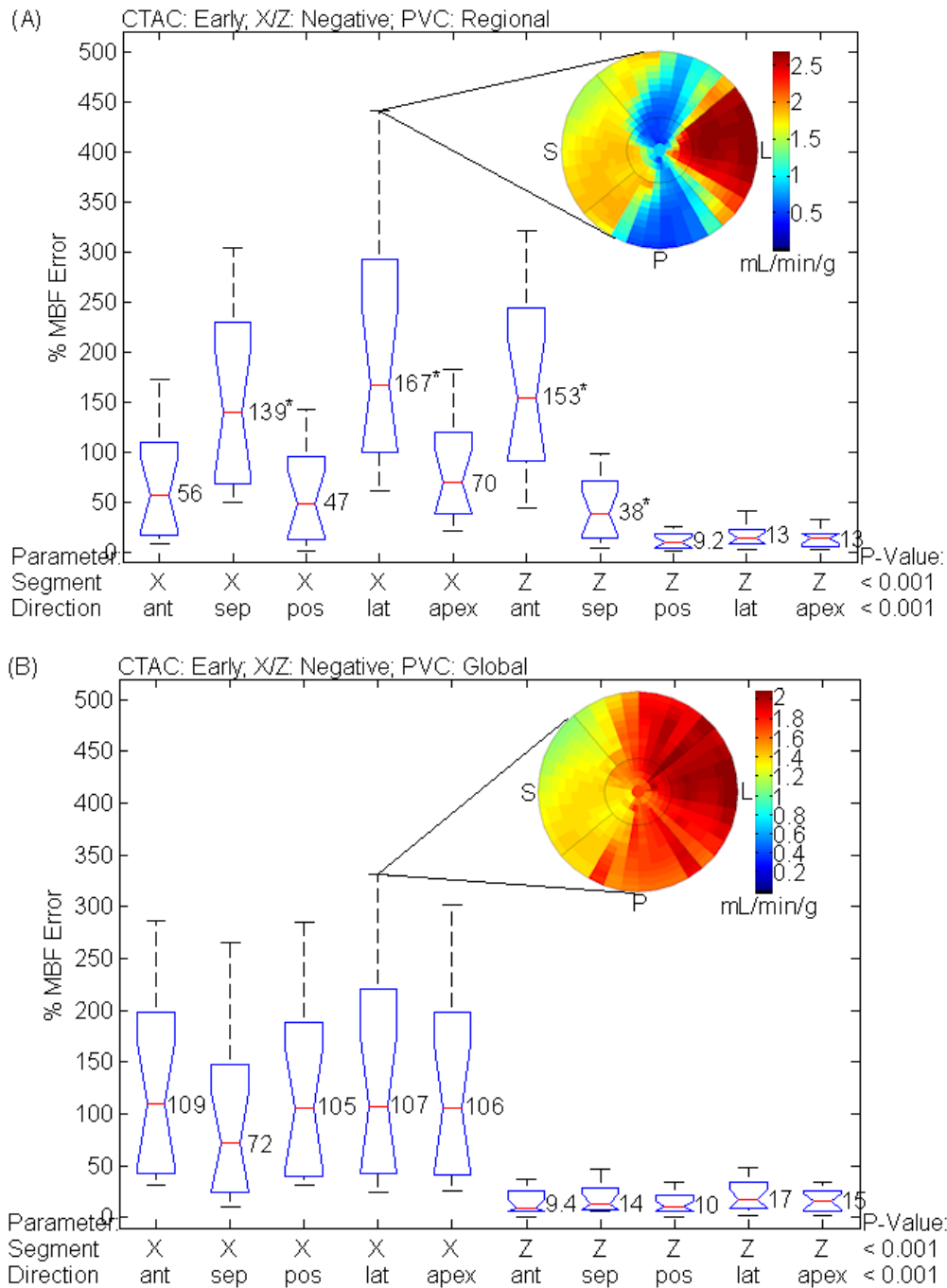


**Figure 3.3.3.7: Three-parameter interaction of motion direction, segment and PVC was highly significant ( $F = 20$ ;  $p < 0.001$ ) by multivariate ANOVA. Data are shown for early CTAC alignment (data with no motion correction and CTAC-alignment correction are combined), for shifts at 60 and 120 s in the left (-X) and inferior (-Z) directions (N=160 (A); N=160 (B)). Median values are shown next to the box-plots.**

**Both X and Z directions are shown with regional (A) and global (B) PVC. Polar map examples are for 2 cm left shift (-X) of the PET data at 60 s (A) and (B) with no motion correction.**

\*p < 0.05 septal/lateral walls vs all others for X and anterior/ septal walls vs all others for Z (A).

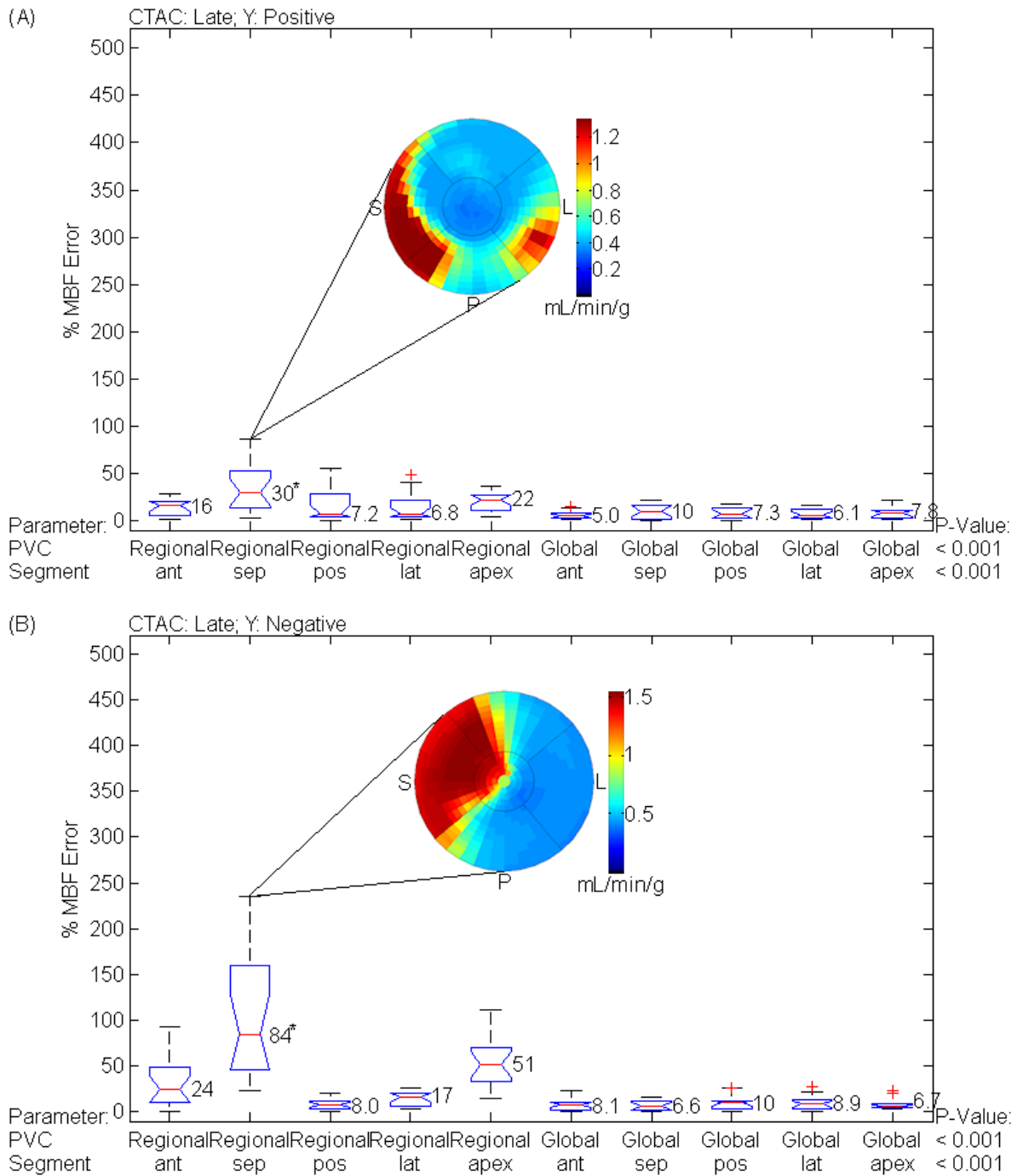


**Figure 3.3.3.8: Three-parameter interaction of motion direction, segment and PVC was highly significant ( $F = 20$ ;  $p < 0.001$ ) by multivariate ANOVA. Data are shown for late CTAC alignment (data with no motion correction and CTAC-alignment correction are combined), for shifts at 60 and 120 s in the up (+Y) (A) and down (-Y) (B).**

**(B) directions (N=160 (A); N=160 (B)). Median values are shown next to the box-plots. Both regional and global PVC are shown. Polar map examples are for 2 cm up shift (+Y) of the PET data at 60 s (A) with no motion correction, and 2 cm down shift (-Y) of the PET data at 60 s (B) with CTAC-alignment correction.**

\*p < 0.05, septal wall vs all others for regional PVC (A).

\*\*p < 0.05, septal wall vs all others for global PVC (A).

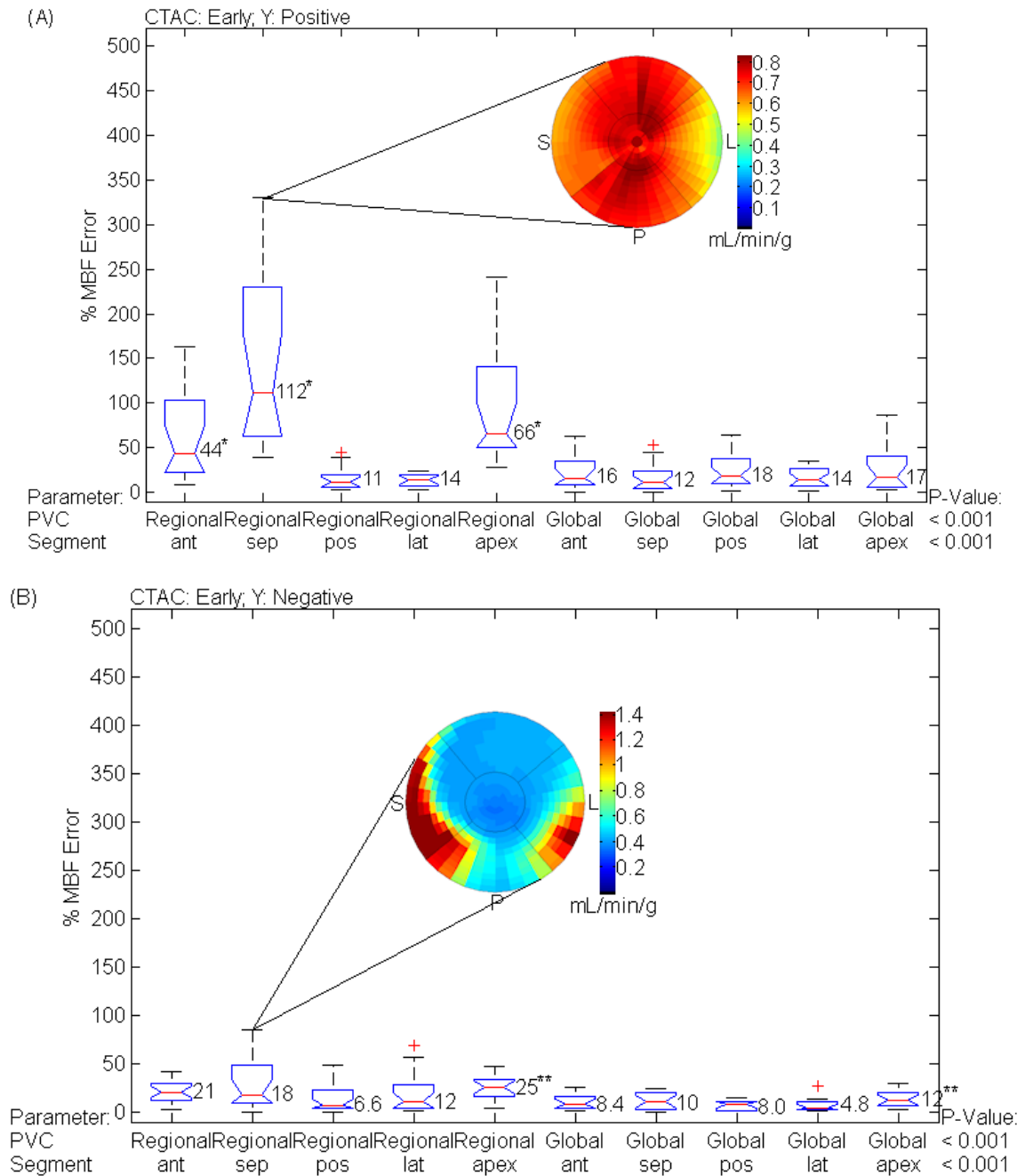


**Figure 3.3.3.9: Three-parameter interaction of motion direction, segment and PVC was highly significant ( $F = 20$ ;  $p < 0.001$ ) by multivariate ANOVA. Data are shown for early CTAC alignment (data with no motion correction and CTAC-alignment correction are combined), for shifts at 60 and 120 s in the up (+Y) (A) and down (-Y) (B) directions (N=160 (A); N=160 (B)). Median values are shown next to the box-**

**plots. Both regional and global PVC are shown. Polar map examples are for 2 cm up shift (+Y) of the PET data at 60 s (A) with no motion correction, and 2 cm down shift (-Y) of the PET data at 60 s (B) with CTAC-alignment correction.**

\* $p < 0.05$ , Anterior, septal and posterior wall were all significant vs posterior and lateral walls for regional PVC (A).

\*\* $p < 0.05$ , apex vs posterior wall for regional PVC, and apex vs posterior and lateral walls for global PVC (B).

### **3.4 Discussion**

To our knowledge this study is the most comprehensive investigation of the common effects of patient body motion on MBF measurement using dynamic  $^{82}\text{Rb}$ -PET imaging. This work confirmed that patient motion is highly prevalent in a clinical population of cardiac perfusion exams, as reported earlier in our preliminary study.[174] In 38% of patients with moderate body motion, the observed average shift was 1 cm, but in severe cases it was as high as 1.8 cm – see **Figure 3.3.1.1**. There was no significant difference in the prevalence of motion between rest and stress (data not shown).

This study confirms that greater MBF errors occur with larger magnitude patient motion (data not shown), with MBF errors exceeding true MBF values by up to a factor of five. Optimal CTAC alignment correction can result in larger MBF error, due to the fact that misaligned frames have higher activity without CTAC artifacts, and thus affect the kinetic modeling by biasing the misaligned frames more strongly. However, optimal correction of dynamic PET alignment alone results in a dramatic reduction of median MBF

errors to 8-12 %, with the residual error resulting from CTAC misalignment in some time-frames – see **Figure 3.3.3.2**. The main finding of this work, therefore, is that motion correction algorithms should prioritize correction of dynamic PET sequence over dynamic CTAC alignment correction. Nevertheless, the optimal long-term goal is to correct for motion effects in both the PET dynamic sequence and corresponding motion-free CTAC alignment.

Perfect motion-correction of the dynamic PET sequence may not be possible. In such cases, it is important to understand what other variables can be controlled to reduce MBF error. For instance, motion in the X direction (left/right) is more detrimental than motion in either the Y (anterior/posterior) or Z (superior/inferior) directions. Fortunately, the prevalence data (**Figure 3.3.1.1**) suggests that X motion is least common, accounting for only 24% of cases with motion, compared to 76% in Y or Z directions.

The simulation results also show that motion which occurs during the middle frame of the scan (60-120 s represent mid frame in a 15-frame scan) results in far greater MBF errors than motion which occurs at the beginning or near the end of the scan (**Figure 3.3.3.3**). However, the effect of motion near the end of the scan is worse than motion near the beginning; likely because the later time frames are used to define the ROIs for TAC sampling, resulting in more mispositioned time points, along with CTAC misalignment in majority of time frames. Furthermore, motion in late frames results in blurring of static myocardial perfusion images (MPI) and electrocardiogram (ECG)-gated images typically averaged over the last 6-8 minutes, which are used for clinical interpretation.[182] We speculate that the maximum MBF error occurs when the largest number of time frames are

misaligned with each other, which is consistent with our findings that mid-scan motion results in the largest MBF errors.

In our prevalence study, almost all motion was detected in the late time frames (**Figure 3.3.1.1**); however motion within the first minute was difficult to assess. Late time frames consist of the majority of the exam time (i.e. 6 minutes of an 8-minute scan) and therefore have a greater likelihood of capturing a motion shift event. In addition, motion is easier to discern in late time frames when the heart uptake is nearly completed, and the spatial distribution is static compared to the early time frames. In the absence of effective motion correction techniques, MBF and MPI errors may be best mitigated by cropping PET acquisition data from the time of motion shift, so long as sufficient data remains to reconstruct diagnostic quality images. Our results suggest that early frame motion may be relatively well tolerated by MBF quantification algorithms, resulting in only small MBF errors. Furthermore, early time frame data is not used to reconstruct MPI or ECG-gated uptake images.

Similar errors are observed with early and late CTAC alignments. The main difference between early and late CTAC alignment are that large errors occur when the CTAC is aligned in the early frames for right(+X) shifts, whereas if the CTAC is aligned in the late frames large errors are observed for left(-X) shifts (compare **Figure 3.3.3.4** vs **Figure 3.3.3.7**). Similar magnitude converse effects are observed for Y and Z shifts (compare **Figure 3.3.3.4** vs **Figure 3.3.3.7** and **Figure 3.3.3.8** vs **Figure 3.3.3.9**).

Similar effects to superior/inferior ( $\pm Z$ ) shifts are observed for anterior/posterior shifts ( $\pm Y$ ) except largest errors in MBF come from the anterior (median = 24 %), septal (median = 84 %) and apex (median = 51 %) for anterior (-Y) shifts, and anterior (median

= 16 %), septal (median = 30 %) and apex (median = 22 %) for posterior (+Y) shifts when calculated using regional PVC. For global PVC the median value for all segments for either anterior or posterior motion drops to 10 % on average (see **Figure 3.3.3.4**, **Figure 3.3.3.5**, **Figure 3.3.3.6**, **Figure 3.3.3.7**, **Figure 3.3.3.8** and **Figure 3.3.3.9**).

The highest over-estimation in MBF occurs with motion in the positive X-direction when CTAC is aligned with the late PET images, using either a regional or global partial-volume correction – see **Figure 3.3.3.1**. Therefore, if the direction of motion can be determined, CTAC alignment and PVC methods can be chosen to minimize the error in MBF. This is important for cases where only approximate corrections for motion can be made. Larger errors in MBF were observed with the high-resolution simulations; these results may be more applicable to longer-lived tracers such as  $^{13}\text{N}$ -ammonia where higher spatial resolution imaging is possible (data not shown). Recent developments in PET-MR and time-of-flight (TOF) PET may offer unique solutions to the problem of patient motion. For instance with MR, tagged myocardial imaging can be used to assess regional motion due to the distortions in the magnetization patterns.[183] Alternatively with TOF PET, both the activity and attenuation images can be reconstructed simultaneously, thus eliminating CTAC-misalignment artifacts for static imaging.[184,185] Further work is needed to develop and evaluate the potential of these emerging methods for dynamic PET motion correction.

Limitations of this study are that these are noiseless simulations, only one direction of motion at a time was simulated, the same TAC based on  $^{82}\text{Rb}$ -PET kinetics was applied to the LV and RV blood, and there was no motion simulated within frames. In addition, only one numerical phantom was used with the same internal organ morphology for all

simulations, and the simulated motion was rigid and thus did not consider non-linear effects from patient motion sometimes present in clinical cases.

### **3.5 Conclusion**

This study highlights the importance of dynamic PET motion correction, as well as the relative effects of motion parameters and corrections. Mild-to-moderate patient motion occurs in more than 60% of clinical scans, and can have highly detrimental effects on MBF calculations. Motion correction of the reconstructed PET dynamic image sequence reduces MBF bias, but CTAC alignment errors should also be addressed to further reduce MBF error. Motion correction algorithms should be developed with highest priority targeting of mid- and late-time-frame motion, high resolution imaging and motion in the X-direction, since these cases produce the largest errors in MBF estimation.

## 4 Chapter: Motion Correction for Cardiac PET Dynamic Imaging using Projection Consistency Conditions

### 4.1 Introduction

This chapter discusses “Motion Correction for Cardiac PET Dynamic Imaging using Projection Consistency Conditions”. This content has been submitted for publication in Medical Image Analysis and has been modified in the current document to improve readability.

Ischemic heart disease including coronary artery disease (CAD) is the leading cause of death among people in the industrialized world.[186] As mentioned in **chapter 3.1**, studies have shown that early diagnosis of CAD with stress PET perfusion imaging can be used to direct optimal therapy, improving patient morbidity and longevity.[187,188] If dynamic images are acquired over time, then tracer kinetic modeling of the spatio-temporal distribution can be used to quantify blood flow to the myocardium in absolute units of mL/min/g. Since tracer kinetic modeling assumes that the tracer activity vs time profiles have been measured with no patient motion, and as **chapter 3.3** shows that patient motion is a common problem, causing detrimental effects in up to 40% of rubidium PET scans for the determination of MBF, motion correction is essential.[167] Previous motion-prevalence studies (see **chapter 3.3**) indicate that head-to-foot translations are the most common, while left-right translations are the most detrimental to accurate estimation of MBF.

One of the most noticeable effects from patient motion is the CT attenuation correction (CTAC) artifacts in the reconstructed images caused by misalignment with the PET data.[44] In typical clinical practice, a single CT scan is used for attenuation

correction of all dynamic PET time frames, and in clinical practice is aligned to the last frame of the dynamic sequence, used for myocardial perfusion imaging (MPI) of the relative uniformity of tracer uptake in the LV. Therefore, in addition to the inconsistent spatial sampling caused by patient motion, the corresponding dynamic PET frames will also have artifacts in the reconstructed images due to the inconsistency between the position of the PET versus the CT data used for attenuation correction.

Various motion detection and compensation methods were reviewed in **chapter 1.2**, and include but are not limited to image-based motion correction, 4D CT imaging in conjunction with respiratory gating, aligning non-AC PET frames to frames with known alignment, edge detection algorithms have been reported, tracking using external radioactive and optical markers, and using MR imaging for motion tracking.[54,56,61,66,72,76,78,189–191]

The Radon transform consistency conditions for PET-CTAC alignment have been reported by Alessio et al and Welch et al.[62,141] As described in **chapter 2.2.7**, accurate attenuation corrected PET data should satisfy these consistency conditions, and deviations from these conditions can be caused by intra-frame motion, CT to PET misalignment, or other degrading factors. This fact can be exploited to align the CT to the PET data thereby extracting the spatial information needed to align dynamic time frames to a common reference frame and thus perform motion correction. However, to our knowledge, correction of patient body motion by exploiting the PET-CTAC projection data consistency conditions has not been reported.

The purpose of this study was to evaluate the efficacy of using the projection data consistency conditions for patient body motion correction. Due to the uncertainty of the

true alignment of PET frames in a typical clinical dynamic sequence, noise-added computer simulations were used to evaluate the performance of this algorithm. Computer simulations have the advantage that the ground-truth of anatomy and tracer distribution over time are known exactly. In addition, cardiac and respiratory motion can be perfectly removed so the ability to correct patient body motion can be characterized uniquely, and any errors can be absolutely known.

## 4.2 Methods

### 4.2.1 NCAT Dynamic Phantom

Positron emission tomography (PET) images of radio-isotope activity and attenuation phantoms (for CT attenuation correction) were created *in silico* using the digital NURBS-based Cardiac-Torso (NCAT) phantom – see **chapter 2.6.1**. [192,193] Arms were positioned above the head and out of the field of view (FOV), to simulate normal clinical practice. Two phantoms of different physical sizes but with similar internal anatomy were generated by scaling to 20 and 35 cm transaxial (left-right) extent. Both phantoms had the same initial voxel size of 3.125 mm, and a final reconstructed PET image resolution of 12 mm FWHM.

Tracer time activity curve (TAC) values were assigned from a previous rubidium-82 dosimetry study in humans [95] to simulate a dynamic PET image series following injection of 10 MBq/kg at rest as described in **chapter 3.2**. This previous study consisted of 10-minute PET dynamic scans in 30 patients with images reconstructed at the following time intervals: 9×10, 3×30, 1×60, 1×120, 1×240 = 600 s. Patient-averaged organ time-

activity curves (TAC) were used to generate the dynamic NCAT phantom images. TAC curves (without isotope decay correction) were assigned to the following anatomical regions: liver, gall bladder, lungs, stomach wall, kidney, spleen, small intestine, large intestine, small intestine and myocardium. A single blood time-activity curve was assigned to the arteries, veins, and heart cavities. To simulate the patient background organs distribution, a small amount of activity was assigned to the lymph nodes taken 10% of the thyroid TAC. In addition, a small amount of activity in the ribs, spine and bone cartilage was taken as 10 % of the red marrow. Finally, the remainder body activity (mainly fat) TAC was assigned as 30% of the measured breast activity.

#### **4.2.2 PET Noise Model**

The NCAT tracer distributions were smoothed using a Gaussian filter to simulate positron range and the intrinsic resolution of the PET scanner (GE Advance) so that the intrinsic resolution was 8.5 mm FWHM prior to image reconstruction. To simulate realistic PET scans, noise was added using the analytical simulator ASIM.[164,194] The analytical simulator required a model of the count-rate statistics of the simulated scanner to determine the correct number of trues, random and scatter events corresponding to the activity within the scanned volume. Two NCAT data sets were produced with added noise that was consistent with the physical sizes of 20 and 35 cm to match the published count-rate measurements for the GE Advance as shown in **Figure 4.2.2.1**.[195] The GE Advance count-rate data was measured using the NEMA NU-2 scatter phantom in 3D-mode with the septa removed.

ASIM uses the Klein-Nishina equation first to determine the mean estimated scatter using a uniform phantom, and then to calculate the added noise due to scatter using a pseudo-random Poisson distribution. The mean estimated scatter is used for scatter correction. A similar process is used to add and correct for random events. The result is a realistic noise-added sinogram, but without photon attenuation, scatter or randoms; which can be considered as fully-corrected for all physical effects including isotope decay, and ready for tomographic image reconstruction. Attenuation is not simulated with ASIM, therefore the noise-added sinograms were attenuated by division with an aligned attenuation sinogram derived by forward projection through the simulated CT image (see Figure 1). Since the attenuation correction sinogram is aligned to the last PET time-frame (as per clinical practice) any frames with motion are reconstructed with realistic CTAC artifacts, as observed in clinical practice.

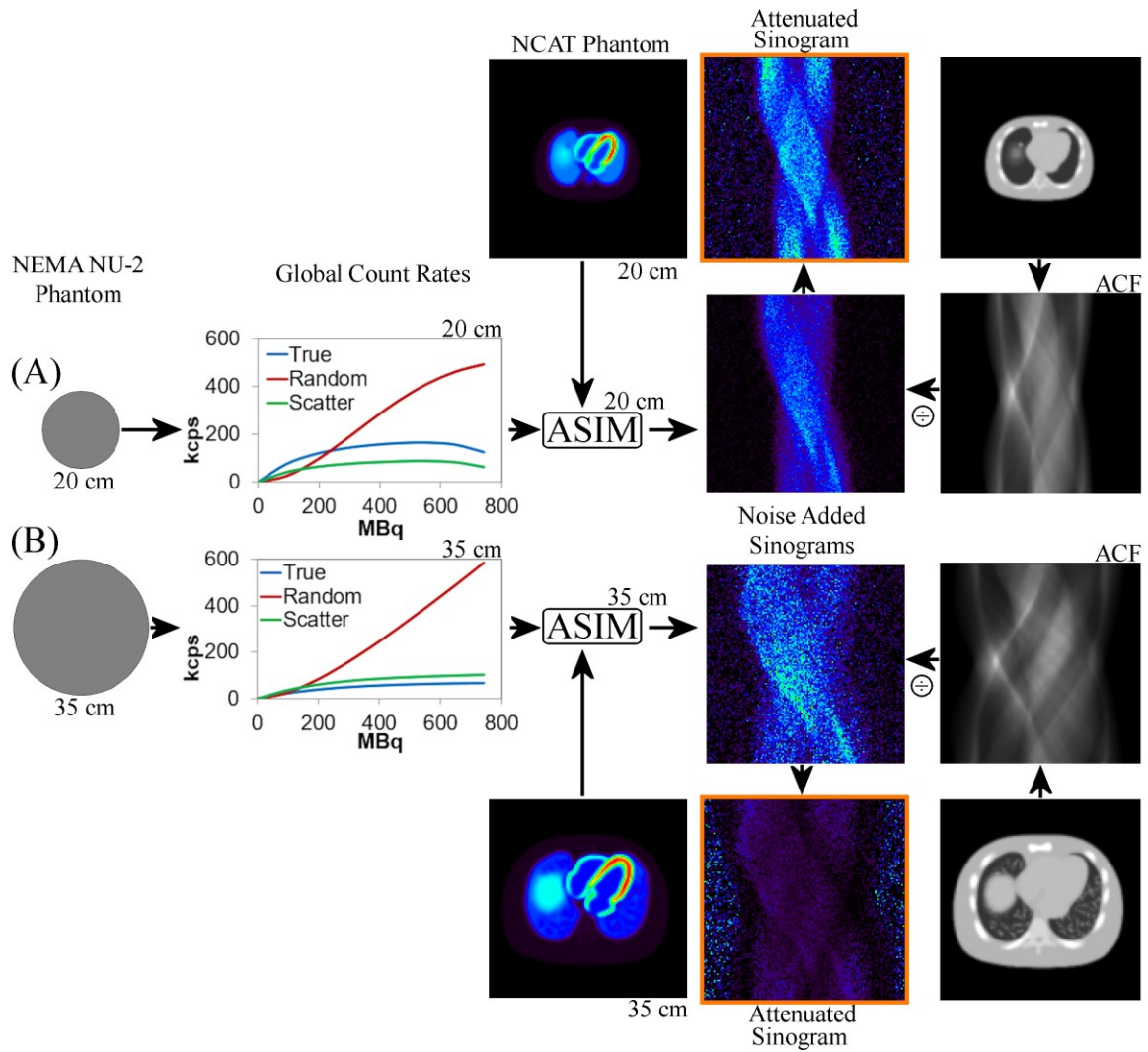


**Figure 4.2.2.1: PET noise model based on global count-rate characteristics [23] measured for 2 different phantom sizes: 20 cm (A), and 35 cm (B).**

Five noise realizations without any motion were simulated for each phantom size, as reference standard cases to which all other data are compared (Table 4.2.3.1). These same cases were also processed by the motion correction algorithm to determine the potential bias and precision in the absence of any body motion.

### 4.2.3 Dynamic PET Body Motion

Patient body motion was simulated with instantaneous shifts in the x (left-right) and z (superior-inferior) directions, based on our previous findings that y-direction shifts are relatively rare [4]. In the time dimension, patient motion in the mid-to-late dynamic time frames was shown to be the most detrimental to blood flow quantification accuracy, therefore motion times were simulated at 90, 120, 150, 180, 240, and 360 seconds. Motion magnitudes of 0.25, 0.5, 1, 2, 3, and 6 voxels (representing shifts of 0.8, 1.6, 3.1, 6.3, 9.4 and 18.8 mm) were simulated at each of the above times. A voxel size of 3.125 mm was chosen so that the trans-axial matrix size of  $128 \times 128$  had a 40-cm field of view. For both phantom sizes, 5 separate noise realizations were simulated for each motion condition, for a total of 1,440 unique dynamic PET scans with 14 time frames each (20,160 volume images).

**Table 4.2.3.1:**

**Motion Simulations.**

<b>Motion</b>	<b>Parameter</b>	<b>DOF</b>	<b>Values</b>
<b>No Motion</b> (n=10) <b>Reference Standard</b>	Phantom Size	2	20, 35 cm diameter
	Noise	5	Independent ASIM realizations
<b>Motion Added</b> (n=1,440)	Phantom Size	2	20, 35 cm diameter
	Noise	5	Independent ASIM realizations
	Direction	4	(left/right) x, (superior/inferior) z
	Time	6	90, 120, 150, 180, 240, 360 s
	Magnitude	6	0.25, 0.5, 1, 2, 3, 6 voxels (0.8, 1.6, 3.1, 6.3, 9.4, 18.8 mm)

DOF = Degrees of Freedom

Motion shifts were applied to the PET activity and CT images (used to create the CT attenuation factors) in image space prior to forward projection, resulting in shifted sinograms. During PET image reconstruction, the CT attenuation correction factors (ACF) were correctly aligned with the PET data at the last time-frame, and were potentially misaligned at early times, due to patient motion that was simulated at the earlier scan-times. This protocol design was used because in clinical practice the CT is typically aligned (either manually or with some automated approach) with the PET perfusion image at late time-frames, and then used to correct for attenuation of the entire dynamic image sequence. Our proposed motion correction algorithm sought to shift the CT image to align with each PET dynamic frame, such that the derived attenuation map was consistent with the PET sinogram data prior to image reconstruction; thereby producing a PET image series with optimal emission and attenuation registration. Then the reconstructed PET data was shifted back into a common reference frame (last time-frame) to produce a motion-free dynamic series.

#### **4.2.4 Motion Correction**

Tracer kinetic modeling for MBF quantification requires dynamic PET imaging for determination of the time-activity curves in arterial blood and heart tissues, and thus assumes all dynamic time frames are spatially aligned and the images are artifact-free.

The proposed motion detection algorithm exploits the fact that the tomographic projection data (sinograms), when fully corrected for all physical measurement effects including photon attenuation, must satisfy certain consistency conditions in order to be

considered fully valid for accurate tomographic image reconstruction. One such metric is Natter's formulation of the Helgason-Ludwig consistency conditions on the 2D Radon transform. A computationally efficient form is shown below in **Equations 4.2.4.1 and 4.2.4.2** [62,141], and has previously been evaluated for late frame PET-CTAC alignment in cylindrical, simple anatomical and NCAT phantoms, and limited patient studies,

$$\Phi_{m,k}(\mathbf{z}) = \int_0^{2\pi} \int_{-\infty}^{\infty} \mathbf{s}^m \mathbf{e}^{ik\theta} \mathbf{e}^{A(s,\theta,z)} \mathbf{E}(\mathbf{s}, \theta, \mathbf{z}) \mathbf{d}\mathbf{s} \mathbf{d}\theta \quad (4.2.4.1)$$

$$\hat{\Phi} = \sum_z \sum_{m=0}^1 \sum_{k=\{C_m\}} \Phi_{m,k}(\mathbf{z}) \quad (4.2.4.2)$$

where:  $C_m = \{1, 3, \dots, 9\}$  for  $m = 0$ , and  $C_m = \{0, 2, \dots, 8\}$  for  $m = 1$ ,  $z$  is the transaxial slice number,  $E(s, \theta, z)$  is the measured (or simulated) PET emission projection sinogram in slice  $z$  without attenuation correction,  $A(s, \theta, z)$  are the corresponding attenuation projections (i.e. fractional units of linear attenuation coefficient ( $\mu$ )  $\times$  distance),  $k$  are the Fourier sampling components,  $m$  are the transform moments (0 and 1 for rigid body motion). In theory, perfectly aligned PET and CTAC images should yield a value  $\hat{\Phi} = 0$ , in the ideal case with no noise and if  $k > m$  or when  $k + m$  is odd as shown by Alessio et al.[62] Here Equation 1 is evaluated for each slice independently then summed over all slices as shown in Equation 2.

Motion correction was achieved by minimization of  $\Phi$  (Eq.2), through transformation of spatially misaligned into aligned attenuation factors, i.e.  $A(s, \theta, z) \rightarrow A(s', \theta', z')$  as illustrated in **Figure 4.2.4.1**. The attenuation correction factors (ACF =  $e^{A(s,\theta,z)}$ ) are calculated, and multiplied by the uncorrected (attenuated) emission data.

The consistency condition is calculated for each trans-axial plane  $\Phi_{m,k}(z)$  and then summed over all planes and m,k indices. Only projection samples with valid (complete) PET and ACF data are used to calculate consistency. Minimization of  $\hat{\Phi}$  was achieved using Powell's method of unconstrained optimization.

The proposed algorithm for generating motion-corrected and uncorrected PET data is illustrated in **Figure 4.2.4.1**. It should be noted that the last time frame of the dynamic sequence was always correctly aligned with the CT, reflecting the clinical practice of careful CTAC alignment with the late dynamic frame(s) for standard MPI. Clinically, often static perfusion images are used for CTAC alignment, here we assume only the last frame was aligned properly. Simulations started with a noise-free PET image  $I(x, y, z)$ , and an aligned CT(x, y, z). Rigid spatial shifts were introduced to the PET image using bi-cubic interpolation, transforming:  $x \rightarrow x + \Delta x = x'$ ,  $y \rightarrow y + \Delta y = y'$  and  $z \rightarrow z + \Delta z = z'$ ; or  $I(x, y, z) \rightarrow I(x', y', z')$ . The shifted PET image was then used as input into ASIM to create noise-added sinograms as shown in **Figure 4.2.2.1**. To simulate a clinical acquisition, the noise-added sinogram must also be attenuated to produce a realistic emission sinogram  $E(s', \theta', z')$ . This is achieved by dividing by the attenuation correction factors (ACF), as computed from a CT aligned with the shifted PET data. The unshifted CT was then transformed (forward-projected) into an ACF dataset  $A(s, \theta, z)$ , properly aligned with the last frame. Therefore, this reference ACF was misaligned with any PET frames that contain patient motion.

The minimization of  $\hat{\Phi}$  produces a new aligned ACF  $A(\hat{s}', \hat{\theta}', \hat{z}')$  with estimates of the shifted parameters  $\hat{s}'$ ,  $\hat{\theta}'$  and  $\hat{z}'$ . When  $A(\hat{s}', \hat{\theta}', \hat{z}')$  is used for attenuation correction it should produce the attenuation-corrected sinogram  $P(\hat{s}', \hat{\theta}', \hat{z}')$ , which has been realigned

according to the best estimate of the detected patient motion. If the original misaligned  $A(s, \theta, z)$  was used for attenuation correction it would produce a corrected sinogram  $P(s', \theta', z')$  which has spatially shifted information without an aligned ACF. After reconstruction  $\hat{I}(x', y', z')$  would have clear motion artifacts due to inconsistent AC. In addition, it would be spatially shifted relative to the last frame of the dynamic sequence. Conversely, the CT-aligned PET image  $\hat{I}(\hat{x}', \hat{y}', \hat{z}')$  should ideally have no discernible attenuation artifacts, but would still be spatially shifted from the reference PET frame. Therefore, the final step after reconstruction is to transform the motion-corrected PET frame by the negative value of the estimated shift distance, i.e. we transform:  $\hat{x}' \rightarrow \hat{x}' - \Delta\hat{x} = \hat{x}$ ,  $\hat{y}' \rightarrow \hat{y}' - \Delta\hat{y} = \hat{y}$  and  $\hat{z}' \rightarrow \hat{z}' - \Delta\hat{z} = \hat{z}$ ; or  $I(\hat{x}', \hat{y}', \hat{z}') \rightarrow I(\hat{x}, \hat{y}, \hat{z})$ .

To summarize, the CT-derived ACF projections are aligned to the motion-shifted PET data frame, then the attenuation corrected PET data are reconstructed into images that are shifted back to the reference ACF frame. Reconstruction was accomplished using STIR and the ordered subsets maximum *a posteriori* one-step-late (OS-MAP-OSL) iterative algorithm.

The consistency metric corrects each frame independently of all other frames and all frames are aligned to a common CT. This gives the consistency metric an advantage over any frame-to-frame comparison methods such as with a post-reconstruction image-based method. In addition, post-reconstruction image-based motion correction methods often have errors due to CTAC misalignment, whereas the consistency metric aligns the CT to each frame independently.

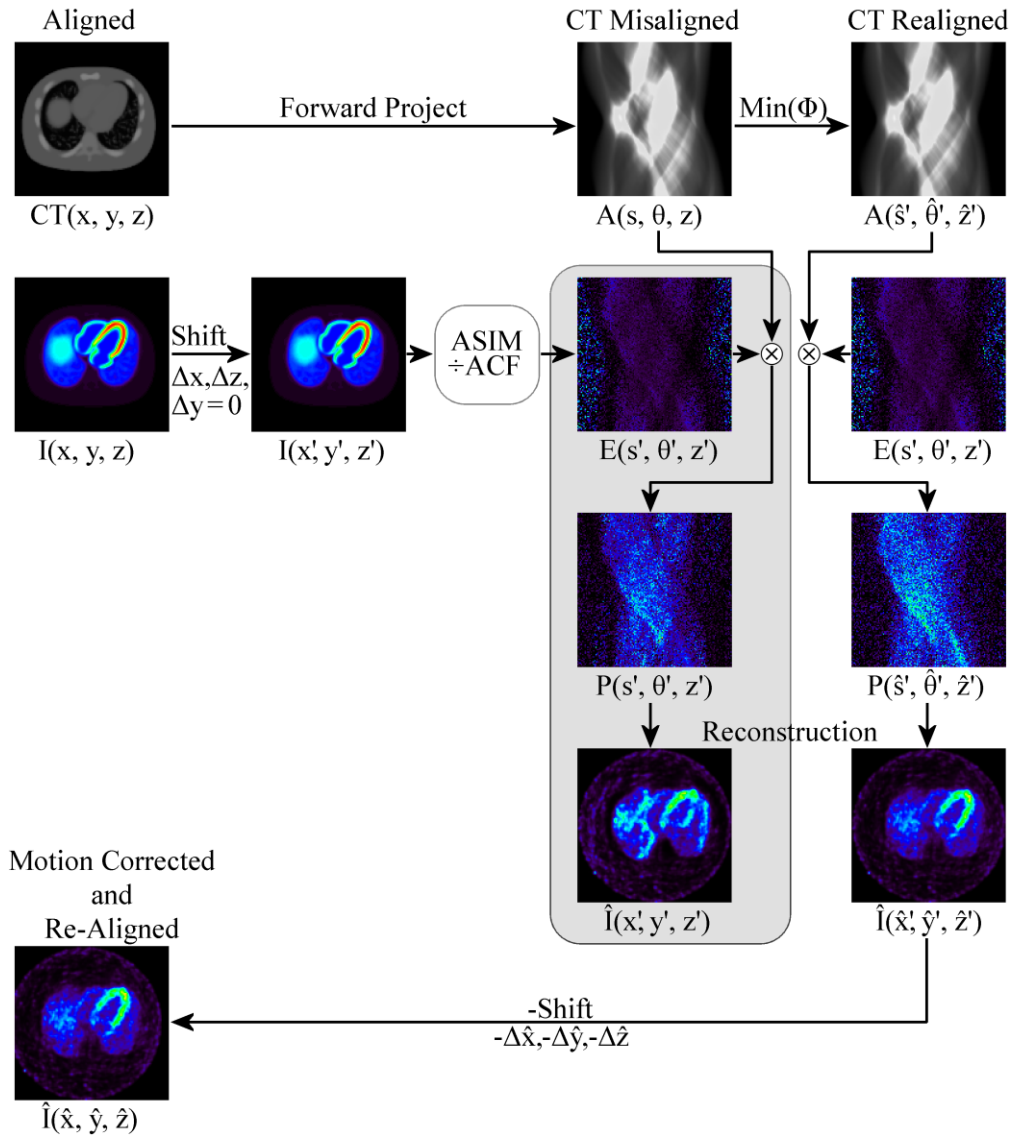


**Figure 4.2.4.1: Motion-correction algorithm illustrated for the simulated NCAT torso phantom (35 cm phantom) with attenuation misalignment artifact (Misaligned) and without attenuation artifact (Realigned) by minimizing  $\Phi$ , to maximize consistency in the attenuation-corrected projection sinograms. Noise is added with ASIM, attenuation is added using an aligned CT and dividing by the attenuation factors. Images in the shaded region represent non-motion-corrected processing and are shown for information only are not necessary for implementation of the method.**

#### 4.2.5 ROC Analysis of Motion Correction

Receiver operator characteristic (ROC) analysis was performed to determine the threshold of motion below which motion may not be reliably detected. Since the algorithm is unlikely to produce zero-value motion estimates, some detected shifts will represent small errors due to noise only, and should be ignored for optimal results. The ROC confusion matrix which defines a true positive, true negative, false positive and false negative is given in **Table 4.2.5.1**. Using the results from the ROC analysis a threshold value of estimated motion was determined, below which motion correction was not performed. The optimal threshold value was selected as the point on the ROC curve where equal weight is given to sensitivity and specificity by use of Youden's index.[196,197]

**Table 4.2.5.1:**

**ROC Confusion Matrix**

	If measured motion is > threshold Motion is detected	If measured motion is > threshold No motion is detected
Motion was present	True positive	False Positive
No motion was present	False Negative	True negative

The motion corrections estimated by the consistency algorithm were compared to the known (simulated) shifted values. Bias was defined as the mean difference between the estimated and simulated shift parameters (i.e.  $\Delta x \pm \Delta \hat{x}$ ,  $\Delta y \pm \Delta \hat{y}$  and  $\Delta z \pm \Delta \hat{z}$ ).

**Table 4.2.5.2:**

**Characterization of Motion Parameters.**

	<b>Dynamic scans (Table 1)</b>	<b>Motion Frames (dynamic scans ×13 frames/scan)</b>	<b>Motion shifts for ROC analysis (motion frames ×3 directions) *</b>	<b>MBF Segments (dynamic scans ×5 segments/scan ×2 PVC methods)</b>
<b>No-motion standard</b>	10			100
<b>No-motion corrected</b>	10			100
<b>Simulated motion</b>	1,440			14,400
<b>Motion-corrected</b>	1,440	18,720	56,160	14,400

\*Note: While motion-shifts in the y-direction were not simulated, motion-correction was applied in the y-direction, with the expected value of 0 for all frames.

**4.2.6 Myocardial Blood Flow Analysis**

MBF values estimated from the motion-corrected dynamic PET scans (N=1,440) were compared to the reference standard case without motion. The reference standard cases (N=10) were simulated by using the properly aligned CT for PET attenuation correction and not inserting any motion nor motion correction.

The automated software program FlowQuant (Ottawa, ON) was used for MBF analysis as illustrated in **Figure 4.2.6.1.**[176] Tracer uptake images (2-10 min activity) were used for identification of the heart wall (myocardium) and three blood pool regions in the LV cavity (C), base (B), and left atrium (A). The blood input function used for tracer kinetic modeling was derived from the median of the three blood pool regions. The parameters of a 1-tissue-compartment kinetic model with globally-derived average distribution volume were estimated from the blood (input) and myocardial (output) TAC functions. From the uptake rate parameter (K1), values of MBF [mL/minute/g] were estimated using regional (Flow) and global (FlowRC) partial-volume recovery corrections (PVC) respectively. LV blood flow polar-maps were divided into the following 5 segments anterior, posterior, septal, lateral, and apex. Reported values are the average flow value within each segment.

The average flow values in each segment of the no-motion reference standards were averaged over the 5 noise realizations. The segmental motion-corrected MBF results (N=1,440) were then compared to the no-motion reference standard values (with perfectly aligned CT). Segmental errors in MBF (bias) were calculated as the percent difference between the motion-corrected or uncorrected cases relative to the average no-motion reference standard values.

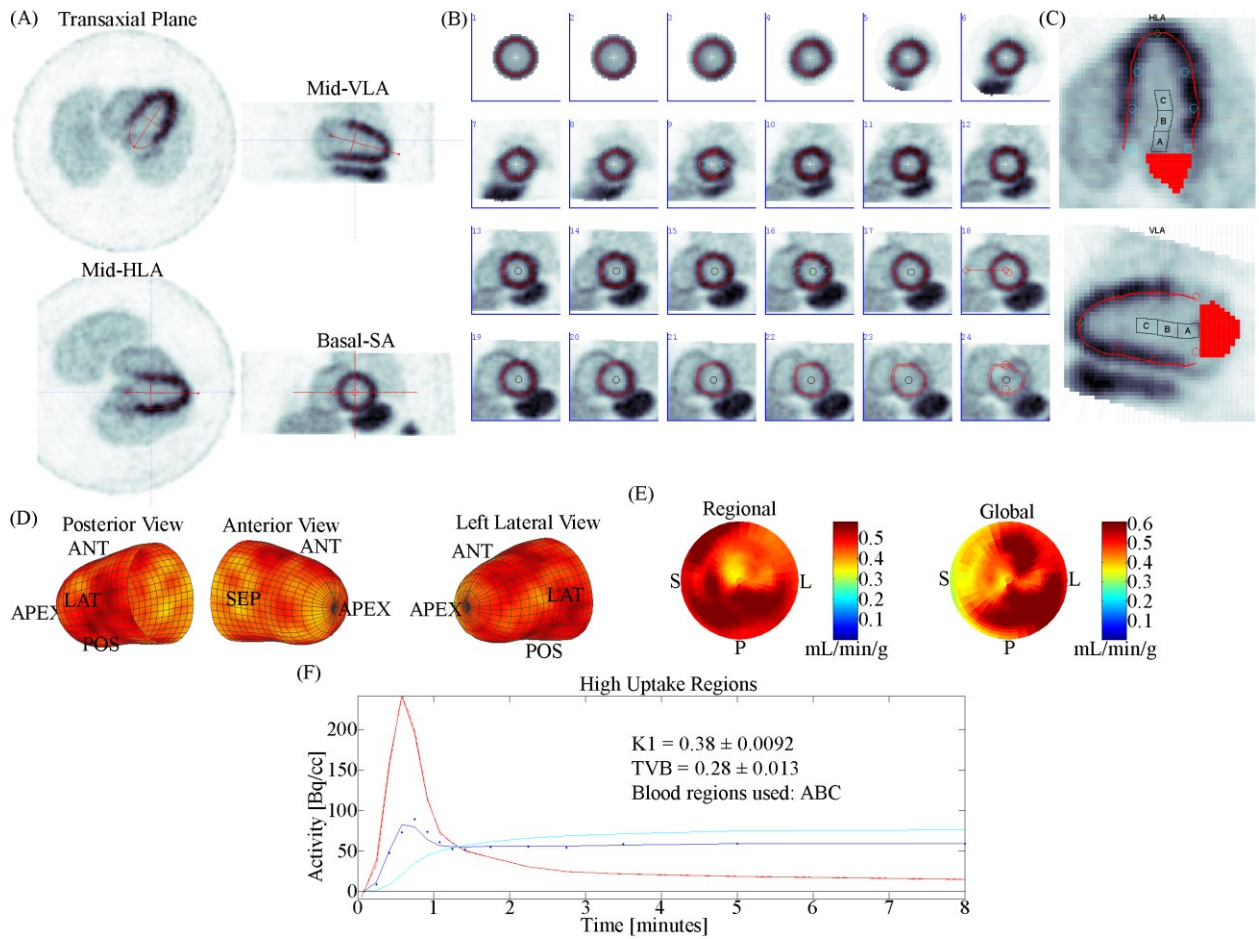


**Figure 4.2.6.1: Initial identification of the heart wall is shown in (A). Short axis slices of the heart wall are shown in (B). The blood pool regions used as the input function for blood flow are shown in (C). The resultant countours of the left ventricle are shown in (D). FlowQuant Analysis of myocardial blood flow (MBF) using regional (Flow) and global (FlowRC) partial volume corrections are shown in (E) as polar maps. The time activity curves are shown in (F).**

## 4.3 Results

### 4.3.1 Motion Detection Results

Figure 4.3.1.1 shows the accuracy and precision of the proposed projection-based correction for all 18,720 simulated motion frames. The motion estimation was highly accurate on average, with standard deviation (precision) for all data points on the order of 1 to 2 mm (N = 630 per simulated shift value) which is less than 1 voxel (3.125 mm). For the larger 35 cm phantom, there was a small positive bias of 2.6 mm in the measured values for all simulated shifts. Comparisons between 20 cm and 35 cm were highly significant for all data points (t-distribution showed that in all cases  $P < 0.01$ ).

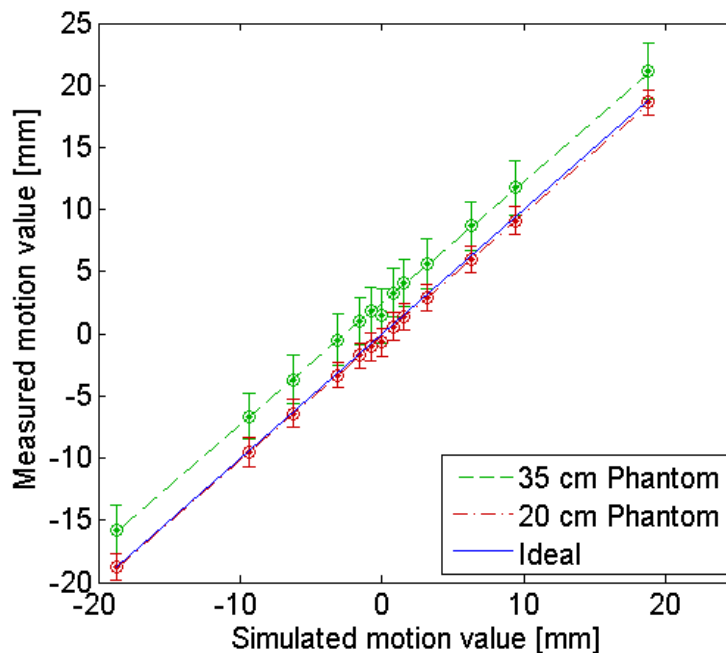
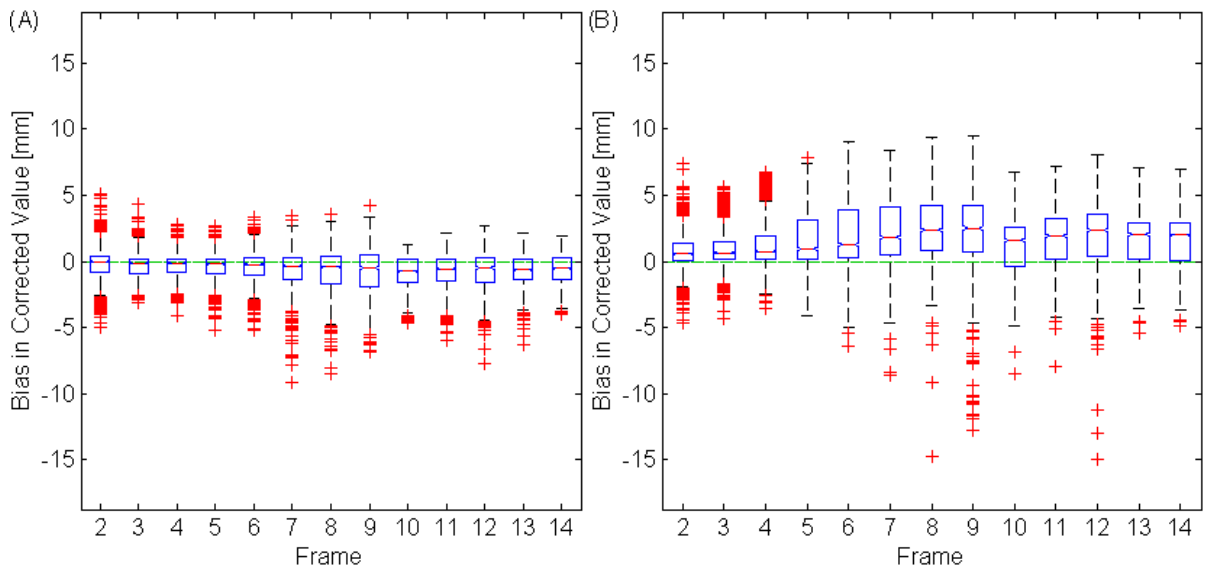


Figure 4.3.1.1: Estimated (measured) versus simulated motion values (mean  $\pm$  standard deviation) for the 20 cm (red) and 35 cm (green) phantom noise models.

Dashed lines are lines of best fit. The blue solid line corresponds to perfect agreement (measured = simulated).

The bias in the measured motion values according to dynamic frame number is shown in **Figure 4.3.1.2**. Larger deviations occurred with the larger 35 cm diameter phantom, primarily due to the lower count-rates and higher image noise of the larger phantom, particularly in the mid-to-late time frames. Median absolute bias values were all <1 mm for the 20-cm phantom, and <2.5 mm for the 35 cm phantom, but some outliers approached deviations as high as 15 mm. Frame 15 is not shown, since it was the reference standard for proper alignment with the CT for attenuation correction, as used in clinical practice. In addition, frame 1 typically had too few counts to support a proper alignment with the CT and therefore was omitted from the analysis.



**Figure 4.3.1.2: Bias in estimated motion values for all dynamic frames using the 20 cm (A) and 35 cm (B) phantom noise models.**

**Figure 4.3.1.3** shows the results from the ROC analysis of 1,440 simulated dynamic PET scans ( $\times 13$  time-frames  $\times 3$  directions = 56,160 values), including  $n=15,120$  values with motion and 41,040 without motion (depending on the time of simulated motion

frames in Table 1), used to evaluate sensitivity and specificity respectively. This analysis demonstrated the algorithm’s ability to correctly identify cases with actual motion and cases without any motion. The 20 cm phantom the optimum cutoff point was measured at a threshold ( $t$ ) of 0.83 voxels (2.6 mm). For the 35 cm it was 1.09 voxels (3.4 mm), and for the combined data it was 0.91 voxels (2.8 mm). The measured area under the curve (AUC) for the 20 cm, 35 cm and combined data was 0.86, 0.82 and 0.80.

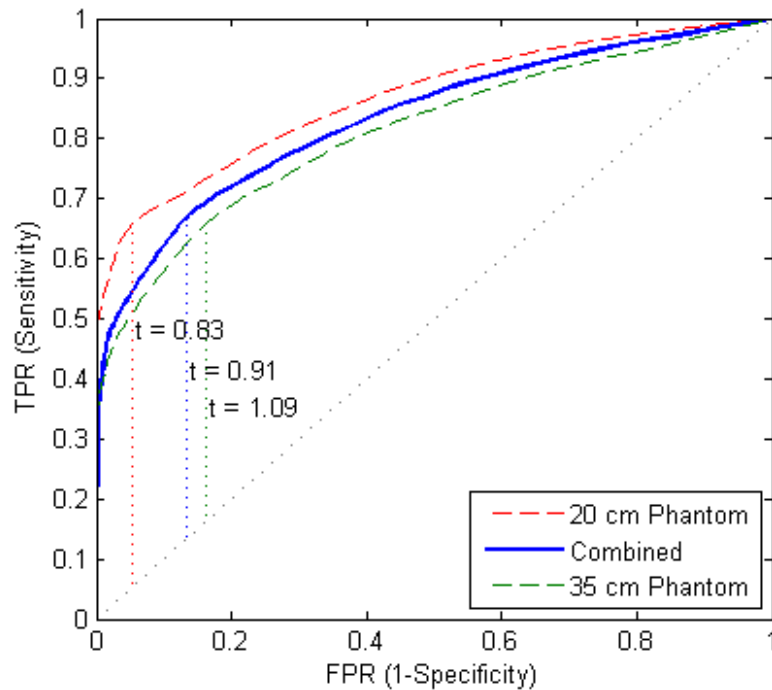


**Figure 4.3.1.3: ROC curve showing the true-positive rate (TPR) and false-positive rate (FPR) for different values of estimated vs. simulated motion, using all 56,160 motion values. Thresholds are also shown, as well as the Youden’s indexes (lines that connect the linear line to the ROC curve).**

**Table 4.3.1.1** shows the bias values (ideally zero) for both phantom noise models, with detected motion values less than a threshold of 2.8 mm (from the ROC analysis) set to zero. The standard deviation and bias tend to increase from the 20 to 35 cm phantom

models. Comparisons between 20 cm and 35 cm using were highly significant for all data points (t-distribution showed that in all cases  $P < 0.001$ ).

**Table 4.3.1.1:**

**Absolute bias in estimated motion, excluding sub-threshold values.**

Simulated motion [mm]	Number of image frames	20 cm		35 cm	
		Bias[mm]	± SD	Bias[mm]	± SD
-18.8	630	0.77	0.76	3.05	1.91
-9.4	630	0.81	0.84	2.79	1.78
-6.3	630	0.81	0.83	2.70	1.83
-3.1	630	0.74	0.76	2.77	1.91
-1.6	630	0.74	0.77	2.65	1.77
-0.8	630	0.79	0.84	2.71	1.76
0.0 (no motion)	20,520	1.02	0.88	1.98	1.66
0.8	630	0.74	0.79	2.64	1.84
1.6	630	0.74	0.76	2.60	1.79
3.1	630	0.74	0.82	2.61	1.85
6.3	630	0.75	0.85	2.53	1.83
9.4	630	0.76	0.83	2.56	2.00
18.8	630	0.71	0.75	2.55	2.09
Non-Zero Total	7,560				

**Table 4.3.1.2** shows the MBF mean and standard deviation (SD) values in the 5 segments of the LV myocardium, for the noise-free and noise-added reference standard cases (perfectly aligned to the CT) using both phantom models and partial-volume

correction methods. Any differences in these values are the result of noise alone since none of these cases contained any simulated motion. Ideally the delta values (and SD values) should be zero; however, there are fluctuations in the determination of blood flow values due to noise. Larger segmental differences were observed for the larger phantom noise model.

**Table 4.3.1.2: Segmental MBF values (mL/min/g) for the no-motion reference standard cases (n = 5 noise realizations) compared to ‘ideal’ noise-free simulations.**

**Regional Partial-volume Correction**

	20 cm				35 cm			
	Noise-free	Noise-added	±SD	Delta	Noise-free	Noise-added	±SD	Delta
<b>Anterior</b>	0.344	0.369	0.026	7.3%	0.436	0.522	0.016	19.7%
<b>Septal</b>	0.483	0.430	0.024	- 11.0%	0.479	0.530	0.041	10.6%
<b>Posterior</b>	0.382	0.398	0.015	4.2%	0.427	0.475	0.016	11.2%
<b>Lateral</b>	0.378	0.388	0.013	2.6%	0.441	0.501	0.016	13.6%
<b>Apex</b>	0.418	0.404	0.012	-3.3%	0.465	0.496	0.018	6.7%
Average	<b>0.401</b>	<b>0.398</b>	<b>0.018</b>	<b>-0.8%</b>	<b>0.450</b>	<b>0.505</b>	<b>0.021</b>	<b>12.3%</b>

**Global Partial-volume Correction**

	20 cm				35 cm			
	Noise-free	Noise-added	±SD	Delta	Noise-free	Noise-added	±SD	Delta
<b>Anterior</b>	0.305	0.343	0.027	12.2%	0.387	0.485	0.014	25.3%
<b>Septal</b>	0.287	0.272	0.013	-5.3%	0.377	0.377	0.019	0.0%
<b>Posterior</b>	0.396	0.430	0.024	8.6%	0.410	0.494	0.007	20.4%
<b>Lateral</b>	0.435	0.458	0.025	5.3%	0.441	0.535	0.023	21.2%
<b>Apex</b>	0.417	0.440	0.032	5.5%	0.479	0.538	0.024	12.4%
Average	<b>0.368</b>	<b>0.388</b>	<b>0.024</b>	<b>5.5%</b>	<b>0.419</b>	<b>0.486</b>	<b>0.018</b>	<b>16.0%</b>

SD = standard deviation; Delta = (Noise-added – Noise-free) ÷ Noise-free

### 4.3.2 MBF Analysis Results

The magnitude of simulated motion tended to increase segmental errors in estimated MBF as illustrated in **Figure 4.3.2.1**. Median errors tended to be higher with the 35-cm phantom model, except for the 18.8 mm motion magnitude, which resulted in the highest errors with the 20 cm phantom model. Small deviations <3.1 mm (or <1 voxel) still resulted in median MBF errors on the order of 5-7 % for the 20 cm phantom model. Variability (SD) values were significantly different for all segments of the 35 cm phantom except the septal wall using global PVC (**Table 4.3.1.2**). In addition, significant differences were observed for the septal wall of the 20 cm phantom calculated with regional PVC and the anterior / posterior walls when calculated with global PVC.

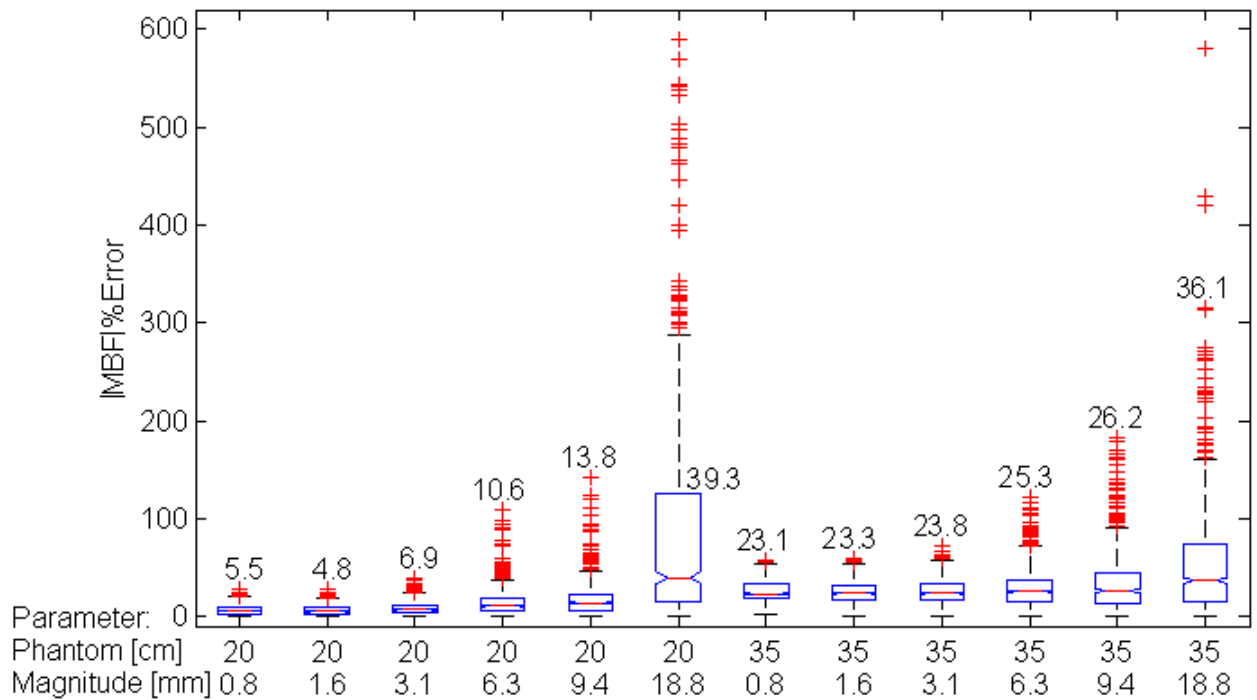


**Figure 4.3.2.1: Absolute MBF error for 20 and 35 cm phantom sizes, before motion correction.**

**Figure 4.3.2.2** shows the polar maps of left ventricular MBF for four individual simulations. In (A) a right shift (shift of the heart wall into lung region) resulted in a global positive bias in MBF. Motion correction of the 2 cm right shift in (B) resulted in flow values much closer to the reference standard. Motion correction of a case without motion in (D) had a minimal effect on the flow values.

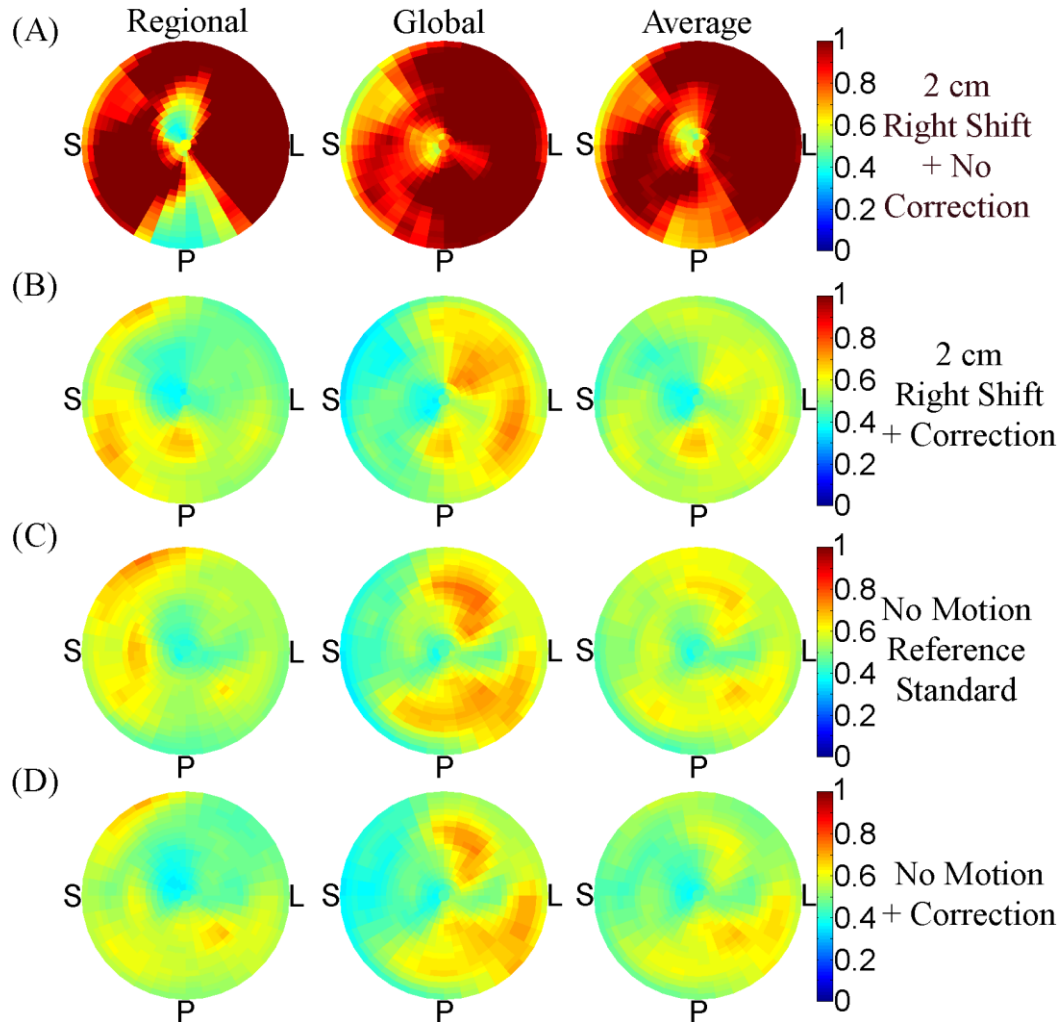


**Figure 4.3.2.2: MBF (mL/min/g) polar-maps from FlowQuant analysis for the 35 cm phantom. The top row (A) shows an uncorrected case using 2 cm motion at 120 s.**

**After motion-correction by the projection-based method artifacts are greatly**

reduced as shown in (B), as compared to the reference standard case with no motion shown in (C). Motion correction of the reference standard case is also shown in (D).

Projection-based motion correction resulted in dramatic reductions in MBF error using both regional and global PVC, as shown in **Figure 4.3.2.3**. There was a significant reduction in the median error in MBF values from 30-40% down to 6-20% and a dramatically reduced variance. Small residual errors in MBF quantification were still observed due to residual bias in the motion correction, resulting in imperfect inter-frame alignment. However, CT alignment attenuation artifacts were greatly reduced and could not be visually observed in any of the motion-corrected images.

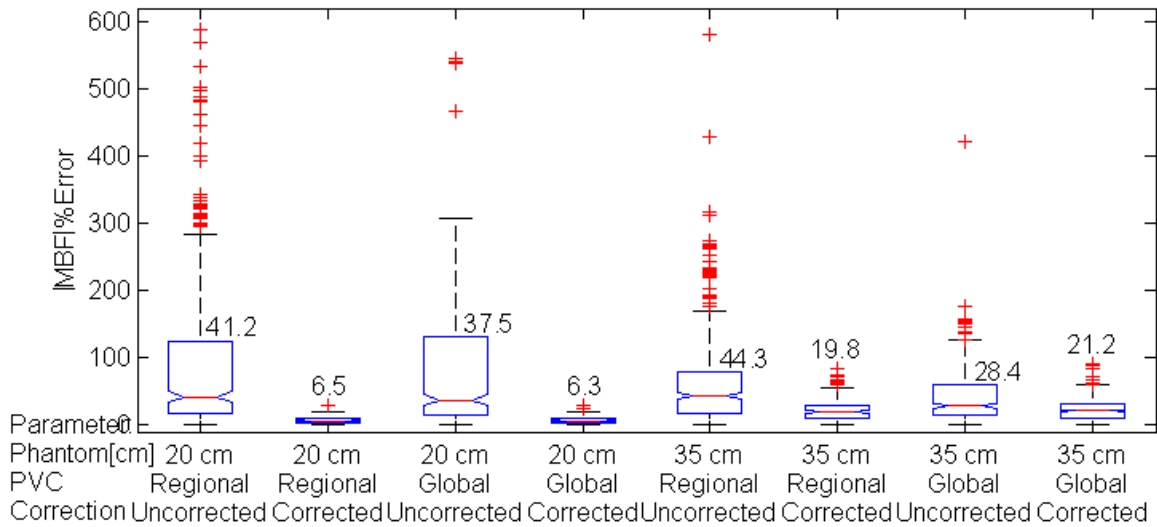


**Figure 4.3.2.3: Motion-corrected vs. uncorrected absolute errors in segmental MBF values (N = 3,600 per group). Errors up to 4000 % occur for uncorrected data for the 35 cm phantom – those extreme outliers are not shown.**

## 4.4 Discussion

This study has demonstrated for the first time that projection sinogram consistency conditions can be used effectively for motion correction of cardiac PET dynamic scans, to improve the estimation of myocardial blood flow.

### 4.4.1 ASIM PET Noise Model

The use of analytic vs. Monte Carlo methods allowed simulation of a large number of independent PET scans (1,440 with >20,000 dynamic frames) with realistic noise-modeling. The total number of simulated events (true (T), random (R) and scatter (S)) and the noise equivalent count rate (NEC) was different, as expected between the two phantom sizes as shown in **Figure 4.4.1.1** and **Figure 4.4.1.2**. For the 35 cm phantom (similar to a 70 kg patient) the random and scatter events were generally higher in all frames than the smaller phantom due to higher simulated ‘injected activity’ and body size, leading to noisier images and larger errors in the estimated motion using the consistency metric. The simulated true count-rates were also similar to those observed in clinical practice using a current 3D PET system (GE Discovery 690), as observed in a Rb-82 scan on a 90 kg patient (**Figure 4.4.1.3**), however the randoms rate is higher. The reason for this is likely due to the fact that the 35 cm phantom simulation is similar to a 70 kg patient with optimal body mass index (BMI), whereas the 90 kg patient is obese. Since activity is injected at 10 MBq/kg we expect a higher injected activity in the 90 kg patient than the 35 cm phantom, and thus a much higher randoms rate.

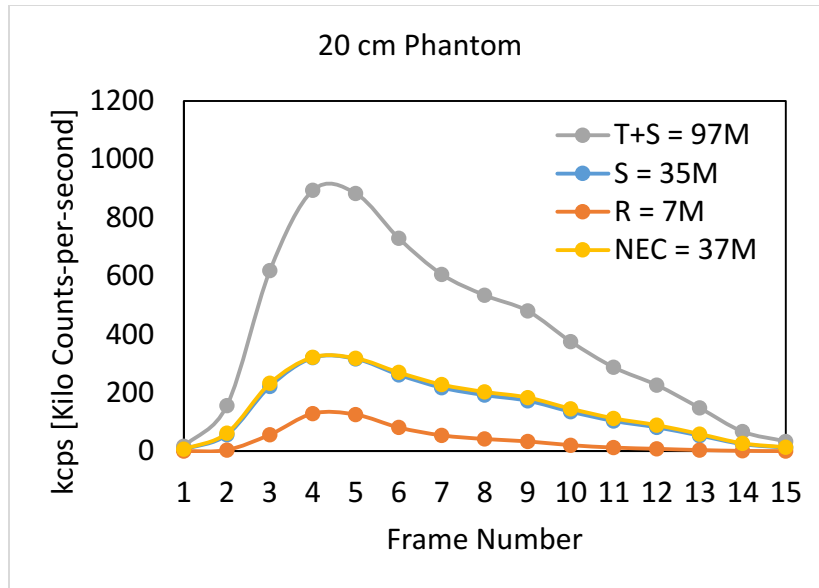


**Figure 4.4.1.1: Simulated count rates by frame for the 20 cm phantom.**

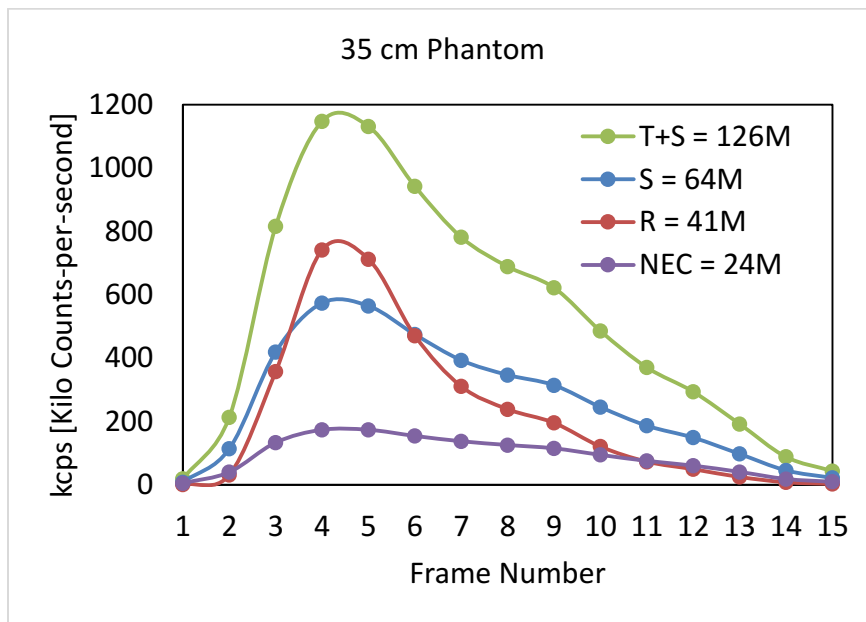


**Figure 4.4.1.2: Simulated count-rates by frame for the 35 cm phantom.**

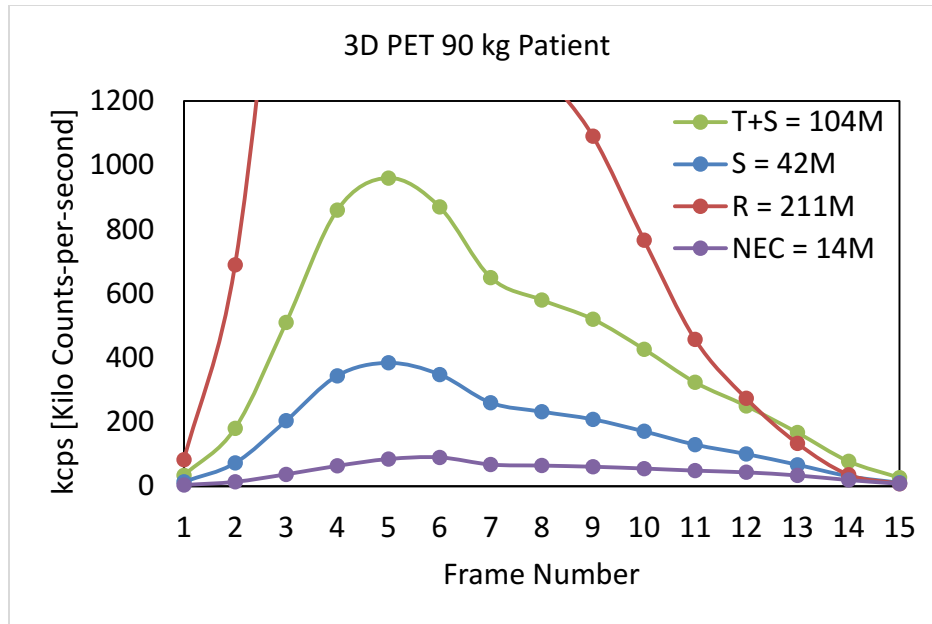


**Figure 4.4.1.3: Measured count-rates by frame for a 90 kg patient.**

#### 4.4.2 Motion Estimation

There was a clear positive bias and a decrease in precision in the estimated motion values for the 35 cm phantom vs the 20 cm phantom as seen in **Figure 4.3.1.1**. This was likely due to the consistency metric losing performance as noise increases. The largest motion estimation errors occurred in the mid- to late-time frames, which was beyond the peak of the blood curve (frames 5 or 6, i.e. 50-60 s from the scan start time) and errors remained high for all subsequent frames (**Figure 4.3.1.2**).

Using ROC analysis it was determined that a threshold value of 2.8 mm provided an optimum balance between sensitivity and specificity for the consistency metric; therefore, corrected values below this threshold might be ignored to improve performance – see **Figure 4.3.1.3**. The mean measured motion correction magnitude values are shown in **Table 4.3.1.1**. The bias for the 20 cm cases was significantly lower ( $P < 0.01$ ) than the

35 cm cases, and the precision for the 20 cm cases was higher than the 35 cm cases. This reflects the earlier finding that performance of the consistency metric for motion correction appears to be count-rate dependent; and that lower errors are observed for scans with higher count densities.

For both phantoms, comparisons of regional to global PVC from the reference standard (ideal) noiseless case to the noise-added case showed an increase in all segmental MBF bias values, except for the septal wall where the mean MBF segment values decreased – see **Table 4.3.1.2**. Deviations in the mean MBF segment values from the noiseless cases were larger for the 35 cm phantom than the 20 cm phantom, indicating greater variability due to noise. Deviations of MBF of the segments up to 20 % were observed for the no-motion reference standard scans. Since the location of the heart wall for these cases is known exactly and there is no motion, these errors are caused by the combination of simulation geometry, tracer kinetic modeling and noise effects. This is a confirmation of earlier work by Moody et al, which showed similar variations using a combination of clinical and Monte Carlo simulations.[198] Therefore, shifts < 1.6 mm which cause errors up to 20 % (see **Figure 4.3.2.1**) could be due to noise.

#### **4.4.3 Motion Effects on MBF**

For uncorrected data, the median MBF error for the 20 cm phantom was in the range of 5-7% for shifts  $\leq 3.1$  mm (**Figure 4.3.2.1**). Maximum errors as high as 150 % were observed for shifts of 6.3 mm. Higher errors were observed for the 35 cm phantom in general, but the 20 cm phantom had higher maximum errors for the largest motion shifts of 18.8 mm. This was likely due to the count-rate dependence on the precision of MBF estimation.

#### **4.4.4 Motion Correction**

Motion correction improved the median MBF error by a factor of 6 for both regional and global partial volume corrections for the high count-rate small phantom (20 cm). In addition, the maximum % MBF percent errors dropped by factors of 29 and 16 for regional and global partial volume correction respectively – see **Figure 4.3.2.3**. For the lower count-rate large phantom (35 cm) the median % MBF error improved by factors of 2.2 and 1.3 for regional and global partial-volume corrections respectively. Additionally, the maximum % MBF errors dropped by a factor of 27 for both regional and global partial volume corrections – see **Figure 4.3.2.3**. Largest % MBF errors occurred with the 20 cm phantom. This was likely caused by the fact that CTAC artifacts were more severe, since motion for smaller patients causes larger relative displacements from the attenuation map. This in turn had detrimental effects on the identification of the heart wall and the kinetic modeling, and ultimately the determination of MBF.

The larger drop in % MBF error for the 20 cm phantom is likely due the higher count rate statistics thus the estimation of motion is more accurately determined. This is a further indication that the utility of the consistency metric is dependent on the count rate statistics of the measurement. Previous work with a simple ellipsoid phantom using Poisson noise modeling showed no bias in the estimated parameters, but only a decrease in precision.[141]

#### **4.5 Study Limitations**

Limitations of this study are that only orthogonal motions were simulated, single motion events were simulated, the same TAC was applied to the LV and RV blood, only

normal blood flow was simulated, and effects from intra-frame motion (motion within a frame) was not considered. In addition, only two numerical phantoms were used, both had the same internal organ morphology although they were physically scaled differently and had appropriate clinically-relevant noise levels. Also, the simulated motion was rigid and thus did not consider non-linear effects from patient motion or rotations sometimes present in clinical cases. In addition, this study uses a noise model from an older PET scanner the GE Advance, results may be different for a more modern scanner. Considering motion correction performance degrades in frames with lower counts, potential improvements to this approach could include intra-frame or inter-frame noise reduction strategies (filtering, down-sampling, etc.). These improvements were beyond the scope of this work.

#### **4.6 Conclusion**

Motion correction using the projection consistency metric is a promising method for both early- (blood pool) and late-frame (tissue uptake) motion correction. Performance is dependent mainly on the count-rate statistics of the scan, and on the magnitude of motion. Further study is warranted to establish definitive clinical benefits with respect to other motion correction methods.

## 5 Chapter: Summary and Future work

The results from **chapter 3.3** clearly demonstrate the necessity for patient body motion correction. In noiseless simulations, MBF errors can approach 500 %, noisy simulations had similar results for the phantom with the same physical size, whereas the smaller phantom had double the maximum MBF errors (1000 %). Motion is also a common problem, with severe motion ( $> 7$  mm) occurring in 38 % of clinical scans. Left uncorrected, errors of this magnitude would likely lead to a misdiagnosis in a significant number of clinical cases. The noiseless study involved 5,760 data points with motion in 6 directions ( $\pm x$ ,  $y$  and  $z$ ), 2 magnitudes (9.4 and 18.8 mm), 4 shift times (36, 60, 120 and 240 s), 2 spatial resolutions (2 and 10 mm FWHM), as well as several other parameters (see **Table 3.2.2.1** for more details). Motion in the axial direction was the most common making up 45 % of all motion cases, and was predominantly in the superior (+Z) direction (30 %) with 15% in the inferior (-Z) direction. Anterior/posterior motion (Y) was almost entirely posterior (29%), whereas motion in the X direction had a similar proportion in the left (+X) and right (-X) directions and accounted for 24% of prevalence cases. Cases where the patient shifted to the right were the most detrimental to MBF, likely due to the severe CTAC artifacts in the myocardium, and that consistent identification of the myocardium and blood pool regions is critical for kinetic modelling. Even if CTAC artifacts are left uncorrected, perfect correction of motion for noiseless data resulted in a drop of MBF error from a maximum of 500 % to 50 % (10-fold improvement). Therefore, if possible, movement in the positive x direction should be restricted as much as possible, or corrected more stringently.

The results from **chapter 4.3** demonstrate the efficacy of motion correction using projection consistency conditions. Using realistic simulations, maximum MBF errors reached 1000 % for the physically smaller phantom (20 cm). The larger phantom (35 cm) was the same size as the noiseless phantom and thus had similar MBF errors. The noiseless study incorporated 56,160 data points over 6 directions ( $\pm x, y$  and  $z$ ), 6 magnitudes (0.8, 1.6, 3.1, 6.3, 9.4 and 18.8 mm), 6 shift times (90, 120, 150, 180, 240 and 360 s), 2 phantom sizes (20 and 35 cm), 5 noise realizations, as well as several other parameters (see **Table 4.2.3.1** for more details). The consistency metric can yield different values due to noise bias for the different realizations. For the 20 cm phantom the bias was 1 mm, whereas for the 35 cm phantom it was more than double at 2.5 mm. This was likely due to the dependence of the consistency metric on the count rate statistics. As such, the 20 cm phantom benefited more from motion correction with the maximum error dropping from 1000 % to 20 %, and the 35 cm phantom maximum MBF error dropped from 600 % to 80 %. The no-motion reference standard cases showed deviations from the known (noiseless) value on the order of 3-10 % and 10-20 % for the 20 and 35 cm phantoms respectively. For the small magnitude cases ( $<1.6$  mm) there was little effect on MBF error above the noise effects. This was true for both the 20 and 35 cm phantoms. Since the threshold value determined by the ROC analysis was 0.91 mm, the algorithm should be accurate enough to correct for all cases where the motion was above 0.91 mm. The consistency metric had the same accuracy for all 6 motion directions, however for the 35 cm phantom there was a clear positive bias for all motion magnitudes. This is another confirmation that the accuracy of the consistency conditions seems to rely on the count rate statistics of the PET acquisition.

Future research is warranted to characterize the algorithm's apparent ability to correct for patient motion at all time-frames, including in the early frames where even visual assessment is problematic. The effects of intra-frame motion were not studied, and prior to clinical use should be characterized. A phantom study may be warranted in this case due to the difficulty of determining how much intra-frame motion has occurred in clinical cases, where there is no gold-standard reference. Physical (capable of motion) or digital phantoms could be used for this purpose. The prevalence of rotational motion could also be studied, since there are indications that this results in severe artifacts as per McCord et al.[44] This could be done by combining external tracking with visual assessment in small patients, where the true count rates are higher. External tracking could be used to flag cases of interest where rotation is suspected. Rotation could be visually assessed on high count rate images by observing the frame-to-frame positions of the liver, heart wall and spleen. These evaluated cases could then be corrected using the consistency metric to evaluate its ability to correct rotational motion. In addition, the effect of rotational motion on MBF could be assessed using digital phantoms, with the severity of rotational motion informed by the prevalence data. Ultimately studies in a clinical population should be conducted. External tracking should be used to select patients without suspected motion, to be used as negative controls. For such cases, known motion could be artificially introduced and corrected using the consistency metric method, and/or evaluated on the no-motion cases. Since patient motion is known (or not present), any deviations from the known position will be errors generated by imperfect estimation of motion by the consistency metric.

Future patient motion-correction studies should demonstrate clinically that the bias and precision effects on MBF estimation are minimized relative to other sources of variability such as the physiological day-to-day changes in MBF or the test-retest measurement variability.

## Appendices

### Appendix A

**Table A- 1: Analysis of variance (ANOVA) for computer simulation parameters – Part 1**

Source	Sum Sq.	d.f.	Mean Sq.	F	Prob>F	Paper Fig.
Correction(None/CTAC/PET)	439570	2	219785	192	<0.001	
CTAC(Early/Late)	21194	1	21194	19	<0.001	
PVC(Global/Regional)	81783	1	81783	71	<0.001	
Resolution(High/Low)	65251	1	65251	57	<0.001	
Direction(X/Y/Z)	438551	2	219276	192	<0.001	
Magnitude(1/2 cm)	673005	1	673005	588	<0.001	
Sign(+/-)	9055	1	9055	7.9	0.0049	
Time(30/60/120/240)	612524	3	204175	178	<0.001	
Segment(ant/pos/sep/lat/apex)	29377	4	7344	6.4	<0.001	
Motion Correction(None/CTAC/PET)*CTAC(Early/Late)	21148	2	10574	9.2	0.0001	
Motion Correction(None/CTAC/PET)*PVC(Global/Regional)	38738	2	19369	17	<0.001	
Motion Correction(None/CTAC/PET)*Resolution(High/Low)	75104	2	37552	33	<0.001	
<b>Motion Correction(None/CTAC/PET)*Direction(X/Y/Z)</b>	<b>256016</b>	<b>4</b>	<b>64004</b>	<b>56</b>	<b>&lt;0.001</b>	<b>Fig 7</b>
Motion Correction(None/CTAC/PET)*Magnitude(1/2 cm)	201667	2	100833	88	<0.001	
Motion Correction(None/CTAC/PET)*Sign(+/-)	2003	2	1001	0.88	0.42	
Motion Correction(None/CTAC/PET)*Time(30/60/120/240)	287637	6	47940	42	<0.001	
Motion Correction(None/CTAC/PET)*Segment(ant/pos/sep/lat/apex)	21233	8	2654	2.3	0.018	
CTAC(Early/Late)*PVC(Global/Regional)	415	1	415	0.36	0.55	
CTAC(Early/Late)*Resolution(High/Low)	35	1	35	0.03	0.86	

**Table A- 2: Analysis of variance (ANOVA) for computer simulation parameters – Part 2**

Source	Sum Sq.	d.f.	Mean Sq.	F	Prob>F	Paper Fig.
CTAC(Early/Late)*Direction(X/Y/Z)	4391	2	2195	1.9	0.15	
CTAC(Early/Late)*Magnitude(1/2 cm)	2551	1	2551	2.2	0.14	
<b>CTAC(Early/Late)*Sign(+/-)</b>	<b>153878</b>	<b>1</b>	<b>153878</b>	<b>134</b>	<b>&lt;0.001</b>	<b>Fig. 6</b>
CTAC(Early/Late)*Time(30/60/120/240)	3930	3	1310	1.1	0.33	
CTAC(Early/Late)*Segment(ant/pos/sep/lat/apex)	12150	4	3037	2.7	0.031	
PVC(Global/Regional)*Resolution(High/Low)	2957	1	2957	2.6	0.11	
<b>PVC(Global/Regional)*Direction(X/Y/Z)</b>	<b>43053</b>	<b>2</b>	<b>21526</b>	<b>19</b>	<b>&lt;0.001</b>	<b>Fig. 9</b>
PVC(Global/Regional)*Magnitude(1/2 cm)	9412	1	9412	8.2	0.0041	
PVC(Global/Regional)*Sign(+/-)	2	1	2	0	0.97	
PVC(Global/Regional)*Time(30/60/120/240)	41480	3	13827	12	<0.001	
PVC(Global/Regional)*Segment(ant/pos/sep/lat/apex)	36190	4	9047	7.9	<0.001	
Resolution(High/Low)*Direction(X/Y/Z)	102726	2	51363	45	<0.001	
Resolution(High/Low)*Magnitude(1/2 cm)	97997	1	97997	86	<0.001	
Resolution(High/Low)*Sign(+/-)	6495	1	6495	5.7	0.017	
Resolution(High/Low)*Time(30/60/120/240)	69048	3	23016	20	<0.001	
Resolution(High/Low)*Segment(ant/pos/sep/lat/apex)	7004	4	1751	1.5	0.19	
Direction(X/Y/Z)*Magnitude(1/2 cm)	279428	2	139714	122	<0.001	
Direction(X/Y/Z)*Sign(+/-)	6164	2	3082	2.7	0.068	
<b>Direction(X/Y/Z)*Time(30/60/120/240)</b>	<b>277570</b>	<b>6</b>	<b>46262</b>	<b>40</b>	<b>&lt;0.001</b>	<b>Fig. 8</b>
Direction(X/Y/Z)*Segment(ant/pos/sep/lat/apex)	232891	8	29111	25	<0.001	
Magnitude(1/2 cm)*Sign(+/-)	9281	1	9281	8.1	0.0044	

**Table A- 3: Analysis of variance (ANOVA) for computer simulation parameters – Part 3**

Source	Sum Sq.	d.f.	Mean Sq.	F	Prob>F	Paper Fig.
Magnitude(1/2 cm)*Time(30/60/120/240)	231718	3	77239	67.5	<0.001	
Magnitude(1/2 cm)*Segment(ant/pos/sep/lat/apex)	22875	4	5719	5	0.0005	
Sign(+/-)*Time(30/60/120/240)	18574	3	6191	5.4	0.001	
Sign(+/-)*Segment(ant/pos/sep/lat/apex)	975	4	244	0.21	0.93	
Time(30/60/120/240)*Segment(ant/pos/sep/lat/apex)	28192	12	2349	2.1	0.017	
Motion Correction(None/CTAC/PET)*CTAC(Early/Late)*PVC(Global/Regional)	1702	2	851	0.74	0.48	
Motion Correction(None/CTAC/PET)*CTAC(Early/Late)*Resolution(High/Low)	8627	2	4314	3.8	0.023	
Motion Correction(None/CTAC/PET)*CTAC(Early/Late)*Direction(X/Y/Z)	7104	4	1776	1.6	0.18	
Motion Correction(None/CTAC/PET)*CTAC(Early/Late)*Magnitude(1/2 cm)	6148	2	3074	2.7	0.068	
Motion Correction(None/CTAC/PET)*CTAC(Early/Late)*Sign(+/-)	119126	2	59563	52	<0.001	
Motion Correction(None/CTAC/PET)*CTAC(Early/Late)*Time(30/60/120/240)	26336	6	4389	3.8	0.0008	
Motion Correction(None/CTAC/PET)*CTAC(Early/Late)*Segment(ant/pos/sep/lat/apex)	5985	8	748	0.65	0.73	
Motion Correction(None/CTAC/PET)*PVC(Global/Regional)*Resolution(High/Low)	1815	2	908	0.79	0.45	
Motion Correction(None/CTAC/PET)*PVC(Global/Regional)*Direction(X/Y/Z)	20491	4	5123	4.5	0.0013	
Motion Correction(None/CTAC/PET)*PVC(Global/Regional)*Magnitude(1/2 cm)	5153	2	2576	2.3	0.11	
Motion Correction(None/CTAC/PET)*PVC(Global/Regional)*Sign(+/-)	53	2	26	0.02	0.98	
Motion Correction(None/CTAC/PET)*PVC(Global/Regional)*Time(30/60/120/240)	21868	6	3645	3.2	0.004	
Motion Correction(None/CTAC/PET)*PVC(Global/Regional)*Segment(ant/pos/sep/lat/apex)	27212	8	3401	3	0.0025	

**Table A- 4: Analysis of variance (ANOVA) for computer simulation parameters – Part 4**

Source	Sum Sq.	d.f.	Mean Sq.	F	Prob>F	Paper Fig.
Motion Correction(None/CTAC/PET)*Resolution(High/Low)*Direction(X/Y/Z)	51888	4	12972	11	<0.001	
Motion Correction(None/CTAC/PET)*Resolution(High/Low)*Magnitude(1/2 cm)	28745	2	14373	13	<0.001	
Motion Correction(None/CTAC/PET)*Resolution(High/Low)*Sign(+/-)	4210	2	2105	1.8	0.16	
Motion Correction(None/CTAC/PET)*Resolution(High/Low)*Time(30/60/120/240)	30668	6	5111	4.5	0.0002	
Motion Correction(None/CTAC/PET)*Resolution(High/Low)*Segment(ant/pos/sep/lat/apex)	1805	8	226	0.2	0.99	
<b>Motion Correction(None/CTAC/PET)*Direction(X/Y/Z)*Magnitude(1/2 cm)</b>	<b>158168</b>	<b>4</b>	<b>39542</b>	<b>35</b>	<b>&lt;0.001</b>	<b>Fig. 7</b>
Motion Correction(None/CTAC/PET)*Direction(X/Y/Z)*Sign(+/-)	8689	4	2172	1.9	0.11	
Motion Correction(None/CTAC/PET)*Direction(X/Y/Z)*Time(30/60/120/240)	150124	12	12510	10.9	<0.001	
Motion Correction(None/CTAC/PET)*Direction(X/Y/Z)*Segment(ant/pos/sep/lat/apex)	79215	16	4951	4.3	<0.001	
Motion Correction(None/CTAC/PET)*Magnitude(1/2 cm)*Sign(+/-)	4432	2	2216	1.9	0.14	
Motion Correction(None/CTAC/PET)*Magnitude(1/2 cm)*Time(30/60/120/240)	117787	6	19631	17	<0.001	
Motion Correction(None/CTAC/PET)*Magnitude(1/2 cm)*Segment(ant/pos/sep/lat/apex)	10822	8	1353	1.2	0.31	
Motion Correction(None/CTAC/PET)*Sign(+/-)*Time(30/60/120/240)	10736	6	1789	1.6	0.15	
Motion Correction(None/CTAC/PET)*Sign(+/-)*Segment(ant/pos/sep/lat/apex)	6822	8	853	0.75	0.65	
Motion Correction(None/CTAC/PET)*Time(30/60/120/240)*Segment(ant/pos/sep/lat/apex)	21948	24	915	0.8	0.74	
CTAC(Early/Late)*PVC(Global/Regional)*Resolution(High/Low)	29	1	29	0.03	0.87	
CTAC(Early/Late)*PVC(Global/Regional)*Direction(X/Y/Z)	1200	2	600	0.52	0.59	
CTAC(Early/Late)*PVC(Global/Regional)*Magnitude(1/2 cm)	148	1	148	0.13	0.72	

**Table A- 5: Analysis of variance (ANOVA) for computer simulation parameters – Part 5**

Source	Sum Sq.	d.f.	Mean Sq.	F	Prob>F	Paper Fig.
CTAC(Early/Late)*PVC(Global/Regional)*Sign(+/-)	19893	1	19893	17.4	<0.001	
CTAC(Early/Late)*PVC(Global/Regional)*Time(30/60/120/240)	873	3	291	0.25	0.86	
CTAC(Early/Late)*PVC(Global/Regional)*Segment(ant/pos/sep/lat/apex)	818	4	205	0.18	0.95	
CTAC(Early/Late)*Resolution(High/Low)*Direction(X/Y/Z)	12896	2	6448	5.6	0.0036	
CTAC(Early/Late)*Resolution(High/Low)*Magnitude(1/2 cm)	2685	1	2685	2.4	0.13	
CTAC(Early/Late)*Resolution(High/Low)*Sign(+/-)	58041	1	58041	51	<0.001	
CTAC(Early/Late)*Resolution(High/Low)*Time(30/60/120/240)	13566	3	4522	4	0.0079	
CTAC(Early/Late)*Resolution(High/Low)*Segment(ant/pos/sep/lat/apex)	841	4	210	0.18	0.95	
CTAC(Early/Late)*Direction(X/Y/Z)*Magnitude(1/2 cm)	6046	2	3023	2.6	0.071	
<b>CTAC(Early/Late)*Direction(X/Y/Z)*Sign(+/-)</b>	<b>568058</b>	<b>2</b>	<b>284029</b>	<b>248</b>	<b>&lt;0.001</b>	<b>Fig. 6</b>
CTAC(Early/Late)*Direction(X/Y/Z)*Time(30/60/120/240)	31483	6	5247	4.6	0.0001	
CTAC(Early/Late)*Direction(X/Y/Z)*Segment(ant/pos/sep/lat/apex)	18872	8	2359	2.1	0.036	
<b>CTAC(Early/Late)*Magnitude(1/2 cm)*Sign(+/-)</b>	<b>133454</b>	<b>1</b>	<b>133454</b>	<b>117</b>	<b>&lt;0.001</b>	<b>Fig. 6</b>
CTAC(Early/Late)*Magnitude(1/2 cm)*Time(30/60/120/240)	9906	3	3302	2.9	0.034	
CTAC(Early/Late)*Magnitude(1/2 cm)*Segment(ant/pos/sep/lat/apex)	4105	4	1026	0.9	0.46	
CTAC(Early/Late)*Sign(+/-)*Time(30/60/120/240)	132939	3	44313	39	<0.001	
CTAC(Early/Late)*Sign(+/-)*Segment(ant/pos/sep/lat/apex)	43161	4	10790	9.4	<0.001	
CTAC(Early/Late)*Time(30/60/120/240)*Segment(ant/pos/sep/lat/apex)	743	12	62	0.05	1	

**Table A- 6: Analysis of variance (ANOVA) for computer simulation parameters – Part 6**

Source	Sum Sq.	d.f.	Mean Sq.	F	Prob>F	Paper Fig.
PVC(Global/Regional)*Resolution(High/Low)*Direction(X/Y/Z)	2754	2	1377	1.2	0.3	
PVC(Global/Regional)*Resolution(High/Low)*Magnitude(1/2 cm)	2	1	2	0	0.97	
PVC(Global/Regional)*Resolution(High/Low)*Sign(+/-)	2	1	2	0	0.97	
PVC(Global/Regional)*Resolution(High/Low)*Time(30/60/120/240)	3664	3	1221	1.1	0.36	
PVC(Global/Regional)*Resolution(High/Low)*Segment(ant/pos/sep/lat/apex)	18787	4	4697	4.1	0.0025	
PVC(Global/Regional)*Direction(X/Y/Z)*Magnitude(1/2 cm)	17951	2	8975	7.8	0.0004	
PVC(Global/Regional)*Direction(X/Y/Z)*Sign(+/-)	1275	2	637	0.56	0.57	
PVC(Global/Regional)*Direction(X/Y/Z)*Time(30/60/120/240)	29630	6	4938	4.3	0.0002	
<b>PVC(Global/Regional)*Direction(X/Y/Z)*Segment(ant/pos/sep/lat/apex)</b>	<b>185418</b>	<b>8</b>	<b>23177</b>	<b>20</b>	<b>&lt;0.001</b>	<b>Fig. 9</b>
PVC(Global/Regional)*Magnitude(1/2 cm)*Sign(+/-)	11	1	11	0.01	0.92	
PVC(Global/Regional)*Magnitude(1/2 cm)*Time(30/60/120/240)	2771	3	924	0.81	0.49	
PVC(Global/Regional)*Magnitude(1/2 cm)*Segment(ant/pos/sep/lat/apex)	35659	4	8915	7.8	<0.001	
PVC(Global/Regional)*Sign(+/-)*Time(30/60/120/240)	428	3	143	0.12	0.95	
PVC(Global/Regional)*Sign(+/-)*Segment(ant/pos/sep/lat/apex)	2016	4	504	0.44	0.78	
PVC(Global/Regional)*Time(30/60/120/240)*Segment(ant/pos/sep/lat/apex)	44699	12	3725	3.3	0.0001	
Resolution(High/Low)*Direction(X/Y/Z)*Magnitude(1/2 cm)	89731	2	44865	39	<0.001	
Resolution(High/Low)*Direction(X/Y/Z)*Sign(+/-)	12106	2	6053	5.3	0.0051	
Resolution(High/Low)*Direction(X/Y/Z)*Time(30/60/120/240)	35075	6	5846	5.1	<0.001	

**Table A- 7: Analysis of variance (ANOVA) for computer simulation parameters – Part 7**

Source	Sum Sq.	d.f.	Mean Sq.	F	Prob>F	Paper Fig.
Resolution(High/Low)*Direction(X/Y/Z)*Segment(ant/pos/sep/lat/apex)	6854	8	857	0.75	0.65	
Resolution(High/Low)*Magnitude(1/2 cm)*Sign(+/-)	7982	1	7982	7	0.0083	
Resolution(High/Low)*Magnitude(1/2 cm)*Time(30/60/120/240)	19548	3	6516	5.7	0.0007	
Resolution(High/Low)*Magnitude(1/2 cm)*Segment(ant/pos/sep/lat/apex)	1478	4	369	0.32	0.86	
Resolution(High/Low)*Sign(+/-)*Time(30/60/120/240)	16838	3	5613	4.9	0.0021	
Resolution(High/Low)*Sign(+/-)*Segment(ant/pos/sep/lat/apex)	2294	4	574	0.5	0.73	
Resolution(High/Low)*Time(30/60/120/240)*Segment(ant/pos/sep/lat/apex)	4281	12	357	0.31	0.99	
Direction(X/Y/Z)*Magnitude(1/2 cm)*Sign(+/-)	7416	2	3708	3.2	0.039	
<b>Direction(X/Y/Z)*Magnitude(1/2 cm)*Time(30/60/120/240)</b>	<b>148086</b>	<b>6</b>	<b>24681</b>	<b>22</b>	<b>&lt;0.001</b>	<b>Fig. 8</b>
Direction(X/Y/Z)*Magnitude(1/2 cm)*Segment(ant/pos/sep/lat/apex)	39777	8	4972	4.4	<0.001	
Direction(X/Y/Z)*Sign(+/-)*Time(30/60/120/240)	22735	6	3789	3.3	0.003	
Direction(X/Y/Z)*Sign(+/-)*Segment(ant/pos/sep/lat/apex)	6758	8	845	0.74	0.66	
Direction(X/Y/Z)*Time(30/60/120/240)*Segment(ant/pos/sep/lat/apex)	78647	24	3277	2.9	<0.001	
Magnitude(1/2 cm)*Sign(+/-)*Time(30/60/120/240)	22029	3	7343	6.4	0.0002	
Magnitude(1/2 cm)*Sign(+/-)*Segment(ant/pos/sep/lat/apex)	1590	4	398	0.35	0.85	
Magnitude(1/2 cm)*Time(30/60/120/240)*Segment(ant/pos/sep/lat/apex)	14343	12	1195	1	0.4	
Sign(+/-)*Time(30/60/120/240)*Segment(ant/pos/sep/lat/apex)	2127	12	177	0.15	1	
Error	5971109	5218	1144			
Total	13828536	5759				

## Appendix B

**Table B- 1: Patient Demographics – Part 1**

#	Age	Gender	#	Age	Gender	#	Age	Gender	#	Age	Gender	#	Age	Gender	#	Age	Gender
1	58	Female	41	67	Male	81	56	Female	121	60	Female	161	72	Female	201	75	Male
2	72	Female	42	62	Male	82	72	Female	122	75	Male	162	83	Female	202	58	Female
3	55	Female	43	58	Female	83	81	Male	123	51	Male	163	52	Female	203	33	Female
4	49	Male	44	59	Female	84	61	Male	124	71	Female	164	49	Male	204	45	Male
5	72	Male	45	62	Male	85	59	Male	125	69	Male	165	63	Male	205	42	Female
6	73	Male	46	56	Male	86	65	Female	126	68	Male	166	65	Male	206	65	Male
7	64	Male	47	60	Female	87	73	Female	127	71	Male	167	53	Female	207	68	Female
8	49	Male	48	72	Female	88	63	Male	128	74	Male	168	47	Male	208	79	Male
9	78	Female	49	49	Male	89	73	Female	129	68	Female	169	55	Female	209	87	Male
10	51	Male	50	62	Female	90	61	Female	130	60	Male	170	69	Male	210	54	Female
11	53	Female	51	68	Female	91	46	Male	131	62	Female	171	58	Female	211	68	Female
12	74	Male	52	73	Female	92	73	Male	132	73	Female	172	67	Female	212	55	Male
13	57	Male	53	72	Male	93	70	Female	133	57	Female	173	57	Male	213	51	Female
14	57	Male	54	59	Female	94	86	Female	134	70	Male	174	69	Male	214	75	Female
15	81	Male	55	58	Female	95	57	Female	135	73	Male	175	88	Female	215	73	Male
16	67	Male	56	80	Male	96	75	Male	136	89	Male	176	78	Female	216	50	Male
17	61	Female	57	38	Female	97	76	Female	137	66	Male	177	68	Female	217	58	Male
18	61	Male	58	76	Male	98	52	Female	138	61	Female	178	73	Female	218	64	Female
19	65	Female	59	67	Female	99	58	Female	139	61	Male	179	57	Male	219	72	Male
20	68	Female	60	83	Male	100	49	Female	140	60	Male	180	52	Female	220	50	Female
21	64	Male	61	45	Male	101	76	Female	141	81	Female	181	82	Male	221	69	Female

**Table B- 2: Patient Demographics – Part 2**

#	Age	Gender	#	Age	Gender	#	Age	Gender	#	Age	Gender	#	Age	Gender	#	Age	Gender
22	67	Female	62	70	Male	102	68	Male	142	57	Male	182	64	Female	222	88	Female
23	60	Female	63	72	Male	103	59	Female	143	56	Female	183	60	Male	223	42	Male
24	64	Male	64	82	Female	104	65	Female	144	83	Male	184	69	Male	224	63	Female
25	67	Male	65	61	Female	105	67	Male	145	63	Male	185	67	Male	225	68	Male
26	69	Male	66	55	Female	106	61	Male	146	74	Female	186	73	Male	226	63	Female
27	53	Male	67	50	Male	107	79	Male	147	62	Male	187	35	Female	227	47	Female
28	68	Male	68	64	Male	108	73	Female	148	88	Female	188	59	Female	228	49	Female
29	56	Female	69	75	Male	109	86	Female	149	35	Female	189	46	Male	229	80	Male
30	69	Female	70	50	Male	110	56	Female	150	46	Male	190	55	Male	230	62	Female
31	74	Female	71	59	Female	111	55	Male	151	53	Male	191	70	Male	231	73	Male
32	71	Male	72	48	Male	112	77	Male	152	69	Female	192	38	Male	232	81	Female
33	55	Female	73	44	Male	113	71	Female	153	70	Male	193	49	Male	233	41	Male
34	51	Female	74	69	Male	114	66	Female	154	67	Female	194	78	Female	234	69	Female
35	51	Male	75	59	Male	115	63	Female	155	52	Female	195	70	Male	235	65	Male
36	78	Female	76	68	Female	116	79	Male	156	66	Male	196	65	Female	236	65	Male
37	79	Male	77	54	Female	117	40	Male	157	59	Male	197	74	Female			
38	61	Female	78	72	Female	118	65	Male	158	57	Male	198	69	Female			
39	74	Female	79	60	Male	119	75	Female	159	38	Male	199	50	Male			
40	50	Female	80	34	Female	120	63	Male	160	62	Female	200	63	Female			

## Bibliography or References

1. Cuocolo A, Acampa W, Imbriaco M, De Luca N, Iovino GL, Salvatore M. The many ways to myocardial perfusion imaging. *Q. J. Nucl. Med. Mol. Imaging Off. Publ. Ital. Assoc. Nucl. Med. AIMN Int. Assoc. Radiopharmacol. IAR Sect. Soc. Radiopharm. Chem. Biol.* 2005;49:4–18.
2. Ballinger JR. Short- and long-term responses to molybdenum-99 shortages in nuclear medicine. *Br. J. Radiol.* 2010;83:899.
3. Renaud J, Mylonas I, Yip K, Turcotte E, Pibarot P, Maguire C, et al. Low-dose 3D PET rubidium ARMI (Alternative Radiopharmaceutical for Myocardial Imaging) multicentre trial standards and quality assurance. *J. Nucl. Med.* 2012;53:1805–1805.
4. Chatal J-F, Rouzet F, Haddad F, Bourdeau C, Mathieu C, Guludec DL. Story of Rubidium-82 and Advantages for Myocardial Perfusion PET Imaging. *Front. Med. [Internet].* 2015 [cited 2016 Aug 8];2. Available from: <http://www.ncbi.nlm.nih.gov/pmc/articles/PMC4566054/>
5. Ghotbi AA, Kjaer A, Hasbak P. Review: comparison of PET rubidium-82 with conventional SPECT myocardial perfusion imaging. *Clin. Physiol. Funct. Imaging.* 2014;34:163–70.
6. Ringer S. An investigation regarding the action of rubidium and cesium salts compared with the action of potassium salts on the ventricle of the frog's heart. *J. Physiol.* 1883;4:370–86.
7. Malley M. The discovery of atomic transmutation: Scientific styles and philosophies in France and Britain. *Isis Publ. Ltd.* 1979;70:213–23.
8. Greenberg DM, Joseph M, Cohn WE, Tufts EV. STUDIES IN THE POTASSIUM METABOLISM OF THE ANIMAL BODY BY MEANS OF ITS ARTIFICIAL RADIOACTIVE ISOTOPE. *Science.* 1938;87:438–438.
9. Noonan TR, Fenn WO, Haege L. THE DISTRIBUTION OF INJECTED RADIOACTIVE POTASSIUM IN RATS. *Am. J. Physiol. -- Leg. Content.* 1941;132:474–88.
10. Fenn WO, Noonan TR, Mullins LJ, Haege L. THE EXCHANGE OF RADIOACTIVE POTASSIUM WITH BODY POTASSIUM. *Am. J. Physiol. -- Leg. Content.* 1941;135:149–63.
11. Noonan TR, Fenn WO, Haege L. THE EFFECTS OF DENERVATION AND OF STIMULATION ON EXCHANGE OF RADIOACTIVE POTASSIUM IN MUSCLE. *Am. J. Physiol. -- Leg. Content.* 1941;132:612–21.
12. Love WD, Romney RB, Burch GE. A Comparison of the Distribution of Potassium and Exchangeable Rubidium in the Organs of the Dog, Using Rubidium<sup>86</sup>. *Circ. Res.* 1954;2:112–22.
13. Relman AS. The Physiological Behavior of Rubidium and Cesium in Relation to That of Potassium. *Yale J. Biol. Med.* 1956;29:248–62.
14. Kilpatrick R, Renschler HE, Munro DS, Wilson GM. A comparison of the distribution of <sup>42</sup>K and <sup>86</sup>Rb in rabbit and man. *J. Physiol.* 1956;133:194.

15. Love WD, Burch GE. Estimation of the rates of uptake of Rb86 by the heart, liver and skeletal muscle of man with and without cardiac disease. *Int. J. Appl. Radiat. Isot.* 1958;3:207–16.
16. Wells LA. Permeability of the blood-brain barrier system to rubidium in euthermia, hibernation and hypothermia. *Comp. Biochem. Physiol. A Physiol.* 1972;42:551–7.
17. Brooks DJ, Beaney RP, Lammertsma AA, Leenders KL, Horlock PL, Kensett MJ, et al. Quantitative measurement of blood-brain barrier permeability using rubidium-82 and positron emission tomography. *J. Cereb. Blood Flow Metab. Off. J. Int. Soc. Cereb. Blood Flow Metab.* 1984;4:535–45.
18. Wrenn FR, Good ML, Handler P. The use of positron-emitting radioisotopes for the localization of brain tumors. *Science.* 1951;113:525–7.
19. Brownell GL. A history of positron imaging [Internet]. Massachusetts General Hospital; 1999 [cited 2016 Aug 3]. Available from: <http://www.petdiagnostik.ch/de/informationen-fuer-fachpersonen/a-history-of-positron-imaging/>
20. Hounsfield GN. Computerized transverse axial scanning (tomography). 1. Description of system. *Br. J. Radiol.* 1973;46:1016–22.
21. Ambrose J. Computerized transverse axial scanning (tomography). 2. Clinical application. *Br. J. Radiol.* 1973;46:1023–47.
22. Chesler DA. Three-dimensional activity distribution from multiple positron scintigraphs. *J. Nucl. Med.* 1971;12:347–8.
23. Robertson JS, Marr RB, Rpsenblum M, Radeka V, Yamamoto YL, Rosenblum M. 32 Crystal positron transverse section detector [Internet]. Brookhaven National Laboratory: Brookhaven National Laboratory; 1983 Jan. Report No.: BNL-17237. Available from: <https://www.scienceopen.com/document?vid=5e7f3a61-8c19-4fc9-91c8-245068217973>
24. Fill H, Buchin M, Harper PV, Muehlllehner G, Walsh W, Resnekov L, et al. Comparison of positron tomography and scintigraphy with <sup>201</sup>Tl for delineation of the myocardium. *Radioact. Isot. Clin. Res.* [Internet]. 1976 [cited 2016 Aug 7];12. Available from: [http://inis.iaea.org/Search/search.aspx?orig\\_q=RN:8299024](http://inis.iaea.org/Search/search.aspx?orig_q=RN:8299024)
25. Budinger TF, Yano Y, Derenzo SE, Huesman RH, Yen C-K, Moyer BR, et al. Infarction sizing and myocardial perfusion measurements using rubidium-82 and positron emission tomography. *Am. J. Cardiol.* 1980;45:399.
26. Selwyn AP, Allan RM, L'Abbate A, Horlock P, Camici P, Clark J, et al. Relation between regional myocardial uptake of rubidium-82 and perfusion: absolute reduction of cation uptake in ischemia. *Am. J. Cardiol.* 1982;50:112–21.
27. Goldstein RA, Mullani NA, Marani SK, Fisher DJ, Gould KL, O'Brien HA. Myocardial perfusion with rubidium-82. II. Effects of metabolic and pharmacologic interventions. *J. Nucl. Med. Off. Publ. Soc. Nucl. Med.* 1983;24:907–15.

28. Goldstein RA, Mullani NA, Wong WH, Hartz RK, Hicks CH, Fuentes F, et al. Positron imaging of myocardial infarction with rubidium-82. *J. Nucl. Med. Off. Publ. Soc. Nucl. Med.* 1986;27:1824–9.
29. Stewart RE, Schwaiger M, Molina E, Popma J, Gacioch GM, Kalus M, et al. Comparison of rubidium-82 positron emission tomography and thallium-201 SPECT imaging for detection of coronary artery disease. *Am. J. Cardiol.* 1991;67:1303–10.
30. Yano Y. Essentials of a rubidium-82 generator for nuclear medicine. *Int. J. Rad. Appl. Instrum. [A]*. 1987;38:205–11.
31. Kinahan PE, Townsend DW, Beyer T, Sashin D. Attenuation correction for a combined 3D PET/CT scanner. *Med. Phys.* 1998;25:2046–53.
32. Kinahan PE, Hasegawa BH, Beyer T. X-ray-based attenuation correction for positron emission tomography/computed tomography scanners. *Semin. Nucl. Med.* 2003;33:166–79.
33. Demer LL, Gould KL, Goldstein RA, Kirkeeide RL. Noninvasive assessment of coronary collaterals in man by PET perfusion imaging. *J. Nucl. Med. Off. Publ. Soc. Nucl. Med.* 1990;31:259–70.
34. Garza D, Tosh AV, Roberti R, Dalal P, Reimers C, Ongseng F, et al. Detection of coronary collaterals using dipyridamole PET myocardial perfusion imaging with rubidium-82. *J. Nucl. Med. Off. Publ. Soc. Nucl. Med.* 1997;38:39–43.
35. Sdringola S, Patel D, Gould KL. High prevalence of myocardial perfusion abnormalities on positron emission tomography in asymptomatic persons with a parent or sibling with coronary artery disease. *Circulation.* 2001;103:496–501.
36. Bateman TM, Heller GV, McGhie AI, Friedman JD, Case JA, Bryngelson JR, et al. Diagnostic accuracy of rest/stress ECG-gated Rb-82 myocardial perfusion PET: comparison with ECG-gated Tc-99m sestamibi SPECT. *J. Nucl. Cardiol. Off. Publ. Am. Soc. Nucl. Cardiol.* 2006;13:24–33.
37. Mc Ardle BA, Dowsley TF, deKemp RA, Wells GA, Beanlands RS. Does rubidium-82 PET have superior accuracy to SPECT perfusion imaging for the diagnosis of obstructive coronary disease?: A systematic review and meta-analysis. *J. Am. Coll. Cardiol.* 2012;60:1828–37.
38. Christensen NL, Hammer BE, Heil BG, Fetterly K. Positron emission tomography within a magnetic field using photomultiplier tubes and lightguides. *Phys. Med. Biol.* 1995;40:691–7.
39. Shao Y, Cherry SR, Farahani K, Meadors K, Siegel S, Silverman RW, et al. Simultaneous PET and MR imaging. *Phys. Med. Biol.* 1997;42:1965–70.
40. Pichler BJ, Kolb A, Nägele T, Schlemmer H-P. PET/MRI: paving the way for the next generation of clinical multimodality imaging applications. *J. Nucl. Med. Off. Publ. Soc. Nucl. Med.* 2010;51:333–6.
41. Zaidi H, Ojha N, Morich M, Griesmer J, Hu Z, Maniawski P, et al. Design and performance evaluation of a whole-body Ingenuity TF PET-MRI system. *Phys. Med. Biol.* 2011;56:3091–106.

42. Vandenberghe S, Marsden PK. PET-MRI: a review of challenges and solutions in the development of integrated multimodality imaging. *Phys. Med. Biol.* 2015;60:R115.
43. Ostertag H, Kübler WK, Doll J, Lorenz WJ. Measured attenuation correction methods. *Eur. J. Nucl. Med.* 15:722–6.
44. McCord ME, Bacharach SL, Bonow RO, Dilsizian V, Cuocolo A, Freedman N. Misalignment between PET transmission and emission scans: its effect on myocardial imaging. *J. Nucl. Med. Off. Publ. Soc. Nucl. Med.* 1992;33:1209-1214-1215.
45. Loghin C, Sdringola S, Gould KL. Common artifacts in PET myocardial perfusion images due to attenuation-emission misregistration: clinical significance, causes, and solutions. *J. Nucl. Med. Off. Publ. Soc. Nucl. Med.* 2004;45:1029–39.
46. Gould KL, Pan T, Loghin C, Johnson NP, Guha A, Sdringola S. Frequent diagnostic errors in cardiac PET/CT due to misregistration of CT attenuation and emission PET images: a definitive analysis of causes, consequences, and corrections. *J. Nucl. Med. Off. Publ. Soc. Nucl. Med.* 2007;48:1112–21.
47. Burrell S, MacDonald A. Artifacts and pitfalls in myocardial perfusion imaging. *J. Nucl. Med. Technol.* 2006;34:193-211-214.
48. Green MV, Seidel J, Stein SD, Tedder TE, Kempner KM, Kertzman C, et al. Head movement in normal subjects during simulated PET brain imaging with and without head restraint. *J. Nucl. Med. Off. Publ. Soc. Nucl. Med.* 1994;35:1538–46.
49. Ruttimann UE, Andreason PJ, Rio D. Head motion during positron emission tomography: is it significant? *Psychiatry Res.* 1995;61:43–51.
50. Picard Y, Thompson CJ. Digitized video subject positioning and surveillance system for PET. *IEEE Trans. Nucl. Sci.* 1995;42:1024–9.
51. Picard Y, Thompson CJ. Motion correction of PET images using multiple acquisition frames. *IEEE Trans. Med. Imaging.* 1997;16:137–44.
52. Goldstein SR, Daube-Witherspoon ME, Green MV, Eidsath A. A head motion measurement system suitable for emission computed tomography. *IEEE Trans. Med. Imaging.* 1997;16:17–27.
53. Rahmim A, Rousset O, Zaidi H. Strategies for Motion Tracking and Correction in PET. *PET Clin.* 2007;2:251–66.
54. Lopresti BJ, Russo A, Jones WF, Fisher T, Crouch DG, Altenburger DE, et al. Implementation and performance of an optical motion tracking system for high resolution brain PET imaging. *IEEE Trans. Nucl. Sci.* 1999;46:2059–67.
55. Nehmeh SA, Erdi YE, Rosenzweig KE, Schoder H, Larson SM, Squire OD, et al. Reduction of respiratory motion artifacts in PET imaging of lung cancer by respiratory correlated dynamic PET: methodology and comparison with respiratory gated PET. *J. Nucl. Med. Off. Publ. Soc. Nucl. Med.* 2003;44:1644–8.

56. Naum A, Laaksonen MS, Tuunanen H, Oikonen V, Teräs M, Kemppainen J, et al. Motion detection and correction for dynamic ( <sup>15</sup>O)-water myocardial perfusion PET studies. *Eur. J. Nucl. Med. Mol. Imaging.* 2005;32:1378–83.
57. Kyme AZ, Zhou VW, Meikle SR, Fulton RR. Real-time 3D motion tracking for small animal brain PET. *Phys. Med. Biol.* 2008;53:2651–66.
58. Kyme AZ, Zhou VW, Meikle SR, Baldock C, Fulton RR. Optimised Motion Tracking for Positron Emission Tomography Studies of Brain Function in Awake Rats. *PLOS ONE.* 2011;6:e21727.
59. Noonan PJ, Howard J, Cootes TF, Hallett WA, Hinz R. Realtime markerless rigid body head motion tracking using the Microsoft Kinect. 2012 IEEE Nucl. Sci. Symp. Med. Imaging Conf. NSSMIC. 2012. p. 2241–6.
60. Koshino K, Watabe H, Enmi J, Hirano Y, Zeniya T, Hasegawa S, et al. Effects of patient movement on measurements of myocardial blood flow and viability in resting <sup>15</sup>O-water PET studies. *J. Nucl. Cardiol. Off. Publ. Am. Soc. Nucl. Cardiol.* 2012;19:524–33.
61. Liu C, Alessio AM, Kinahan PE. Respiratory motion correction for quantitative PET/CT using all detected events with internal-external motion correlation. *Med. Phys.* 2011;38:2715–23.
62. Alessio AM, Kinahan PE, Champley KM, Caldwell JH. Attenuation-emission alignment in cardiac PET/CT based on consistency conditions. *Med. Phys.* 2010;37:1191–200.
63. Chamberland M, deKemp R, Xu T. List-mode motion tracking for positron emission tomography imaging using low-activity fiducial markers. *IEEE; 2014 [cited 2017 Jan 16].* p. 1–3. Available from: <http://ieeexplore.ieee.org/document/7430809/>
64. Song SM, Leahy RM. Computation of 3-D velocity fields from 3-D cine CT images of a human heart. *IEEE Trans. Med. Imaging.* 1991;10:295–306.
65. Nehmeh SA, Erdi YE, Pan T, Pevsner A, Rosenzweig KE, Yorke E, et al. Four-dimensional (4D) PET/CT imaging of the thorax. *Med. Phys.* 2004;31:3179–86.
66. Muzik O, Beanlands R, Wolfe E, Hutchins GD, Schwaiger M. Automated region definition for cardiac nitrogen-13-ammonia PET imaging. *J. Nucl. Med. Off. Publ. Soc. Nucl. Med.* 1993;34:336–44.
67. Khurshid K, Wu L, Berger K, McGough R. Automated PET/CT Cardiac Registration for Accurate Attenuation Correction. *IEEE; 2006 [cited 2017 Jan 16].* p. 409–14. Available from: <http://ieeexplore.ieee.org/document/4017730/>
68. Friston KJ, Ashburner J, Frith CD, Poline J-B, Heather JD, Frackowiak RSJ. Spatial registration and normalization of images. *Hum. Brain Mapp.* 1995;3:165–89.
69. Maes F, Collignon A, Vandermeulen D, Marchal G, Suetens P. Multimodality image registration by maximization of mutual information. *IEEE Trans. Med. Imaging.* 1997;16:187–98.

70. Bond S, Kadir T, Hamill J, Casey M, Platsch G, Burckhardt D, et al. Automatic registration of cardiac PET/CT for attenuation correction. *IEEE*; 2008 [cited 2017 Jan 16]. p. 5512–7. Available from: <http://ieeexplore.ieee.org/document/4774500/>
71. Studholme C, Hill DLG, Hawkes DJ. An overlap invariant entropy measure of 3D medical image alignment. *Pattern Recognit.* 1999;32:71–86.
72. Khurshid K, McGough RJ, Berger K. Automated cardiac motion compensation in PET/CT for accurate reconstruction of PET myocardial perfusion images. *Phys. Med. Biol.* 2008;53:5705–18.
73. Horn BKP, Schunck BG. Determining optical flow. *Artif. Intell.* 1981;17:185–203.
74. Dawood M, Buther F, Jiang X, Schafers KP. Respiratory motion correction in 3-D PET data with advanced optical flow algorithms. *IEEE Trans. Med. Imaging.* 2008;27:1164–75.
75. Gigengack F, Ruthotto L, Burger M, Wolters CH, Xiaoyi Jiang, Schafers KP. Motion Correction in Dual Gated Cardiac PET Using Mass-Preserving Image Registration. *IEEE Trans. Med. Imaging.* 2012;31:698–712.
76. Woo J, Tamarappoo B, Dey D, Nakazato R, Le Meunier L, Ramesh A, et al. Automatic 3D registration of dynamic stress and rest (82)Rb and flurpiridaz F 18 myocardial perfusion PET data for patient motion detection and correction. *Med. Phys.* 2011;38:6313–26.
77. Martinez-Möller A, Souvatzoglou M, Navab N, Schwaiger M, Nekolla SG. Artifacts from misaligned CT in cardiac perfusion PET/CT studies: frequency, effects, and potential solutions. *J. Nucl. Med. Off. Publ. Soc. Nucl. Med.* 2007;48:188–93.
78. Ye H, Wong K-P, Wardak M, Dahlbom M, Kepe V, Barrio JR, et al. Automated movement correction for dynamic PET/CT images: evaluation with phantom and patient data. *PLoS One.* 2014;9:e103745.
79. Turkington TG, DeGrado TR, Hanson MW, Coleman RE. Alignment of dynamic cardiac PET images for correction of motion. *IEEE Trans. Nucl. Sci.* 1997;44:235–42.
80. Slomka PJ, Diaz-Zamudio M, Dey D, Motwani M, Brodov Y, Choi D, et al. Automatic registration of misaligned CT attenuation correction maps in Rb-82 PET/CT improves detection of angiographically significant coronary artery disease. *J. Nucl. Cardiol. Off. Publ. Am. Soc. Nucl. Cardiol.* 2015;22:1285–95.
81. Slomka PJ, Rubeaux M, Meunier LL, Dey D, Lazewatsky JL, Pan T, et al. Dual-Gated Motion-Frozen Cardiac PET with Flurpiridaz F 18. *J. Nucl. Med.* 2015;56:1876–81.
82. Le Meunier L, Slomka PJ, Dey D, Ramesh A, Thomson LEJ, Hayes SW, et al. Motion frozen 18F-FDG cardiac PET. *J. Nucl. Cardiol.* 2011;18:259–66.
83. Fulton RR, Hutton BF, Braun M, Ardekani BA. Correction of gross patient motion artifacts in positron emission tomography. 1993 [cited 2016 Sep 21]. p. 166–70. Available from: <http://dx.doi.org/10.1117/12.146598>

84. Rahmim A, Bloomfield P, Houle S, Lenox M, Michel C, Buckley KR, et al. Motion compensation in histogram-mode and list-mode EM reconstructions: beyond the event-driven approach. *IEEE Trans. Nucl. Sci.* 2004;51:2588–96.
85. Thielemans K, Mustafovic S, Schnorr L. Image reconstruction of motion corrected sinograms. 2003 IEEE Nucl. Sci. Symp. Conf. Rec. 2003. p. 2401–2406 Vol.4.
86. W Zhou V, Kyme AZ, Meikle SR, Fulton R. A scheme for PET data normalization in event-based motion correction. *Phys. Med. Biol.* 2009;54:5321–39.
87. Verhaeghe J, Gravel P, Mio R, Fukasawa R, Rosa-Neto P, Soucy J-P, et al. Motion compensation for fully 4D PET reconstruction using PET superset data. *Phys. Med. Biol.* 2010;55:4063–82.
88. Mohy-ud-Din H, Karakatsanis NA, Ay MR, Endres CJ, Wong DF, Rahmim A. Generalized inter-frame and intra-frame motion correction in PET imaging - a simulation study. *IEEE*; 2011 [cited 2016 Sep 26]. p. 3858–62. Available from: <http://ieeexplore.ieee.org/lpdocs/epic03/wrapper.htm?arnumber=6153734>
89. Lamare F, Carbayo MJL, Cresson T, Kontaxakis G, Santos A, Rest CCL, et al. List-mode-based reconstruction for respiratory motion correction in PET using non-rigid body transformations. *Phys. Med. Biol.* 2007;52:5187–204.
90. Catana C. Motion correction options in PET/MRI. *Semin. Nucl. Med.* 2015;45:212–23.
91. Hamill JJ, Panin VY. TOF-MLAA for attenuation correction in thoracic PET/CT. *IEEE*; 2012 [cited 2017 Jan 16]. p. 4040–7. Available from: <http://ieeexplore.ieee.org/document/6551924/>
92. Dirac P a. M. A Theory of Electrons and Protons. *Proc. R. Soc. Lond. Math. Phys. Eng. Sci.* 1930;126:360–5.
93. Anderson CD. The Positive Electron. *Phys. Rev.* 1933;43:491.
94. ICRP. Radionuclide Transformations - Energy and Intensity of Emissions. *Ann. ICRP.* 1983;38.
95. Hunter CRRN, Hill J, Ziadi MC, Beanlands RSB, deKemp RA. Biodistribution and radiation dosimetry of <sup>82</sup>Rb at rest and during peak pharmacological stress in patients referred for myocardial perfusion imaging. *Eur. J. Nucl. Med. Mol. Imaging.* 2015;42:1032–42.
96. Grasty RL, LaMarre JR. The annual effective dose from natural sources of ionising radiation in Canada. *Radiat. Prot. Dosimetry.* 2004;108:215–26.
97. Suri J, Wilson D, Laxminarayan S. *Handbook of Biomedical Image Analysis: Volume 1: Segmentation Models Part A.* Springer Science & Business Media; 2005.
98. Zanzonico P. Positron emission tomography: a review of basic principles, scanner design and performance, and current systems. *Semin. Nucl. Med.* 2004;34:87–111.

99. Basics of PET Imaging - Physics, Chemistry, and Regulations | Gopal B. Saha | Springer [Internet]. [cited 2016 Aug 11]. Available from: <http://www.springer.com/us/book/9781489984715>
100. deKemp RA. Rubidium generator for cardiac perfusion imaging and method of making and maintaining same [Internet]. 2011 [cited 2016 Oct 27]. Available from: <http://www.google.com/patents/US8071959>
101. Beringer R, Montgomery CG. The Angular Distribution of Positron Annihilation Radiation. *Phys. Rev.* 1942;61:222.
102. Ramirez RA, Wong W-H, Kim S, Baghaei H, Li H, Wang Y, et al. A comparison of BGO, GSO, MLS, LGSO, LYSO and LSO scintillation materials for high-spatial-resolution animal PET detectors. *IEEE Nucl. Sci. Symp. Conf. Rec.* 2005. 2005. p. 2835–9.
103. Nikl M. Scintillation detectors for x-rays. *Meas. Sci. Technol.* 2006;17:R37.
104. Melcher CL. Scintillation crystals for PET. *J. Nucl. Med. Off. Publ. Soc. Nucl. Med.* 2000;41:1051–5.
105. Casey ME, Nutt R. A Multicrystal Two Dimensional BGO Detector System for Positron Emission Tomography. *IEEE Trans. Nucl. Sci.* 1986;33:460–3.
106. Handbook of Biomedical Image Analysis - Volume 1: Segmentation | David Wilson | Springer [Internet]. [cited 2016 Aug 13]. Available from: <http://www.springer.com/us/book/9780306485503>
107. Fahey FH. Data acquisition in PET imaging. *J. Nucl. Med. Technol.* 2002;30:39–49.
108. Turkington TG. Introduction to PET Instrumentation. *J. Nucl. Med. Technol.* 2001;29:4–11.
109. Prince JL, Links J. *Medical Imaging Signals and Systems*. 1 edition. Upper Saddle River, NJ: Prentice Hall; 2005.
110. Bettinardi V, Presotto L, Rapisarda E, Picchio M, Gianolli L, Gilardi MC. Physical performance of the new hybrid PET/CT Discovery-690. *Med. Phys.* 2011;38:5394–411.
111. Cherry SR, Meikle SR, Hoffman EJ. Correction and characterization of scattered events in three-dimensional PET using scanners with retractable septa. *J. Nucl. Med. Off. Publ. Soc. Nucl. Med.* 1993;34:671–8.
112. Bailey DL, Meikle SR. A convolution-subtraction scatter correction method for 3D PET. *Phys. Med. Biol.* 1994;39:411.
113. Ollinger JM. Model-based scatter correction for fully 3D PET. *Phys. Med. Biol.* 1996;41:153–76.

114. Watson CC, Newport D, Casey ME, deKemp RA, Beanlands RS, Schmand M. Evaluation of simulation-based scatter correction for 3-D PET cardiac imaging. *IEEE Trans. Nucl. Sci.* 1997;44:90–7.
115. Werling A, Bublitz O, Doll J, Adam L-E, Brix G. Fast implementation of the single scatter simulation algorithm and its use in iterative image reconstruction of PET data. *Phys. Med. Biol.* 2002;47:2947–60.
116. Watson CC, Casey ME, Michel C, Bendriem B. Advances in scatter correction for 3D PET/CT. 2004 IEEE Nucl. Sci. Symp. Conf. Rec. 2004. p. 3008–12.
117. Vandervoort E, Sossi V. An analytical scatter correction for singles-mode transmission data in PET. *IEEE Trans. Med. Imaging.* 2008;27:402–12.
118. Levin CS, Dahlbom M, Hoffman EJ. A Monte Carlo correction for the effect of Compton scattering in 3-D PET brain imaging. *IEEE Trans. Nucl. Sci.* 1995;42:1181–5.
119. Ye J, Song X, Hu Z. Scatter correction with combined single-scatter simulation and Monte Carlo simulation for 3D PET. 2014 IEEE Nucl. Sci. Symp. Med. Imaging Conf. NSSMIC. 2014. p. 1–3.
120. Holte S, Eriksson L, Dahlbom M. A preliminary evaluation of the scanditronix PC2048-15B brain scanner. *Eur. J. Nucl. Med.* 15:719–21.
121. Knoop BO, Jordan K, Spinks T. Evaluation of PET count rate performance. *Eur. J. Nucl. Med.* 15:705–11.
122. Smith RJ, Karp JS. A practical method for randoms subtraction in volume imaging PET from detector singles countrate measurements. 1995 IEEE Nucl. Sci. Symp. Med. Imaging Conf. Rec. 1995. 1995. p. 992–6 vol.2.
123. Spinks TJ, Guzzardi R, Bellina CR. Performance characteristics of a whole-body positron tomograph. *J. Nucl. Med. Off. Publ. Soc. Nucl. Med.* 1988;29:1833–41.
124. PET - Physics, Instrumentation, and Scanners | Michael E. Phelps | Springer [Internet]. [cited 2016 Aug 13]. Available from: <http://www.springer.com/gp/book/9780387323022>
125. Moncayo VM, Garcia EV. Prompt-gamma compensation in Rb-82 myocardial perfusion 3D PET/CT: Effect on clinical practice. *J. Nucl. Cardiol. Off. Publ. Am. Soc. Nucl. Cardiol.* 2016;
126. Positron Emission Tomography - Clinical Practice | Peter E. Valk | Springer [Internet]. [cited 2016 Aug 16]. Available from: <http://www.springer.com/la/book/9781852339715>
127. Moszynski M, Kapusta M, Wolski D, Szawlowski M, Klamra W. Energy resolution of scintillation detectors readout with large area avalanche photodiodes and photomultipliers. *IEEE Trans. Nucl. Sci.* 1998;45:472–7.
128. Weele DN ter, Schaart DR, Dorenbos P. Scintillation Detector Timing Resolution; A Study by Ray Tracing Software. *IEEE Trans. Nucl. Sci.* 2015;62:1972–80.

129. Lempicki A, Wojtowicz AJ, Berman E. Fundamental limits of scintillator performance. Nucl. Instrum. Methods Phys. Res. Sect. Accel. Spectrometers Detect. Assoc. Equip. 1993;333:304–11.
130. Eriksson L. A simple data loss model for positron camera systems. Nucl. Sci. Symp. Med. Imaging Conf. 1993 IEEE Conf. Rec. 1993. p. 1548–52 vol.3.
131. Moisan C, Rogers JG, Douglas JL. A count rate model for PET and its application to an LSO HR PLUS scanner. IEEE Trans. Nucl. Sci. 1997;44:1219–24.
132. Meunier LL, Mathy F, Fagret PD. Validation of a PET Monte-Carlo simulator with random events and dead time modeling. 2002 IEEE Nucl. Sci. Symp. Conf. Rec. 2002. p. 1108–12 vol.2.
133. Guerin B, Fakhri GE. Realistic PET Monte Carlo Simulation With Pixelated Block Detectors, Light Sharing, Random Coincidences and Dead-Time Modeling. IEEE Trans. Nucl. Sci. 2008;55:942–52.
134. Schmidtlein CR, Kirov AS, Nehmeh SA, Erdi YE, Humm JL, Amols HI, et al. Validation of GATE Monte Carlo simulations of the GE Advance/Discovery LS PET scanners. Med. Phys. 2006;33:198–208.
135. Count Rate Lost Model for D690 (Personal Communication with GE). 2015.
136. Yamamoto S, Amano M, Miura S, Iida H, Kanno I. Deadtime correction method using random coincidence for PET. J. Nucl. Med. Off. Publ. Soc. Nucl. Med. 1986;27:1925–8.
137. Buzug TM. Computed tomography: from photon statistics to modern cone-beam CT [Internet]. Berlin: Springer; 2008 [cited 2016 Nov 6]. Available from: <http://proxy.library.carleton.ca/login?url=http://books.scholarsportal.info/viewdoc.html?id=/ebooks/ebooks0/springer/2009-12-01/5/9783540394082>
138. Shima H. Functional Analysis for Physics and Engineering: An Introduction. CRC Press; 2016.
139. Prince JL, Willsky AS. Hierarchical reconstruction using geometry and sinogram restoration. IEEE Trans. Image Process. 1993;2:401–16.
140. Prince JL, Willsky AS. A geometric projection-space reconstruction algorithm. Linear Algebra Its Appl. 1990;130:151–91.
141. Welch A, Campbell C, Clackdoyle R, Natterer F, Hudson M, Bromiley A, et al. Attenuation correction in PET using consistency information. IEEE Trans. Nucl. Sci. 1998;45:3134–41.
142. Moses WW. Fundamental Limits of Spatial Resolution in PET. Nucl. Instrum. Methods Phys. Res. Sect. Accel. Spectrometers Detect. Assoc. Equip. 2011;648 Supplement 1:S236–40.
143. Radon J. On the determination of functions from their integral values along certain manifolds. IEEE Trans. Med. Imaging. 1986;5:170–6.
144. Bracewell RN. Strip Integration in Radio Astronomy. Aust. J. Phys. 1956;9:198.

145. Scudder HJ. Introduction to computer aided tomography. Proc. IEEE. 1978;66:628–37.
146. Bruyant PP. Analytic and Iterative Reconstruction Algorithms in SPECT. J. Nucl. Med. 2002;43:1343–58.
147. Thielemans K, Tsoumpas C, Mustafovic S, Beisel T, Aguiar P, Dikaios N, et al. STIR: software for tomographic image reconstruction release 2. Phys. Med. Biol. 2012;57:867–83.
148. Markiewicz P, Thielemans K, Burgos N, Manber R, Jiao J, Barnes A, et al. Image reconstruction of mMR PET data using the open source software STIR. EJNMMI Phys. 2014;1:A44.
149. Labbé C, Thielemans K, Zaidi H, Morel C. An object-oriented library incorporating efficient projection/backprojection operators for volume reconstruction in 3D PET. 1999.
150. Fuster BM, Falcon C, Tsoumpas C, Livieratos L, Aguiar P, Cot A, et al. Integration of advanced 3D SPECT modeling into the open-source STIR framework. Med. Phys. 2013;40:092502.
151. Marti-Fuster B, Erlandsson K, Falcon C, Tsoumpas C, Livieratos L, Ros D, et al. Evaluation of the novel 3D SPECT modelling algorithm in the STIR reconstruction framework: Simple vs. full attenuation correction. 2013 IEEE Nucl. Sci. Symp. Med. Imaging Conf. 2013 NSSMIC. 2013. p. 1–3.
152. Beisel T, Lietsch S, Thielemans K. A method for OSEM PET reconstruction on parallel architectures using STIR. 2008 IEEE Nucl. Sci. Symp. Conf. Rec. 2008. p. 4161–8.
153. Mustafovic S, Thielemans K. Additive and multiplicative versions of the maximum a posteriori algorithm with median root prior. 2001 IEEE Nucl. Sci. Symp. Conf. Rec. 2001. p. 1783–5 vol.3.
154. Goodd IJ, Gaskins RA. Nonparametric roughness penalties for probability densities. Biometrika. 1971;58:255–77.
155. Green PJ. On Use of the EM for Penalized Likelihood Estimation. J. R. Stat. Soc. Ser. B Methodol. 1990;52:443–52.
156. Bettinardi V, Pagani E, Gilardi MC, Alenius S, Thielemans K, Teras M, et al. Implementation and evaluation of a 3D one-step late reconstruction algorithm for 3D positron emission tomography brain studies using median root prior. Eur. J. Nucl. Med. Mol. Imaging. 2002;29:7–18.
157. Morris ED, Endres CJ, Schmidt KC, Christian BT, Muzic Jr. RF, Fisher RE. Chapter 23 - Kinetic Modeling in Positron Emission Tomography A2 - Wernick, Miles N. In: Aarsvold JN, editor. Emiss. Tomogr. [Internet]. San Diego: Academic Press; 2004 [cited 2016 Sep 4]. p. 499–540. Available from: <http://www.sciencedirect.com/science/article/pii/B9780127444826500260>
158. Castillo JP, Rui H, Basilio D, Das A, Roux B, Latorre R, et al. Mechanism of potassium ion uptake by the Na(+)/K(+)-ATPase. Nat. Commun. 2015;6:7622.

159. Lortie M, Beanlands RSB, Yoshinaga K, Klein R, DaSilva JN, deKemp RA. Quantification of myocardial blood flow with  $^{82}\text{Rb}$  dynamic PET imaging. *Eur. J. Nucl. Med. Mol. Imaging.* 2007;34:1765–74.
160. Klein R, Beanlands RSB, deKemp RA. Quantification of myocardial blood flow and flow reserve: Technical aspects. *J. Nucl. Cardiol. Off. Publ. Am. Soc. Nucl. Cardiol.* 2010;17:555–70.
161. Segars WP, Lalush DS, Tsui BMW. A realistic spline-based dynamic heart phantom. *IEEE Trans. Nucl. Sci.* 1999;46:503–6.
162. Garrity JM, Segars WP, Knisley S, Tsui BMW. Development of a dynamic model for the lung lobes and airway tree in the NCAT phantom. 2002 IEEE Nucl. Sci. Symp. Conf. Rec. 2002. p. 1858–62 vol.3.
163. Segars W, Tsui BM, Lalush DS, Frey EC, King MA, Manocha D. Development and application of the new dynamic Nurbs-based Cardiac-Torso (NCAT) phantom. *Coll. Nurs. Fac. Publ. Ser.* [Internet]. 2001;42. Available from: [http://scholarworks.umass.edu/nursing\\_faculty\\_pubs/86](http://scholarworks.umass.edu/nursing_faculty_pubs/86)
164. Comtat C, Kinahan PE, Defrise M, Michel C, Lartzien C, Townsend DW. Simulating whole-body PET scanning with rapid analytical methods. 1999 IEEE Nucl. Sci. Symp. 1999 Conf. Rec. 1999. p. 1260–4 vol.3.
165. Watson CC. New, faster, image-based scatter correction for 3D PET. 1999 IEEE Nucl. Sci. Symp. 1999 Conf. Rec. 1999. p. 1637–41 vol.3.
166. Wollenweber SD. Parameterization of a model-based 3-D PET scatter correction. *IEEE Trans. Nucl. Sci.* 2002;49:722–7.
167. Hunter CRRN, Klein R, Beanlands RS, deKemp RA. Patient motion effects on the quantification of regional myocardial blood flow with dynamic PET imaging. *Med. Phys.* 2016;43:1829–40.
168. Schwaiger M, Hutchins G. Quantification of regional myocardial perfusion by PET: rationale and first clinical results. *Eur. Heart J.* 1995;16 Suppl J:84–91.
169. Camici PG, Gropler RJ, Jones T, L'Abbate A, Maseri A, Melin JA, et al. The impact of myocardial blood flow quantitation with PET on the understanding of cardiac diseases. *Eur. Heart J.* 1996;17:25–34.
170. Kaufmann PA, Camici PG. Myocardial blood flow measurement by PET: technical aspects and clinical applications. *J. Nucl. Med. Off. Publ. Soc. Nucl. Med.* 2005;46:75–88.
171. Prior JO, Allenbach G, Valenta I, Kosinski M, Burger C, Verdun FR, et al. Quantification of myocardial blood flow with  $^{82}\text{Rb}$  positron emission tomography: clinical validation with  $^{15}\text{O}$ -water. *Eur. J. Nucl. Med. Mol. Imaging.* 2012;39:1037–47.
172. Ziadi MC, Dekemp RA, Williams K, Guo A, Renaud JM, Chow BJW, et al. Does quantification of myocardial flow reserve using rubidium-82 positron emission tomography facilitate detection of multivessel coronary artery disease? *J. Nucl. Cardiol.* 2012;19:670–80.

173. Burrell S, MacDonald A. Artifacts and Pitfalls in Myocardial Perfusion Imaging. *J. Nucl. Med. Technol.* 2006;34:193–211.
174. Klein R, Hunter C, Beanlands R, deKemp R. Prevalence of patient motion in dynamic PET. *Soc. Nucl. Med. Annu. Meet. Abstr.* 2011;52:2105.
175. Mohy-ud-Din H, Karakatsanis NA, Goddard JS, Baba J, Wills W, Tahari AK, et al. Generalized dynamic PET inter-frame and intra-frame motion correction - Phantom and human validation studies. 2012 IEEE Nucl. Sci. Symp. Med. Imaging Conf. NSSMIC. 2012. p. 3067–78.
176. Klein R, Renaud JM, Ziadi MC, Thorn SL, Adler A, Beanlands RS, et al. Intra- and inter-operator repeatability of myocardial blood flow and myocardial flow reserve measurements using rubidium-82 pet and a highly automated analysis program. *J. Nucl. Cardiol.* 2010;17:600–16.
177. Veress AI, Segars WP, Tsui BMW, Weiss JA, Gullberg GT. Physiologically realistic LV models to produce normal and pathological image and phantom data. 2004 IEEE Nucl. Sci. Symp. Conf. Rec. 2004. p. 4231–5.
178. Veress AI, Segars WP, Weiss JA, Tsui BMW, Gullberg GT. Normal and pathological NCAT image and phantom data based on physiologically realistic left ventricle finite-element models. *IEEE Trans. Med. Imaging.* 2006;25:1604–16.
179. Klein R, Beanlands RSB, deKemp RA. Quantification of myocardial blood flow and flow reserve: Technical aspects. *J. Nucl. Cardiol.* 2010;17:555–70.
180. Efseaff M, Klein R, Ziadi MC, Beanlands RS, deKemp RA. Short-term repeatability of resting myocardial blood flow measurements using rubidium-82 PET imaging. *J. Nucl. Cardiol.* 2012;19:997–1006.
181. Watabe H, Ikoma Y, Kimura Y, Naganawa M, Shidahara M. PET kinetic analysis--compartmental model. *Ann. Nucl. Med.* 2006;20:583–8.
182. Klocke FJ, Baird MG, Lorell BH, Bateman TM, Messer JV, Berman DS, et al. ACC/AHA/ASNC Guidelines for the Clinical Use of Cardiac Radionuclide Imaging—Executive Summary A Report of the American College of Cardiology/American Heart Association Task Force on Practice Guidelines (ACC/AHA/ASNC Committee to Revise the 1995 Guidelines for the Clinical Use of Cardiac Radionuclide Imaging). *Circulation.* 2003;108:1404–18.
183. Chun SY, Reese TG, Ouyang J, Guerin B, Catana C, Zhu X, et al. MRI-based nonrigid motion correction in simultaneous PET/MRI. *J. Nucl. Med. Off. Publ. Soc. Nucl. Med.* 2012;53:1284–91.
184. Rezaei A, Defrise M, Bal G, Michel C, Conti M, Watson C, et al. Simultaneous reconstruction of activity and attenuation in time-of-flight PET. *IEEE Trans. Med. Imaging.* 2012;31:2224–33.
185. Salomon A, Goedicke A, Schweizer B, Aach T, Schulz V. Simultaneous reconstruction of activity and attenuation for PET/MR. *IEEE Trans. Med. Imaging.* 2011;30:804–13.

186. WHO | World Health Statistics 2016: Monitoring health for the SDGs [Internet]. WHO. [cited 2016 Jul 4]. Available from: [http://www.who.int/gho/publications/world\\_health\\_statistics/2016/en/](http://www.who.int/gho/publications/world_health_statistics/2016/en/)
187. Hachamovitch R, Rozanski A, Shaw LJ, Stone GW, Thomson LEJ, Friedman JD, et al. Impact of ischaemia and scar on the therapeutic benefit derived from myocardial revascularization vs. medical therapy among patients undergoing stress-rest myocardial perfusion scintigraphy. *Eur. Heart J.* 2011;32:1012–24.
188. al ZM et. Does quantification of myocardial flow reserve using rubidium-82 positron emission tomography facilitate detection of multivessel coronary artery d... - PubMed - NCBI [Internet]. [cited 2016 Jul 4]. Available from: <http://www.ncbi.nlm.nih.gov/pubmed/22415819>
189. Schleyer PJ, O'Doherty MJ, Barrington SF, Morton G, Marsden PK. Comparing approaches to correct for respiratory motion in NH3 PET-CT cardiac perfusion imaging. *Nucl. Med. Commun.* 2013;34:1174–84.
190. Ouyang J, Li Q, Fakhri GE. MR-based Motion Correction for PET Imaging. *Semin. Nucl. Med.* 2013;43:60–7.
191. Huang C, Ackerman JL, Petibon Y, Brady TJ, El Fakhri G, Ouyang J. MR-based motion correction for PET imaging using wired active MR microcoils in simultaneous PET-MR: phantom study. *Med. Phys.* 2014;41:041910.
192. Veress AI, Segars WP, Tsui BMW, Weiss JA, Gullberg GT. Physiologically realistic LV models to produce normal and pathological image and phantom data. 2004 IEEE Nucl. Sci. Symp. Conf. Rec. 2004. p. 4231–5.
193. Veress AI, Segars WP, Weiss JA, Tsui BMW, Gullberg GT. Normal and pathological NCAT image and phantom data based on physiologically realistic left ventricle finite-element models. *IEEE Trans. Med. Imaging.* 2006;25:1604–16.
194. Ljungberg M, Strand S-E, King MA. Monte Carlo Calculations in Nuclear Medicine, Second Edition: Applications in Diagnostic Imaging. CRC Press; 2012.
195. Schmitz RE, Harrison RL, Stearns CW, Lewellen TK, Kinahan PE. Optimization of noise equivalent count rate performance for a partially collimated PET scanner by varying the number of septa. *IEEE Trans. Med. Imaging.* 2007;26:935–44.
196. Youden WJ. Index for rating diagnostic tests. *Cancer.* 1950;3:32–5.
197. Schisterman EF, Perkins NJ, Liu A, Bondell H. Optimal cut-point and its corresponding Youden Index to discriminate individuals using pooled blood samples. *Epidemiol. Camb. Mass.* 2005;16:73–81.
198. Moody JB, Murthy VL, Lee BC, Corbett JR, Ficaro EP. Variance Estimation for Myocardial Blood Flow by Dynamic PET. *IEEE Trans. Med. Imaging.* 2015;34:2343–53.